UNIVERSITY OF CALIFORNIA
RIVERSIDE

Investigating Chemical Transformations of Multicomponent Levitated Particles Using a Linear Quadrupole Electrodynamic Balance Coupled With Mass Spectrometry

A Dissertation submitted in partial satisfaction
of the requirements for the degree of

Doctor of Philosophy

in

Chemistry

by

Ravleen Kaur

March 2023

Dissertation Committee:
Dr. James F. Davies, Chairperson
Dr. Joseph Genereux
Dr. Haofei Zhang

The Dissertation of Ravleen Kaur is approved:

_____

_____

_____

Committee Chairperson

University of California, Riverside

ACKNOWLEDGMENTS

First and foremost, my sincere gratitude is to my Ph.D. advisor, Dr. James F. Davies for his pioneering leadership. I am very fortunate that he trusted me to expand upon his research work and present it at several conferences and seminar talks. I must acknowledge his enthusiasm, insightful guidance and invaluable experience that has helped me develop my innovative mind and problem-solving skills. I am always grateful for his outstanding inspiration, positive attitude, encouragement and trust in me. If I may, I would love to award him with the "World's Best Boss" title for being so calm, supportive and understanding of his staff's situations. A special thanks to all the past and current members of Davies Laboratory for their support, assistance and care throughout my time at UCR. A shout-out to my friend and ex-coworker, Chelsea Price, for the continued encouragement, and being my moral support.

I am indebted to many aerosol scientists whose past and ongoing research made my work possible. It was a privilege to be working with some scientists who contributed to my research work. A special thanks to Dr. Gary V. Berkel for his expert advice and contributions to the research work discussed in Chapter 4. I am thankful to have worked closely with Dr. Kevin Wilson and Ryan Reynolds for the studies discussed in Chapter 7. Another thanks to Dr. Kevin Wilson and Dr. Megan Willis for their invaluable insights for the work included in Chapter 3. Thank you to my lab members, Chelsea Price, Stephanie Salas and Bilal Shakoor for their contributions in research work discussed in Chapter 6.

I would like to extend my gratitude to my dissertation core committee, Dr. Joseph Genereux and Dr. Haofei Zhang, for their valuable time, encouragement and insightful suggestions throughout my research work. I am thankful to the Department of Chemistry at UC Riverside for acknowledging my research contributions in the analytical chemistry field and awarding me the “2022 Donald T. Sawyer Award”. I also want to thank UCR’s Metabolomics Core Facility for giving me the opportunity to advance my understanding of mass spectrometry. I also want to acknowledge the financial support from the ACS Petroleum Research Fund. Finally, I am grateful to everyone else who have supported me throughout my Ph.D. program.

COPYRIGHT ACKNOWLEDGEMENTS

DEDICATION

This thesis is wholeheartedly dedicated to my beloved husband, Vindeep Singh Kohli, and my caring dad, Manjeet Singh, who have been my constant source of inspiration. I am thankful to my husband for being my support system throughout the Ph.D. and motivating me immensely to achieve my desire of attaining a Doctorate Degree. The list of my husband's contributions is never ending. Without his love, support, delicious food and soothing head massages, this Ph.D. would not have been possible. Thank you and love you!

I want to extend my gratitude to my families, both my own and my in-laws, for always believing in me. Thank you to my grand maa, Surinder Kaur, for her blessings. A special thanks to my in-laws, Harinder Singh and Amarjit Kaur, for never forgetting to wish me good luck for the important events, continued support and applauding for me. A special feeling of gratitude to my parents, Manjeet Singh and Harvinder Kaur, for showering their unconditional love and always being there for me. Becoming an academic doctor was my dad's dream before it became mine. I would like to extend my thanks to my big brother, Parmeet, and his wife, Mandeep, for their moral and emotional support that has helped me to accomplish this research. The late-night calls with my mom and brother would help me ease my mind from challenging research tasks. I also want to thank my bro-in-law, Manpreet, for helping me practice my research talks and being so encouraging. A special mention must go to my little niece, Janice, for always being my cheerleader.

Last, but never the least, praises and thanks to the Waheguru, the Almighty, for always showering his blessings upon me that help me succeed professionally.

ABSTRACT OF THE DISSERTATION

Investigating Chemical Transformations of Multicomponent Levitated Particles Using a Linear Quadrupole Electrodynamic Balance Coupled With Mass Spectrometry

by

Ravleen Kaur

Doctor of Philosophy, Graduate Program in Chemistry
University of California, Riverside, March 2023
Dr. James F. Davies, Chairperson

Aerosol particles are ubiquitous in the Earth's atmosphere and play an important role in climate, air quality and health. The chemical composition of aerosol particles is complex and primarily associated with their source of origin. Once in the atmosphere, their composition is continuously evolving as a result of heterogeneous and photochemical transformations. Consequently, composition-dependent properties that define the physical state and optical characteristics are also continuously changing, with important consequences on the dynamics and impacts of aerosols in the atmosphere. Laboratory-based methods have allowed an extensive exploration of the physicochemical properties and chemical transformations of atmospheric aerosols. Single particle levitation methods are used to measure the microphysical properties of particles and connect with their evolving chemical composition. Properties such as size, hygroscopicity, phase morphology, and composition can be precisely measured by coupling levitation methods with analytical tools, such as mass spectrometry.

This dissertation describes the development of a new experimental platform connecting a linear quadrupole electrodynamic balance (LQ-EDB) with mass spectrometry (MS) that is capable of interrogating single levitated particles undergoing atmospherically relevant transformations. Two sampling methods, paper spray (PS) and an open port sampling interface (OPSI), were developed to ionize and transfer chemical analytes from levitated particles to the MS for compositional analysis. Laboratory studies were carried out to understand both non-reactive transformations and heterogeneous oxidation of levitated particles by precisely measuring their physical and optical properties as a function of evolving chemical composition. Non-reactive transformations include the particle-to-gas partitioning of semi-volatile species, while heterogeneous oxidation includes ozonolysis measurements on oleic and elaidic acid particles to understand the influence of particle phases on transformation kinetics and product distribution.

A key objective of this dissertation is to gain molecular-level understanding of how aerosol particles evolve due to chemical transformations and provide size-resolved detailed knowledge of their characteristics. It is essential to link the microphysical properties, composition, and reaction timescales for particles to quantify these evolving properties. Ultimately, the developments and measurements reported in this dissertation provide a foundation for exploring the chemistry of aerosol particles of complex composition and morphology to better understand their role in the environment.

TABLE OF CONTENTS

LIST OF FIGURES ..…..…..……...….**xviii**

LIST OF TABLES ..……...…**xxviii**

Chapter 1. Introduction ……..…..…..….**1**

1.1. Abstract ……1

1.2. Background on Aerosol Particles .....…….…….2

1.2.1. Aerosol Particles in the Atmosphere …….……3

1.2.1.1. Size Classification and Timescales of Aerosol Particles …….....5

1.2.1.2. Role and Impacts of Aerosol Particles …….…….…….....7

1.2.2. Aerosol Particles in the Health …….……...……...9

1.2.3. Aerosol Particles in the Industry …….…..…...11

1.3. Characteristics of Aerosol Particles …….....……12

1.3.1. Chemical Composition of Aerosol Particles ……13

1.3.2. Physical Characteristics of Aerosol Particles …….....15

1.3.2.1. The Phase State and Morphology …….…….…….15

1.3.2.2. Particle Size and Shape …….……16

1.3.2.3. Optical Properties of Aerosol Particles …….…….17

1.4. Chemical Transformations of Aerosol Particles ……..…19

1.4.1. Non-reactive transformations of Organic Aerosols ……...…...…...20

1.4.2. Heterogeneous Oxidation of Organic Aerosols ……...…...….21

1.5. Techniques to Study Aerosol Transformations ……..…….23

1.5.1. Ensemble Methods ……..……..……24

1.5.2. Single Particle Methods ……...……..……..….25

1.6. Thesis Aim and Overview ……..……...……..…….28

1.6.1. Research Motivation ……..……..……..….28

1.6.2. Research Significance ……...……..…….29

1.6.3. Thesis Outline ……..……30

1.7. References ……...……...……...……32

Chapter 2. Linear Quadrupole Electrodynamic Balance Coupled with Mie Resonance Spectroscopy and Mass Spectrometry to Study Chemical Transformations ……..….**48**

2.1. Abstract ……..….48

2.2. Linear Quadrupole Electrodynamic Balance (LQ-EDB) for Particle Levitation …...49

2.2.1. Controlled Conditions for Chemical Transformations on Particles 52

2.3. Mie Resonance Spectroscopy for the Analysis of Physical Characteristics ……....54

2.3.1. Online Monitoring of Size, Refractive Index and Morphology …….....….56

2.4. Mass Spectrometry (MS) for the Analysis of Chemical Composition ……....58

2.4.1. Particle Sampling and Ionization Sources to Couple LQ-EDB with MS ……..61

2.4.1.1. Paper Spray (PS) Ionization Source …….…….....62

2.4.1.2. Open Port Sampling Interface (OPSI) - Electrospray Ionization (ESI) Source …….……...65

2.4.2. Qualitative and Quantitative Analysis of Particle Composition ……...…67

2.5. Summary and Conclusions ……69

2.6. References ……71

Chapter 3. Paper Spray Mass Spectrometry for the Analysis of Picoliter Droplets…79

3.1. Abstract ……79

3.2. Introduction ……80

3.3. Experimental Section ……83

3.3.1. Chemicals and Sample Preparation ……83

3.3.2. Technique Design and Analytical Procedure ……84

3.3.3. Droplet Paper Spray ……86

3.3.4. Data Processing ……87

3.4. Results and Discussion ……87

3.4.1. Compositional Analysis of Single Analyte Droplets ……87

3.4.1.1. Chemical Identification ……87

3.4.1.2. Reproducibility ……90

3.4.1.3. Quantification ……94

3.4.2. Compositional Analysis of Binary Analyte Droplets ……97

3.4.2.1. Relative Intensity and Ionization Efficiency ……97

3.4.2.2. Evaluating the Relative Abundance ……99

3.5. Summary and Conclusions ……101

3.6. References ……104

Chapter 4. An Open Port Sampling Interface for the Chemical Characterization of Levitated Microparticles ……..…….**111**

4.1. Abstract ……111

4.2. Introduction …..……...……112

4.3. Experimental Section …..…….…..……..……113

4.3.1. Chemicals and Sample Preparation ..…….…….……...…...…113

4.3.2. Technique Design and Analytical Procedure ……...……..……114

4.4. Results and Discussion …….116

4.4.1. Experimental Conditions and Operation Parameters …..……...…116

4.4.2. Establishing the Analytical Performance of LQ-EDB-OPSI-MS …….....117

4.4.2.1. Signal Stability and Reproducibility ……...…….....117

4.4.2.2. Quantitation ……...……..121

4.5. Summary and Conclusions ……..….126

4.6. References ……...……128

Chapter 5. Measuring the Chemical Evolution of Levitated Particles: A Study on the Evaporation of Multicomponent Organic Aerosol …….…….**131**

5.1. Abstract ……131

5.2. Introduction …..…….…..……...…….132

5.3. Experimental Section …..…….…..……..……136

5.3.1. Chemicals and Sample Preparation …….....136

5.3.2. Technique Setup and Analytical Procedure ……...……...….137

5.3.2.1. Particle Levitation ……..……..137

5.3.2.2. Mie Resonance Spectroscopy ……...…...138

5.3.2.3. Paper Spray Mass Spectrometry ……...139

5.3.2.4. Errors and Uncertainty ……...……..143

5.4. Results and Discussion ……144

5.4.1. Evaporation under Dry Conditions ……...…...……..145

5.4.1.1. Analysis of Binary Particles ……...……..146

5.4.1.2. Analysis of Ternary Particles ……...……153

5.4.2. Evaporation under Humid Conditions ……...……155

5.5. Summary and Conclusions ……...160

5.6. References ……...……162

Chapter 6. Connecting the Phase State and Volatility of Single and Binary Component Dicarboxylic Acid Particles at Elevated Temperatures ….....….**170**

6.1. Abstract ……...……...……..……170

6.2. Introduction …..……..……..……...…....171

6.3. Experimental Section ……...175

6.3.1. Chemicals and Sample Preparation ……...……175

6.3.2. Technique Setup and Analytical Procedure ……...……176

6.3.3. Mie Resonance Spectroscopy ……178

6.3.4. Electrostatic Analysis ……...…….179

6.3.5. Mass Spectrometry Analysis ……...……..180

6.3.6. Evaporation Model ……...…….182

6.4. Results and Discussion ……..184

6.4.1. In-Situ Temperature Calibration ……184

6.4.2. Morphology and Vapor Pressure of Single Component Particles ……...…...188

6.4.2.1. Succinic Acid ……..……189

6.4.2.2. Adipic Acid ……..……191

6.4.2.3. Glutaric Acid ……192

6.4.2.4. Malonic Acid ……...…197

6.4.3. Morphology and Composition of Binary Component Particles …..…….....201

6.4.3.1. Malonic Acid and Succinic Acid Mixture ……...…….201

6.4.3.2. Succinic Acid and Glutaric Acid Mixture ……...…….203

6.4.3.3. Glutaric Acid and Adipic Acid Mixture ……...……204

6.5. Summary and Conclusions ……...205

6.5.1. Atmospheric Relevance ……..……209

6.6. References ……...……211

Chapter 7. Reaction Kinetics Dependence on the Phase State: A Comparison Between Cis and Trans Isomers Towards Ozonolysis on Levitated Particles ……..…..…**216**

7.1. Abstract ……..……..……216

7.2. Introduction …..……..……...…….217

7.3. Experimental Section ……...222

7.3.1. Single Particle Levitation ……..……...……..222

7.3.1.1. Chemicals and Sample Preparation ……..……222

7.3.1.2. Particle Levitation and Environmental Control ……223

7.3.1.3. Mie Resonance Spectroscopy ……...……...225

7.3.1.4. Compositional Analysis Using Mass Spectrometry ……...……..226

7.3.2. Flow-Tube Measurements ……227

7.3.2.1. Particle Generation and Characterization ……227

7.3.2.2. Flow Tube Reactor and Temperature Control ……...……...229

7.3.2.3. APCI Mass Spectrometry ……229

7.3.3. Kinetic Analysis ……..……...……...230

7.4. Results and Discussion ……231

7.4.1. Evolution of Size, Refractive Index and Phase State of Single Levitated Particles ……232

7.4.1.1. Oleic Acid ……...……232

7.4.1.2. Elaidic Acid ……...……..234

7.4.2. Chemical Evolution of Single Levitated Particles ……...……..236

7.4.3. Oleic Acid and Elaidic Acid Reaction Kinetics ……...……..237

7.4.4. Influence of Temperature on Phase and Kinetics …….……..241

7.4.5. Influence of Ozone Concentration and Relative Humidity ……243

7.5. Summary and Conclusions ……...245

7.6. References ……...……248

Chapter 8. Summary, Implications and Future Directions ……...….**257**

8.1. Thesis Summary and Conclusions ……...……257

8.2. Wider Implications of this research ……..261

8.3. Future Directions ……...……..…..……...…263

8.4. References ……...……266

LIST OF FIGURES

Chapter 1. Introduction ……...**1**

Figure 1: Natural and anthropogenic sources of the aerosol particles in the atmosphere. Natural sources like sea spray and volcanic eruptions emit mostly primary aerosol particles (PAPs) while anthropogenic sources like biomass burning and industries generate PAPs through direct emissions and secondary aerosol particles (SAPs) through gas-to-particle conversion of low volatility chemical compounds ……...**4**

Figure 2: Schematic distribution of various aerosol particle modes in the atmosphere depending on their size and lifetime. The sources of origin and processes of formation of these different aerosol particle modes have been described in detail in the text ……..….**5**

Figure 3: Physicochemical transformations, such as heterogeneous oxidation, of primary and secondary aerosols along with their direct and indirect effects in atmosphere ……...**9**

Figure 4: Breakdown of the average global chemical composition of the ambient aerosol particles into organic and inorganic subsets. These subsets are further broken down into their further classifications along with their average abundances, as explained in text …..**13**

Figure 5: A schematic representation of the different phase morphologies associated with aerosol particles. The ambient aerosol particles can exhibit either homogeneous or phase separated morphologies as shown in the figure. The phase state and morphologies can interchange with each other depending on the surrounding environmental conditions and the particle composition ……**16**

Figure 6: An overview of the light interaction with a spherical aerosol particle resulting in various optical processes, such as diffraction, refraction, absorption, reflection and scattering. These properties depend on chemical composition and physical state of the particle ……...**18**

Chapter 2. Linear Quadrupole Electrodynamic Balance Coupled with Mie Resonance Spectroscopy and Mass Spectrometry to Study Chemical Transformations ……..….**48**

Figure 1: An arrangement of droplet piezoelectric droplet dispenser with the induction electrode mounted on the LQ-EDB. The solvent filled in glass capillary inside the dispenser is propelled out as liquid jet which forms a droplet caused by a temporary deformation of piezo material due to the application of pulse voltage. This jet and the droplet then get

positively charged due to the coulombic repulsions caused by negative potential maintained at the induction electrode mounted on the LQ-EDB. Finally, the charge on droplets helps in levitating them inside the LQ-EDB chamber ……**50**

Figure 2: A linear quadrupole electrodynamic balance (LQ-EDB) showing a stack of multiple droplets, AC parallel electrodes and DC disc electrode. The AC voltage arrangement applied to diagonally opposite pair of electrodes, and a 532 nm laser beam for particles illumination is shown. The lowermost droplet is imaged individually by adjusting the position of the entire stack .....…**51**

Figure 3: Schematic configuration of Mie Resonance Spectrometry (MRS) for the characterization of a spherical particle's physical properties, such as size and RI ……..**55**

Figure 4 : The interaction of broadband light from red LED with the spherical particle is shown which results in the phenomenon of total internal reflection generating the backscattered light as described in the text. Figure 4A presents a comparison of the morphology dependent resonance (MDR) peak structure of the best-fit theoretical prediction (red) and experimental measurement (black) in the Mie resonance spectrum ...**56**

Figure 5 : A comparison between the Mie resonance spectra of the levitated particle before (black) and after (red) a chemical transformation which leads to the changes in particle's morphology. The spectrum presented in black shows the sharp peaks indicative of a spherical and homogeneous particle which undergoes liquid-liquid phase separation (LLPS) as a result of a reaction. The spectrum becomes distorted due to peak broadening following LLPS, depicted as red spectra, as a result of the morphological transformations that interrupt the sharp peak structure ……...**58**

Figure 6: Paper spray (PS) setup coupled to MS for sampling and ionizing the analytes in the sample particles ejected from LQ-EDB. Periodic measurements of the composition related to lowermost particle at a time in LQ-EDB is carried out to determine the transformation parameters. Paper substrate is maintained at a high voltage with continuous supply of solvent to ionize the analytes present in the sample particles which are subsequently vaporized as they travel towards the MS heated inlet for their compositional analysis ……..**64**

Figure 7: Illustration of open port sampling interface (OPSI) coupled with the conventional heated electrospray ionization (ESI) source of Orbitrap mass spectrometer (MS). The schematic demonstrates the particle transfer from LQ-EDB into the OPSI interface for real-time analysis of its composition by MS without the need of any sample preparation ……..……..…**65**

Figure 8: (A) Representative mass spectrum of a single citric acid particle for its compositional analysis. The red signals in the mass spectrum represent the background

before the compositional analysis of the particle while the black signals in the mass spectrum represent the composition of a single citric acid particle. (B) The mass chronograms show the droplet deposition event for three consecutive citric acid droplets at 191 m/z depicting the parent ion ……..……...**69**

Chapter 3. Paper Spray Mass Spectrometry for the Analysis of Picoliter Droplets…**79**

Figure 1: Schematic configuration of the paper spray ionization source coupled to the mass spectrometer. Droplets are deposited on-demand from a microdispenser above the paper at locations near the solvent delivery tube (position A), towards the tip (position B) and at the tip (position C). The MS inlet extension improves the ion collection efficiency in the absence of heated gases, serving to funnel the ions and aid in evaporation of the electrospray plume. The PS-MS interface is housed within a 3D printed enclosure with the paper protruding into the open lab environment …….……...…**85**

Figure 2: (A) A sequence of single five citric acid (CA) solution droplets as obtained by the extracted ion chronogram of the ion of interest. The droplets have an approximate diameter of ~50 µm and a concentration of 1 g/L (65 pg of CA) were sampled by PS-MS. The counts correspond to the intensity of the molecular ion peak for citric acid ($C_6H_7O_7^-$). (B) The background mass spectrum measured in the paper spray. (C) The mass spectrum corresponding to the peak intensity from a single droplet of citric acid. Note that the axis range is 40X larger than in Figure 2B ……...……..…**88**

Figure 3: Mass spectra obtained for single droplets deposited on the paper for equimolar mixtures of dicarboxylic acids (A), polyethylene glycols (t = tetra, p = penta, h = hexa, EG = ethylene glycol) (B) and oleic acid (and its configurational isomer elaidic acid) (C). The acids were sampled in negative ionization mode, while the glycols were sampled in positive mode and the spectra shows peaks corresponding to $M+H^+$, $M+NH^{4+}$ and $M+Na^+$ …...…**90**

Figure 4: (A) For the citric acid solution droplets as Figure 2, the peak area corresponding to the molecular ion was found, shown here for each individual droplet in a sequence of 10. Two datasets are shown for the same solution, and the differences can be attributed to the variations in the system on an experiment-by-experiment basis, as discussed in the text. The solid blue lines shows the average while the dash lines represent an uncertainty range of one standard deviation. (B) The citric acid chromatograms were ratioed against the bisulphate (HSO_4^-) chromatogram, a consistent background peak in the paper spray. The average peak area ratio for the two experiments converge, although the signal variability increases due to the variability of the relatively low intensity bisulphate signal. The solid lines show the average while the dash lines show the new standard deviation range associated with the ratio ……..……...…**91**

Figure 5: The signal from a single droplet exhibits a time-dependence that varies with deposition location. Position C, at the tip of the paper, shows the highest intensity in the

peak, while position A, far from the tip, has the longest duration. Position B, around 1mm from the tip and used throughout this study, shows the highest integrated peak area …....**92**

Figure 6: The integrated peak area of citric acid sampled from droplets as a function of analyte mass increases linearly over a mass range of at least two orders of magnitude. The analyte mass was varied by deposition of between 1 and 200 droplets of a 0.01 g/L citric acid solution in burst method, as discussed in the text. Each line represents data collected during different experiments on different days using the same solution. The inter-experimental variability is discussed in the text. (Inset) Low mass range analysis with higher resolution also shows linearity ……...…….**95**

Figure 7: The integrated peak area of citric acid sampled from droplets as a function of analyte mass sampled using methanol as the PS solvent. The analyte mass was varied by deposition of between 1 and 200 droplets of a 0.01 g/L citric acid solution in burst method, as discussed in the manuscript text. Each color represents data collected during different experiments. The inter-experiment variability is discussed in the text, but unlike the data shown in Figure 5, these data do not exhibit linearity of signal with analyte mass …….**96**

Figure 8: (A) Chromatogram of peaks corresponding to single droplets containing citric acid (red) and maleic acid (black) in an equimolar mixture. (B) Mass spectrum showing contribution from citric acid (191.02) and maleic acid (115.00) molecular ions. (C) Ionization efficiency (as defined in the text) determined for maleic acid and citric acid as a function of total analyte mass for experiments in burst mode and single droplet mode. Both methods exhibit a trend towards an ionization efficiency of ~1.5 with total analyte mass >0.1 ng ……...……....**98**

Figure 9: (A) The ratio of maleic acid (MA) to citric acid (CA) peak areas is shown as a function of the molar ratio in the droplet. A linear trend with a slope of 0.54 is observed up to n_MA \/n_CA≈2, but beyond that some deviation is observed (inset: black dash line shows the fit up to n_MA \/n_CA≈2 versus a linear fit to all the data shown as a gray dash line). Taking a linear fit to the data up to n_MA \/n_CA≈2, an ionization efficiency of 1.84 is determined. (B) The peak area of MA as a fraction of the total peak area from CA and MS is shown as a function of mole fraction of MA in the droplet (black points). The curvature arises due to the ionization efficiency effects. Accounting for the ionization efficiency using the slope of the data in Figure 9A and equation 3, the mole fraction can be estimated (red points) using equation 1. The 1:1 line is shown as a red dash ……....**101**

Chapter 4. An Open Port Sampling Interface for the Chemical Characterization of Levitated Microparticles ……..…….**111**

Figure 1: Schematic configuration of the linear quadrupole electrodynamic balance coupled with the open port sampling interface for the compositional analysis using mass spectrometry analysis ……..**115**

Figure 2: (A) A sequence of five citric acid (CA) particles, with each peak arising from an ejected particle sampled by OPSI probe and delivered to conventional ESI-MS for its compositional analysis. At a solvent flow rate of 50 μL / min, and with signal persisting for ~20 s, the dilution factor of a 5 μm particle is estimated to be on the order of 1 in 10^7. (B) Integrated peak areas for the molecular ion for individual CA particles measured over 6 hours. Open circle points represent individual CA particles sampled by OPSI using continuous solvent flow throughout the experiment, whereas solid circle points represent individual CA particles sampled using periodic (on/off) flow of solvent ……..…....**118**

Figure 3: Background corrected mass spectra for a single particle of citric acid (A), maleic acid (B) and tetraethylene glycol (C) sampled by OPSI-MS. The mass spectra correspond to the peak intensity from a single particle of respective sample ……...……...**120**

Figure 4: Compositional evolution in terms of relative mass for consecutive tetraethylene glycol (TEG) particles evaporating under dry conditions (0% RH). The compositional analysis was carried out by the mass spectrometer. The solid line shows the data output from model simulation while the open circle points correspond to the experimental observation and show the relative analyte mass calculated from the integrated peak intensities, as described in the text. Error bars indicate a ±5% uncertainty ….....…..**121**

Figure 5: Size evolution of an evaporating tetraethylene glycol particle in dry conditions as measured by Mie resonance spectrometer. Plot is made up of 8 similar sized particles that were introduced into the trap at t = 0 s. Individual particles were ejected and sampled by the OPSI-MS at the times indicated in Figure 3 ……...**122**

Figure 6: (A) Compositional evolution of evaporating tetraethylene glycol (TEG) particles evaporating in a range of RH conditions. The compositional analysis was carried out by the mass spectrometer. (B) Size evolution of evaporating tetraethylene glycol particles evaporating in a range of RH conditions as measured by Mie resonance spectrometer …**123**

Figure 7: Integrated peak areas for CA, MA, and TEG single particles with the mass derived from the size of the particles as measured using Mie resonance spectroscopy. The dashed lines indicate linear fits constrained to a zero y-intercept ……..…...…**124**

Figure 8: Background corrected mass spectra for a single particle of citric acid (A), maleic acid (B) and tetraethylene glycol (C) sampled by OPSI-MS. The mass spectra correspond to the peak intensity from a single particle of respective sample. Note y-axis has a different range in each spectrum which is based on the abundance of individual sample particle ...**125**

Chapter 5. Measuring the Chemical Evolution of Levitated Particles: A Study on the Evaporation of Multicomponent Organic Aerosol ……..……**131**

Figure 1: Schematic configuration of the linear quadrupole electrodynamic balance (LQ-

EDB) coupled with paper-spray mass spectrometer (PS-MS) for studying physicochemical trans-formations on single levitated particles. A stack of 5 to 10 particles is levitated in the LQ-EDB, and the lowermost particle is probed using Mie resonance spectroscopy. The same particle is then ejected to paper spray platform for sampling in the mass spectrometer for compositional analysis. This is followed by periodic measurements of subsequent particles in the levitated stack …….....**138**

Figure 2: Mie resonance spectrum for a 3655 nm (radius) particle with an RI of 1.468 at a wavelength of 589 nm, as determined from the peak positions. The black line shows the intensity- normalized experimental spectrum, while red line shows predicted spectrum using Mie theory ……..**139**

Figure 3: Mass chromatogram showing $M+Na^+$ ion intensity for each n-EG compound (3-EG, 4-EG and 6-EG) in three evaporating levitated ternary particles ejected for PS-MS analysis at 0.5 mins, 3 mins, and 7.5 mins. The peak intensities corresponding to the 3-EG and 4-EG components decrease as a result of their evaporation from the particles while the peak intensity of 6-EG component increases due to its enhanced abundance with time ...**141**

Figure 4: (A) Background mass spectrum recorded prior to particle sampling. (B) Mass spectrum recorded at the peak of particle signal for a ternary mixture of 3, 4, and 6-EG, indicated by green, blue and red boxes, respectively. Each component has a set of peaks in the mass spectrum due to the H^+, Na^+, and NH_4^+ adducts of respective n-EGs ….……..…**142**

Figure 5: Evaporation of a pure hexaethylene glycol (6-EG) particle under the dry conditions …….....**143**

Figure 6: (A) Size evolution of consecutive binary 3-EG particles evaporating in the levitated particle stack under dry conditions. The trend in the size evolution was obtained with the help of Mie resonance spectroscopy. The time of ejection of each particle corresponds to the points in panel B. (B) Mass ratio of 3-EG relative to 6-EG, calculated from the PS-MS signal as described in the Experimental Section, during evaporation. In both plots, individual black points correspond to the experimental observations, and the red dashed line is the model prediction, as described in the Experimental Section ……...**146**

Figure 7: Functional group breakdown of 3-EG, 4-EG, and 6-EG (top to bottom) used in the AIOMFAC predictions described in the text. Some ambiguity on assignment of alkyl groups next to ethers may lead to some errors, but minimal differences were observed in model output ……**149**

Figure 8: (A) Size evolution of consecutive binary 4-EG particles evaporating in the levitated particle stack under dry conditions. (B) Mass ratio of 4-EG relative to 6-EG for particles undergoing evaporation, calculated as described in the Experimental Section. In both plots, individual black points correspond to the experimental observations, and the red dashed line is the model prediction, as described in the Experimental Section …...…**152**

Figure 9: (A) Size evolution of consecutive ternary 3-EG and 4-EG particles evaporating in the levitated particle stack under dry conditions. Individual black points correspond to the experimental observations, and the red dashed line is the model prediction. (B) Mass ratios of 3-EG and 4-EG relative to the internal standard (6-EG). 3-EG is shown in green and 4-EG is shown in blue, with their respective model predictions given by dashed lines of the same colors ……....**154**

Figure 10: (A) Size evolution of consecutive binary 3-EG particles evaporating under 25, 50, and 75% RH conditions. (B) Composition evolution of 3-EG relative to the internal standard (6-EG) during evaporation under each RH. Model predictions are shown by dashed lines in both panels and use the activity coefficients reported in Table 2 ……..…**157**

Figure 11: (A) Size evolution of consecutive binary 4-EG particles evaporating under 25, 50, and 75% RH conditions (B) Composition evolution of 4-EG relative to the internal standard (6-EG) during evaporation under each RH. Model predictions are shown by dashed lines in both panels and use the activity coefficients reported in Table 2 ……..…**158**

Figure 12: (A) Size evolution of consecutive binary 3-EG particles evaporating under 25, 50, and 75% RH conditions (B) Composition evolution of 3-EG relative to the internal standard (6-EG) during evaporation under each RH. Model predictions are shown by dashed lines in both panels assuming an activity coefficient of 1 ……..……**159**

Chapter 6. Connecting the Phase State and Volatility of Single and Binary Component Dicarboxylic Acid Particles at Elevated Temperatures ……..…....**170**

Figure 1: (A) Mass spectra recorded for a binary mixture of succinic acid and glutaric acid. Red data represents the mass spectrum recorded prior to particle sampling whereas black data represents the mass spectra of the individual chemical species recorded during MS analysis of particle composition. Note that the y-axis corresponds to the relative abundance of each acid in the same particle. (B) Extracted ion chronogram of the peaks corresponding to glutaric acid present in a mixture with succinic acid. The counts correspond to the intensity of the molecular ion peak relating to the glutaric acid. The intensity decreases with time as a result of the evaporation of the glutaric acid from the particles ….……**181**

Figure 2: (A) Radius evolution of glycerol particles evaporating at temperatures from 303 – 323 K using MRS. (B) Temperature dependence on evaporation rate with the influence of size omitted ……...……..**186**

Figure 3: (A) The evaporation of a glycerol particle was used to derive the temperature in the LQ-EDB. Determination of the actual temperature inside the LQ-EDB using the linear relationship between calculated and set temperature. (B) The vapor pressure trend of 1,2,6-hexanetriol is shown as a function of temperature for our data and that of Logozzo and Preston. Figure inset shows the calculated value for the enthalpy of vaporization of 1,2,6-

hexanetriol using the linear slope of $\log_e(P_{sat})$ versus 1/T for our data. See text for a discussion of the connection with the data reported by Logozzo and Preston …….....**187**

Figure 4: The experimentally determined vapor pressure as a function of temperature for: (A) Succinic acid, and (B) Adipic acid. Inset figures show Clausius-Clapeyron plots (note that the y-axis is represented with $\log_{10}$ rather than $\log_e$) along with enthalpy of sublimation derived from the linear slope of $\log_e(P_{sat})$ and 1/T. Error bars represent the standard deviation in the vapor pressure values for repeat measurement at each temperature ….....**191**

Figure 5: Comparison of the normalized DC voltage from a non-spherical (black) and spherical (red) glutaric acid particle as derived from the respective electrostatic analysis. Over the same period, spherical particles evaporate much quicker than their non-spherical counterpart ……...…**194**

Figure 6: Comparison of Mie resonance spectra for a non-spherical (back) and spherical (red) glutaric acid particle. Absence of sharp peaks in the Mie resonance spectrum indicates a non-spherical particle ……...…….**195**

Figure 7: (A) Comparison between the derived vapor pressures for both spherical (red) and non-spherical (black) glutaric acid particles. The non-spherical vapor pressures were consistently lower than the spherical particle vapor pressures across all temperatures due to the differences in morphology. (B) The enthalpy of sublimation for both spherical and non-spherical morphologies of glutaric acid was calculated using the linear relationship between $\log_e P_{sat}$ and 1/T. Again, non-spherical enthalpies were lower at each temperature compared to spherical particles and error bars represent their respective standard deviation in the vapor pressure values for different measurement trials at each temperature ……...**196**

Figure 8: The evaporation of malonic acid over 3000s showed an evolution in both the radius and refractive index (RI) as described by the Mie resonance spectroscopy. Three distinct slopes were observed which are marked by the shaded region. This also corresponds to a simultaneous increase in RI over the course of the measurement ……..**197**

Figure 9: (A) A comparison of the derived vapor pressure for the first (black) and second (red) slopes observed during the evaporation of MA. The second slope vapor pressure is lower than the first slope due to their difference in evaporation rate. (B) Relationship between $\log_e(P_{sat})$ and 1/T for four different phases attributed to three distinct MA polymorphs (black, red, and blue) and the MA solid phase (green). The corresponding enthalpy of vaporization was derived for both slopes 1 and 2 ……..……**199**

Figure 10: (A) The compositional evolution of malonic acid (MA) due to its evaporation in the levitated particle stack under dry conditions. (B) The compositional evolution of succinic acid (SA) due to its evaporation in the levitated particle stack under dry conditions. In both plots, the color coded data points represent the evaporation trends at specific

temperatures as listed on the right side of the figures. The fit to the data points is shown by the dashed lines corresponding to respective data points having same color coding ……**202**

Figure 11: (A) The compositional evolution of succinic acid (SA) due to its evaporation in the levitated particle stack under dry conditions. (B) The compositional evolution of glutaric acid (GA) due to its evaporation in the levitated particle stack under dry conditions. In both plots, the color coded data points represent the evaporation trends at specific temperatures as listed on the right side of the figures. The fit to the data points is shown by the dashed lines corresponding to respective data points having same color coding ……...**204**

Figure 12: (A) The compositional evolution of glutaric acid (GA) due to its evaporation in the levitated particle stack under dry conditions. (B) The compositional evolution of adipic acid (AA) due to its evaporation in the levitated particle stack under dry conditions. In both plots, the color coded data points represent the evaporation trends at specific temperatures as listed on the right side of the figures. The fit to the data points is shown by the dashed lines corresponding to respective data points having same color coding ……...**205**

Chapter 7. Reaction Kinetics Dependence on the phase state: A comparison between cis and trans isomers towards ozonolysis on levitated particles ……..…**216**

Figure 1: Schematic configuration of the ozonolysis setup including the linear quadrupole electrodynamic balance (LQ-EDB) coupled with mass spectrometer (MS) using open port sampling interface (OPSI) for studying ozonolysis on single levitated particles. A dry or humid flow of nitrogen with ozone generated from a photochemical ozone generator was introduced into the LQ-EDB for initiating heterogeneous transformation. A stack of 5 to 10 particles underwent ozonolysis at the same time, and the lowermost particle was probed in real-time using broadband spectroscopy and then ejected to the OPSI platform for sampling by mass spectrometry ……...…**225**

Figure 2: Flow-tube experimental apparatus showing the particle generation, ozone generation, temperature control using a recirculating pump and thermostatic bath, a DMA and CPC for characterizing particle size distributions, and the atmospheric pressure chemical ionization (APCI) source on the mass spectrometer. A full description of the apparatus is provided in the text ……...…**228**

Figure 3: (A) Size and RI evolution of liquid OA particles exposed to 2.3 ppm of O_3 under dry conditions. The black points correspond to the sequentially measured radius of all particles in the stack, and the blue points correspond to the RI of the particles. The accuracy of size is determined to be within 5 nm and the RI is within 0.001 to 0.005 for homogeneous and spherical particles. The green shaded region in indicates where LLPS occurs, with the spectra degrading and leading to much larger scatter in the size and RI. (B) Mie resonance spectra before and after ozonolysis of OA shows clear peaks indicative of a homogeneous spherical particle initially that becomes distorted following LLPS, consistent with the

formation of surface islands due to product formation that interrupt the spherical cavity. (C) Size and RI evolution of supercooled liquid EA particles exposed to 2.3 ppm of O_3 under dry conditions. (D) Mie resonance spectra before and after ozonolysis of EA particles, showing a spherical homogeneous morphology is retained ……..**233**

Figure 4: (A) Mass spectra of oleic acid particles with a diameter of ~10 μm before and after ozonolysis. The black data represents mass spectrum before the start of ozonolysis reaction whereas the red data represents mass spectrum after ozonolysis. (B) Mass chronograms show the time-dependent ion intensity of $[M-H]^-$ signal for a decrease in oleic

acid reactant peaks (281 m/z, black) with simultaneous increase of first-generation product peaks, such as 9-oxononanoic acid (m/z 171) and azelaic acid (m/z 187 m/z) ……**236**

Figure 5: Normalized intensity of reactant and 1st generation products in OA (A) and supercooled EA (B) for particles with a starting diameter of ~10 μm exposed to 4.1 ppm of ozone. Note the x-axis reflects the ozone exposure in units of concentration (ppm) × time (s). The solid lines reflect exponential decay fits to the data as discussed in text …..**237**

Figure 6: (A) A comparison of the decay of supercooled liquid EA particles compared to solid EA particles under the same reaction conditions. The solid lines represent an exponential fit. The inset figure C shows the signal for products AA (m/z 187) and ONA (m/z 171) for the solid particle. (B) A comparison of the decay of homogeneously frozen EA particles at -20 °C and supercooled liquid EA at 20 °C, along with inset figures D and E showing the AA and ONA signal for frozen and supercooled particles respectively. Note that compositional analysis was carried out with help of mass spectrometry technique ...**240**

Figure 7: Uptake coefficients from temperature-controlled flow tube reactor studies. Red open circles correspond to measurements of oleic acid, and green open shapes correspond to measurements of elaidic acid with (diamond) and without (circle) the precooling step described in the experimental section. Shaded horizontal regions show the linear quadrupole electrodynamic balance (LQ-EDB) measurements for comparison, the vertical size of the bar indicating the uncertainty. We use the term "solid" here, although care should be taken with this description as described in the text ……..….**242**

Figure 8: (A) Comparison of uptake coefficients for liquid OA and supercooled EA undergoing ozonolysis as a measure of varying ozone concentrations under dry conditions using MS. (B) Comparison of uptake coefficients for liquid OA and supercooled EA undergoing ozonolysis as a measure of varying relative humidity at 2.3 ppm of ozone. For both sets of measurements, liquid OA data is represented as red open circles and supercooled EA data is represented as green open circles. The error bars represent the standard deviations based on repeated trials at similar experimental conditions ……..…**244**

LIST OF TABLES

Chapter 5. Measuring the Chemical Evolution of Levitated Particles: A Study on the Evaporation of Multicomponent Organic Aerosol ……..…….**131**

Table 1: Experimental conditions, such as RH, temperature, and, starting n-EG mass ratios and water mole fractions, for measurements reported in this study. The mole fractions of water are estimated using AIOMFAC predictions for single component aqueous solutions and ZSR mixing rules, as described in the text ……..……**145**

Table 2: Physicochemical properties of the n-EG molecules studied. The vapor pressure is taken from Price et al.,[65] the gas phase diffusion coefficients from Krieger et al.,[70] and the activity coefficients at each RH are determined from the measurements, as described in the text. x_i is the mole fraction of i when a particle containing pure i is exposed to a specific RH, as determined from AIOMFAC and explained in greater detail in the text ……...…**151**

Chapter 6. Connecting the Phase State and Volatility of Single and Binary Component Dicarboxylic Acid Particles at Elevated Temperatures …….…....**170**

Table 1. Values for the collision diameter (σ**)** and collision integral (Ω) used to calculate the diffusion coefficient (D_i) for all compounds (MA, SA, GA, AA). See references in the main text ……..….**183**

Table 2: Summary of particle morphology at each temperature for each diacid as determined by Mie resonance spectroscopy. 'C' represents crystalline morphology whereas 'A' represents amorphous morphology. Note that Mie resonance sizing was performed for only amorphous particles, whereas electrostatic analysis was performed for both amorphous and crystalline particles ……**189**

Table 3: Summary of all data corresponding to the measurements and relevant literature. Literature values were obtained from Bilde et al.[11] from their comprehensive analysis and averaging of the literature data. We refer readers to the reference contained therein for original sources ……...……**206**

CHAPTER 1

Introduction

1.1. Abstract

Aerosol particles are an important component in many fields of scientific interest. They are ubiquitous in the Earth's atmosphere and consequently affect the radiation budget, determine cloud properties, provide surfaces for chemical reactions, and negatively impact air quality and human health. Along with atmospheric implications, aerosol particles contribute immensely to various industrial processes and household applications. A major area of focus in present day aerosol research is understanding the dynamics associated with evolving physicochemical properties and associated role of these aerosol particles. This chapter provides a general description of aerosol particles, including their significance in the atmosphere, health, and industry. This is followed by a brief overview of prior research developments relating to ensemble and single particle methods for examining the chemical transformations of aerosol particles. Finally, a discussion on the motivation for aerosol research and overall significance of our research work provides a basis for the studies included in this dissertation.

1.2. Background on Aerosol Particles

Aerosol particles* are defined as fine particles suspended in air or gas, having a size between a few nanometers to several tens of micrometers.[1] They play a key role in numerous areas of science, including various atmospheric and industrial processes.[2–4] The term "aerosol" has been presumably associated with Frederick G. Donnan during World War I to describe clouds of microscopic particles in the air with relation to the chemical smokes used in military applications.[5] Since then, these particles have been a subject of growing research importance and gained more attention during the late 20th century as a result of the technological developments to study their ever-increasing role in climate and human health. Several great mathematicians and physicists were attracted by the peculiar properties displayed by clouds and discovered various scientific aspects which have since become associated with their names such as Aitken mode (particles smaller than 100nm in diameter that are generally formed from gas-to-particle conversion processes),[6–8] Rayleigh limit (maximum amount of charge on a droplet after which it would undergo fission and disintegrate into much smaller charged droplets),[9–11] and Stokes' law (measure of the drag force exerted on a particle which determines its aerodynamic behavior).[12–14]

The study of aerosol particles is interdisciplinary, and involves physics, chemistry, meteorology, and environmental sciences. The scientific interest in aerosol particles may thus be broadly divided into three areas - aerosol in the atmosphere, aerosol in engineering applications, and aerosol in health.[15–20] The significance of aerosol particles in these areas

* The term "particles" throughout the dissertation is used generally to refer to either solid particles or liquid droplets. The term "droplets" is used specifically in the case of liquid droplets.

is dependent on their size distribution, varying from 1 nm up to 100 µm, and associated physicochemical properties like refractive index, morphology, and chemical composition.[5] Aerosol particles play a complex role in the Earth's atmosphere and have a wide range of impacts on the environment, climate, and human health.[3,21] These particles, also known as particulate matter, have played a major role in the development of our knowledge of air pollution. The presence of these particles in highly polluted areas is of great importance because of the negative health impacts associated with inhaled particulate matter, resulting in various respiratory and cardiovascular illnesses.[22–24] Besides their role in the atmosphere and health, aerosol particles also play a key part in industrial processes, such as fuel delivery, combustion and spray drying, and are extensively used in day-to-day applications as cosmetics, disinfectants, aerosolized drugs, spray paints, etc.[25–29] A detailed role of aerosol particles in these different areas is discussed in subsequent sections.

1.2.1. Aerosol Particles in the Atmosphere

Aerosol particles, ubiquitous in atmosphere, have a wide range of sources and impacts on the environment, climate, and human health.[30–32] Atmospheric aerosol particles are extremely variable in their concentrations and properties which is attributed to the heterogeneity in their origin sources.[33–35] Natural sources of origin consist of biogenic emissions, sea spray and volcanic eruptions, whereas anthropogenic sources are dominated by emissions from combustion engines, biomass burning and industrial activities.[36,37] On a global scale, the contribution of aerosol mass from natural sources (69–82% of the total mass concentration) exceeds anthropogenic sources by a wide margin.[38] However, natural

sources are well distributed around the globe whereas anthropogenic sources, which may be smaller in amount, are concentrated in a small portion of the globe resulting in greater effects in at atmosphere.

Aerosol particles can be divided into two main categories based on the process of their formation. Primary aerosol particles (PAPs) are emitted directly into the atmosphere as solid or liquid particles from their origin while secondary aerosol particles (SAPs) are formed in the atmosphere either through gas-to-particle conversion due to the chemical processing of low volatility gaseous species or condensation of vapors on pre-existing PAPs.[24,39–41]

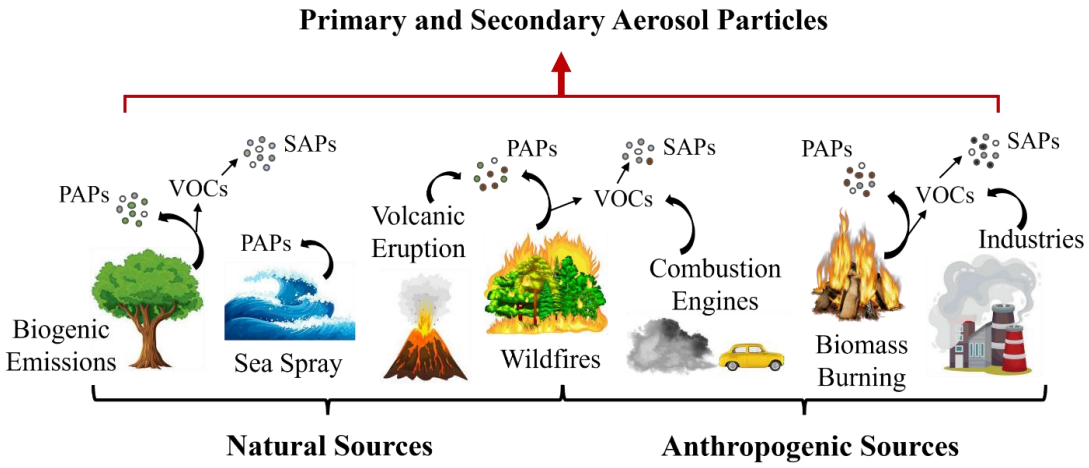

Figure 1: Natural and anthropogenic sources of the aerosol particles in the atmosphere. Natural sources like sea spray and volcanic eruptions emit mostly primary aerosol particles (PAPs) while anthropogenic sources like biomass burning and industries generate PAPs through direct emissions and secondary aerosol particles (SAPs) through gas-to-particle conversion of low volatility chemical compounds.

Figure 1 shows a schematic of the various natural and anthropogenic sources contributing to the formation of primary aerosol particles (PAPs) through direct emission

and secondary aerosol particles (SAPs) through gas-to-particle conversion in the atmosphere. Natural sources mostly generate PAPs which are emitted directly into the atmosphere, such as sea salt from ocean waves, pollens released from plants, and mineral dust from desert sand. Anthropogenic sources may either introduce PAPs directly into the atmosphere, such as soot emissions from biomass burning and combustion engines, or generate SAPs, such as sulphate, nitrate, and low volatility organic particles, formed from their precursor gases emitted from road transport and power plants.[42,43]

1.2.1.1. Size Classification and Timescales of Aerosol Particles

Once airborne, aerosol particles can evolve in their size due to evaporation of their components, coalescence with other particles, or by condensation of low volatility gaseous species.[44] This evolution based on their size classification along with their lifetime and decay modes is shown in **Figure 2**.[21,45]

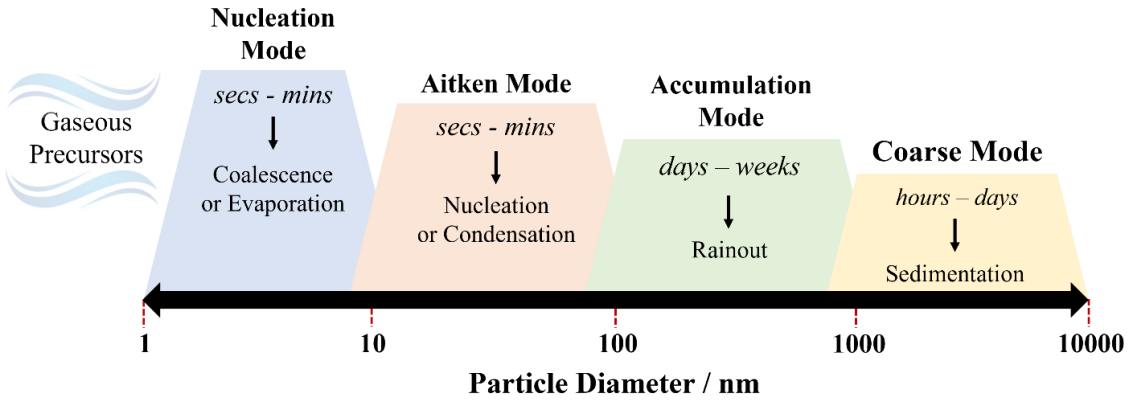

Figure 2: Schematic distribution of various aerosol particle modes in the atmosphere depending on their size and lifetime. The sources of origin and processes of formation of these different aerosol particle modes have been described in detail in the text.

Particles smaller than 10 nm in diameter are known as nucleation mode particles (also referred to as lower Aitken mode particles) which are generally formed from gas-to-particle conversion of low volatility vapor species.[46] Aitken mode particles, which are generally transient, have a size range between 10 – 100 nm and are formed by coagulation process or condensation of vapor precursors on nucleation mode particles.[47] Particles in the size range of 100 – 1000 nm are classified as accumulation mode particles, growing further in size by rapid coagulation of smaller particles, chemical transformations resulting from gaseous condensation or PAPs emitted directly from incomplete combustion processes.[48] They have the longest atmospheric lifetimes and account for a significant fraction of total aerosol mass due to the inefficiency of particle removal mechanisms.[49] Accumulation mode particles may exhibit hygroscopicity and uptake water, leading to an increase in their size and eventually growing into the cloud droplets, depending on their chemical composition and ambient relative humidity.[50,51] Rainout and gravitational setting are the most common ways for these particles to be removed from the atmosphere. Finally, coarse mode particles have the biggest size range between 1000 – 10000 nm, and are created when winds blow either salt spray or dust from Earth's surface to form PAPs from natural sources, or further coalescence of accumulation mode.[52] These particles have a shorter lifespan of days to hours, as compared to accumulation mode, as a result of their removal from the atmosphere due to sedimentation at the Earth's surface.[53]

On a global scale, PAPs generated from natural sources are 4 to 5 times larger than anthropogenic emissions while the regional variations in anthropogenic pollution may change this ratio significantly based on the characteristics of emission sources.[21] The ever-

evolving size of these aerosol particles results in their residence times in the troposphere varying from only a few minutes to days or weeks (besides other factors like chemical composition, atmospheric interactions, etc.), and they may eventually be lost as a result of gravitational settling, complete evaporation or rain-out.[54–56]

1.2.1.2. Role and Impacts of Aerosol Particles

Aerosol populations from numerous sources continuously interact with the regional atmospheric conditions, or mix and interact with each other due to the transportation by winds, resulting in the evolution of their chemical composition, and associated physical and optical properties throughout their lifetime.[57,58] A detailed discussion on the various chemical transformations and associated characteristics of aerosol particles is presented in *Sections 1.3 and 1.4*. In brief, aerosol particles are subject to a variety of chemical transformations in the atmosphere that can change their properties and behavior. Aerosol particles can exchange numerous semi-volatile organic compounds (SVOCs) present in the atmosphere and undergo evaporation or condensation transformations.[59] Photochemical reactions can occur when these particles interact with the UV component of the sunlight causing chemical reactions to occur that lead to the formation of highly reactive radical species which can participate in further chemical reactions.[60] Heterogeneous oxidation reactions occur when aerosol particles come in contact with gas phase oxidants such as ozone, hydroxyl and nitrate radicals resulting in formation of oxidized products.[61] As a result of these chemical transformations, aerosol particles undergo changes in their physicochemical characteristics and exhibit a range of effects in the atmosphere.

Aerosol particles have a complicated yet significant role in our climate, and have both direct and indirect effects in the atmosphere.[62] The direct effects are based on the aerosol particles themselves while the indirect effects are based on their ability to influence cloud formation and thus the characteristics of the clouds. One of the most important ways that aerosol particles can directly impact the climate is through their ability to scatter, absorb or refract the sunlight thus influencing the radiative balance of the atmosphere and affecting the air quality and visibility.[63] The chemical compounds present in these particles, such as sulfates and nitrates, scatter the solar radiation back into space resulting in a cooling effect while the presence of chemical species, such as black and brown carbon compounds, absorb the solar radiation resulting in a heating effect. The indirect effects caused by the aerosol particles is due to their role as cloud condensation nuclei (CCN).[64] These particles influence the albedo of the clouds and Earth's energy budget due to the perturbations of cloud droplet number concentrations, also known as Twomey effect. Further, the properties exhibited by aerosol particles influence the clouds in terms of lifetime, thickness, and rate of precipitation, also known as Albrecht effect. **Figure 3** shows an overview of various interactions and transformations aerosol particles could experience in addition to their direct and indirect effects in the atmosphere.[65]

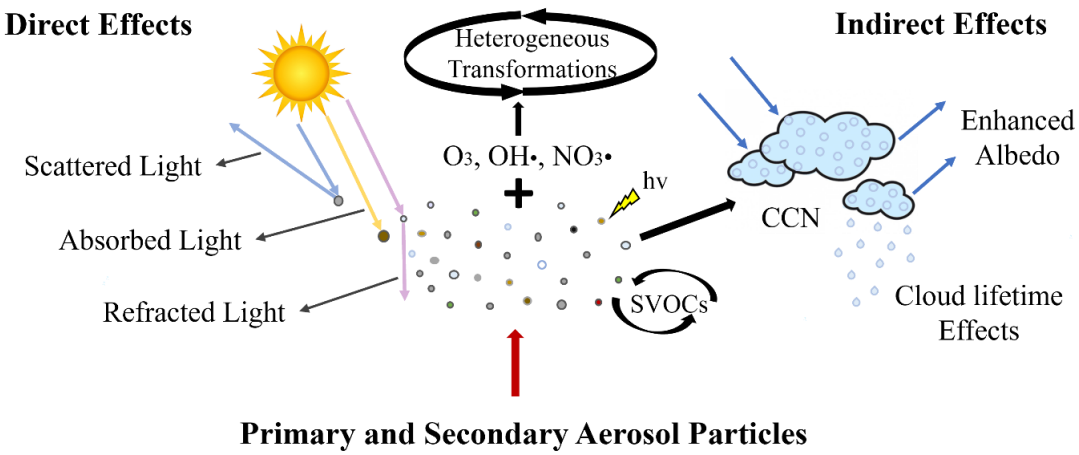

Figure 3: Physicochemical transformations, such as heterogeneous oxidation, evaporation or condensation of SVOCs and photochemical reaction, of primary and secondary aerosol particles along with their direct and indirect effects in atmosphere.

1.2.2. Aerosol Particles in the Health

Aerosol particles, classified as particulate matter (PM), have a significant impact on human health and can contribute to a variety of health issues.[66,67] Inhalation of PM present in a polluted region is associated with their penetration into the human respiratory system. Based on size of PM existing in the atmosphere, they can penetrate into different parts of human respiratory system.[68,69] Larger particles (PM_{10}) do not transit deep into the lungs and are deposited in the nose, pharynx, or larynx while smaller particles ($PM_{2.5}$) penetrate more deeply into the lungs, trachea, bronchioles, or even alveoli. Scientific studies have linked the inhalation of PM to various respiratory and cardiovascular diseases, such as aggravated asthma, decreased lung function, difficulty breathing, coughing, irregular heartbeat and heart attack.[70,71] The World Health Organization (WHO) estimates that the combined effects of indoor and outdoor air pollution are responsible for approximately 7 million deaths per year.[72] To limit the negative health impacts associated the PM, the

United States Environmental Protection Agency (US EPA) has set stringent standards to limit the levels of $PM_{2.5}$ and PM_{10} in ambient air.[73]

Pathogen-bearing aerosol particles can result in the spread of respiratory infectious diseases and pose a threat to public health. The unprecedented pandemic of the coronavirus disease - 2019 (COVID-19) highlights the important role of aerosol particles in the airborne transmission of pathogens, such as severe acute respiratory syndrome coronavirus 2 (SARS-COV-2).[71,74–76] During the spread of such respiratory illnesses, an infectious aerosol particle laden with pathogens is exhaled by a sick person into the atmosphere which can drift through the air to enter a healthy person's respiratory system and causes infection.[77,78] Once in the air, these particles can remain suspended for several hours and cover great distances. An improved understanding of aerosol particles has caused increased awareness and concerns about their role in the spread of well-known respiratory illnesses, such as COVID-19.[79]

Contrary to the negative impacts, aerosol particles may also have positive influences on human health. They offer medicinal uses as aerosolized drugs, in the form of inhalers and nebulizers, by delivering active pharmaceutical ingredient directly to the lungs, decreasing the time response of action due to rapid transport into bloodstream and bypassing the digestive system, thereby reducing some unwanted side-effects.[80,81] Pain relief sprays are another form of aerosolized drugs that are used externally and applied directly onto the particular affected area of the body to deliver the active ingredient into the body tissues for instant pain relief.

1.2.3. Aerosol Particles in Industry

Aerosols in industry refer to the utilization of pressurized sprays in various manufacturing, industrial and agricultural applications. They play a vital role in many techniques and industrial processes, including lubrication, combustion, spray drying, cleaning, coating, and agricultural pesticides.[82,83] They are useful for hard-to-reach areas and also for applying precise amounts of materials to specific areas, reducing waste, and increasing efficiency. Some of the important aerosol applications in the industry are discussed below.

For spray drying applications, a solution containing the desired compound is aerosolized into droplets by spraying followed by evaporation to form dry powder.[25] This technique is commonly used in the food industries to produce dehydrated powders, such as instant coffee and milk powders, as well as pharmaceutical industries to produce powdered drugs for ingestion or external applications, such as dry powder inhalers and antibiotic powders. Thermally sensitive materials for powder formulations benefit from this technique as the shorter drying period and significant cooling of droplets help preserve the characteristics of the desired compounds. Aerosolized solutions are also used as fuel sprayers for combustion engines that deliver greater concentrations of vapors as compared to bulk liquids, increasing the combustion efficiency of the fuel. This method of fuel delivery is used in turbines, diesel engines and various other industrial furnaces. Aerosol lubricants are typically made up of a combination of oil, solvents, and propellants.[84] They are used to lubricate machinery and equipment in a variety of areas, including automotive and aerospace industries. As industrial cleaning agents, aerosol particles are used to remove

grim, dirt, rust, and other contaminants from narrow spaces in the equipment, such as nooks and crevices. As spray paints, they are used to apply thin and precise layer of paint or coating on the surfaces of vehicles and machines. Another common application of aerosol particles in industry is in cooling processes in which they are used to cool down the temperature of products by spraying them with a fine mist of a cooling agent that can help prevent overheating and damage to equipment.[85] Additionally, aerosol sprays have been widespread used to disperse precise quantities of pesticides for agricultural and public health applications.[83] The dispersal of pesticides in the form of liquid solutions or powders is accomplished with the help of several techniques, involving ground-based aircrafts which have been used for over a century now. It is essential that the deposition efficiency of aerosol particles ensures that they remain localized to the areas of application. Finally, the utilization of aerosols in industrial applications has many benefits, including increased efficiency and reduced wastage. However, it is also crucial to use them safely and responsibly to minimize any potential health risks or hazards.

1.3. Characteristics of Aerosol Particles

The physical and chemical properties of aerosol particles, such as size, morphology, refractive index, and chemical composition, play a significant role in determining their impact on the atmosphere and human health.[4,86] While these properties are connected and influence each other, it is useful to discuss them separately.

1.3.1. Chemical Composition of Aerosol Particles

Many of the effects exhibited by aerosol particles depend on their chemical composition, which consists of a mixture of chemical species from a number of sources.[33,87–89] The chemical composition determines the types of chemical transformations (*refer Section 1.4*) that can occur in/on these particles due to reactive conditions of the atmosphere. As a result of chemical transformation, the chemical composition is constantly evolving, linking the compositional complexity and reactivity into a coupled problem. **Figure 4** shows a break-down of the global chemical composition of ambient aerosol particles and the compositional contributions along with their possible sources represented in each of the subsets are explained below.[90]

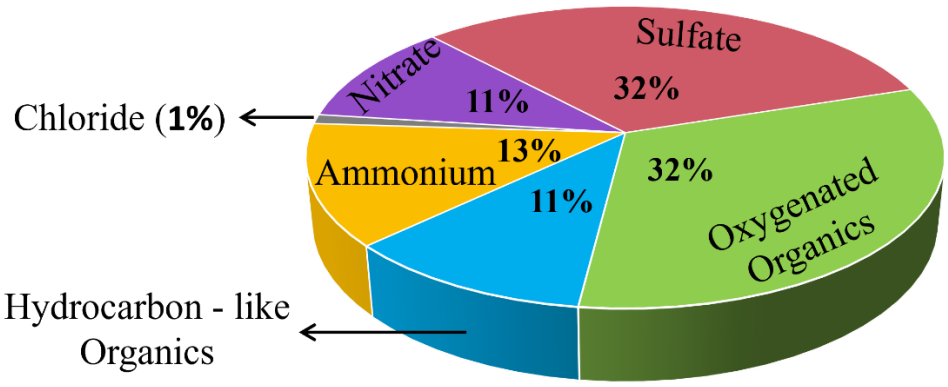

Figure 4: Breakdown of the average global chemical composition of the ambient aerosol particles into organic and inorganic subsets. These subsets are further broken down into their further classifications along with their average abundances, as explained in the text.

Organic species comprise a major mass fraction (20 to 90%) of the sub-micron ambient aerosols as demonstrated by the mass spectrometry data acquired especially in the Northern Hemisphere field studies.[87,91] Extensive mass spectra analysis of the organic components

classifies them into hydrocarbon-like organic compounds representing primary combustion emissions like fossil fuel combustion and biomass burning emissions, and oxygenated organic compounds which accounts for 65 – 95% of the total organic composition and represents a majority of aged secondary organic aerosols (SOAs).[89,92–94] Secondary aerosol particles are formed as a result of gas-to-particle conversions or condensation processes as discussed in *Section 1.2.1*. The carbonaceous mass fraction of the aerosol particles also consists of elemental carbon in addition to hydrocarbon-like organic compounds. A variety of combustion processes contribute to particle mass by emitting elemental carbon directly into the atmosphere in the form of black carbon, graphite, or soot. Most of the ambient measurements for compositional determination of aerosol particles have resulted from the employment of aerosol mass spectrometer that can analyze the organic aerosol quantitatively in real-time.[95–97] The rest of the aerosol particle mass comprises of sulfate (10 – 67%), nitrate (1.2 – 28%), ammonium (6.9 – 19%), chloride (< 1%) and trace amounts of other chemical species.[90] The sulfate and nitrate components in the aerosol particles are derived predominantly from the atmospheric oxidation of sulfur dioxide and nitrogen dioxide emitting mainly from anthropogenic sources that first get converted into sulfuric and nitric acid, and then to sulfate and nitrate species. The ammonium component is a result of neutralization of sulfuric and nitric acids with the atmospheric ammonia to form ammonium salts. The main contribution of chlorides to the particle mass fraction is from the sea spray emissions. It is noted that the individual contribution of these components changes rigorously depending on the sampling period and location. Furthermore, chemical species from numerous sources continuously mix with each other during the aging of the

aerosol particles throughout their lifetime, resulting in the complex nature of particulate organic matter made up of hundreds of different compounds.[98] As a consequence, the chemical nature of aerosol particles is difficult to define and the researchers have adopted several indirect methods, such as use of tracer compounds and model systems, to identify particle composition and emission sources. The mixed composition of the aerosol particles may exhibit complex morphologies where hydrophilic and hydrophobic components may phase separate into core-shell, inclusions, or engulfed morphologies as described in the next section.

1.3.2. Physical Characteristics of Aerosol Particles

1.3.2.1. The Phase State and Morphology

Phase state and morphology play a crucial role in determining the behavior of aerosol particles in the atmosphere, including how they interact with their surrounding environment and other particles. Depending on the viscosity, the phase state can be determined as liquid (viscosity less than 10^2 Pa s), semi-solid (viscosity between 10^2 and 10^{12} Pa s) or crystalline solid (viscosity greater than 10^{12} Pa s).[99–101] The viscosity and consequently the phase state of the particles can vary based on the environmental conditions, such as relative humidity and temperature.[102–105] The chemical composition of a particle also affects its phase state due to the solubility strength of constituent chemical species in the bulk. In case of a particle having hydrophobic species present in water, phase separation can occur as a consequence to reduce the unfavorable interactions between the constituents and bulk.[106,107] This results in the formation of different morphologies like

core-shell and partially engulfed structures.[106] When both the constituents and bulk are hydrophilic (or hydrophobic), they result in the homogeneous morphology of the particle. **Figure 5** represents the different morphologies that the particle can attain depending on its phase state, solubility of constituents in its bulk medium, and the environmental conditions.[108] Understanding the physical state and phase morphologies associated with aerosol particles, and their dynamic response to the changes in environmental conditions is important to accurately predict their behavior.

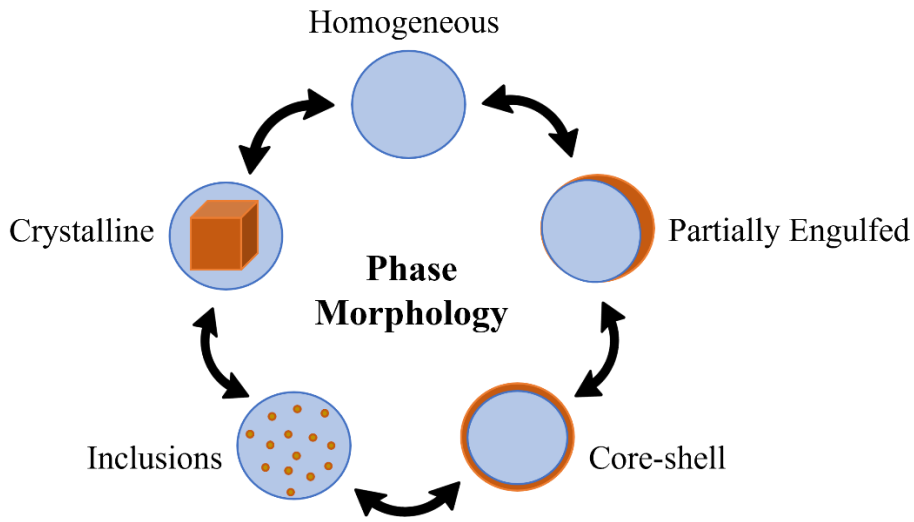

Figure 5: A schematic representation of the different phase morphologies associated with aerosol particles. The ambient aerosol particles can exhibit either homogeneous or phase separated morphologies as described in the figure. The phase state and morphologies can interchange with each other depending on the surrounding environmental conditions and the particle composition.

1.3.2.2. Particle Size and Shape

Besides the phase state, and morphology, the size and shape of aerosol particles are also defining characteristics which affect their behavior in the atmosphere.[49,109] Aerosol

particles in the atmosphere can range in size form a few nanometers to several micrometers as discussed in *Section 1.2.1.1*. Their size distribution is typically characterized by the number of particles per unit volume in different ranges of the sizes. Smaller particles, such as $PM_{2.5}$, can stay levitated in the air for longer periods of time and be transported over great distances than the bigger particles, such as those greater than PM_{10}, which tend to settle down more quickly due to gravitational settling.[110] Therefore, the information on aerosols' size distribution is important for understanding their effects on visibility, cloud formation, solar radiation budget and human health. Further, the particle shape determines its role in the atmosphere by affecting its surface area, optical properties, and aerodynamic behavior.[111] Ambient aerosol particles existing in liquid phase states are mainly spherical while the particles existing as solids or crystalline usually have variable shapes (like crystalline, aggregate, amorphous and fractal) as confirmed by the studies utilizing scanning electron microscopy.

1.3.2.3. Optical Properties of Aerosol Particles

Aerosol particles interact with the electromagnetic radiation of incident solar light and cause a variety of optical processes, namely diffraction, reflection, refraction, absorption, and scattering, as shown in **Figure 6**. Absorption and scattering caused by aerosol particles contribute significantly to the radiative balance of the atmosphere.[112] The determination of these optical properties associated with aerosol particles depends on their physicochemical properties such as size, shape, refractive index, morphology, and chemical composition.[113,114]

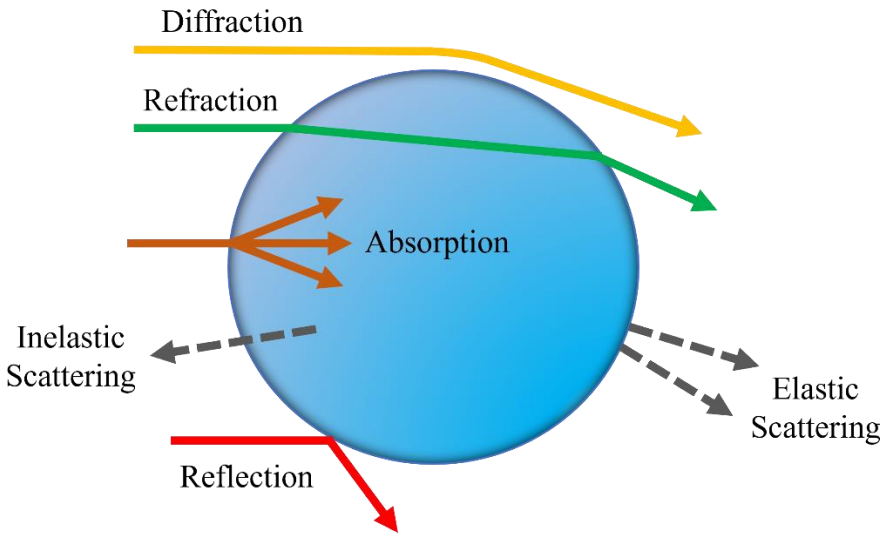

Figure 6: An overview of the light interaction with a spherical aerosol particle resulting in different optical processes, such as diffraction, refraction, absorption, reflection and scattering. These properties depend on chemical composition and physical state of particle.

The atmosphere experiences a warming effect as a result of the absorption of solar radiation by the constituents present in particles, or a cooling effect as a result of light scattering by particles.[115] The scattering of the light by particles can be further classified as elastic and inelastic scattering. In elastic scattering, emitted light has same wavelength as incident light and is dependent on the size, RI, and composition, while in inelastic scattering, the wavelength associated with emitted light is increased due to the energy loss caused by absorption, and is dependent on composition. The refractive index (RI), which indicates the light bending based on incoming wavelengths, play a role in determining the light scattering efficiency.[116] RI is composed of two parts: *real part* which quantifies the change in speed of light due to elastic scattering, and imaginary part which describes the attenuation of light due to inelastic scattering. For our measurements, Mie theory is used

to describe the light interaction with particles by providing a solution to Maxwell's equations, and the values for real part of RI are utilized for tracking the elastic scattering of spherical particles undergoing chemical transformations (*refer Section 2.3*).[117–119]

The detailed exploration of these physicochemical properties (discussed in above sections) helps in gaining the necessary knowledge to understand how they influence the chemical interactions of aerosol particles with the environment. Moreover, the chemical transformations occurring in/on the aerosol particles due to their interactions with the environment, such as chemical reactions and non-reactive transformations, results in the alteration of their chemical composition. The compositional changes further lead to changes in their physical properties, such as size, volatility, hygroscopicity, phase state, morphology and optical properties, which determine their role as well as fate due to various atmospheric interactions.

1.4. Chemical Transformations of Aerosol Particles

Due to the diverse composition of aerosol particles, along with supporting environmental conditions, the properties and composition of aerosol particles continuously transform due to various non-reactive transformations, such as evaporation and condensation, and chemical reactions, due to heterogeneous oxidation or photochemistry.[90,120] These transformations can happen in the bulk and at the surface of aerosol particles, resulting in the evolution of chemical composition and composition-dependent properties, such as size, phase morphology, RI, volatility and hygroscopicity. Understanding the properties associated with evolving chemical composition is important for predicting the role and

impacts of aerosol particles in different areas as discussed in *Section 1.2*. The aerosol particles generated under laboratory conditions have much less complicated composition and properties as compared to naturally occurring aerosol particles which are composed of mixtures of chemical compounds originating from a variety of sources, resulting in highly complex properties. Consequently, laboratory transformations on aerosol particles can be explored relatively easily by known techniques while the chemistry associated with ambient aerosol particles need to be studied with the help of a combination of different analytical techniques and chemical methodologies.[121]

1.4.1. Non-Reactive Transformations of Organic Aerosols

A non-reactive transformation (NRT) of an organic aerosol (OA) particle is described as a process that involves exchange or transfer of matter or energy between the particle and its surrounding environment resulting in the changes in its chemical composition and properties (like size, mass, phase state and morphology), without the involvement of a chemical reaction.[59] NRT can happen due to a variety of environmental conditions, such as potential of hydrogen (pH), temperature, relative humidity (RH), and presence of volatile organic species, surrounding the aerosol particles. An exchange of semi-volatile organic compounds (SVOCs) or water vapor molecules between the particles and the gas phase, in the form of evaporation or condensation, results in a transformation. NRT of pre-existing aerosol particles involving gas-to-particle partitioning through SVOCs condensation on them contributes to the formation of SOA in the atmosphere. The vapor pressure of SVOCs present in the atmosphere plays an important role in the gas-to-particle

partitioning, and atmospheric impacts of the aerosol particles.[122] For exchange of water molecules, OA particles consisting of hydrophilic chemical species can respond quickly to changes in the RH conditions surrounding the particle. Efficient uptake of water vapor can result in the hygroscopic growth of the particle resulting in the formation of aqueous droplet and substantial increase in particle size even at lower RH.[109,123] The rate of transformation is dependent on the size, and the fine particles having a high surface-to-volume ratio can be effectively transformed as a result of NRT.

1.4.2. Heterogeneous Oxidation of Organic Aerosols

Organic aerosol (OA) particles are subject to heterogeneous oxidation reactions due to their interactions with atmospheric gas-phase oxidants such as ozone, and hydroxyl and nitrate radicals (O_3, ·OH, and NO_3·, respectively).[90,124] These heterogeneous transformation processes modify the chemical composition of the OA particles which further affects their physicochemical characteristics as well as interactions with the immediate environment causing numerous effects in the atmosphere. In general, oxidative chemical aging of OA particles is initiated by the collision of gas-phase reactant species with the particle surface and follows respective reaction pathways outlined previously by numerous researchers.[125] The oxidation by radical species is typically initiated due to the hydrogen abstraction by the radical while the oxidation by ozone results in the addition of O_3 molecule to the double bonds present in alkene carbons. The chemical mechanism of heterogeneous oxidation broadly leads to three possible reactive outcomes – fragmentation, functionalization, or oligomerization.[126] Fragmentation occurs when reactant molecules are

broken via C–C bond cleavage to form lower-molecular weight compounds. Functionalization results in the addition of functional groups to the reactant molecules, such as carbonyls, alcohols, carboxylic acids, etc. Oligomerization is marked by the formation of high-molecular weight products due to the association of multiple reactant molecules.

Oxidation reactions lead to changes in the chemical composition, which can cause phase transitions, form oxidized products, release volatile organics, increase hygroscopicity, and possibly decrease further oxidation reactivity along with the evolution of other measurable physical characteristics like size, mass, and RI.[108] The reaction kinetics and product branching ratio are dependent on several environmental factors such as oxidant concentration, RH, temperature and particle characteristics like constituent molecules, reactant concentration, oxidant diffusion, phase state and morphology.[103,124,127] It is generally reported in terms of the reactive uptake coefficient, which is defined as the fraction of collisions between gas-phase reactant and particle-bound species that lead to a successful reaction.[128] Measurements of uptake coefficients are used to compare reaction rates between aerosol particles of varying size and chemical composition. Thus, the non-reactive chemical transformations and heterogeneous oxidation reactions of the ambient particles result in the evolution of their chemical composition which further changes their physical and optical properties. A detailed exploration of these chemical transformations related to the atmospheric aerosols helps in understanding their roles and impacts in the environment.

1.5. Techniques to Study Aerosol Transformations

A major area of focus in present day environmental research is to understand and predict how aerosol particles evolve in the atmosphere due to their various interactions with the environment.[129] These interactions result in the chemical transformations of aerosol particles which play a key role in determining their direct and indirect effects in the atmosphere. To facilitate research, the scientific approaches used to study characteristics and transformations of aerosol particles can be classified into three categories: field measurements, modeling analysis and laboratory studies.[130–132] A combination of these three approaches is essential to fully study the role and impacts of aerosol particles in the atmosphere. Field measurements are deployed to measure the chemical composition, optical properties, size distributions etc. of aerosol particles present naturally in the environment. Observations are connected with known sources and atmospheric lifetimes to understand the atmospheric impacts of the aerosol.[130] Modeling analysis is carried out to predict the impact of aerosol particles by assessing various parameters with the help of numeric models or computational simulations. Local and global scales models rely on both field measurements and laboratory studies to effectives predict the evolving atmosphere.[104] Laboratory studies typically focus on idealized systems under well-controlled conditions, which are representatives of atmospheric aerosols, and used to elucidate the influence of specific factors by reducing the chemical complexity.[133]

The methods described in this section focus on laboratory studies, which includes ensemble and single particle levitation methods. These methods have been extensively developed to provide an essential link between field measurements and modeling analysis,

and assist in measuring the evolving physicochemical characteristics of aerosol particles as a result of chemical transformations.

1.5.1. Ensemble Methods

Ensemble methods, such as smog chambers and flow tubes, are utilized for studying new particle formation from gaseous precursors and the subsequent chemical transformations, due to photochemical reactions, gas–particle exchange, and heterogeneous oxidative aging.[134–136] The ultimate goal of ensemble studies is motivated by field studies and involves the simulation of a variety of atmospheric conditions in laboratory setting under well-controlled conditions to acquire detailed laboratory mechanistic data.[86,133] The poorly understood factors in the field measurements that affect the formation and role of the SOA particles are being experimentally analyzed with the help of smog chambers and flow tubes. Important aerosol properties, such as size distributions, hygroscopicity, vapor pressures, mass transport, optical properties, chemical composition, and reaction kinetics, have been studied with the help of ensemble measurements. Both on-line (direct real-time sampling) and off-line (filter-based sample collection) analytical methods are used in conjunction with the ensemble methods to characterize the evolving properties and composition.[137,138] Generally, the conditions (like concentrations of reactants and oxidants) used to simulate the chemical processes of SOAs in flow tube methods are enhanced in their magnitudes for achieving relatively shorter reaction timescales whereas the smog chamber measurements are now being conducted at more realistic concentrations and timescales with the help on on-line instruments. Ensemble methods provide a good

representation of aerosol processes happening in the atmosphere, however, the properties determined tend to be averaged over the whole aerosol population and the influence of subtle effects such as changes in phase state, are difficult to resolve. Single particle levitation methods are an alternative approach that simplifies the ensemble system to an individual levitated particle, allowing particles properties and chemical transformations to be probed more precisely.

1.5.2. Single Particle Methods

Single particle methods are laboratory techniques that aim at understanding and linking the microphysical properties and chemical composition of individual particles.[108,139] The exploration of chemical processes happening at single particle level helps in quantifying how these processes affect the behavior of individual atmospheric aerosol particles.[140] These methods use various mechanisms for contactless particle levitation, such as the electric fields of an electrodynamic balance, the optical forces of a tightly focused laser, or standing sound wave of an acoustic trap. These methods help us to study single levitated particles in the absence of any interactions with other particles, allowing the interrogation of time-dependent processes on individual particles. For this, measurements are made on the particles under controlled environmental conditions and the particle response is determined *in-situ*. A brief discussion of a variety of single particle methods is presented below.

Acoustic techniques employ high frequency sound waves to trap single or multiple particles for understanding their properties during chemical transformations. Researchers

have employed acoustic techniques to measure the evaporation rate of particles, surface tension, and interfacial transport kinetics of organic coated particles.[141] However, this method is limited to particles larger than 100 μm, restricting the general application of these experimental methods to probing atmospheric transformations.

Optical techniques work on the basic principle of confining the particle in three dimensions with the help of a strong optical force generated by tightly focused laser beam. The confinement of the particle depends on the radiation pressure force applied which comprises the scattering force and gradient force.[142] Upon illumination, scattering force results from the transfer of momentum of light photons to the particle that pushes the particle along the light propagating direction while the gradient force tends to pull the particle towards high intensity region of light. The optical tweezers is an important optical method used extensively in aerosol research in which the light source is tightly focused resulting in the gradient forces in the particle will pull it to the focal point of the beam, creating a three-dimensional trap.[143,144] Particles in the size range of 3 – 8 μm can be confined for accurately measuring the properties of the particles undergoing chemical transformations.[143] This technique is limited by sample introduction methods that require aqueous solubility and large amounts of sample that leads to a perturbation of the environment inside trapping chamber. It is also limited to spherical particles that are non-light absorbing.

Electrodynamic techniques spatially confine one or multiple charged particles inside an electrodynamic balance with the help of electric fields produced by AC and DC voltages

applied to set of electrodes.[118,123,145] The range of particle sizes accessible to electrodynamic balance is 1 – 100 μm which can be introduced individually without perturbing the environmental conditions inside the chamber, eliminating the limitation of optical methods. The electrodynamic balances are available in different configurations, such as double ring and linear quadrupole electrodynamic balance, while performing similar functions.[146] Linear quadrupole electrodynamic balance is a powerful tool that can be employed for exploring various kinds of chemical transformations, such as, heterogeneous oxidation, photochemistry, evaporation dynamics and hygroscopicity of aerosol particles by controlling the environmental conditions inside the trapping chamber.[145] The oscillatory forces generated by AC voltage stabilize the confined particles whereas applied DC voltage balances any net forces, such as gravity, on the levitated particles. EDB levitation traps can be coupled with different optical spectroscopy techniques to measure the physical properties, and mass spectroscopy methods to study the chemical composition of the aerosol particles. A detailed discussion on the working principle of linear quadrupole electrodynamic balance employed in our measurements is presented in *Section 2.2*.

Overall, the discussed single particle methods allow levitation as well as manipulation of a single or multiple particles while offering significant advantages such as contactless confinement, ambient environmental conditions, versatility to any particle composition, limited sample preparation, and real-time analysis of both physical and chemical characteristics.[140,146] Particle properties such as size, volatility, hygroscopicity, phase morphology and reaction kinetics can be directly examined by coupling the above

levitation methods with non-intrusive analytical techniques, such as electron microscopy, broadband spectroscopy, elastic light scattering, and Raman spectroscopy.[108,147,148] To obtain chemical information of a single particle, certain levitation methods can additionally be coupled effectively with mass spectrometry by utilizing different kinds of sampling and ionization techniques (*refer Section 2.4*).[149,150]

1.6. Thesis Aim and Overview

The key objective of the thesis research is to gain molecular-level understanding of how aerosol particles evolve due to atmospheric transformations. Understanding the chemical aging of atmospheric particles helps in evaluating their role and impacts in the environment. In this section, the general motivation and significance of the laboratory-based research work are discussed.

1.6.1. Research Motivation

The advancement in understanding aerosols characteristics has led to the extensive exploration of their role and impacts in the atmosphere, technological applications in industries, and effects on human health. A major focus of aerosol research is to explore the chemical transformations of the aerosol particles present in the atmosphere.[87,120] Atmospheric aerosol particles consist of multitude of organic species (>1000s), and owing to these complex functionalities along with the environmental conditions, aerosols become transformed by non-reactive, photochemical, and heterogeneous oxidation reactions.[90,151] These chemical transformations cause chemical aging of these particles and alter their

physical and chemical properties. Finally, the products of such reactions regulate the dynamics of aerosols and ultimately have a significant impact on the role of these particles in atmosphere.

The advancement in laboratory-based methods have led to extensive exploration of aerosol chemical transformations and related physicochemical properties. Laboratory studies utilizing ensemble techniques provide a good representation of atmospheric processes of aerosols, however, these measurements do not track down the changes happening at single particle level and tend to average out the properties over the whole aerosol population.[134,152] Thus, the motivation of our research is to gain molecular-level understanding of transforming aerosol particles by utilizing single particle technique which helps in precise and accurate determination of physical and optical properties, and connect them with the evolving chemical composition to get a complete picture of an individual aerosol particle undergoing transformations.[121]

1.6.2. Research Significance

The work described in this thesis is focused on developing experimental platform, namely linear quadrupole electrodynamic balance coupled with mass spectrometry (LQ-EDB-MS), capable of interrogating single levitated particles undergoing atmospherically relevant transformations by precisely measuring their microphysical characteristics as a function of evolving chemical composition. Experimental studies included in this research reduces the complexity of atmospheric aerosol composition into simplified one or multi-component model systems as representative of real atmospheric aerosols. Limiting the use

of any contact surface or particle-particle interactions will be beneficial for understanding the nature of an aerosol particle undergoing such transformations in atmosphere. Therefore, LQ-EDB-MS is a versatile technique that is expected to provide real-time, size-resolved detailed knowledge of complete physicochemical characteristics which is challenging to be studied by other techniques.

1.6.3. Thesis Outline

The overview on aerosol particles covered in this *Chapter 1* provides the scientific basis for the importance of aerosol particles, not just in the atmosphere but also in the industrial, healthcare, and day-to-day applications. It also includes a discussion on the properties and chemical transformations of atmospheric aerosol particles, along with the techniques adopted to study them by aerosol science researchers. *Chapter 2* reports the principle of operation and development of laboratory-based methods utilized in our research work which include linear quadrupole electrodynamic balance (LQ-EDB), Mie resonance spectroscopy (MRS), and mass spectrometry (MS). *Chapter 3* describes the investigation of the capability of paper spray mass spectrometry (PS-MS) method for the qualitative and quantitative analysis of single picoliter droplets. *Chapter 4* discusses the development and capability of open port sampling interface (OPSI) as a new electrospray-based sampling method coupled to particle levitation for improved analysis of analytes in single particles. *Chapter 5* reports the investigations of chemical transformations on levitated particles for understanding the evaporation dynamics of semi-volatile organics present in multi-component systems. *Chapter 6* describes the utilization of a specialized electrodynamic

balance capable of attaining above-ambient temperatures for exploring the influence of phase states on evaporation dynamics of single and multicomponent organics at elevated temperatures, thereby assisting in deriving their vapor pressures. *Chapter 7* continues the transformation investigations on levitated particles undergoing heterogeneous oxidation reaction, namely ozonolysis, to determine the phase effects of stereoisomers on reaction kinetics. Finally, *Chapter 8* presents a summary of our research findings, thesis conclusions and suggests directions for future work.

1.7. References

(1) Heyder, J. Definition of an Aerosol. *J. Aerosol Med.* **1991**, *4* (3), 217–221. https://doi.org/10.1089/jam.1991.4.217.

(2) Remer, L.A. Dynamic aerosol model: Urban/industrial aerosol. *J. Geophys. Res.* **1998**, *103* (D12), 13859–13871. https://doi.org/10.1029/98JD00994.

(3) Twomey, S. Atmospheric Aerosols. **1977**. https://www.osti.gov/biblio/6747246

(4) Prospero, J. M.; Charlson, R. J.; Mohnen, V.; Jaenicke, R.; Delany, A. C.; Moyers, J.; Zoller, W.; Rahn, K. The Atmospheric Aerosol System: An Overview. *Rev. Geophys.* **1983**, *21* (7), 1607–1629. https://doi.org/10.1029/RG021i007p01607.

(5) Held, A.; Mangold, A. Measurement of Fundamental Aerosol Physical Properties. *Springer Handbook of Atmospheric Measurements* **2021**, 533–563. https://doi.org/10.1007/978-3-030-52171-4_18.

(6) Pöhlker, M. L.; Zhang, M.; Campos Braga, R.; Krüger, O. O.; Pöschl, U.; Ervens, B. Aitken Mode Particles as CCN in Aerosol- and Updraft-Sensitive Regimes of Cloud Droplet Formation. *Atmos. Chem. Phys.* **2021**, *21* (15), 11723–11740. https://doi.org/10.5194/acp-21-11723-2021.

(7) Vaattovaara, P.; Huttunen, P. E.; Yoon, Y. J.; Joutsensaari, J.; Lehtinen, K. E. J.; O'Dowd, C. D.; Laaksonen, A. The Composition of Nucleation and Aitken Modes Particles during Coastal Nucleation Events: Evidence for Marine Secondary Organic Contribution. *Atmos. Chem. Phys.* **2006**, *6* (12), 4601–4616. https://doi.org/10.5194/acp-6-4601-2006.

(8) Haaf, W.; Jaenicke, R. Results of Improved Size Distribution Measurements in the Aitken Range of Atmospheric Aerosols. *J. Aerosol Sci.* **1980**, *11* (3), 321–330. https://doi.org/10.1016/0021-8502(80)90106-8.

(9) Wilm, M. Principles of Electrospray Ionization. *Mol. Cell Proteomics* **2011**, *10* (7), 009407-1–009407-8. https://doi.org/10.1074/mcp.M111.009407.

(10) Konermann, L.; Ahadi, E.; Rodriguez, A. D.; Vahidi, S. Unraveling the Mechanism of Electrospray Ionization. *Anal. Chem.* **2013**, *85* (1), 2–9. https://doi.org/10.1021/ac302789c.

(11) Smith, J. N.; Flagan, R. C.; Beauchamp, J. L. Droplet Evaporation and Discharge Dynamics in Electrospray Ionization. *J. Phys. Chem. A* **2002**, *106* (42), 9957–9967. https://doi.org/10.1021/jp025723e.

(12) Clifton, J.; McDonald, P.; Plater, A.; Oldfield, F. An Investigation into the Efficiency of Particle Size Separation Using Stokes' Law. *Earth Surf. Process*

Landf. **1999**, *24* (8), 725–730. https://doi.org/10.1002/(SICI)1096-9837(199908)24:8<725::AID-ESP5>3.0.CO;2-W.

(13) Kunkel, W. B. Magnitude and Character of Errors Produced by Shape Factors in Stokes' Law Estimates of Particle Radius. *J. Appl. Phys.* **1948**, *19* (11), 1056–1058. https://doi.org/10.1063/1.1698010.

(14) Crowder, T. M.; Rosati, J. A.; Schroeter, J. D.; Hickey, A. J.; Martonen, T. B. Fundamental Effects of Particle Morphology on Lung Delivery: Predictions of Stokes' Law and the Particular Relevance to Dry Powder Inhaler Formulation and Development. *Pharm. Res.* **2002**, *19* (3), 239–245. https://doi.org/10.1023/A:1014426530935.

(15) Harrison, R. M.; Yin, J. Particulate Matter in the Atmosphere: Which Particle Properties Are Important for Its Effects on Health? *Sci. Total Environ.* **2000**, *249* (1), 85–101. https://doi.org/10.1016/S0048-9697(99)00513-6.

(16) Mauderly, J. L.; Chow, J. C. Health Effects of Organic Aerosols. *Inhal. Toxicol.* **2008**, *20* (3), 257–288. https://doi.org/10.1080/08958370701866008.

(17) Ault, A. P.; Axson, J. L. Atmospheric Aerosol Chemistry: Spectroscopic and Microscopic Advances. *Anal. Chem.* **2017**, *89 (1)*, 430–452. https://doi.org/10.1021/acs.analchem.6b04670.

(18) Houle, F. A.; Wiegel, A. A.; Wilson, K. R. Predicting Aerosol Reactivity Across Scales: From the Laboratory to the Atmosphere. *Environ. Sci. Technol.* **2018**, *52* (23), 13774–13781. https://doi.org/10.1021/acs.est.8b04688.

(19) Pope III, C. A.; Burnett, R. T.; Thun, M. J.; Calle, E. E.; Krewski, D.; Ito, K.; Thurston, G. D. Lung Cancer, Cardiopulmonary Mortality, and Long-Term Exposure to Fine Particulate Air Pollution. *JAMA* **2002**, *287* (9), 1132–1141. https://doi.org/10.1001/jama.287.9.1132.

(20) Stein, S. W.; Thiel, C. G. The History of Therapeutic Aerosols: A Chronological Review. *J. Aerosol Med. Pulm.* **2017**, *30* (1), 20–41. https://doi.org/10.1089/jamp.2016.1297.

(21) Seinfeld, J. H.; Pandis, S. N. From Air Pollution to Climate Change. *Atmos. Chem. Phy.* **1998**. https://doi.org/10.1080/00139157.1999.10544295.

(22) Dockery, D. W.; Schwartz, J.; Spengler, J. D. Air Pollution and Daily Mortality: Associations with Particulates and Acid Aerosols. *Environ. Res.* **1992**, *59* (2), 362–373. https://doi.org/10.1016/S0013-9351(05)80042-8.

(23) Pope, C. A.; Ezzati, M.; Dockery, D. W. Fine Particulate Air Pollution and Life Expectancies in the United States: The Role of Influential Observations. *J. Air Waste*

Manag. Assoc. **2013**, *63* (2), 129–132. https://doi.org/10.1080/10962247.2013.760353.

(24) Finlayson-Pitts, B. J. Tropospheric Air Pollution: Ozone, Airborne Toxics, Polycyclic Aromatic Hydrocarbons, and Particles. *Science* **1997**, *276* (5315), 1045–1051. https://doi.org/10.1126/science.276.5315.1045.

(25) Vehring, R. Pharmaceutical Particle Engineering via Spray Drying. *Pharm. Res.* **2008**, *25* (5), 999–1022. https://doi.org/10.1007/s11095-007-9475-1.

(26) Yan, Z.; Guo, J. High-Performance Silicon-Carbon Anode Material via Aerosol Spray Drying and Magnesiothermic Reduction. *Nano Energy* **2019**, *63*, 103845. https://doi.org/10.1016/j.nanoen.2019.06.041.

(27) Dolovich, M. B.; Dhand, R. Aerosol Drug Delivery: Developments in Device Design and Clinical Use. *Lancet* **2011**, *377* (9770), 1032–1045. https://doi.org/10.1016/S0140-6736(10)60926-9.

(28) Forbes, B.; Asgharian, B.; Dailey, L. A.; Ferguson, D.; Gerde, P.; Gumbleton, M.; Gustavsson, L.; Hardy, C.; Hassall, D.; Jones, R.; Lock, R.; Maas, J.; McGovern, T.; Pitcairn, G. R.; Somers, G.; Wolff, R. K. Challenges in Inhaled Product Development and Opportunities for Open Innovation. *Adv. Drug Deliv. Rev.* **2011**, *63* (1–2), 69–87. https://doi.org/10.1016/j.addr.2010.11.004.

(29) Gardenhire, D. S.; Burnett, D.; Strickland, S.; Myers, T. R. Aerosol Delivery Devices for Respiratory Therapists. *Am. Asso. Respir. Care* **2017**, *61* (4).

(30) McNeill, V. F. Atmospheric Aerosols: Clouds, Chemistry, and Climate. *Annu. Rev. Chem. Biomol. Eng.* **2017**, *8* (1), 427–444. https://doi.org/10.1146/annurev-chembioeng-060816-101538.

(31) Menon, S.; Unger, N.; Koch, D.; Francis, J.; Garrett, T.; Sednev, I.; Shindell, D.; Streets, D. Aerosol Climate Effects and Air Quality Impacts from 1980 to 2030. *Environ. Res. Lett.* **2008**, *3* (2), 024004-1–024004-12. http://doi.org/10.1088/1748-9326/3/2/024004.

(32) Kanakidou, M.; Seinfeld, J. H.; Pandis, S. N.; Barnes, I.; Dentener, F. J.; Facchini, M. C.; Van Dingenen, R.; Ervens, B.; Nenes, A.; Nielsen, C. J.; Swietlicki, E.; Putaud, J. P.; Balkanski, Y.; Fuzzi, S.; Horth, J.; Moortgat, G. K.; Winterhalter, R.; Myhre, C. E. L.; Tsigaridis, K.; Vignati, E.; Stephanou, E. G.; Wilson, J. Organic aerosol and global climate modelling: a review. *Atmos. Chem. Phys.* **2005**, *5* (4), 1053–1123, https://doi.org/10.5194/acp-5-1053-2005.

(33) Calvo, A. I.; Alves, C.; Castro, A.; Pont, V.; Vicente, A. M.; Fraile, R. Research on Aerosol Sources and Chemical Composition: Past, Current and Emerging Issues. *Atmos. Res.* **2013**, 120–121, 1–28. https://doi.org/10.1016/j.atmosres.2012.09.021.

(34) Dubovik, O.; Lapyonok, T.; Kaufman, Y. J.; Chin, M.; Ginoux, P.; Kahn, R. A.; Sinyuk, A. Retrieving Global Aerosol Sources from Satellites Using Inverse Modeling. *Atmos. Chem. Phys.* **2008**, *8* (2), 209–250. https://doi.org/10.5194/acp-8-209-2008.

(35) Pöschl, U. Atmospheric Aerosols: Composition, Transformation, Climate and Health Effects. *Angew. Chem. Int. Ed.* **2005**, *44* (46), 7520–7540. https://doi.org/10.1002/anie.200501122.

(36) Hoyle, C. R.; Boy, M.; Donahue, N. M.; Fry, J. L.; Glasius, M.; Guenther, A.; Hallar, A. G.; Huff Hartz, K.; Petters, M. D.; Petäjä, T.; Rosenoern, T.; Sullivan, A. P. A Review of the Anthropogenic Influence on Biogenic Secondary Organic Aerosol. *Atmos. Chem. Phys.* **2011**, *11* (1), 321–343. https://doi.org/10.5194/acp-11-321-2011.

(37) Srivastava, D.; Vu, T. V.; Tong, S.; Shi, Z.; Harrison, R. M. Formation of Secondary Organic Aerosols from Anthropogenic Precursors in Laboratory Studies. *Clim. Atmos. Sci.* **2022**, *5* (1), 1–30. https://doi.org/10.1038/s41612-022-00238-6.

(38) Ramachandran, S.; Srivastava, R.; Kedia, S.; Rajesh, T. A. Contribution of Natural and Anthropogenic Aerosols to Optical Properties and Radiative Effects over an Urban Location. *Environ. Res. Lett.* **2012**, *7* (3), 034028-1–034028-11. https://doi.org/10.1088/1748-9326/7/3/034028.

(39) Turpin, B. J.; Huntzicker, J. J.; Larson, S. M.; Cass, G. R. Los Angeles Summer Midday Particulate Carbon: Primary and Secondary Aerosol. *Environ. Sci. Technol.* **1991**, *25* (10), 1788–1793. https://doi.org/10.1021/es00022a017.

(40) Chen, C.; Qiu, Y.; Xu, W.; He, Y.; Li, Z.; Sun, J.; Ma, N.; Xu, W.; Pan, X.; Fu, P.; Wang, Z.; Sun, Y. Primary Emissions and Secondary Aerosol Processing During Wintertime in Rural Area of North China Plain. *J. Geophys. Res. Atmos.* **2022**, *127* (7), e2021JD035430. https://doi.org/10.1029/2021JD035430.

(41) Sun, Y.; Du, W.; Fu, P.; Wang, Q.; Li, J.; Ge, X.; Zhang, Q.; Zhu, C.; Ren, L.; Xu, W.; Zhao, J.; Han, T.; Worsnop, D. R.; Wang, Z. Primary and Secondary Aerosols in Beijing in Winter: Sources, Variations and Processes. *Atmos. Chem. Phys.* **2016**, *16* (13), 8309–8329. https://doi.org/10.5194/acp-16-8309-2016.

(42) Tomasi, C.; Lupi, A. Primary and Secondary Sources of Atmospheric Aerosol. *Atmos. Aerosols* **2017**, 1–86. https://doi.org/10.1002/9783527336449.ch1.

(43) Sartelet, K. Secondary Aerosol Formation and Their Modeling. *Atmospheric Chemistry in the Mediterranean Region-From Air Pollutant Sources to Impacts* **2022**, 165–183. https://doi.org/10.1007/978-3-030-82385-6_10.

(44) Willeke, K.; Whitby, K. T. Atmospheric Aerosols: Size Distribution Interpretation. *J. Air Pollut. Control Assoc.* **1975**, *25*, 529–534. https://doi.org/10.1080/00022470.1975.10470110.

(45) Cosgrove, T. Colloid Science: Principles, Methods and Applications. *John Wiley & Sons*, **2010**.

(46) Kulmala, M.; Kontkanen, J.; Junninen, H.; Lehtipalo, K.; Manninen, H. E.; Nieminen, T.; Petäjä, T.; Sipilä, M.; Schobesberger, S.; Rantala, P.; Franchin, A.; Jokinen, T.; Järvinen, E.; Äijälä, M.; Kangasluoma, J.; Hakala, J.; Aalto, P. P.; Paasonen, P.; Mikkilä, J.; Vanhanen, J.; Aalto, J.; Hakola, H.; Makkonen, U.; Ruuskanen, T.; Mauldin, R. L.; Duplissy, J.; Vehkamäki, H.; Bäck, J.; Kortelainen, A.; Riipinen, I.; Kurtén, T.; Johnston, M. V.; Smith, J. N.; Ehn, M.; Mentel, T. F.; Lehtinen, K. E. J.; Laaksonen, A.; Kerminen, V. M.; Worsnop, D. R. Direct Observations of Atmospheric Aerosol Nucleation. *Science* **2013**, *339* (6122), 943–946. https://doi.org/10.1126/science.1227385.

(47) Bulatovic, I.; Igel, A. L.; Leck, C.; Heintzenberg, J.; Riipinen, I.; Ekman, A. M. L. The Importance of Aitken Mode Aerosol Particles for Cloud Sustenance in the Summertime High Arctic – a Simulation Study Supported by Observational Data. *Atmos. Chem. Phys.* **2021**, *21* (5), 3871–3897. https://doi.org/10.5194/acp-21-3871-2021.

(48) Kavouras, I. G.; Stephanou, E. G. Particle Size Distribution of Organic Primary and Secondary Aerosol Constituents in Urban, Background Marine, and Forest Atmosphere. *J. Geophys. Res. Atmos.* **2002**, *107* (D8), 7-1–7-12. https://doi.org/10.1029/2000JD000278.

(49) Wu, Z.; Hu, M.; Lin, P.; Liu, S.; Wehner, B.; Wiedensohler, A. Particle Number Size Distribution in the Urban Atmosphere of Beijing, China. *Atmos. Environ.* **2008**, *42* (34), 7967–7980. https://doi.org/10.1016/j.atmosenv.2008.06.022.

(50) Myhre, G.; Lund Myhre, C.; Samset, B. H.; Storelvmo, T. Aerosols and Their Relation to Global Climate and Climate Sensitivity. *Nature Educ. Knowl.* **2013**, *4* (5). http://www.nature.com/scitable/knowledge/library/aerosols-and-their-relation-to-global-climate-102215345.

(51) Orr, C.; Hurd, F. K.; Corbett, W. J. Aerosol Size and Relative Humidity. *J. Colloid Sci.* **1958**, *13* (5), 472–482. https://doi.org/10.1016/0095-8522(58)90055-2.

(52) Koulouri, E.; Saarikoski, S.; Theodosi, C.; Markaki, Z.; Gerasopoulos, E.;

Kouvarakis, G.; Mäkelä, T.; Hillamo, R.; Mihalopoulos, N. Chemical Composition and Sources of Fine and Coarse Aerosol Particles in the Eastern Mediterranean. *Atmos. Environ.* **2008**, *42* (26), 6542–6550. https://doi.org/10.1016/j.atmosenv.2008.04.010.

(53) Williams, J.; de Reus, M.; Krejci, R.; Fischer, H.; and Ström, J. Application of the variability-size relationship to atmospheric aerosol studies: estimating aerosol lifetimes and ages. *Atmos. Chem. Phys.* **2002**, *2* (2), 133–145. https://doi.org/10.5194/acp-2-133-2002.

(54) Finlayson-Pitts, B. J.; Jr, J. N. P. Chemistry of the Upper and Lower Atmosphere: Theory, Experiments, and Applications. *Elsevier* **1999**. https://doi.org/10.1016/B978-0-12-257060-5.X5000-X.

(55) Roelofs, G.-J. Aerosol Lifetime and Climate Change. *Atmos. Chem. Phys. Discuss.* **2012**, *12*, 16493–16514. https://doi.org/10.5194/acpd-12-16493-2012.

(56) Hodzic, A.; Kasibhatla, P. S.; Jo, D. S.; Cappa, C. D.; Jimenez, J. L.; Madronich, S.; Park, R. J. Rethinking the Global Secondary Organic Aerosol (SOA) Budget: Stronger Production, Faster Removal, Shorter Lifetime. *Atmos. Chem. Phys.* **2016**, *16* (12), 7917–7941. https://doi.org/10.5194/acp-16-7917-2016.

(57) Ziemann, P. J.; Atkinson, R. Kinetics, Products, and Mechanisms of Secondary Organic Aerosol Formation. *Chem. Soc. Rev.* **2012**, *41* (19), 6582–6605. https://doi.org/10.1039/C2CS35122F.

(58) Andreae, M. O.; Crutzen, P. J. Atmospheric Aerosols: Biogeochemical Sources and Role in Atmospheric Chemistry. *Science* **1997**, *276* (5315), 1052–1058. https://doi.org/10.1126/science.276.5315.1052.

(59) Vesala, T.; Kulmala, M.; Rudolf, R.; Vrtala, A.; Wagner, P. E. Models for Condensational Growth and Evaporation of Binary Aerosol Particles. *Journal of Aerosol Science* **1997**, *28* (4), 565–598. https://doi.org/10.1016/S0021-8502(96)00461-2.

(60) Vione, D.; Maurino, V.; Minero, C.; Pelizzetti, E.; Harrison, M. A. J.; Olariu, R.-I.; Arsene, C. Photochemical Reactions in the Tropospheric Aqueous Phase and on Particulate Matter. *Chem. Soc. Rev.* **2006**, *35* (5), 441–453. https://doi.org/10.1039/B510796M.

(61) George, I.; Abbatt, J. Heterogeneous oxidation of atmospheric aerosol particles by gas-phase radicals. *Nature Chem.* **2010**, *2*, 713–722. https://doi.org/10.1038/nchem.806.

(62) Srivastava, A. K.; Dey, S.; Tripathi, S. N. Aerosol Characteristics over the Indo-Gangetic Basin: Implications to Regional Climate. *Atmos. Aerosols - Regional Charac. Chem. Phys.* **2012**, https://doi.org/10.5772/47782.

(63) Yu, H.; Kaufman, Y. J.; Chin, M.; Feingold, G.; Remer, L. A.; Anderson, T. L.; Balkanski, Y.; Bellouin, N.; Boucher, O.; Christopher, S.; DeCola, P.; Kahn, R.; Koch, D.; Loeb, N.; Reddy, M. S.; Schulz, M.; Takemura, T.; Zhou, M. A review of measurement-based assessments of the aerosol direct radiative effect and forcing. *Atmos. Chem. Phys.* **2006**, *6* (3), 613–666. https://doi.org/10.5194/acp-6-613-2006.

(64) Mahowald, N. Aerosol Indirect Effect on Biogeochemical Cycles and Climate. *Science* **2011**, *334* (6057), 794–796. https://doi.org/10.1126/science.1207374.

(65) Levy II, H.; Horowitz, L. W.; Schwarzkopf, M. D.; Ming, Y.; Golaz, J.-C.; Naik, V.; Ramaswamy, V. The Roles of Aerosol Direct and Indirect Effects in Past and Future Climate Change. *J. Geophys. Res. Atmos.* **2013**, *118* (10), 4521–4532. https://doi.org/10.1002/jgrd.50192.

(66) Després, VivianeR.; Huffman, J. A.; Burrows, S. M.; Hoose, C.; Safatov, AleksandrS.; Buryak, G.; Fröhlich-Nowoisky, J.; Elbert, W.; Andreae, MeinratO.; Pöschl, U.; Jaenicke, R. Primary Biological Aerosol Particles in the Atmosphere: A Review. *Tellus B Chem. Phys. Meteorol.* **2012**, *64* (1), 15598. https://doi.org/10.3402/tellusb.v64i0.15598.

(67) Shiraiwa, M.; Ueda, K.; Pozzer, A.; Lammel, G.; Kampf, C. J.; Fushimi, A.; Enami, S.; Arangio, A. M.; Fröhlich-Nowoisky, J.; Fujitani, Y.; Furuyama, A.; Lakey, P. S. J.; Lelieveld, J.; Lucas, K.; Morino, Y.; Pöschl, U.; Takahama, S.; Takami, A.; Tong, H.; Weber, B.; Yoshino, A.; Sato, K. Aerosol Health Effects from Molecular to Global Scales. *Environ. Sci. Technol.* **2017**, *51* (23), 13545–13567. https://doi.org/10.1021/acs.est.7b04417.

(68) Taulbee, D. B.; Yu, C. P. A Theory of Aerosol Deposition in the Human Respiratory Tract. *J. Appl. Physiol.* **1975**, *38*, 77–85. https://doi.org/10.1152/jappl.1975.38.1.77.

(69) Miguel, A. F. Penetration of Inhaled Aerosols in the Bronchial Tree. *Med. Eng. Phys.* **2017**, *44*, 25–31. https://doi.org/10.1016/j.medengphy.2017.03.004.

(70) Longest, P. W.; Vinchurkar, S.; Martonen, T. Transport and Deposition of Respiratory Aerosols in Models of Childhood Asthma. *J. Aerosol Sci.* **2006**, *37* (10), 1234–1257. https://doi.org/10.1016/j.jaerosci.2006.01.011.

(71) Anderson, E. L.; Turnham, P.; Griffin, J. R.; Clarke, C. C. Consideration of the Aerosol Transmission for COVID-19 and Public Health. *Risk Anal.* **2020**, *40* (5), 902–907. https://doi.org/10.1111/risa.13500.

(72) Kuehn, B. M. WHO: More Than 7 Million Air Pollution Deaths Each Year. *JAMA* **2014**, *311* (15), 1486. https://doi.org/10.1001/jama.2014.4031.

(73) Sloss, L. L.; Smith, I. M. PM10 and PM2.5: An International Perspective. *Fuel Process. Technol.* **2000**, *65–66*, 127–141. https://doi.org/10.1016/S0378-3820(99)00081-8.

(74) Priyanka; Choudhary, O. P.; Singh, I.; Patra, G. Aerosol Transmission of SARS-CoV-2: The Unresolved Paradox. *Travel Med. Infect. Dis.* **2020**, *37*, 101869. https://doi.org/10.1016/j.tmaid.2020.101869.

(75) Ehsanifar, M. Airborne Aerosols Particles and COVID-19 Transition. *Environ. Res.* **2021**, *200*, 111752. https://doi.org/10.1016/j.envres.2021.111752.

(76) Pyankov, O. V.; Bodnev, S. A.; Pyankova, O. G.; Agranovski, I. E. Survival of Aerosolized Coronavirus in the Ambient Air. *J. Aerosol Sci.* **2018**, *115*, 158–163. https://doi.org/10.1016/j.jaerosci.2017.09.009.

(77) Tellier, R. COVID-19: The Case for Aerosol Transmission. *Interface Focus* **2022**, *12* (2), 20210072. https://doi.org/10.1098/rsfs.2021.0072.

(78) Moschovis, P. P.; Yonker, L. M.; Shah, J.; Singh, D.; Demokritou, P.; Kinane, T. B. Aerosol Transmission of SARS-CoV-2 by Children and Adults during the COVID-19 Pandemic. *Pediatr. Pulmonol.* **2021**, *56* (6), 1389–1394. https://doi.org/10.1002/ppul.25330.

(79) Tang, S.; Mao, Y.; Jones, R. M.; Tan, Q.; Ji, J. S.; Li, N.; Shen, J.; Lv, Y.; Pan, L.; Ding, P.; Wang, X.; Wang, Y.; MacIntyre, C. R.; Shi, X. Aerosol Transmission of SARS-CoV-2? Evidence, Prevention and Control. *Environ. Int.* **2020**, *144*, 106039. https://doi.org/10.1016/j.envint.2020.106039.

(80) Watts, A. B.; McConville, J. T.; Williams, R. O. Current Therapies and Technological Advances in Aqueous Aerosol Drug Delivery. *Drug Dev. Ind. Pharm.* **2008**, *34* (9), 913–922. https://doi.org/10.1080/03639040802144211.

(81) Kuhn, R. J. Pharmaceutical Considerations in Aerosol Drug Delivery. *Pharmacoth.: J. Human Pharmacol. and Drug Thera.* **2002**, *22* (3P2), 80S–85S. https://doi.org/10.1592/phco.22.6.80S.33907.

(82) Maa, Y.-F.; Nguyen, P.-A.; Sweeney, T.; Shire, S. J.; Hsu, C. C. Protein Inhalation Powders: Spray Drying vs Spray Freeze Drying. *Pharm. Res.* **1999**, *16* (2), 249–254. https://doi.org/10.1023/A:1018828425184.

(83) Stejskal, V.; Vendl, T.; Aulicky, R.; Athanassiou, C. Synthetic and Natural Insecticides: Gas, Liquid, Gel and Solid Formulations for Stored-Product and Food-

Industry Pest Control. *Insects* **2021**, *12* (7), 590. https://doi.org/10.3390/insects12070590.

(84) Ghani, J.A.; Yap, P.H.; Mahmood, W.M.F.W. Study on liquid nano-atomization systems for minimum quantity lubrication—a review. *J. Adv. Manuf. Technol.* **2022**, *121*, 5637–5649. https://doi.org/10.1007/s00170-022-09612-3.

(85) Zhang, X.; Ismail, M. H. S.; Ahmadun, F.-R. b; Abdullah, N. bt H.; Hee, C. Hot Aerosol Fire Extinguishing Agents and the Associated Technologies: A Review. *Braz. J. Chem. Eng.* **2015**, *32*, 707–724. https://doi.org/10.1590/0104-6632.20150323s00003510.

(86) Prather, K. A.; Hatch, C. D.; Grassian, V. H. Analysis of Atmospheric Aerosols. *Annual Rev. Anal. Chem.* **2008**, *1* (1), 485–514. https://doi.org/10.1146/annurev.anchem.1.031207.113030.

(87) Kolb, C. E.; Worsnop, D. R. Chemistry and Composition of Atmospheric Aerosol Particles. *Annu. Rev. Phys. Chem.* **2012**, *63* (1), 471–491. https://doi.org/10.1146/annurev-physchem-032511-143706.

(88) Shao, Y.; Voliotis, A.; Du, M.; Wang, Y.; Pereira, K.; Hamilton, J.; Alfarra, M. R.; McFiggans, G. Chemical Composition of Secondary Organic Aerosol Particles Formed from Mixtures of Anthropogenic and Biogenic Precursors. *Atmos. Chem. Phys.* **2022**, *22* (15), 9799–9826. https://doi.org/10.5194/acp-22-9799-2022.

(89) Zhang, Q.; Jimenez, J. L.; Canagaratna, M. R.; Allan, J. D.; Coe, H.; Ulbrich, I.; Alfarra, M. R.; Takami, A.; Middlebrook, A. M.; Sun, Y. L.; Dzepina, K.; Dunlea, E.; Docherty, K.; DeCarlo, P. F.; Salcedo, D.; Onasch, T.; Jayne, J. T.; Miyoshi, T.; Shimono, A.; Hatakeyama, S.; Takegawa, N.; Kondo, Y.; Schneider, J.; Drewnick, F.; Borrmann, S.; Weimer, S.; Demerjian, K.; Williams, P.; Bower, K.; Bahreini, R.; Cottrell, L.; Griffin, R. J.; Rautiainen, J.; Sun, J. Y.; Zhang, Y. M.; Worsnop, D. R. Ubiquity and Dominance of Oxygenated Species in Organic Aerosols in Anthropogenically-Influenced Northern Hemisphere Midlatitudes. *Geophys. Res. Lett.* **2007**, *34* (13), L13801. https://doi.org/10.1029/2007GL029979.

(90) Davies, J. F.; Wilson, K. R. Heterogeneous Reactions in Aerosol. *Physical Chemis. of Gas-Liquid Interf.* **2018**, 403–433. https://doi.org/10.1016/B978-0-12-813641-6.00013-3.

(91) Kanakidou, M.; Seinfeld, J. H.; Pandis, S. N.; Barnes, I.; Dentener, F. J.; Facchini, M. C.; Dingenen, R. V.; Ervens, B.; Nenes, A.; Nielsen, C. J.; Swietlicki, E.; Putaud, J. P.; Balkanski, Y.; Fuzzi, S.; Horth, J.; Moortgat, G. K.; Winterhalter, R.; Myhre, C. E. L.; Tsigaridis, K.; Vignati, E.; Stephanou, E. G.; Wilson, J. Organic Aerosol

and Global Climate Modelling: A Review. *Atmos. Chem. Phys.* **2005**, *5* (4), 1053–1123. https://doi.org/10.5194/acp-5-1053-2005.

(92) Zhang, Q.; Worsnop, D. R.; Canagaratna, M. R.; Jimenez, J. L. Hydrocarbon-like and oxygenated organic aerosols in Pittsburgh: insights into sources and processes of organic aerosols. *Atmos. Chem. Phys.* **2005** *5* (12), 3289–3311. https://doi.org/10.5194/acp-5-3289-2005.

(93) Salcedo, D.; Onasch, T. B.; Dzepina, K.; Canagaratna, M. R.; Zhang, Q.; Huffman, J. A.; DeCarlo, P. F.; Jayne, J. T.; Mortimer, P.; Worsnop, D. R.; Kolb, C. E.; Johnson, K. S.; Zuberi, B.; Marr, L. C.; Volkamer, R.; Molina, L. T.; Molina, M. J.; Cardenas, B.; Bernabé, R. M.; Márquez, C.; Gaffney, J. S.; Marley, N. A.; Laskin, A.; Shutthanandan, V.; Xie, Y.; Brune, W.; Lesher, R.; Shirley, T.; Jimenez, J. L. Characterization of Ambient Aerosols in Mexico City during the MCMA-2003 Campaign with Aerosol Mass Spectrometry: Results from the CENICA Supersite. *Atmos. Chem. Phys.* **2006**, *6* (4), 925–946. https://doi.org/10.5194/acp-6-925-2006.

(94) Miyazaki, Y.; Kondo, Y.; Takegawa, N.; Komazaki, Y.; Fukuda, M.; Kawamura, K.; Mochida, M.; Okuzawa, K.; Weber, R. J. Time-Resolved Measurements of Water-Soluble Organic Carbon in Tokyo. *J. Geophys. Res. Atmos.* **2006**, *111*, D23206. https://doi.org/10.1029/2006JD007125.

(95) Jayne, J. T.; Leard, D. C.; Zhang, X.; Davidovits, P.; Smith, K. A.; Kolb, C. E.; Worsnop, D. R. Development of an Aerosol Mass Spectrometer for Size and Composition Analysis of Submicron Particles. *Aerosol Sci Technol.* **2000**, *33* (1–2), 49–70. https://doi.org/10.1080/027868200410840.

(96) Lanz, V. A.; Prevot, A. S. H.; Alfarra, M. R.; Weimer, S.; Mohr, C.; DeCarlo, P. F.; Gianini, M. F. D.; Hueglin, C.; Schneider, J.; Favez, O.; D'Anna, B.; George, C.; Baltensperger, U.; Institut, P. S. Characterization of Aerosol Chemical Composition with Aerosol Mass Spectrometry in Central Europe: An Overview. *Atmos. Chem. Phys.* **2010**, *10* (21), 10453–10471. https://doi.org/10.5194/acp-10-10453-2010.

(97) Alfarra, M. R.; Coe, H.; Allan, J. D.; Bower, K. N.; Boudries, H.; Canagaratna, M. R.; Jimenez, J. L.; Jayne, J. T.; Garforth, A. A.; Li, S.-M.; Worsnop, D. R. Characterization of Urban and Rural Organic Particulate in the Lower Fraser Valley Using Two Aerodyne Aerosol Mass Spectrometers. *Atmos. Environ.* **2004**, *38* (34), 5745–5758. https://doi.org/10.1016/j.atmosenv.2004.01.054.

(98) Dennis-Smither, B. J.; Miles, R. E. H.; Reid, J. P. Oxidative Aging of Mixed Oleic Acid/Sodium Chloride Aerosol Particles. *J. Geophys. Res.* **2012**, *117*, D20204. https://doi.org/10.1029/2012JD018163.

(99) Zobrist, B.; Marcolli, C.; Pedernera, D. A.; Koop, T. Do Atmospheric Aerosols

Form Glasses? *Atmos. Chem. Phys.* **2008**, *8* (17), 5221–5244. https://doi.org/10.5194/acp-8-5221-2008.

(100) Reid, J.P.; Bertram, A.K.; Topping, D.O. The viscosity of atmospherically relevant organic particles. *Nature Commun.* **2018**, *9*, 956. https://doi.org/10.1038/s41467-018-03027-z.

(101) Koop, T.; Bookhold, J.; Shiraiwa, M.; Pöschl, U. Glass transition and phase state of organic compounds: dependency on molecular properties and implications for secondary organic aerosols in the atmosphere. *Phys. Chem. Chem. Phys.* **2011**, *13*, 19238–19255. https://doi.org/10.1039/C1CP22617G.

(102) Song, Y.-C.; Lilek, J.; Lee, J. B.; Chan, M. N.; Wu, Z.; Zuend, A.; Song, M. Viscosity and Phase State of Aerosol Particles Consisting of Sucrose Mixed with Inorganic Salts. *Atmos. Chem. Phys.* **2021**, *21* (13), 10215–10228. https://doi.org/10.5194/acp-21-10215-2021.

(103) Shen, C.; Zhang, W.; Choczynski, J.; Davies, J. F.; Zhang, H. Phase State and Relative Humidity Regulate the Heterogeneous Oxidation Kinetics and Pathways of Organic-Inorganic Mixed Aerosols. *Environ. Sci. Technol.* **2022**, *56* (22), 15398–15407. https://doi.org/10.1021/acs.est.2c04670.

(104) Zaveri, R. A.; Easter, R. C.; Shilling, J. E.; Seinfeld, J. H. Modeling Kinetic Partitioning of Secondary Organic Aerosol and Size Distribution Dynamics: Representing Effects of Volatility, Phase State, and Particle-Phase Reaction. *Atmos. Chem. Phys.* **2014**, *14* (10), 5153–5181. https://doi.org/10.5194/acp-14-5153-2014.

(105) Shiraiwa, M.; Seinfeld, J. H. Equilibration timescale of atmospheric secondary organic aerosol partitioning. *Geophys. Res. Lett.* **2012**, *39*, L24801. doi:10.1029/2012GL054008.

(106) Reid, J. P.; Dennis-Smither, B. J.; Kwamena, N.-O. A.; Miles, R. E. H.; Hanford, K. L.; Homer, C. J. The Morphology of Aerosol Particles Consisting of Hydrophobic and Hydrophilic Phases: Hydrocarbons, Alcohols and Fatty Acids as the Hydrophobic Component. *Phys. Chem. Chem. Phys.* **2011**, *13* (34), 15559–15572. https://doi.org/10.1039/C1CP21510H.

(107) Freedman, M. A. Liquid–Liquid Phase Separation in Supermicrometer and Submicrometer Aerosol Particles. *Acc. Chem. Res.* **2020**, *53* (6), 1102–1110. https://doi.org/10.1021/acs.accounts.0c00093.

(108) Krieger, U. K.; Marcolli, C.; Reid, J. P. Exploring the Complexity of Aerosol Particle Properties and Processes Using Single Particle Techniques. *Chem. Soc. Rev.* **2012**, *41* (19), 6631. https://doi.org/10.1039/c2cs35082c.

(109) Kaaden, N.; Massling, A.; Schladitz, A.; MüLLER, T.; Kandler, K.; SchüTZ, L.; Weinzierl, B.; Petzold, A.; Tesche, M.; Leinert, S.; Deutscher, C.; Ebert, M.; Weinbruch, S.; Wiedensohler, A. State of Mixing, Shape Factor, Number Size Distribution, and Hygroscopic Growth of the Saharan Anthropogenic and Mineral Dust Aerosol at Tinfou, Morocco. *Tellus B Chem. Phys. Meteorol.* **2009**, *61* (1), 51–63. https://doi.org/10.1111/j.1600-0889.2008.00388.x.

(110) Tsyro, S. First Estimates of the Effects of Aerosol Dynamics in the Calculation of PM_{10} and $PM_{2.5}$. **2002**. http://emep/msc-wnote4/2002.

(111) Zeller, W. Direct Measurement of Aerosol Shape Factors. *Aerosol Sci. Technol.* **1985**, *4* (1), 45–63. https://doi.org/10.1080/02786828508959038.

(112) Liu, Y.; Jia, R.; Dai, T; Xie, Y.; Shi, G. A review of aerosol optical properties and radiative effects. *J. Meteorol. Res.* **2015**, *28*, 1003–1028. https://doi.org/10.1007/s13351-014-4045-z.

(113) Liu, X.; Cheng, Y.; Zhang, Y.; Jung, J.; Sugimoto, N.; Chang, S.-Y.; Kim, Y. J.; Fan, S.; Zeng, L. Influences of Relative Humidity and Particle Chemical Composition on Aerosol Scattering Properties during the 2006 PRD Campaign. *Atmos. Environ.* **2008**, *42* (7), 1525–1536. https://doi.org/10.1016/j.atmosenv.2007.10.077.

(114) Titos, G.; Foyo-Moreno, I.; Lyamani, H.; Querol, X.; Alastuey, A.; Alados-Arboledas, L. Optical Properties and Chemical Composition of Aerosol Particles at an Urban Location: An Estimation of the Aerosol Mass Scattering and Absorption Efficiencies: Aerosol Mass Efficiency. *J. Geophys. Res.* **2012**, *117* (D04206). https://doi.org/10.1029/2011JD016671.

(115) Bohren, C. F.; Huffman, D. R. Absorption and Scattering of Light by Small Particles. *John Wiley and Sons* **2008**.

(116) Dingle, J. H.; Zimmerman, S.; Frie, A. L.; Min, J.; Jung, H.; Bahreini, R. Complex Refractive Index, Single Scattering Albedo, and Mass Absorption Coefficient of Secondary Organic Aerosols Generated from Oxidation of Biogenic and Anthropogenic Precursors. *Aerosol Sci. Technol.* **2019**, *53* (4), 449–463. https://doi.org/10.1080/02786826.2019.1571680.

(117) Preston, T. C.; Reid, J. P. Determining the Size and Refractive Index of Microspheres Using the Mode Assignments from Mie Resonances. *J. Opt. Soc. Am. A* **2015**, *32* (11), 2210. https://doi.org/10.1364/JOSAA.32.002210.

(118) Price, C. L.; Bain, A.; Wallace, B. J.; Preston, T. C.; Davies, J. F. Simultaneous Retrieval of the Size and Refractive Index of Suspended Droplets in a Linear

Quadrupole Electrodynamic Balance. *J. Phys. Chem. A* **2020**, *124* (9), 1811–1820. https://doi.org/10.1021/acs.jpca.9b10748.

(119) Bain, A.; Rafferty, A.; Preston, T. C. Determining the Size and Refractive Index of Single Aerosol Particles Using Angular Light Scattering and Mie Resonances. *J. Quant. Spectrosc. Radiat. Transf.* **2018**, *221*, 61–70. https://doi.org/10.1016/j.jqsrt.2018.09.026.

(120) Molina, M. J.; Ivanov, A. V.; Trakhtenberg, S.; Molina, L. T. Atmospheric evolution of organic aerosol. *Geophys. Res. Lett.* **2004**, *31*, L22104, doi:10.1029/2004GL020910.

(121) Kaur Kohli, R.; Davies, J. F. Measuring the Chemical Evolution of Levitated Particles: A Study on the Evaporation of Multicomponent Organic Aerosol. *Anal. Chem.* **2021**, *93* (36), 12472–12479. https://doi.org/10.1021/acs.analchem.1c02890.

(122) Ling, Z.; Wu, L.; Wang, Y.; Shao, M.; Wang, X.; Huang, W. Roles of Semivolatile and Intermediate-Volatility Organic Compounds in Secondary Organic Aerosol Formation and Its Implication: A Review. *J. Environ. Sci.* **2022**, *114*, 259–285. https://doi.org/10.1016/j.jes.2021.08.055.

(123) Choczynski, J. M.; Kaur Kohli, R.; Sheldon, C. S.; Price, C. L.; Davies, J. F. A Dual-Droplet Approach for Measuring the Hygroscopicity of Aqueous Aerosol. *Atmos. Meas. Tech.* **2021**, *14* (7), 5001–5013. https://doi.org/10.5194/amt-14-5001-2021.

(124) C. Chapleski, R.; Zhang, Y.; Troya, D.; R. Morris, J. Heterogeneous Chemistry and Reaction Dynamics of the Atmospheric Oxidants, O 3 , NO 3 , and OH, on Organic Surfaces. *Chem. Soc. Rev.* **2016**, *45* (13), 3731–3746. https://doi.org/10.1039/C5CS00375J.

(125) Abbatt, J. P. D.; Lee, A. K. Y.; Thornton, J. A. Quantifying Trace Gas Uptake to Tropospheric Aerosol: Recent Advances and Remaining Challenges. *Chem. Soc. Rev.* **2012**, *41* (19), 6555. https://doi.org/10.1039/c2cs35052a.

(126) Kroll, J. H.; Smith, J. D.; Che, D. L.; Kessler, S. H.; Worsnop, D. R.; Wilson, K. R. Measurement of Fragmentation and Functionalization Pathways in the Heterogeneous Oxidation of Oxidized Organic Aerosol. *Phys. Chem. Chem. Phys.* **2009**, *11* (36), 8005–8014. https://doi.org/10.1039/B905289E.

(127) Berkemeier, T.; Mishra, A.; Mattei, C.; Huisman, A. J.; Krieger, U. K.; Pöschl, U. Ozonolysis of Oleic Acid Aerosol Revisited: Multiphase Chemical Kinetics and Reaction Mechanisms. *ACS Earth Space Chem.* **2021**, *5* (12), 3313–3323. https://doi.org/10.1021/acsearthspacechem.1c00232.

(128) Wilson, K. R.; Prophet, A. M.; Willis, M. D. A Kinetic Model for Predicting Trace Gas Uptake and Reaction. *J. Phys. Chem. A* **2022**, *126* (40), 7291–7308. https://doi.org/10.1021/acs.jpca.2c03559.

(129) McMurry, P. H. A Review of Atmospheric Aerosol Measurements. *Atmos. Environ.* **2000**, *34* (12), 1959–1999. https://doi.org/10.1016/S1352-2310(99)00455-0.

(130) DeCarlo, P. F.; Kimmel, J. R.; Trimborn, A.; Northway, M. J.; Jayne, J. T.; Aiken, A. C.; Gonin, M.; Fuhrer, K.; Horvath, T.; Docherty, K. S.; Worsnop, D. R.; Jimenez, J. L. Field-Deployable, High-Resolution, Time-of-Flight Aerosol Mass Spectrometer. *Anal. Chem.* **2006**, *78* (24), 8281–8289. https://doi.org/10.1021/ac061249n.

(131) Rudich, Y. Laboratory Perspectives on the Chemical Transformations of Organic Matter in Atmospheric Particles. *Chem. Rev.* **2003**, *103* (12), 5097–5124. https://doi.org/10.1021/cr020508f.

(132) Shiraiwa, M.; Pfrang, C.; Poschl, U. Kinetic Multi-Layer Model of Aerosol Surface and Bulk Chemistry (KM-SUB): The Influence of Interfacial Transport and Bulk Diffusion on the Oxidation of Oleic Acid by Ozone. *Atmos. Chem. Phys*. **2010**, *10*, 3673–3691. https://doi.org/10.5194/acp-10-3673-2010.

(133) Rudich, Y.; Donahue, N. M.; Mentel, T. F. Aging of Organic Aerosol: Bridging the Gap Between Laboratory and Field Studies. *Annu. Rev. Phys. Chem.* **2007**, *58* (1), 321–352. https://doi.org/10.1146/annurev.physchem.58.032806.104432.

(134) Cocker, D. R.; Flagan, R. C.; Seinfeld, J. H. State-of-the-Art Chamber Facility for Studying Atmospheric Aerosol Chemistry. *Environ. Sci. Technol.* **2001**, *35* (12), 2594–2601. https://doi.org/10.1021/es0019169.

(135) Friebel, F.; Mensah, A. A. Aging Aerosol in a Well-Mixed Continuous-Flow Tank Reactor: An Introduction of the Activation Time Distribution. *Atmos. Meas. Tech.* **2019**, *12* (5), 2647–2663. https://doi.org/10.5194/amt-12-2647-2019.

(136) Kinetics of the heterogeneous reaction of nitric acid with mineral dust particles: an aerosol flowtube study. *Phys. Chem. Chem. Phys.* **2009**, *11*, 7921-7930. https://doi.org/10.1039/B904290N

(137) Alfarra, M. R.; Paulsen, D.; Gysel, M.; Garforth, A. A.; Dommen, J.; Prévôt, A. S. H.; Worsnop, D. R.; Baltensperger, U.; Coe, H. A Mass Spectrometric Study of Secondary Organic Aerosols Formed from the Photooxidation of Anthropogenic and Biogenic Precursors in a Reaction Chamber. *Atmos. Chem. Phys.* **2006**, *6* (12), 5279–5293. https://doi.org/10.5194/acp-6-5279-2006.

(138) Du, M.; Voliotis, A.; Shao, Y.; Wang, Y.; Bannan, T. J.; Pereira, K. L.; Hamilton, J. F.; Percival, C. J.; Alfarra, M. R.; McFiggans, G. Combined Application of Online FIGAERO-CIMS and Offline LC-Orbitrap Mass Spectrometry (MS) to Characterize the Chemical Composition of Secondary Organic Aerosol (SOA) in Smog Chamber Studies. *Atmos. Meas. Tech.* **2022**, *15* (14), 4385–4406. https://doi.org/10.5194/amt-15-4385-2022.

(139) Kaur Kohli, R.; Van Berkel, G. J.; Davies, J. F. An Open Port Sampling Interface for the Chemical Characterization of Levitated Microparticles. *Anal. Chem.* **2022**, *94* (8), 3441–3445. https://doi.org/10.1021/acs.analchem.1c05550.

(140) Lee, A. K. Y.; Chan, C. K. Single Particle Raman Spectroscopy for Investigating Atmospheric Heterogeneous Reactions of Organic Aerosols. *Atmos. Environ.* **2007**, *41* (22), 4611–4621. https://doi.org/10.1016/j.atmosenv.2007.03.040.

(141) Kaduchak, G.; Sinha, D. N.; Lizon, D. C. Novel Cylindrical, Air-Coupled Acoustic Levitation/Concentration Devices. *Rev. Sci. Instrum.* **2002**, *73* (3), 1332–1336. https://doi.org/10.1063/1.1448900.

(142) Kalume, A.; Wang, C.; Pan, Y.-L. Optical-Trapping Laser Techniques for Characterizing Airborne Aerosol Particles and Its Application in Chemical Aerosol Study. *Micromachines* **2021**, *12* (4), 466. https://doi.org/10.3390/mi12040466.

(143) Nieminen, T. A.; Knöner, G.; Heckenberg, N. R.; Rubinsztein-Dunlop, H. Physics of Optical Tweezers. *Methods Cell Biol.* **2007**, *82*, 207–236. https://doi.org/10.1016/S0091-679X(06)82006-6.

(144) Gorkowski, K.; Donahue, N. M.; Sullivan, R. C. Aerosol Optical Tweezers Constrain the Morphology Evolution of Liquid-Liquid Phase-Separated Atmospheric Particles. *Chem* **2020**, *6* (1), 204–220. https://doi.org/10.1016/j.chempr.2019.10.018.

(145) Davies, J. F. Mass, Charge, and Radius of Droplets in a Linear Quadrupole Electrodynamic Balance. *Aerosol Sci. Technol.* **2019**, *53* (3), 309–320. https://doi.org/10.1080/02786826.2018.1559921.

(146) Birdsall, A. W.; Krieger, U. K.; Keutsch, F. N. Electrodynamic Balance–Mass Spectrometry of Single Particles as a New Platform for Atmospheric Chemistry Research. *Atmos. Meas. Tech.* **2018**, *11* (1), 33–47. https://doi.org/10.5194/amt-11-33-2018.

(147) Cotterell, M. I.; Knight, J. W.; Reid, J. P.; Orr-Ewing, A. J. Accurate Measurement of the Optical Properties of Single Aerosol Particles Using Cavity Ring-Down Spectroscopy. *J. Phys. Chem. A* **2022**, *126* (17), 2619–2631. https://doi.org/10.1021/acs.jpca.2c01246.

(148) Preston, R. E.; Lettieri, T. R.; Semerjian, H. G. Characterization of Single Levitated Droplets by Raman Spectroscopy. *Langmuir* **1985**, *1*, 365–367. https://doi.org/10.1021/la00063a018.

(149) Jacobs, M. I.; Davies, J. F.; Lee, L.; Davis, R. D.; Houle, F.; Wilson, K. R. Exploring Chemistry in Microcompartments Using Guided Droplet Collisions in a Branched Quadrupole Trap Coupled to a Single Droplet, Paper Spray Mass Spectrometer. *Anal. Chem.* **2017**, *89* (22), 12511–12519. https://doi.org/10.1021/acs.analchem.7b03704.

(150) Müller, M. Oxidation Pathways of Linoleic Acid Revisited with Electrodynamic Balance–Mass Spectrometry. *Environ. Sci.: Atmos.*, **2022**, *3* (1), 85–96. https://doi.org/10.1039/D2EA00127F.

(151) Griffin, R. J.; Cocker, D. R.; Seinfeld, J. H.; Dabdub, D. Estimate of Global Atmospheric Organic Aerosol from Oxidation of Biogenic Hydrocarbons. *Geophys. Res. Lett.* **1999**, *26* (17), 2721–2724. https://doi.org/10.1029/1999GL900476.

(152) Zhang, X.; Cappa, C. D.; Jathar, S. H.; McVay, R. C.; Ensberg, J. J.; Kleeman, M. J.; Seinfeld, J. H. Influence of Vapor Wall Loss in Laboratory Chambers on Yields of Secondary Organic Aerosol. *Proc. Natl. Acad. Sci.* **2014**, *111* (16), 5802–5807. https://doi.org/10.1073/pnas.1404727111.

CHAPTER 2

Linear Quadrupole Electrodynamic Balance Coupled with Mie Resonance Spectroscopy and Mass Spectrometry to Study Chemical Transformations

2.1. Abstract

This chapter focuses on our research developments to demonstrate the capability of laboratory-based methods for examining the atmospherically relevant chemical transformations on single levitated microparticles. This involves a detailed discussion on the principle of operation and development of a linear quadrupole electrodynamic balance (LQ-EDB) for particle levitation, the application of Mie resonance spectroscopy (MRS) for characterizing the size and optical properties of levitated particles, and the development of mass spectrometry (MS) methods to determine the chemical composition of levitated particles. Additionally, different sampling and ionization methods, namely paper spray (PS) and open port sampling interface (OPSI) – electrospray (ES), are discussed for effective transfer of chemical analytes from levitated particles in the LQ-EDB to the MS for compositional analysis. The combined LQ-EDB-MS technique allows for the real-time analysis of both physical and optical properties as well as chemical composition of the levitated particles undergoing chemical transformations.

2.2. Linear Quadrupole Electrodynamic Balance (LQ-EDB) for Particle Levitation

A linear quadrupole electrodynamic balance (LQ-EDB) is a particle levitation system that can spatially confine single or an array of micrometer-sized particles in an electric field.[1–4] Droplets with a known initial composition are generated on-demand either individually or in burst mode with the help of a piezoelectric droplet dispenser and introduced into the LQ-EDB for trapping. The basic working principle of a droplet dispenser involves the application of square electrical pulses, with pulse widths around 30 μs and a voltage peak of up to 50 V, on a piezoelectric material (like crystal, ceramic, etc.) sandwiched between two electrodes.[5–7] This causes the material to deform, creating a pressure wave that propels a jet of liquid out of dispenser that breaks down into single droplets due to surface tension. These droplets are given a charge as they emerge from the dispenser due to the presence of a DC induction electrode (150 – 500 V) which is mounted external to the LQ-EDB. The resulting droplets possess a charge of 10 – 100 fC with an initial diameter of approximately 50 μm and travel inside the quadrupole electrode where they are confined along the central axis due to the oscillating electric field. **Figure 1** shows the generation of droplets from droplet dispenser that are being charged upon their entry into the LQ-EDB trap due to the presence of induction voltage.

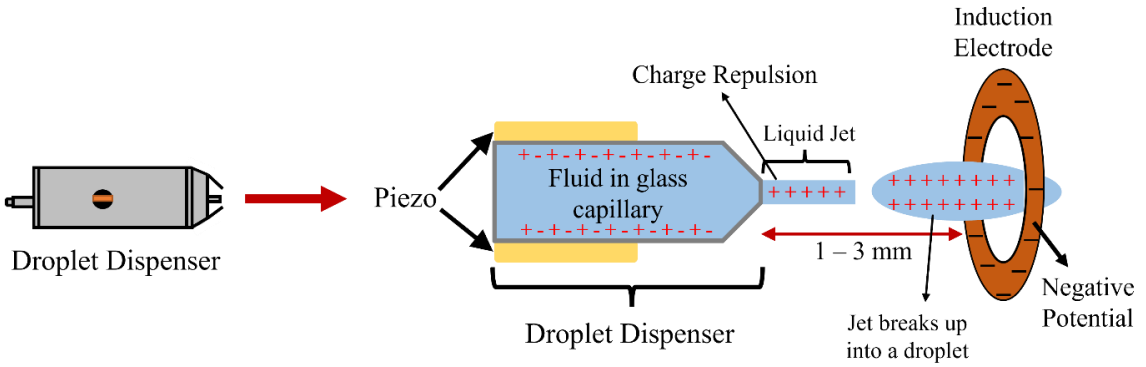

Figure 1: An arrangement of droplet piezoelectric droplet dispenser with the induction electrode mounted on the LQ-EDB. The solvent filled in glass capillary inside the dispenser is propelled out as liquid jet which forms a droplet caused by a temporary deformation of piezo material due to the application of pulse voltage. This jet and the droplet then get positively charged due to the coulombic repulsions caused by negative potential maintained at the induction electrode mounted on the LQ-EDB. Finally, the charge on droplets helps in levitating them inside the LQ-EDB chamber. The components in the figure are zoomed in for better illustration.

The electric field inside the LQ-EDB is a result of the application of opposing alternating current (AC) voltage (600 – 1200 V) to diagonally opposite pairs of four parallel stainless-steel electrodes of the quadrupole enclosed in an aluminum chamber and mounted on the PEEK end caps.[8–10] The droplets with a net charge are guided centrally by the electric field and fall under the influence of gravity. To hold these droplets in place, a repulsive electrostatic force caused by a disc electrode with an applied direct current (DC) voltage is applied. The required DC voltage, a function of mass and droplet size, balances the vertically acting downward forces such as gravity and drag forces. For the purposes of our research studies, multiple droplets are stacked in a linear array inside LQ-EDB and separated by electrostatic repulsion. The arrangement of the LQ-EDB, including its key components involved in particle levitation, is depicted in **Figure 2**.[1]

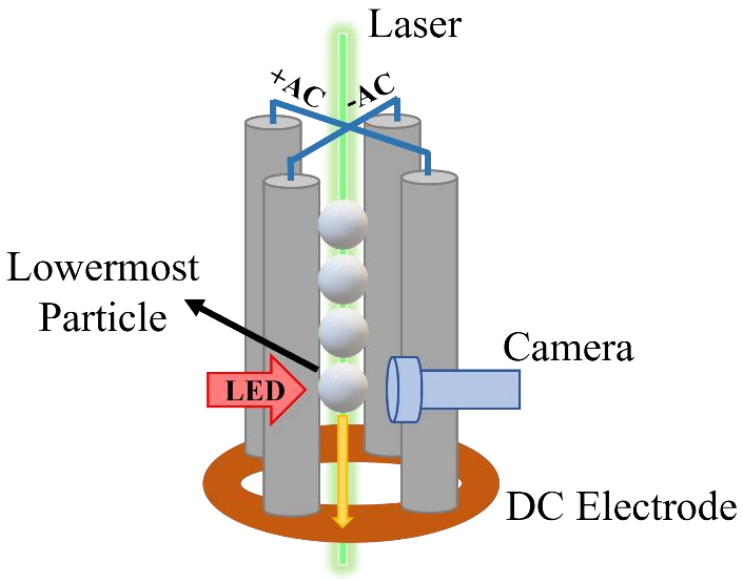

Figure 2: A linear quadrupole electrodynamic balance (LQ-EDB) showing a stack of multiple droplets, AC parallel electrodes and DC disc electrode. The AC voltage arrangement applied to diagonally opposite pair of electrodes, and a 532 nm laser beam for particles illumination is shown. The lowermost droplet is imaged individually by adjusting the position of the entire stack. The figure is not to scale and is for illustration only.

Once the droplets are trapped inside the LQ-EDB, they shrink or swell in size depending on the environmental conditions inside the chamber. Under dry conditions, the droplets immediately lose the solvent and become much smaller in size. Depending on the environmental conditions and chemical composition, the droplets can remain as liquid droplets or transform to solid particles upon levitation. As discussed earlier, the term "particle" is generally used to describe both solid and liquid physical state. The size range of particles accessible to LQ-EDB for trapping is usually between 1 – 100 µm. A 532 nm laser with a power of 5 mW is used to illuminate the particles during levitation for the visual verification of the particle number and stability of the stack. A CMOS camera is fixed with one of the viewing windows of LQ-EDB chamber which generates an image of

the lowermost particle in the stack. Additionally, the lowermost particle is continuously illuminated with red LED for analyzing its physical and optical characteristics using Mie Resonance Spectroscopy (MRS), which is discussed in *Section 2.3*. By adjusting the strength of DC balancing voltage, the vertical position of the entire particle stack can be altered to bring the lowermost particle in the frame for camera and MRS for real-time imaging and sizing analysis.

2.2.1. Controlled Conditions for Chemical Transformations on Particles

Specific environmental conditions are used inside the LQ-EDB chamber to carry out a broad range of experimental studies on the levitated particles, including non-reactive transformations like particle-to-gas partitioning of SVOCs and hygroscopicity measurements, and chemical transformations like ozonolysis reactions.[11–14] Once the entire stack of particles is levitated, environmental conditions inside the LQ-EDB chamber can be altered in a controlled manner. Various parameters, such as nitrogen gas flow, relative humidity (RH), temperature and oxidant concentration, are controlled manually or automatically with the help of LabVIEW software.

A typical nitrogen flow rate of approximately 200 sccm was supplied from the top of the LQ-EDB which helps in regulating the necessary environmental conditions, such as relative humidity and oxidant concentration, around the levitated particles inside the chamber. The aerodynamic drag force on the particles produced by the nitrogen flow is balanced by a counter voltage applied by the DC electrode to ensure consistent levitation of the particles. The gas flow in the LQ-EDB was continuously exhausted through an open

port at the bottom of the chamber unless some minor modifications were made (discussed below) for the measurements of ozonolysis transformations.

For measurements exploring the influence of relative humidity (RH), the required RH was achieved by controlling the ratio of dry to humidified nitrogen (using water bubbler) introduced from the top of the LQ-EDB chamber. Automated RH cycles were used for determining the hygroscopicity and phase change characteristics of sample particles.[15] For exploring the evaporation kinetics at ambient conditions, temperature inside LQ-EDB was not controlled and was assumed to be equal to the ambient temperature of the laboratory, typically in the range of 18 to 22 ºC, determined using an external temperature probe. Whereas the studies conducted to explore the evaporation dynamics of particles above ambient temperatures, elevated temperatures (up to ~350 K) were used in specialized LQ-EDB equipped with heating cartridges (*refer Chapter 6*).

For studies focused on ozonolysis transformations, ozone was generated photochemically from pure oxygen exposed to UV light and mixed with nitrogen prior to delivery to the LQ-EDB chamber. To maintain a consistent total gas flow in experiments, the nitrogen flow was slightly reduced whenever mixed with ozone to keep the flow rate constant during the entire measurement. The combined flow of nitrogen and ozone was diverted before entering the chamber with the help of a T-valve for measuring the ozone concentration. For these measurements, the outlet gases containing ozone were actively exhausted through an ozone scrubber using an external suction pump. The temperature inside the chamber was maintained at the ambient laboratory conditions whereas the RH

was adjusted based on the specifics of the measurement. A discussion on the working principle and the innovative development of techniques coupled with LQ-EDB for analyzing the physicochemical properties of levitated particles is presented in the subsequent sections.

2.3. Mie Resonance Spectroscopy for the Analysis of Physical Characteristics

Mie resonance spectroscopy (MRS) is a technique used to characterize the physical properties of spherical particles using a broadband light source. It is based on the principle of optical spectroscopy by applying the Mie theory, which was developed by Gustav Mie in the early 20th century to describe the elastic scattering of light by small particles.[16–18] **Figure 3** shows the schematic of the MRS setup describing the light path generated from red LED light source. In the measurements reported in this thesis, the lowermost particle levitated in the LQ-EDB was illuminated by broadband red LED (640 – 680 nm) centered at 660 nm. Light originating from red LED passes through a 50/50 beam splitter which reflects half of the incident light to the beam-steering mirror. The mirror reflects this light to the biconvex lens having an anti-reflective (AR) coating which then sends it to LQ-EDB chamber through an AR-window. The light is focused on the lowermost droplet in the chamber and backscattered light is generated because of the light resonance inside droplet. This backscattered light then follows the same optical path in reverse direction till it finally falls on the fiber-optic which sends signal to the spectrophotometer.

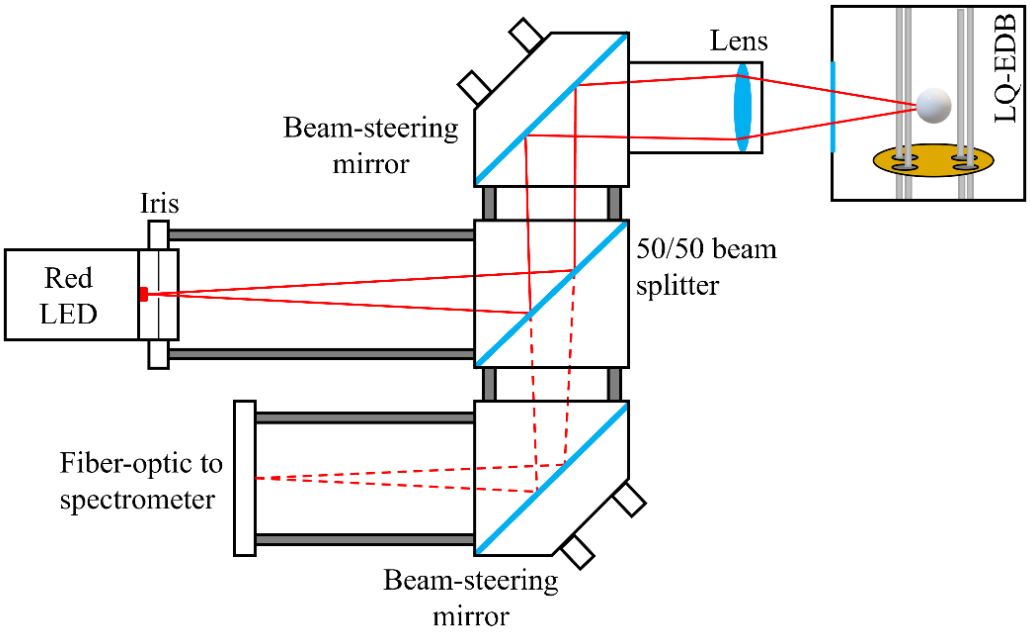

Figure 3: Schematic configuration of the Mie Resonance Spectrometry (MRS) for the characterization of a spherical particle's physical properties, such as size and RI.

The light from the red LED is scattered by the particle and specific wavelengths become resonant in the spherical cavity, resulting in stronger scattering at wavelengths that satisfy the condition for total internal reflection (**Figure 4**). The light undergoes multiple reflections inside the levitated particle and is eventually emitted at specific wavelengths. The backscattered light from the particle was collected by an optical fiber and measured using a spectrometer to yield the experimental Mie resonance spectrum shown as black peaks which is background subtracted to eliminate the contribution of reflected light (**Figure 4A**). These sharp peaks in the Mie resonance spectrum is associated with wavelength positions of morphology dependent resonances (MDRs).[19] Each MDR is described by its own mode number and mode order which are size-dependent features of the spherical particle and describes the penetration depth of the incident light.[20] The

wavelength position of these MDR peaks in the experimental spectrum was determined using a peak fitting algorithm and delivered to a sizing algorithm (MRFIT) developed by Preston and Reid.[21] By applying Mie theory, MRFIT program compares the MDR positions from a library of size and refractive index combinations and the best-fit to the experimental observations is determined through the method of least-squares minimization process.[22] This is confirmed by the good agreement between experimental (black peaks) and simulated (red) Mie spectra as shown in **Figure 4A**. The output of this process yields size and refractive index of levitated particle with high precision as the size is determined with an accuracy of ±5 nm and RI within an uncertainty of 0.001 to 0.005.

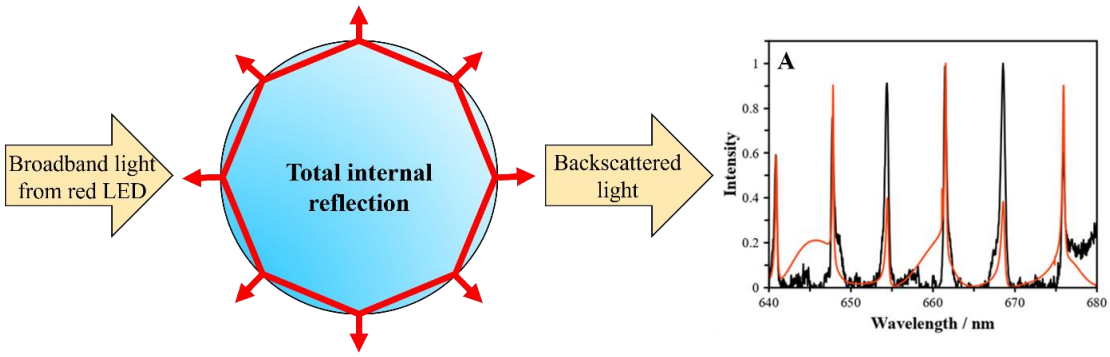

Figure 4 : The interaction of broadband light from red LED with the spherical particle is shown which results in the phenomenon of total internal reflection generating the backscattered light as described in the text. **Figure 4A** presents a comparison of the morphology dependent resonance (MDR) peak structure of the best-fit theoretical prediction (red) and experimental measurement (black) in the Mie resonance spectrum as described in the text.

2.3.1. Online Monitoring of Size, Refractive Index and Morphology

The MDR wavelength positions in the Mie spectra are indicative of size, refractive index (RI) and morphology of the particle as described *Section 2.3*.[20,23] The size is determined

with an accuracy of ±5 nm and RI within an uncertainty of 0.001 to 0.005, depending on the type and number of resonance peaks in Mie spectrum.[16,24] For our measurements, a stack of 5-10 particles is levitated inside LQ-EDB chamber for carrying out chemical transformations in which all the particles behave very uniformly based on our preliminary experimental studies.[12,25] Such chemical transformations happening in the particles can be analyzed in real-time using MRS by determining any changes in lowermost particle's size and RI at a time. Variations in the peak positions can be reflective of the changes in size of the spherical particle. For example, a decreasing peak intensity can confirm that the particle is becoming smaller in size due to chemical transformation. Mie resonance spectra can also reveal information on the evolving morphology and phase state of the levitated particles.[26–28] Deviations in peak structure of the Mie spectra, such as broadening of the peaks and a loss of fine structure, can be indicative of phase transitions which results in different morphology during chemical transformations. An example of morphological changes occurring in the oleic acid particle undergoing ozonolysis transformation is shown in **Figure 5.** As a consequence of chemical transformation, liquid-liquid phase separation occurs which changes the morphology of the levitated particle, resulting in the broadening of peaks and thus, losing the sharp peak structure in the Mie resonance spectrum.[29] Additionally, non-spherical or crystalline particles (such as effloresced NaCl particles) undergo random reflection as opposed to spherical particles which only reflect light from their surface, resulting in the absence of sharp peaks in the Mie spectra due to the absence of light resonance within the particle.

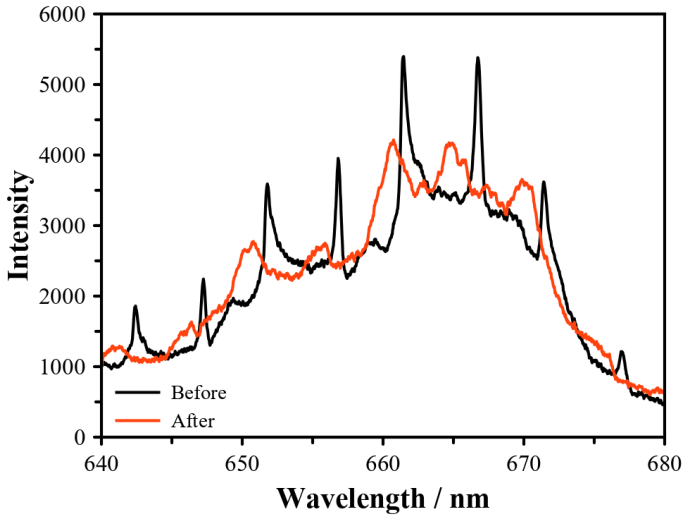

Figure 5 : A comparison between the Mie resonance spectra of the levitated particle before (black) and after (red) a chemical transformation which leads to the changes in particle's morphology. The spectrum presented in black shows the sharp peaks indicative of a spherical and homogeneous particle which undergoes liquid-liquid phase separation (LLPS) as a result of a reaction. The spectrum becomes distorted due to peak broadening following LLPS, depicted as red spectra, as a result of the morphological transformations that interrupt the sharp peak structure.

For our measurements, each lowermost particle was periodically ejected out of the LQ-EDB to be sent to the mass spectrometer for compositional analysis which is discussed in the following section. The next particle in the stack was subsequently moved into its position for MRS analysis.

2.4. Mass Spectrometry for the Analysis of Chemical Composition

Mass spectrometry (MS) is a widely used analytical technique in the field of aerosol science that allows the chemical composition and associated properties of particles in both laboratory measurements and field studies to be determined.[9,30–34] MS provides fast response time with high sensitivity and ability to detect a wide range of chemical species

to analyze chemically complex particles. The utilization of MS for studying the real-time compositional evolution of laboratory-generated levitated particles has gained popularity in last few years and the technique developments discussed in this thesis work have made significant contributions to this field.[33,35–38] It is important to understand the chemical trajectory of a particle with a known starting composition as it becomes transformed. To achieve this with levitated particles, we collected a series of mass spectra for a set of particles with identical starting composition but varying residence time in the LQ-EDB chamber before transfer to the MS. In this section, we will discuss the generalized working principle of the MS technique and its applications in our research work involving single particle levitation approach.

MS instruments broadly consist of three main components: an ion source, a mass analyzer, and a detector. A brief working principle of MS involves the ionization of a sample followed by the determination of the mass-to-charge ratio (m/z) of the analyte ions of interest.[32,39–41] This is accomplished by passing the generated ions from the ionization source through a mass analyzer, which is the heart of the spectrometer. The analyzer uses magnetic and electric fields to measure the mass to charge ratio (m/z) of the ions and separate the ions based on their m/z ratio. Finally, the ions are detected with the help of a detector, and the generated mass spectrum of the ion signal as a function of the m/z ratio yields information of the molecular mass and abundance of each chemical species. Thus, the MS measurements are utilized for describing the compositional characteristics and abundance of individual species of interest which is used to infer the chemical composition of the particle. Several different types of mass spectrometers, such as time-of-flight, triple

quadrupole and orbitrap mass spectrometer, have been successfully employed in conjunction with particle levitation techniques for compositional measurements in aerosol science.[9,11,42,43] These mass spectrometers differ from each other in terms of their sensitivity, selectivity and resolution. In general, MS can detect sample particle having analyte concentrations as low as a few ppb, making it possible to study particles that have analytes present in very low concentrations.

For our research work, the combined use of an LQ-EDB with a Q Exactive Focus Orbitrap MS facilitates the experimental interrogation of levitated particles and allow particles properties to be measured as a function of evolving composition. The fundamentals and working principle of Orbitrap MS has been extensively discussed by other researchers.[44–48] For our measurements, Orbitrap MS was operated in either negative or positive ion mode with a typical scan range of 50 to 1000 m/z, a resolution of 35000 and maximum ion injection time of 100 ms.[49] A single particle is released from LQ-EDB by pulsing the DC balancing voltage to zero for tens of milliseconds resulting in ejection out of the trap. The particle falls propelled by gravity and drag forces and is guided by the electrical fields of the quadrupole to fall directly into the sampling and ionization interface. This interface then transfers the formed ions into the MS for the compositional determination. A fourier transform of the signal in the frequency domain yields mass spectrum in the m/z domain that is characteristic of the composition of the particle at that time. The resulting mass spectra are analyzed for both qualitative and quantitative interpretation of the chemical species present in the particle. To do this, Xcalibur 4.1 software is used to initially analyze the mass spectra which yields the qualitative

information, and extracted ion chronograms for the peaks of interest are exported to MagicPlot Pro 2.8.2 for their quantitative analysis. A detailed description of qualitative and quantitative analysis of the particle composition is given in *Section 2.4.2*. The different sampling and ionization platforms developed and utilized in our laboratory studies for analyzing the composition of particles using MS are discussed in the subsequent sections.

2.4.1. Particle Sampling and Ionization Sources to Couple LQ-EDB with MS

Recent developments in the field of single particle levitation focus on the coupling of LQ-EDB with MS. This has been achieved with the help of developments in the ambient sampling and ionization techniques that effectively sample the levitated particles as ions into the MS for the analysis of their chemical composition. Birdsall et al. described a setup in which particles are transferred from electrodynamic balance (EDB) to the ionization source assembly through a transfer tube via a gas flow.[38] The single droplets are transferred from the EDB to a heated vaporization platform situated in the ionization assembly which results in the formation of gas-phase species that are being ionized with the help of a corona discharge generated by the high-voltage needle. The generated ions are then sampled into the inlet region of a time-of-flight mass spectrometer for compositional analysis. In a laboratory study by Jacobs et al., a paper spray (PS) ionization source is used to couple the branched quadrupole trap with the mass spectrometer.[9] The PS ionization and sampling source utilized a triangle substrate cut from a chromatography paper to serve as a sampling platform and tip of the paper helps to transfer the ionized analytes into the mass spectrometer via a spray plume. A similar approach based on PS ionization was utilized by

Willis et. al to probe the composition of a stack of the particles levitated in a specialized quadrupole electrodynamic trap.[33] This ionization method was further complemented with another ionization technique, namely thermal desorption glow discharge ionization, to analyze the composition of oxygenated organic acids in single droplets using an Orbitrap mass spectrometer. In another study by Müller et. al, the ejected droplet first strikes the heated evaporation unit, and the resulting vapors are ionized with the help of a cold plasma dielectric barrier discharge ion source that are then sent to a triple quadrupole mass spectrometer for the determination of composition.[37] In general, these techniques are based on the working principle of transforming the analytes present in particles by ionizing the chemical components to be analyzed by MS as naked ions.[39] Finally, our experimental studies on levitated particles involve the development of sampling and ionization methods based around the mechanism of electrospray ionization using paper spray and open-port sampling interfaces, as discussed in the following sections.

2.4.1.1. Paper Spray (PS) Ionization Source

Paper-spray ionization is an ambient pressure ionization method that requires minimal sample preparation.[50–52] The PS source was constructed in-house to capture levitated particles, ionize the analytes and deliver the ions to the inlet of an Orbitrap MS (**Figure 6**).[49] The working principle of PS involves generating an electrospray from tip of a solvent-soaked chromatography paper by applying 3 – 5 kV voltage. The chromatography papers were cut into triangular substrates with scissors roughly with a base of 1 cm, height of 1 cm, leading to the spray angle tip of 53º. The particle ejected out of LQ-EDB is solubilized

in the spray solution on impact with the substrate and the supplied high voltage causes the aerosolization of solvent mixture into a fine mist composed of charged solvent droplets. As solvent evaporates, the droplets break down into highly charged smaller droplets which then splits into charged progeny droplets due to a process called Coulomb fission upon reaching the Rayleigh limit.[53–55] These charged progeny droplets undergo desolvation (aided by heated MS inlet and extension) to form gaseous naked ions that are sampled by MS inlet for the compositional analysis. An appropriately selected paper spray solvent aids in effective transfer and ionization of the analytes. Different solvent may have different sensitivities to the analyte ions which affects the limit of detection.[56] The paper spray approach with certain solvents may limit the comprehensive analysis of a wide range of chemical species with high sensitivity as the chemical species must be soluble in that solvent. Additionally, solvents having high viscosities are also not suitable for the PS ionization as the viscosity plays a major role in the generation of the spray. Considering the above factors and based on the literature survey on electrospray solutions, different combinations of solvent mixtures were tested to determine the most effective solvent. A 50–50 mixture of methanol and chloroform was deemed to be an effective solvent for the samples of our interest.

A wide range of samples can be sampled and ionized with the help of PS, including both liquid and solid levitated particles. PS ionization can be used in both positive and negative mode, depending on the particle composition and the desired outcome. In positive mode, the sample analytes are ionized by protonation which is useful for particle compositions such as simple alcohols and glycols. In negative mode, sample ionization is due to

deprotonation and is typically limited to acidic molecules. Preliminary studies using a PS ionization source (*refer Chapter 3*) have proved its effectiveness towards the qualitative and quantitative MS analysis of sample particles. A use of internal standard used within the levitated particles is proven necessary to account for variabilities in the MS signal caused due to the different sampling positions on the paper substrate (*refer Chapter 3*) and the changing spray mode due to deterioration of paper during longer measurements caused by the roughly cut paper substrates.[52,57] In addition, good sensitivity of this method for a range of samples ensures that compounds of atmospheric interest and products from atmospherically relevant reactions can be effectively analyzed using this method.

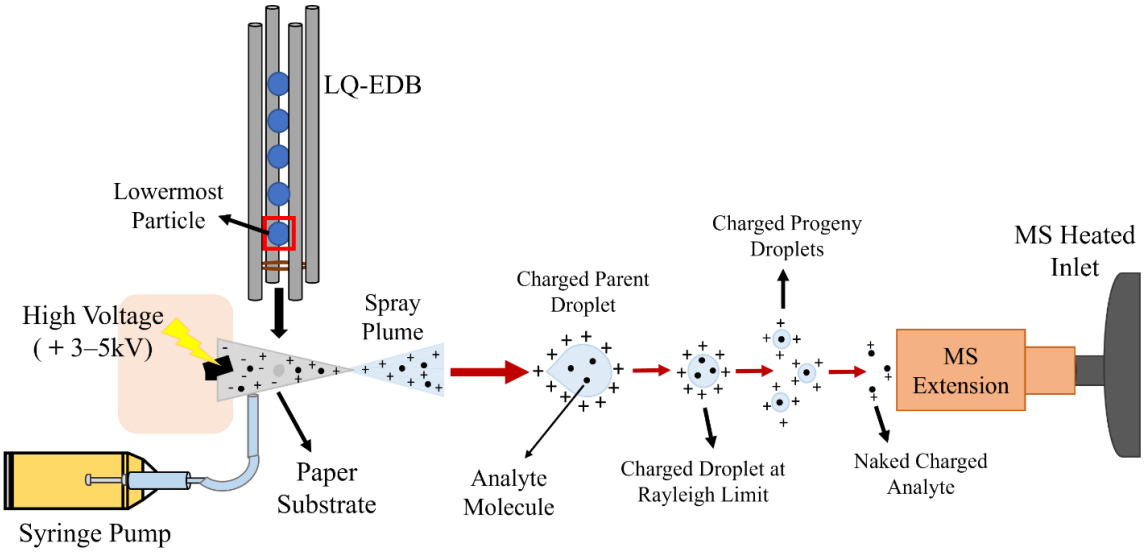

Figure 6: Paper spray (PS) setup coupled to MS for sampling and ionizing the analytes in the sample particles ejected from LQ-EDB. Periodic measurements of the composition related to lowermost particle at a time in LQ-EDB is carried out to determine the transformation parameters. Paper substrate is maintained at a high voltage with continuous supply of solvent to ionize the analytes present in the sample particles which are subsequently vaporized as they travel towards the MS heated inlet for their compositional analysis.

2.4.1.2. Open Port Sampling Interface (OPSI) – Electrospray Ionization (ESI) Source

The OPSI platform is designed to capture, dilute, and transport the analytes of sample particles ejected from LQ-EDB to the conventional heated ESI source to be introduced into the MS for compositional analysis.[25] An "open-port" can be understood as an interface that allows for the direct sampling of analytes without the need of any sample preparation or internal standard, thereby limiting the artifacts and analyzing the samples in real-time.[58–60] A schematic illustration of the OPSI-ESI setup used for our experimental measurements is presented in **Figure 7**.[25]

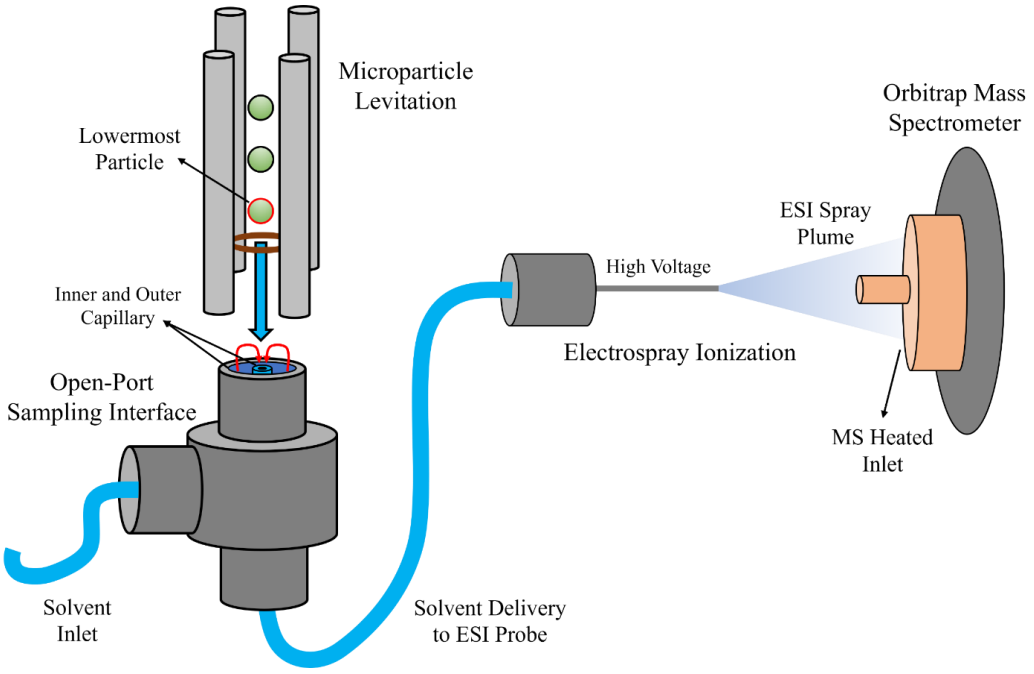

Figure 7: Illustration of open port sampling interface (OPSI) coupled with the conventional heated electrospray ionization (ESI) source of Orbitrap mass spectrometer (MS). The schematic demonstrates the particle transfer from LQ-EDB into the OPSI interface for real-time analysis of its composition by MS without the need of any sample preparation. The figure is not to scale.

An OPSI consists of a coaxial capillary design having an outer and inner capillary for solvent injection and delivery to ESI, respectively. A solvent mixture of methanol doped with trace amounts trans-3-(3-pyridyl)acrylic acid (TPAA) to act as an external standard is supplied with the help of a syringe pump to the OPSI interface. The use of TPAA is to visually confirm spray stability in mass chronogram and is not used for any data analysis or interpretation. The continuous solvent flow results in the formation of a solvent pool on top of the OPSI interface which helps in efficient particle capture and its further dissolution in the solvent. The solubilized analytes are carried towards the heated ESI probe as a result of the Venturi effect due to low pressure at the ESI tip where they are charged and sprayed as a plume.[62,63] The charged droplets undergo extensive solvent evaporation until it becomes unstable upon reaching its Raleigh limit.[64–66] At this point, the parent droplet deforms due to electrostatic repulsion of same charges and undergoes series of desolvation and coulombic fission to result in naked ions which are finally sampled into MS inlet for compositional analysis. A detailed description of the development of OPSI-ESI setup and some of the important preliminary studies using the LQ-EDB-OPSI-ESI-MS technique is presented in **Chapter 4**. The OPSI-ESI is an effective sampling and ionization setup for quantitative analysis of sample levitated particles over extended periods of time without compromising its spray quality and stability in both positive and negative ionization modes. The conventional ESI source used in conjunction with OPSI is a new platform for single particle analysis, however it has been widely used in other fields of research to analyze big molecules like proteins and peptides, and small molecules like metabolites and drugs.[59,61] Our studies reveal that MS can be effectively used to identify and quantify the chemical

composition in real-time to understand the kinetics of chemical transformations on levitated particles with known starting compositions as discussed in the next section.

2.4.2. Qualitative and Quantitative Analysis of Particle Composition

Qualitative analysis using MS is done to identify the presence and relative abundance of chemical species of interest in the sample particles. This method is based on the principle that all chemical species have a unique m/z ratio, which can be used to distinguish one species from another.[12] The mass spectrum emerged as a result of sample introduction into the MS is a plot of the relative abundance of ions as a function of their m/z ratio. Each peak in the mass spectrum corresponds to a different ion, and the height of the peak indicates its relative abundance in the sample. By analyzing the mass spectrum, it is possible to identify the chemical compounds present in the sample. A high resolving power offered by orbitrap MS allows to differentiate between ions with similar m/z ratios along with high mass accuracy which helps to accurately determine the m/z ratio of the ions.[67] Further, due to the high sensitivity and specificity of the Orbitrap MS used in our research studies, it is possible to detect very low concentration of ions in the levitated particles. Qualitative analysis is done to understand the chemical composition of sample particles in terms of evolving mass spectra during a chemical transformation. Any emergence of new peaks or absence of existing peaks can confirm the compositional changes in the levitated particles.

Quantitative analysis using MS is used to determine the precise amount of specific compounds present in sample particles relative to their starting composition. MS measurements assist in analyzing very low concentrations of chemical compounds in

smaller particles, expanding the scope of this method close to the size range associated with atmospheric aerosols.[68–71] The m/z peaks related to chemical compounds of interest are analyzed for quantitation to understand the transformation kinetics of levitated particles undergoing chemical changes. For this, the mass spectra are analyzed using Xcalibur 4.1 software (ThermoFisher Scientific) to determine the m/z peaks respective of the chemical compounds of interest and their extracted ion chronograms are exported for processing using data analysis software (MagicPlot Pro 2.8.2). An example of the mass spectra associated with the compositional measurements of the citric acid droplets is shown in **Figure 8A**.[49] The red signals represent the background mass spectrum associated with the spray solution supplied by the ionization source into the MS while the black signals correspond to the peak intensity of the parent ion (191 m/z) from a single citric acid droplet. The chronograms of the parent ion peak for a sequence of three citric acid droplets is shown in **Figure 8B**. The integrated peak area corresponding to each chronogram signal was determined for every particle analyzed for its compositional quantitation. The quantification of the analytes in the particle is done by calculating their compositional abundance in terms of their peak areas relative to the starting composition. The peak areas are analyzed to confirm the reproducibility and stability of the ion signals since they are the important facets of these measurements as the entire stack of levitated particles is expected to behave uniformly during chemical transformations. Finally, quantitation of MS peak respective of the spray standard helps in confirming the stability of the spray during the chemical transformations.

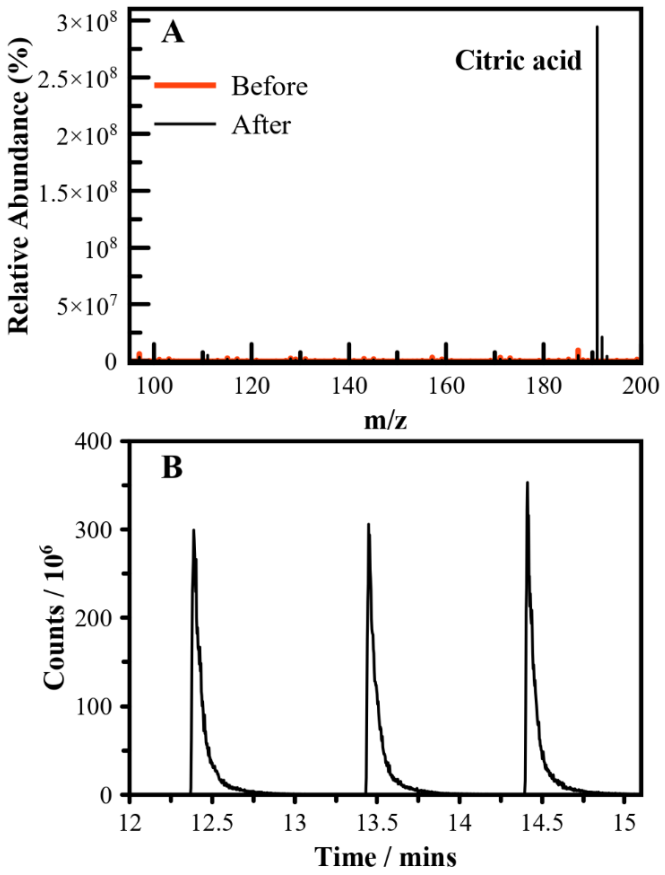

Figure 8: (A) Representative mass spectrum of a single citric acid particle for its compositional analysis. The red signals in the mass spectrum represent the background before the compositional analysis of the particle while the black signals in the mass spectrum represent the composition of a single citric acid particle. **(B)** The mass chronograms show the droplet deposition event for three consecutive citric acid droplets at 191 m/z depicting the parent ion.

2.5. Summary and Conclusions

This chapter summarizes the development, principle of operation and capabilities of the in-house built levitation system coupled with mass spectrometry through different sampling and ionization platforms, namely paper spray and open-port sampling interface. For understanding the chemical transformations on atmospheric aerosols, an LQ-EDB chamber is an effective tool for levitating a stack of microparticles in which all of them

have the same starting chemical composition and behaves very similarly to each other throughout the timescales of our experiments. Within the LQ-EDB, levitated particles may be exposed to a variety of conditions, and the methods discussed in this chapter will be applied for evaluating the response of particles to chemical transformations. Some of the important physical and chemical characteristics, namely size, RI, morphology, and composition, are studied in real-time as the particles are undergoing a chemical change. Mie spectroscopy setup coupled to the LQ-EDB chamber helps in analyzing the physical and optical properties of the levitated particles in real-time as a result of compositional evolutional determined by the MS.

The utilization of both PS and OPSI-ESI as sampling and ionization sources offer exceptional qualitative and quantitative determination of analyte ions yet OPSI offers even more advantages over PS ionization source. OPSI-ESI offers better MS signal stability and efficient particle capture, resulting in least variations in the spray mode thereby eliminating the use of internal standard. Conventional ESI probe used in OPSI-ESI interface is very robust and well-developed which is expected to result in better sensitivity as the particles are not directly interacting with highly charged paper substrate rather directly dissolved in carrier solvent offering controlled dilution rates. Finally, the combined LQ-EDB-MS technique has the potential to act as an all-in-one method for a complete qualitative and quantitative characterization of physicochemical characteristics of levitated particles. This has important implications for the atmospheric aerosol particles that experience similar chemical transformations over their lifetime resulting in the evolution of their characteristics and related impacts in the atmosphere.[72,73]

2.6. References

(1) Davies, J. F. Mass, Charge, and Radius of Droplets in a Linear Quadrupole Electrodynamic Balance. *Aerosol Sci. Technol.* **2019**, *53* (3), 309–320. https://doi.org/10.1080/02786826.2018.1559921.

(2) Hart, M. B.; Sivaprakasam, V.; Eversole, J. D.; Johnson, L. J.; Czege, J. Optical Measurements from Single Levitated Particles Using a Linear Electrodynamic Quadrupole Trap. *Appl. Opt.* **2015**, *54* (31), F174–F181. https://doi.org/10.1364/AO.54.00F174.

(3) J. Wallace, B.; L. Price, C.; F. Davies, J.; C. Preston, T. Multicomponent Diffusion in Atmospheric Aerosol Particles. *Environ. Sci. Atmos.* **2021**, *1* (1), 45–55. https://doi.org/10.1039/D0EA00008F.

(4) Singh, M.; Mayya, Y. S.; Gaware, J.; Thaokar, R. M. Levitation Dynamics of a Collection of Charged Droplets in an Electrodynamic Balance. *J. App. Phys.* **2017**, *121* (5), 054503. https://doi.org/10.1063/1.4974470.

(5) Ulmke, H.; Wriedt, T.; Bauckhage, K. Piezoelectric Droplet Generator for the Calibration of Particle-Sizing Instruments. *Chem. Eng. Technol.* **2001**, *24* (3), 265–268. https://doi.org/10.1002/1521-4125(200103)24:3<265::AID-EAT265>3.0.CO.

(6) Yang, J. C.; Chien, W.; King, M.; Grosshandler, W. L. A Simple Piezoelectric Droplet Generator. *Exp. Fluids* **1997**, *23* (5), 445–447. https://doi.org/10.1007/s003480050134.

(7) Davies, J. F.; Haddrell, A. E.; Reid, J. P. Time-Resolved Measurements of the Evaporation of Volatile Components from Single Aerosol Droplets. *Aerosol Sci. Technol.* **2012**, *46* (6), 666–677. https://doi.org/10.1080/02786826.2011.652750.

(8) Woźniak, M.; Derkachov, G.; Kolwas, K.; Archer, J.; Wojciechowski, T.; Jakubczyk, D.; Kolwas, M. Formation of Highly Ordered Spherical Aggregates from Drying Microdroplets of Colloidal Suspension. *Langmuir* **2015**, *31* (28), 7860–7868. https://doi.org/10.1021/acs.langmuir.5b01621.

(9) Jacobs, M. I.; Davies, J. F.; Lee, L.; Davis, R. D.; Houle, F.; Wilson, K. R. Exploring Chemistry in Microcompartments Using Guided Droplet Collisions in a Branched Quadrupole Trap Coupled to a Single Droplet, Paper Spray Mass Spectrometer. *Anal. Chem.* **2017**, *89* (22), 12511–12519. https://doi.org/10.1021/acs.analchem.7b03704.

(10) Price, C. L.; Preston, T. C.; Davies, J. F. Hygroscopic Growth, Phase Morphology, and Optical Properties of Model Aqueous Brown Carbon Aerosol. *Environ. Sci. Technol.* **2022**, *56* (7), 3941–3951. https://doi.org/10.1021/acs.est.1c07356.

(11) Willis, M. D.; Wilson, K. R. Coupled Interfacial and Bulk Kinetics Govern the Timescales of Multiphase Ozonolysis Reactions. *J. Phys. Chem. A* **2022**, *126* (30), 4991–5010. https://doi.org/10.1021/acs.jpca.2c03059.

(12) Kaur Kohli, R.; Davies, J. F. Measuring the Chemical Evolution of Levitated Particles: A Study on the Evaporation of Multicomponent Organic Aerosol. *Anal. Chem.* **2021**, *93* (36), 12472–12479. https://doi.org/10.1021/acs.analchem.1c02890.

(13) Price, C. L.; Kaur Kohli, R.; Shokoor, B.; Davies, J. F. Connecting the Phase State and Volatility of Dicarboxylic Acids at Elevated Temperatures. *J. Phys. Chem. A* **2022**, *126* (39), 6963–6972. https://doi.org/10.1021/acs.jpca.2c04546.

(14) Wu, L.; Ro, C.-U. Aerosol Hygroscopicity on A Single Particle Level Using Microscopic and Spectroscopic Techniques: A Review. *Asian J. Atmos. Environ.* **2020**, *14* (3), 177–209. https://doi.org/10.5572/ajae.2020.14.3.177.

(15) Choczynski, J. M.; Kaur Kohli, R.; Sheldon, C. S.; Price, C. L.; Davies, J. F. A Dual-Droplet Approach for Measuring the Hygroscopicity of Aqueous Aerosol. *Atmos. Meas. Tech.* **2021**, *14* (7), 5001–5013. https://doi.org/10.5194/amt-14-5001-2021.

(16) Price, C. L.; Bain, A.; Wallace, B. J.; Preston, T. C.; Davies, J. F. Simultaneous Retrieval of the Size and Refractive Index of Suspended Droplets in a Linear Quadrupole Electrodynamic Balance. *J. Phys. Chem. A* **2020**, *124* (9), 1811–1820. https://doi.org/10.1021/acs.jpca.9b10748.

(17) Steimer, S. S.; Krieger, U. K.; Peter, T. Electrodynamic Balance Measurements of Thermodynamic, Kinetic, and Optical Aerosol Properties Inaccessible to Bulk Methods. *Atmos. Meas. Tech.* **2015**, *8* (6), 2397–2408. https://doi.org/10.5194/amt-8-2397-2015.

(18) Mie, G. Sättigungsstrom und Stromkurve einer schlecht leitenden Flüssigkeit. *Ann. Phys.* **1908**, *331* (8), 597–614. https://doi.org/10.1002/andp.19083310810.

(19) Temperature-Controlled Dual-Beam Optical Trap for Single Particle Studies of Organic Aerosol. *J. Phys. Chem. A* **2022**, *126* (1), 109–118. https://pubs.acs.org/doi/full/10.1021/acs.jpca.1c09363.

(20) Lew, L. J. N.; Ting, M. V.; Preston, T. C. Determining the Size and Refractive Index of Homogeneous Spherical Aerosol Particles Using Mie Resonance Spectroscopy. *Appl. Opt.* **2018**, *57* (16), 4601–4609. https://doi.org/10.1364/AO.57.004601.

(21) Preston, T. C.; Reid, J. P. Determining the Size and Refractive Index of Microspheres Using the Mode Assignments from Mie Resonances. *J. Opt. Soc. Am. A.* **2015**, *32* (11), 2210–2217. https://doi.org/10.1364/JOSAA.32.002210.

(22) Bain, A.; C. Preston, T. The Wavelength-Dependent Optical Properties of Weakly Absorbing Aqueous Aerosol Particles. *Chem. Commun.* **2020**, *56* (63), 8928–8931. https://doi.org/10.1039/D0CC02737E.

(23) Bain, A.; Rafferty, A.; Preston, T. C. Determining the Size and Refractive Index of Single Aerosol Particles Using Angular Light Scattering and Mie Resonances. *J. Quant. Spectrosc. Radiat. Transf.* **2018**, *221*, 61–70. https://doi.org/10.1016/j.jqsrt.2018.09.026.

(24) Preston, T. C.; Reid, J. P. Accurate and Efficient Determination of the Radius, Refractive Index, and Dispersion of Weakly Absorbing Spherical Particle Using Whispering Gallery Modes. *J. Opt. Soc. Am. B* **2013**, *30* (8), 2113–2122. https://doi.org/10.1364/JOSAB.30.002113.

(25) Kaur Kohli, R.; Van Berkel, G. J.; Davies, J. F. An Open Port Sampling Interface for the Chemical Characterization of Levitated Microparticles. *Anal. Chem.* **2022**, *94* (8), 3441–3445. https://doi.org/10.1021/acs.analchem.1c05550.

(26) Gorkowski, K.; Donahue, N. M.; Sullivan, R. C. Emulsified and Liquid–Liquid Phase-Separated States of α-Pinene Secondary Organic Aerosol Determined Using Aerosol Optical Tweezers. *Environ. Sci. Technol.* **2017**, *51* (21), 12154–12163. https://doi.org/10.1021/acs.est.7b03250.

(27) Moridnejad, A.; Preston, T. C.; Krieger, U. K. Tracking Water Sorption in Glassy Aerosol Particles Using Morphology-Dependent Resonances. *J. Phys. Chem. A* **2017**, *121* (42), 8176–8184. https://doi.org/10.1021/acs.jpca.7b06774.

(28) Sullivan, R. C.; Boyer-Chelmo, H.; Gorkowski, K.; Beydoun, H. Aerosol Optical Tweezers Elucidate the Chemistry, Acidity, Phase Separations, and Morphology of Atmospheric Microdroplets. *Acc. Chem. Res.* **2020**, *53* (11), 2498–2509. https://doi.org/10.1021/acs.accounts.0c00407.

(29) Song, M.; Marcolli, C.; Krieger, U. K.; Lienhard, D. M.; Peter, T. Morphologies of Mixed Organic/Inorganic/Aqueous Aerosol Droplets. *Faraday Discuss.* **2013**, *165* (0), 289–316. https://doi.org/10.1039/C3FD00049D.

(30) DeCarlo, P. F.; Kimmel, J. R.; Trimborn, A.; Northway, M. J.; Jayne, J. T.; Aiken, A. C.; Gonin, M.; Fuhrer, K.; Horvath, T.; Docherty, K. S.; Worsnop, D. R.; Jimenez, J. L. Field-Deployable, High-Resolution, Time-of-Flight Aerosol Mass Spectrometer. *Anal. Chem.* **2006**, *78* (24), 8281–8289. https://doi.org/10.1021/ac061249n.

(31) Jayne, J. T.; Leard, D. C.; Zhang, X.; Davidovits, P.; Smith, K. A.; Kolb, C. E.; Worsnop, D. R. Development of an Aerosol Mass Spectrometer for Size and Composition Analysis of Submicron Particles. *Aerosol Sci. Technol.* **2000**, *33* (1–2), 49–70. https://doi.org/10.1080/027868200410840.

(32) Nash, D. G.; Baer, T.; Johnston, M. V. Aerosol Mass Spectrometry: An Introductory Review. *Int. J. Mass Spectrom.* **2006**, *258* (1–3), 2–12. https://doi.org/10.1016/j.ijms.2006.09.017.

(33) Willis, M. D.; Rovelli, G.; Wilson, K. R. Combining Mass Spectrometry of Picoliter Samples with a Multicompartment Electrodynamic Trap for Probing the Chemistry of Droplet Arrays. *Anal. Chem.* **2020**, *92* (17), 11943–11952. https://doi.org/10.1021/acs.analchem.0c02343.

(34) Lanz, V. A.; Prévôt, A. S. H.; Alfarra, M. R.; Weimer, S.; Mohr, C.; DeCarlo, P. F.; Gianini, M. F. D.; Hueglin, C.; Schneider, J.; Favez, O.; D'Anna, B.; George, C.; Baltensperger, U. Characterization of Aerosol Chemical Composition with Aerosol Mass Spectrometry in Central Europe: An Overview. *Atmos. Chem. Phys.* **2010**, *10* (21), 10453–10471. https://doi.org/10.5194/acp-10-10453-2010.

(35) Noble, C. A.; Prather, K. A. Real-time Single Particle Mass Spectrometry: A Historical Review of a Quarter Century of the Chemical Analysis of Aerosols. *Mass Spectrom. Rev.* **2000**, 19, 248–274. https://doi.org/10.1002/1098-2787(200007)19:4<248::AID-MAS3>3.0.CO;2-I.

(36) Müller, M.; Mishra, A.; Berkemeier, T.; Hausammann, E.; Peter, T.; Krieger, U. K. Electrodynamic balance–mass spectrometry reveals impact of oxidant concentration on product composition in the ozonolysis of oleic acid. *Phys. Chem. Chem. Phys.* **2022**, *24* (44), 27086–27104. https://doi.org/10.1039/D2CP03289A.

(37) Müller, M.; Stefanetti, F.; Krieger, U. K. Oxidation Pathways of Linoleic Acid Revisited with Electrodynamic Balance–Mass Spectrometry. *Environ. Sci.* **2022**, 3, 85–96. https://doi.org/10.1039/d2ea00127f.

(38) Birdsall, A. W.; Krieger, U. K.; Keutsch, F. N. Electrodynamic Balance–Mass Spectrometry of Single Particles as a New Platform for Atmospheric Chemistry Research. *Atmos. Meas. Tech.* **2018**, *11* (1), 33–47. https://doi.org/10.5194/amt-11-33-2018.

(39) Milman, B. L. General Principles of Identification by Mass Spectrometry. *Trends Analyt. Chem.* **2015**, *69*, 24–33. https://doi.org/10.1016/j.trac.2014.12.009.

(40) Johnston, M. V. Sampling and Analysis of Individual Particles by Aerosol Mass Spectrometry. *J. Mass Spectrom.* **2000**, *35* (5), 585–595. https://doi.org/10.1002/(SICI)1096-9888(200005)35:5<585::AID-JMS992>3.0.CO.

(41) Glish, G. L.; Vachet, R. W. The Basics of Mass Spectrometry in the Twenty-First Century. *Nat. Rev. Drug Discov.* **2003**, *2* (2), 140–150. https://doi.org/10.1038/nrd1011.

(42) Berkemeier, T.; Mishra, A.; Mattei, C.; Huisman, A. J.; Krieger, U. K.; Pöschl, U. Ozonolysis of Oleic Acid Aerosol Revisited: Multiphase Chemical Kinetics and Reaction Mechanisms. *ACS Earth Space Chem.* **2021**, *5* (12). 3313–3323. https://doi.org/10.1021/acsearthspacechem.1c00232.

(43) Birdsall, A. W.; Hensley, J. C.; Kotowitz, P. S.; Huisman, A. J.; Keutsch, F. N. Single-Particle Experiments Measuring Humidity and Inorganic Salt Effects on Gas-Particle Partitioning of Butenedial. *Atmos. Chem. Phys.* **2019**, *19* (22), 14195–14209. https://doi.org/10.5194/acp-19-14195-2019.

(44) Zubarev, R. A.; Makarov, A. Orbitrap Mass Spectrometry. *Anal. Chem.* **2013**, *85* (11), 5288–5296. https://doi.org/10.1021/ac4001223.

(45) Du, M.; Voliotis, A.; Shao, Y.; Wang, Y.; Bannan, T. J.; Pereira, K. L.; Hamilton, J. F.; Percival, C. J.; Alfarra, M. R.; McFiggans, G. Combined Application of Online FIGAERO-CIMS and Offline LC-Orbitrap Mass Spectrometry (MS) to Characterize the Chemical Composition of Secondary Organic Aerosol (SOA) in Smog Chamber Studies. *Atmos. Meas. Tech.* **2022**, *15* (14), 4385–4406. https://doi.org/10.5194/amt-15-4385-2022.

(46) Hecht, E. S.; Scigelova, M.; Eliuk, S.; Makarov, A. Fundamentals and Advances of Orbitrap Mass Spectrometry. *Encyclopedia Anal. Chem.* **2019**. 1–40. https://doi.org/10.1002/9780470027318.a9309.pub2.

(47) Roveretto, M.; Li, M.; Hayeck, N.; Brüggemann, M.; Emmelin, C.; Perrier, S.; George, C. Real-Time Detection of Gas-Phase Organohalogens from Aqueous Photochemistry Using Orbitrap Mass Spectrometry. *ACS Earth Space Chem.* **2019**, *3* (3), 329–334. https://doi.org/10.1021/acsearthspacechem.8b00209.

(48) Perry, R. H.; Cooks, R. G.; Noll, R. J. Orbitrap Mass Spectrometry: Instrumentation, Ion Motion and Applications. *Mass Spectrom. Rev.* **2008**, *27* (6), 661–699. https://doi.org/10.1002/mas.20186.

(49) Kaur Kohli, R.; Davies, J. F. Paper Spray Mass Spectrometry for the Analysis of Picoliter Droplets. *Analyst* **2020**, *145* (7), 2639–2648. https://doi.org/10.1039/C9AN02534K.

(50) Espy, R. D.; Muliadi, A. R.; Ouyang, Z.; Cooks, R. G. Spray Mechanism in Paper Spray Ionization. *Int. J. Mass Spectrom.* **2012**, *325–327*, 167–171. https://doi.org/10.1016/j.ijms.2012.06.017.

(51) Liu, J.; Wang, H.; Manicke, N. E.; Lin, J.-M.; Cooks, R. G.; Ouyang, Z. Development, Characterization, and Application of Paper Spray Ionization. *Anal. Chem.* **2010**, *82* (6), 2463–2471. https://doi.org/10.1021/ac902854g.

(52) Wang, H.; Liu, J.; Cooks, R. G.; Ouyang, Z. Paper Spray for Direct Analysis of Complex Mixtures Using Mass Spectrometry. *Angew. Chem.* **2010**, *122* (5), 889–892. https://doi.org/10.1002/ange.200906314.

(53) Taflin, D. C.; Ward, T. L.; Davis, E. J. Electrified Droplet Fission and the Rayleigh Limit. *Langmuir* **1989**, *5* (2), 376–384. https://doi.org/10.1021/la00086a016.

(54) Shrimpton, J. S. Dielectric Charged Drop Break-up at Sub-Rayleigh Limit Conditions. *IEEE Trans. Dielectr. Electr. Insul.* **2005**, *12* (3), 573–578. https://doi.org/10.1109/TDEI.2005.1453462.

(55) Davis, E. J.; Bridges, M. A. The Rayleigh Limit of Charge Revisited: Light Scattering from Exploding Droplets. *J. Aerosol Sci.* **1994**, *25* (6), 1179–1199. https://doi.org/10.1016/0021-8502(94)90208-9.

(56) Kim, D.; Lee, J.; Kim, B.; Kim, S. Optimization and Application of Paper-Based Spray Ionization Mass Spectrometry for Analysis of Natural Organic Matter. *Anal. Chem.* **2018**, *90* (20), 12027–12034. https://doi.org/10.1021/acs.analchem.8b02668.

(57) Yang, Q.; Wang, H.; Maas, J. D.; Chappell, W. J.; Manicke, N. E.; Cooks, R. G.; Ouyang, Z. Paper Spray Ionization Devices for Direct, Biomedical Analysis Using Mass Spectrometry. *Int. J. Mass Spectrom.* **2012**, *312*, 201–207. https://doi.org/10.1016/j.ijms.2011.05.013.

(58) Swanson, K. D.; Worth, A. L.; Glish, G. L. Use of an Open Port Sampling Interface Coupled to Electrospray Ionization for the On-Line Analysis of Organic Aerosol Particles. *J. Am. Soc. Mass Spectrom.* **2018**, *29* (2), 297–303. https://doi.org/10.1007/s13361-017-1776-y.

(59) Gary J. Van Berkel; Vilmos Kertesz; Harry Boeltz. Immediate Drop on Demand Technology (I-DOT) Coupled with Mass Spectrometry via an Open Port Sampling Interface. *Bioanalysis 9* **2017**, 1667–1679. https://doi.org/10.4155/bio-2017-0104.

(60) Van Berkel, G. J.; Kertesz, V.; Orcutt, M.; Bentley, A.; Glick, J.; Flarakos, J. Combined Falling Drop/Open Port Sampling Interface System for Automated Flow Injection Mass Spectrometry. *Anal. Chem.* **2017**, *89* (22), 12578–12586. https://doi.org/10.1021/acs.analchem.7b03899.

(61) Forbes, T. P.; Lawrence, J.; Hao, C.; Gillen, G. Open Port Sampling Interface Mass Spectrometry of Wipe-Based Explosives, Oxidizers, and Narcotics for Trace Contraband Detection. *Anal. Methods* **2021**, *13*, 3453–3460. https://doi.org/10.1039/D1AY01038G.

(62) Tonin, A. P. P.; Poliseli, C. B.; Ribeiro, M. A. S.; Moraes, L. A. B.; Visentainer, J. V.; Eberlin, M. N.; Meurer, E. C. Venturi Electrospray Ionization: Principles and Applications. *Int. J. Mass Spectrom.* **2018**, *431*, 50–55. https://doi.org/10.1016/j.ijms.2018.06.004.

(63) Ribeiro, M. A. S.; Tonin, A. P. P.; Poliseli, C. B.; Lima, B. B.; Castro, L. E. N.; Silva, V. M.; Valério, M.; Cedran, J. C.; Meurer, E. C. Teaching Venturi Electrospray Mass Spectrometry with Amino Acid Analysis. *Int. J. Mass Spectrom.* **2019**, *444*, 116183. https://doi.org/10.1016/j.ijms.2019.116183.

(64) Smith, J. N.; Flagan, R. C.; Beauchamp, J. L. Droplet Evaporation and Discharge Dynamics in Electrospray Ionization. *J. Phys. Chem. A* **2002**, *106* (42), 9957–9967. https://doi.org/10.1021/jp025723e.

(65) Wilm, M. Principles of Electrospray Ionization. *Mol. Cell Proteomics.* **2011**, *10* (7). M111.009407. https://doi.org/10.1074/mcp.M111.009407.

(66) Hager, D. B.; Dovichi, N. J.; Klassen, John.; Kebarle, Paul. Droplet Electrospray Mass Spectrometry. *Anal. Chem.* **1994**, *66* (22), 3944–3949. https://doi.org/10.1021/ac00094a015.

(67) Bateman, K. P.; Kellmann, M.; Muenster, H.; Papp, R.; Taylor, L. Quantitative-Qualitative Data Acquisition Using a Benchtop Orbitrap Mass Spectrometer. *J Am Soc Mass Spectrom* **2009**, *20* (8), 1441–1450. https://doi.org/10.1016/j.jasms.2009.03.002.

(68) Pourasil, R. S. M.; Cristale, J.; Lacorte, S.; Tauler, R. Non-Targeted Gas Chromatography Orbitrap Mass Spectrometry Qualitative and Quantitative Analysis of Semi-Volatile Organic Compounds in Indoor Dust Using the Regions of Interest Multivariate Curve Resolution Chemometrics Procedure. *J. Chromatogr. A* **2022**, *1668*, 462907. https://doi.org/10.1016/j.chroma.2022.462907.

(69) Hernández, F., Sancho, J.V., Ibáñez, M. et al. Current use of high-resolution mass spectrometry in the environmental sciences. *Anal. Bioanal. Chem.* **2012**, 403, 1251–1264. https://doi.org/10.1007/s00216-012-5844-7.

(70) Pratt, K. A.; Prather, K. A. Mass Spectrometry of Atmospheric Aerosols-Recent Developments and Applications. Part II: On-Line Mass Spectrometry Techniques. *Mass Spectrom. Rev.* **2012**, *31* (1), 17–48. https://doi.org/10.1002/mas.20330.

(71) Schuetzle, D. Analysis of Complex Mixtures by Computer Controlled High Resolution Mass Spectrometry: I—Application to Atmospheric Aerosol Composition. *Biol. Mass Spectrom.* **1975**, *2* (6), 288–298. https://doi.org/10.1002/bms.1200020603.

(72) Pöschl, U. Atmospheric Aerosols: Composition, Transformation, Climate and Health Effects. *Angew. Chem. Int. Ed.* **2005**, *44* (46), 7520–7540. https://doi.org/10.1002/anie.200501122.

(73) Jacobson, M. C.; Hansson, H.-C.; Noone, K. J.; Charlson, R. J. Organic Atmospheric Aerosols: Review and State of the Science. *Rev. Geophys.* **2000**, *38* (2), 267–294. https://doi.org/10.1029/1998RG000045.

CHAPTER 3

Paper Spray Mass Spectrometry for the Analysis of Picoliter Droplets

3.1. Abstract

Recent experimental efforts have shown that single particle levitation methods may be effectively coupled with mass spectrometry (MS) using paper spray (PS) ionization for compositional analysis of picoliter droplets. In this work, we characterize the response of PS-MS to analytes delivered in the form of picoliter droplets and explore its potential for identification and quantification of these samples. Using a microdroplet dispenser to generate droplets, we demonstrate sensitivity to a range of oxygenated organic molecules typical of compounds found in atmospheric secondary organic aerosol. We assess experimental factors that influence the reproducibility and sensitivity of the method and explore the linearity of the system response to increasing analyte mass in droplets containing single or multicomponent analytes. We show that the ratio of analyte signal from multicomponent samples may be used to characterize the relative composition of the system. These measurements demonstrate that the droplet PS-MS method is an effective tool for qualitative and quantitative analysis of single picoliter droplets containing picogram levels of analyte. The potential applications of this technique for characterizing the composition of levitated particles will be discussed.

3.2. Introduction

Aerosol particles are a major component of the atmosphere and affect the formation, lifetime and optical properties of clouds,[1–3] absorb and scatter incoming solar radiation,[4,5] provide surfaces on which chemistry can occur,[6–8] and negatively influence air quality and health.[9,10] Their composition spans a broad range of compounds and due to the oxidizing conditions in the atmosphere their composition is continuously evolving.[11,12] The composition of aerosol particles play a defining role in regulating their impacts in the atmosphere. Efforts to measure the composition of aerosol have relied on mass spectrometry, and the aerosol mass spectrometer (AMS) has been used extensively.[13–15] The AMS has been used in both field campaigns and laboratory measurements and works by directly sampling an aerosol via flash vaporization and electron-impact ionization to provide composition information.[15,16] Soft ionization methods have also been used to gain more insight into aerosol samples, such as chemical ionization (CI),[17,18] plasma-based methods such as direct analysis in real-time (DART) ionization[19–21] and flowing atmospheric-pressure afterglow ionization,[16] droplet-assisted inlet ionization,[22] and photoionization.[23] These ionization methods yield more detailed molecular information, improving our knowledge of the composition of atmospheric aerosol. Composition alone, however, is not enough to classify and understand the impacts of aerosol in the atmosphere and we must couple knowledge of particle composition with their physical and optical properties and chemical reactivity.[24]

Single particle levitation methods have been developed over many years as effective tools for probing the physical and optical properties of micron-sized samples.[25] The application

of these methods to probing the dynamics of atmospheric aerosol and their proxies have revealed important information relating to the hygroscopicity, volatility, optical properties, viscosity, surface tension and diffusive characteristics.[26–35] Although functional group information is available through the use of Raman scattering,[34] these methods are typically blind to the exact composition of the sample and instead rely on indirect indicators of composition (size, refractive index etc.). Droplet-based ionization methods, such as field-induced droplet ionization (FIDI), laser desorption ionization and droplet electrospray ionization, have been applied to droplet trains and acoustically levitated droplets.[36–39] However, there is a growing effort to develop experimental platforms capable of measuring the composition of much smaller levitated particles held in electrodynamic traps, and recent work by Jacobs et al.[40] and Birdsall et al.[41,42] have demonstrated the coupling of these methods with mass spectrometry.

In the works of Birdsall et al.,[41] a double-ring electrodynamic balance was used to levitate populations of particles that were then deposited, vaporized and ionized in a corona discharge to be sampled by MS. At the same time, Jacobs et al.[40] reported similar levitation methodology using a linear-quadrupole electrodynamic balance (LQ-EDB) and a paper spray (PS) ionization source. These techniques demonstrated that qualitative information on the composition of 20 – 50 μm sized droplets could be obtained, however the quantitative nature of the methods remains unclear. In more recent work, Birdsall et al.[42] show that vapor pressures may be elucidated from evaporating multi-component droplets, and measurements revealed the role of inorganic salts on the vapor partitioning of the organic compound 2-butenedial. However, the uncertainties reported in their approach

limit the accuracy to which thermochemical data may be quantified. To measure chemical kinetics, the sensitivity and precision of the instrument must be sufficient to detect the formation of products, and the response of the system must be well characterized in order to account for the effects of ionization efficiency and non-linearity of signal. As yet, no single particle mass spectrometry method has demonstrated an effective quantitation for the analysis of chemical kinetics during a chemical transformation.

The paper spray ionization used by Jacobs et al.[40] is based on a relatively new method used in analytical chemistry. Paper spray was introduced by R. Graham Cooks and co-workers as a tool for quick and simple sampling of material.[43–45] Initially conceived as a disposable sampling platform, recent work has shown that a continuous solvent flow may be applied for longer sampling periods.[46] The ionization mechanism is similar to that of classical electrospray ionization (ESI) where charged droplets are emitted in a spray, rapidly lose solvent to evaporation and fission due to the Rayleigh charge instability. This produces gas phase ions and clusters that are sampled by the MS. The facets that determine the effectiveness of ESI, such as the composition of the solvent and size distribution of droplets in the spray, may also influence the effectiveness of PS.[47,48] The PS ionization platform can be effectively applied to droplet measurements due to the ease of transfer of a droplet from a LQ-EDB onto the paper substrate. Despite the simplicity of this ionization method, it offers many advantages, such as a constant background measurement between droplet samples and sensitivity to sub-picogram amounts of analyte.[49]

In order to make effective use of the paper spray method for the analysis of picolitre droplets held in our newly developed LQ-EDB platform, a characterization of its sensitivity and quantitative ability is necessary.[50] In this work, we explore the basic response of paper spray ionization to sampling material contained within picolitre droplets. We demonstrate a range of compounds that may be detected using this technique and establish the conditions and experimental practices required to ensure the data can be interpreted quantitatively. We report the limit of quantification for a model oxygenated organic compound (citric acid) and the limit of linearity for both single and multi-component systems. We conclude by discussing the applications and limitations of the technique when applied to sample droplets from the LQ-EDB.

3.3. Experimental Section

3.3.1. Chemicals and Sample Preparation

The chemicals used in this study were purchased and used without further purification. Quantitative measurements were performed using citric acid (Sigma-Aldrich, USA; ≥99.5% purity) and maleic acid (Sigma-Aldrich, USA; ≥99% purity) prepared in aqueous solution using purified water (Fisher Chemical, USA; Submicron Filtered). Various polyethylene glycols, dicarboxylic acids and fatty acids (Sigma-Aldrich, USA) were also measured and used as supplied. Solutions of single and mixed solutes were prepared at known concentrations (ranging from 0.01 to 20 g/L) and transferred to a microdroplet dispenser (Microfab MJ-ABP-01 w/ 30 µm orifice) to generate picoliter droplet samples. The droplet dispenser was powered by an in-house constructed pulse generator controlled

by a DAQ card and LabVIEW software, delivering 20 – 50 µs pulses with a voltage peak of up to 50 V. Droplets were generated on-demand either individually or in burst mode with a known total number of droplets.

The paper spray was operated with either pure methanol (Fisher Chemical, USA; 0.2 micron filtered) or an equal volume mix of methanol and chloroform (Fisher Chemicals, USA; Approx. 0.75% ethanol as preservative) delivered at a flow rate of 20 µL min^{-1} using a syringe pump.

3.3.2. Technique Design and Analytical Procedure

All measurements were carried out using a Q Exactive Focus Orbitrap Mass Spectrometer (ThermoFisher Scientific, USA). The paper spray ion source was constructed in-house to deliver ions to the inlet of the MS through a metal extension loosely affixed to the inlet to act as a funnel. The funnel was observed to increase signal intensity and improve stability, attributed to the increased time over which electrospray droplets could evaporate. The MS was operated in negative polarity mode to detect acids and positive mode to detect the glycols, with typical scan settings of 90-300 m/z, a resolution of 35000 and maximum ion injection time of 100 ms.

Two different types of paper spray substrate were used in this study: VWR filter paper (Filter Paper, Qualitative, 413) and Whatman chromatography paper (Standard chromatography paper, Thickness: 0.18 mm; Flow Rate: 130 mm/30min). Triangular substrates were prepared from a 1 cm x 1 cm square by cutting from the corner to the center

to produce isosceles triangles with base 1 cm and height 1 cm, leading to a tip angle of 53˚. Other geometries were also sampled, however a rigorous comparison was not performed as previous works addressed the effects of tip angle.[51]

The paper substrate was attached to a stainless-steel alligator clip mounted to a 3D printed enclosure and connected to a high voltage power supply (Stanford Research Systems PS350). The paper substrate was loosely connected to a PEEK solvent delivery tube to receive solvent flow from a 10 mL syringe (Hamilton, USA; Model: GasTight #1010) pushed by a syringe pump (Chemyx Inc., USA; Model: Fusion 100T) operating at 20 µL min^{-1}. The droplet dispenser was mounted using optomechanical components (Thorlabs) and positioned above the paper substrate. A schematic of the PS ionization platform is shown in **Figure 1**.

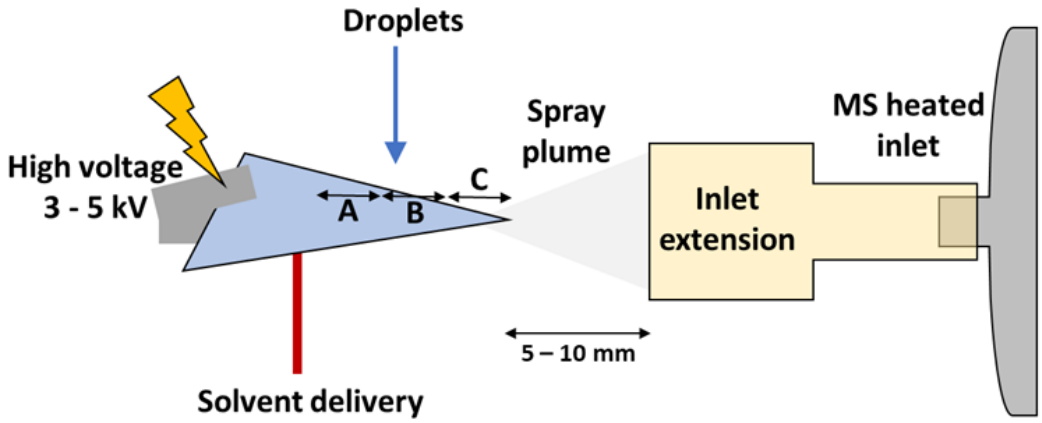

Figure 1: Schematic configuration of the paper spray ionization source coupled to the mass spectrometer. Droplets are deposited on-demand from a microdispenser above the paper at locations near the solvent delivery tube (position A), towards the tip (position B) and at the tip (position C). The MS inlet extension improves the ion collection efficiency in the absence of heated gases, serving to funnel the ions and aid in evaporation of the electrospray plume. The PS-MS interface is housed within a 3D printed enclosure with the paper protruding into the open lab environment.

3.3.3. Droplet Paper Spray

The basic principles of paper spray have been discussed elsewhere and are recounted only briefly here.[43] To generate an electrospray from the tip of the paper, a voltage of 3 – 5 kV was applied to the solvent-soaked substrate. Above a certain voltage threshold, an electrospray plume was emitted from the tip of the paper towards the MS inlet (held at 50 V). Unlike more traditional paper spray implementations, solvent was continuously delivered to the paper allowing the spray to be maintained indefinitely. The tip of the paper was positioned 5 – 10 mm from the inlet to the MS resulting in a spray plume that expands to the width of modified inlet region at inlet (**Figure 1**).

Picoliter aqueous droplets containing the sample analyte were deposited onto the paper substrate during paper spray operation. The deposition location was not rigorously measured due to the difficulties associated with imaging the droplets and assessing their trajectories. However, the location was categorized crudely into three regions, indicated in **Figure 1**: A – near the solvent delivery site; B – between the solvent delivery site and the tip; C – near the tip. The spacing between these regions was approximately 1 mm. Once deposited on the surface, droplets were solubilized by the solvent and the solution flowed towards the tip of the paper, eventually being sprayed in the plume resulting in sample ionization. Depending on deposition location and analyte mass in the sample, the material was present in the spray for seconds to minutes. Ions from the spray were continuously sampled by the MS and a clear increase in intensity corresponding to analyte peaks was observed following deposition, followed by a decay as the material was depleted. This approach leads to two main advantages – firstly, the distinction between background and

noise peaks in the spectrum compared to analyte peaks is very clear and secondly, many samples can be analyzed and compared in succession without the modification of ionization assembly.

3.3.4. Data Processing

Experimental mass spectra were initially analyzed using Xcalibur 4.1 software (ThermoFisher Scientific) and chromatograms of relevant peaks were exported to MagicPlot for further analysis.

3.4. Results and Discussion

To explore the nature of the paper spray method as applied to analyte contained within single picolitre droplets, we explore the response to a series of single and mixed analyte samples. We first demonstrate sensitivity of PS-MS to a range of compounds relevant for the study of oxidized organic material present in atmospheric aerosol and explore the reproducibility. We go on to assess the quantitative nature of the response of signal intensity to the mass of analyte contained within the deposited droplets and the relative signal arising from mixed analyte samples.

3.4.1. Compositional Analysis of Single Analyte Droplets

3.4.1.1. Chemical Identification

Individual picoliter droplets produced from a 1 g/L solution of citric acid (CA) were deposited on the paper spray substrate and the resulting ions were sampled by PS-MS.

Based on previous work, the droplets produced using the microdispenser were on the order of 50 µm in diameter, leading to a total mass of citric acid in a single droplet of ~65 pg.[52] Following deposition, the signal in the mass spectrum corresponding to the single deprotonated citric acid molecule (m/z 191.02) increased significantly and decayed over subsequent seconds. A chromatogram of several droplet deposition events is shown in **Figure 2A**, with each peak in the sequence arising from a single droplet deposited on the paper. With each droplet giving rise to a peak that persists for around 0.2 mins, and a solvent flow rate of 20 µL min^{-1}, we can estimate the average concentration of analyte in the electrospray solution to be on the order of 10 pg $µL^{-1}$.

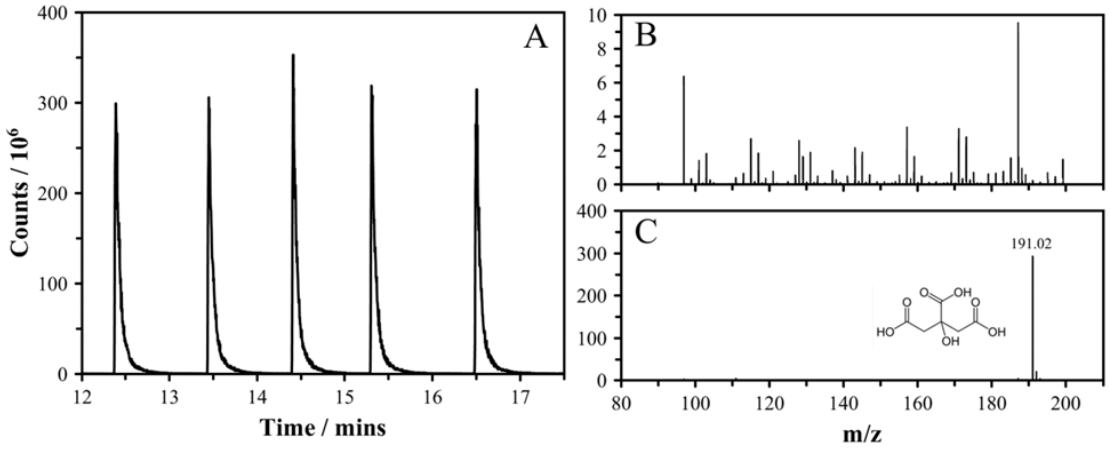

Figure 2: (A) A sequence of single five citric acid (CA) solution droplets as obtained by the extracted ion chronogram of the ion of interest. The droplets have an approximate diameter of ~50 µm and a concentration of 1 g/L (65 pg of CA) were sampled by PS-MS. The counts correspond to the intensity of the molecular ion peak for citric acid ($C_6H_7O_7^+$). **(B)** The background mass spectrum measured in the paper spray. **(C)** The mass spectrum corresponding to the peak intensity from a single droplet of citric acid. Note that the axis range is 40 × larger than in *Figure 2B.*

Figure 2B shows the mass spectrum prior to deposition of a droplet and **Figure 2C** shows the mass spectrum at the peak of signal arising from the droplet. While there is intensity in background peaks arising solely from the paper spray, the spectrum shows a clear contribution from the droplet following deposition. The ability to unambiguously identify peaks arising from our sample makes this technique useful for characterizing samples of unknown composition. To explore the breadth of application of the technique for the chemical identification of atmospherically relevant species, we measured mass spectra for a series of polyethylene glycol droplets (tetra, penta and hexa-ethylene glycols), long-chain fatty acids (oleic and elaidic acid) and a series of dicarboxylic acids (glutaric, succinic and adipic acid). We have limited our exploration to oxidized molecules as these form the majority of secondary organic aerosol species in the atmosphere.[53] **Figure 3** clearly shows that the droplet PS-MS method is capable of identification of these dicarboxylic acids (**Figure 3A**), glycols (**Figure 3B**) and fatty acids (**Figure 3C**). These molecules span a range of solubility (in water) and molecular mass. For the acids, the major ion is the singly deprotonated molecular ion, while for the glycols (measured in positive mode) the major ions were the sodium and ammonium adducts with the parent molecule, and the singly protonated ion.[54] These results demonstrate that there is broad applicability of the technique to sample oxygenated species representative of atmospheric secondary organic aerosol material.

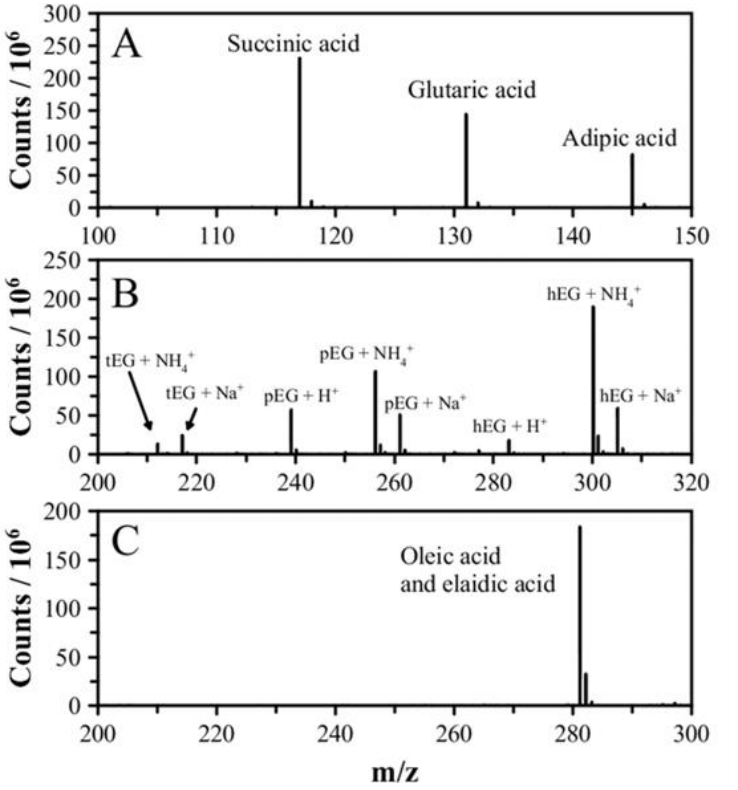

Figure 3: Mass spectra obtained for single droplets deposited on the paper for equimolar mixtures of dicarboxylic acids **(A)**, polyethylene glycols (t = tetra, p = penta, h = hexa, EG = ethylene glycol) **(B)** and oleic acid (and its configurational isomer elaidic acid) **(C)**. The acids were sampled in negative ionization mode, while the glycols were sampled in positive mode and the spectra shows peaks corresponding to $M+H^+$, $M+NH_4^+$ and $M+Na^+$.

3.4.1.2. Reproducibility

Qualitative identification of a wide range of analytes in picoliter droplets is possible using the developed PS-MS method. However, in order to apply it to measuring reaction rates and chemical abundances, the method must also produce reproducible data that quantitatively reflects the sample composition. The chromatogram signal corresponding to a single droplet may be integrated to determine the area under the curve, hereby referred to as the peak area or I_X, where X reflects the analyte of interest. We will assess the assumption that peak area is proportional to the mass of analyte sampled. For a series of

droplets where the mass of analyte is approximately constant, we observed reproducibility within a few percent between individual droplets. **Figure 4A** shows representative data for the peak area for two separate experiments with 10 droplets of a 1 g/L citric acid solution collected sequentially. In these cases, the standard deviation is around 10% of the mean, with no systematic trend. This reproducibility was observed in the majority of experiments.

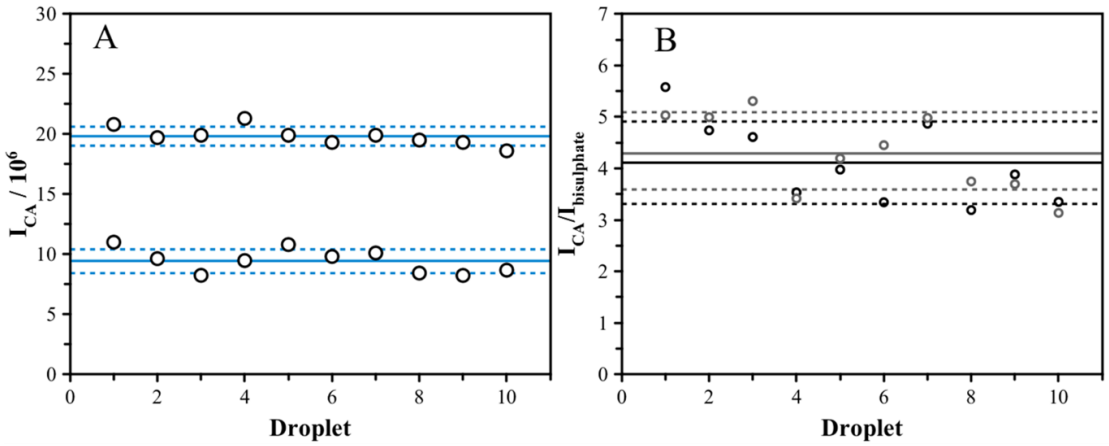

Figure 4: (A) For the citric acid solution droplets as *Figure 2*, the peak area corresponding to the molecular ion was found, shown here for each individual droplet in a sequence of 10. Two datasets are shown for the same solution, and the differences can be attributed to the variations in the system on an experiment-by-experiment basis, as discussed in the text. The solid blue lines shows the average while the dash lines represent an uncertainty range of one standard deviation. **(B)** The citric acid chromatograms were ratioed against the bisulphate (HSO_4^-) chromatogram, a consistent background peak in the paper spray. The average peak area ratio for the two experiments converge, although the signal variability increases due to the variability of the relatively low intensity bisulphate signal. The solid lines show the average while the dash lines show the new standard deviation range associated with the ratio.

It should be clear from **Figure 4** that although there is good reproducibility over the course of a measurement, there is little reproducibility when comparing the same concentration on different days. **Figure 4A** shows two sets of data, collected with the same 1 g/L CA sample solution and droplet dispenser pulse settings, that exhibit a factor of two

difference in the average peak intensity. In **Figure 4B**, the peak at m/z 96.96, a consistent feature in the paper spray plume and likely arising from bisulfate ($HSO4^-$), is used to normalize the citric acid data from **Figure 4A**. The data becomes more scattered, as now the variability in two peaks contributes. However, the mean values for these data are consistent, within a few percent. This suggests that the differences in the signal intensity between experiments arise from the variability in dispenser position as well as spray characteristics and may be accounted for by normalizing to a peak that is representative of the spray efficiency. There are several factors that might be responsible for the differences in the signal intensity:

Deposition location: The deposition location may differ when the experiment is set up on successive occasions. **Figure 5** shows the chromatogram for individual droplets deposited at three locations on the paper (defined as A, B and C).

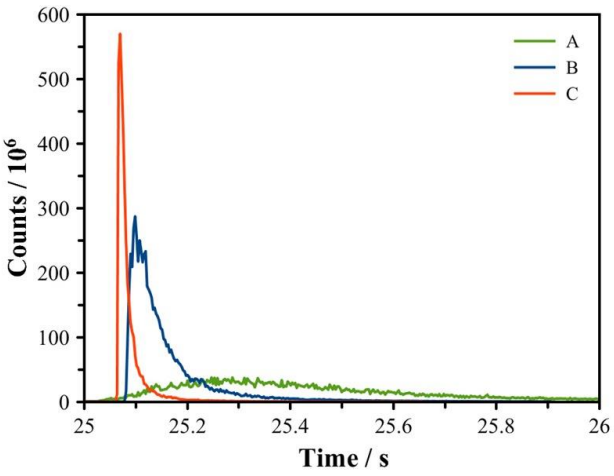

Figure 5: The signal from a single droplet exhibits a time-dependence that varies with deposition location. Position C, at the tip of the paper, shows the highest intensity in the peak, while position A, far from the tip, has the longest duration. Position B, around 1mm from the tip and used throughout this study, shows the highest integrated peak area.

In the case when the dispenser is placed very close to the tip (C), we observe a very sharp and narrow peak. This is due to the small surface area and volume of solvent in which the analyte can dissolve, leading to a high effective concentration in the spray. However, with the dispenser positioned far from the tip (position A), we observe a slow rise in signal and broad peaks that persist for longer. The low peak intensity and long duration over which the analyte may become absorbed to the porous paper might limit the sensitivity in this configuration. Position B (between positions A and C) leads to the largest peak area (~2× the area for the peak at position C), while the peak at position C shows the smallest area. It is clear that a consistent deposition location (position B is considered the most suitable throughout study) is vital for gaining consistent signal in PS-MS.

Spray Characteristics: Although in principle the spray can be maintained indefinitely with continuous supply of solvent, in reality it must be restarted every 4 – 5 hours to refill the solvent syringe. Typically, the measured signal is consistent across this time period. However, when the spray stops and is restarted, even with the same voltage settings, the signal intensity can be quite different. This is likely due to the changes in microscopic structure of the paper and the protrusions that are actively producing electrosprays.[43] This sensitivity to changes is even more pronounced when the paper substrate is changed, as the microscopic structure will be totally transformed.

Droplet Size: Each time the droplet dispenser is loaded with sample solution, the capillary forces that pull the liquid to the tip can change marginally. This can result in differently sized droplets being produced, which can lead to inter-experimental variability.

Although the micro dispensers have been shown to produce consistently sized droplets within a few % of mean diameter, this marginal change in size could lead to a large variation in the mass due to the cubic relationship between size and mass and account for some of the uncertainty.

The factors discussed above affect the reproducibility of the data by changing over the course of an experiment (inconsistent spray and variable dispenser location). Therefore, ensuring that the factors that give rise to variability are constrained will improve the reproducibility of results between experiments. In addition, an internal standard can be used that gives an indication of the efficiency of the spray.

3.4.1.3. Quantification

In order to assess the quantitative nature of the method, and in light of the signal reproducibility observations when aspects of the setup are changed, we used the droplet dispenser in burst mode to vary the analyte mass and explore the response in the MS. While this is not directly equivalent to a large or more highly concentrated single droplet, it provides an effective means of quickly varying the analyte mass while maintaining the experimental configuration in a fixed state. Droplets were generated at up to 200 per burst, allowing the analyte mass to span over two orders of magnitude. Experiments were performed using a 0.1 g/L citric acid solution and repeated several times over different days. The results are shown in **Figure 6** using chloroform/methanol as the spray solvent. We observe clear variability on an experiment-to-experiment basis, as already discussed. However, within a single experiment, we observe a linear relationship between the signal

intensity and analyte mass (calculated assuming a droplet diameter of 50 µm). The slope of the dependence varies, but in all cases the R^2 is greater than 0.9 indicating that the response of the system is linear to analyte mass over the range explored here, from around 50 pg to 1.3 ng.

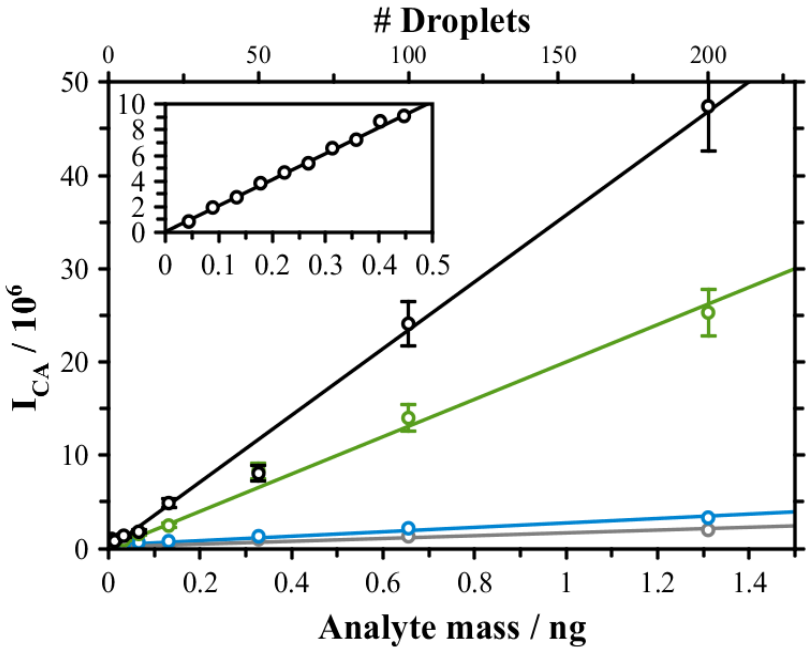

Figure 6: The integrated peak area of citric acid sampled from droplets as a function of analyte mass increases linearly over a mass range of at least two orders of magnitude. The analyte mass was varied by deposition of between 1 and 200 droplets of a 0.01 g/L citric acid solution in burst method, as discussed in the text. Each line represents data collected during different experiments on different days using the same solution. The inter-experimental variability is discussed in the text. **(Inset)** Low mass range analysis with higher resolution also shows linearity.

Over a narrow range of mass (**Figure 6** inset), the linearity is excellent with an R^2 >0.99. The full mass range explored here is equivalent to a particle of pure CA with diameter from 1.4 µm to 4.4 µm. The limit of detection, estimated by analyte mass that results in signal to noise of 10:1, is on order of 0.5 pg, equivalent to a pure CA particle diameter of 0.3 µm.

Earlier measurements with pure methanol as the spray solvent show linearity only over a narrower range of mass, with clear curvature as low analyte mass loadings are approached (**Figure 7**). The reason for this is unclear but may arise due to the voltage required to generate a stable spray. For the mixed solvent, voltages of > 4 kV were used, while for pure methanol, a spray was typically stable at 3.2–3.5 kV. The greater electric field required to generate stable electrospray from the chloroform/methanol solvent might have improved ion production at high analyte concentrations and make the measurement less susceptible to charge limitations.[55]

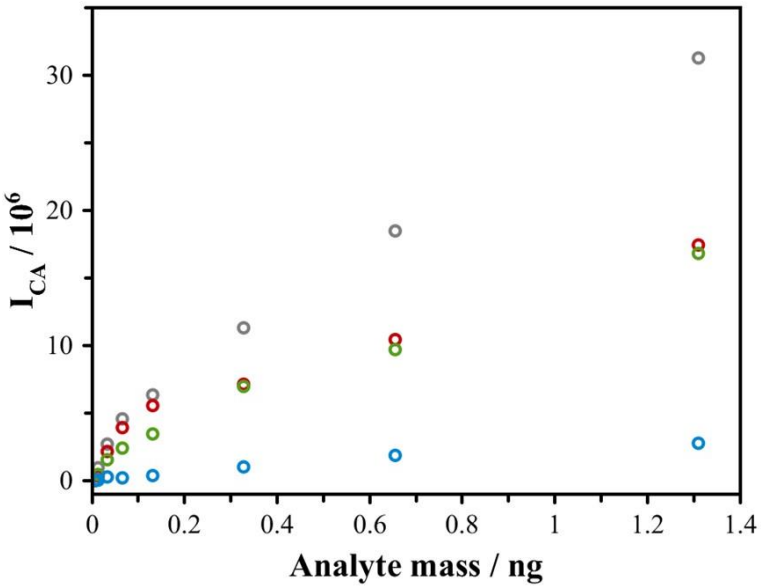

Figure 7: The integrated peak area of citric acid (CA) sampled from droplets as a function of analyte mass sampled using methanol as the PS solvent. The analyte mass was varied by deposition of between 1 droplet and 200 droplets of a 0.01 g/L citric acid solution in burst method, as discussed in the manuscript text. Each color represents data collected during different experiments. The inter-experiment variability is discussed in the text, but unlike the data shown in *Figure 5*, these data do not exhibit linearity of signal with the increase in analyte mass.

In the case of citric acid, these results demonstrate that for a single component analyte sampled under consistent conditions, the signal is both reproducible and linear. These factors are vital for applications of the PS-MS in the analysis of compositional changes in levitated droplets. However, in most measurements, droplets will not contain just one analyte and instead consist of two or more (and up to thousands for ambient samples) different chemical species. Such analysis can be simplified by considering the peak area of an analyte relative to other analytes within the sample to normalize the data. However, relative ionization efficiencies of these compounds must be known or measured in order the gain quantitative information from these data. Here, we will focus our discussion on a binary system to assess the key features of the droplet PS-MS method when applied to a droplet containing mixed analytes.

3.4.2. Compositional Analysis of Binary Analyte Droplets

3.4.2.1. Relative Intensity and Ionization Efficiency

When dealing with droplets containing mixed analytes, we can consider the ratio of the intensity of analyte peaks. The mole fraction in a binary droplet (in this case consisting of maleic acid (MA) and citric acid (CA) can be written as a function of the peak area in the mass chromatogram according to:

$$x_{MA} = \frac{\gamma I_{MA}}{\gamma I_{MA} + I_{CA}} \qquad (1)$$

where I_{MA} and I_{CA} are the peak areas of the analytes in the chromatogram. γ denotes the relative ionization efficiency of maleic acid to citric acid, according to:

$$\gamma = \frac{I_{CA} n_{MA}}{I_{MA} n_{CA}} \qquad (2)$$

where n_{MA} and n_{CA} are the molar amounts of MA and CA in the sample droplet.

For an equimolar mixture of MA and CA, the mole ratio is equal to one, and the ionization efficiency is determined directly from the relative intensity of the signals from each analyte. The chromatogram for MA and CA in a droplet comprised of an equimolar mixture is shown in **Figure 8A** and a representative mass spectrum for this composition is shown in **Figure 8B**.

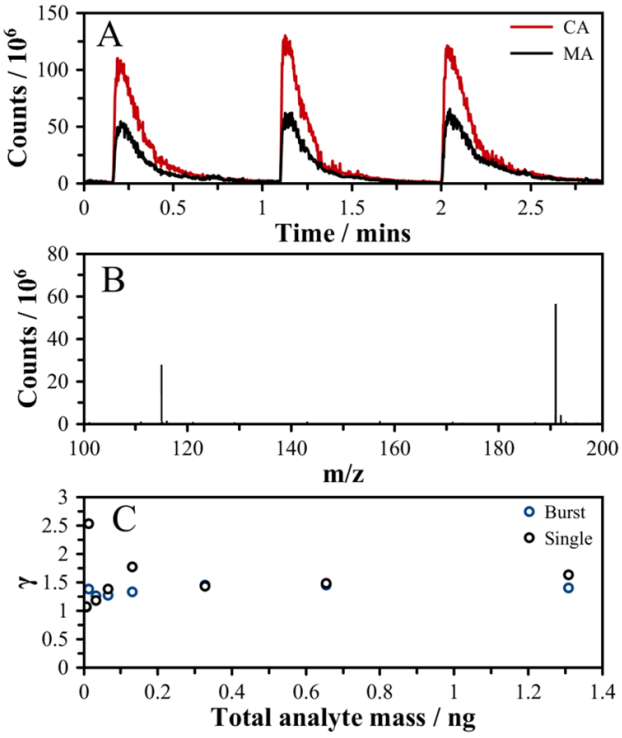

Figure 8: (A) Chromatogram of peaks corresponding to single droplets containing citric acid (CA, red) and maleic acid (MA, black) in an equimolar mixture. **(B)** Mass spectrum showing contribution from CA (191.02) and MA (115.00) molecular ions. **(C)** Ionization efficiency (as defined in the text) determined for MA and CA as a function of total analyte mass for experiments in burst mode and single droplet mode. Both methods exhibit a trend towards an ionization efficiency of ~1.5 with total analyte mass > 0.1 ng.

The relative ionization efficiency is determined to be 1.89. However, there is significant variability in this value, especially at low analyte mass. At high analyte mass, the ionization ratio tends towards a consistent value. **Figure 8C** compares the ionization efficiency for equimolar mixtures of citric acid and maleic acid for increasing analyte mass. These measurements were performed using both burst mode and single droplets with increasing solute concentration. For the single droplet measurements, there is large variability in the ratio until the analyte total mass is greater than around 0.1 ng, while for the burst mode the variability is much smaller. The comparison of these datasets indicates once again that the deposition location is a key factor in the reproducibility of data. In burst mode, the droplet dispenser location is fixed, and all droplets are deposited at the same location. In single droplet mode, the dispenser was removed and replaced each time with a new sample solution, introducing some variability.

3.4.2.2. Evaluating the Relative Abundance

To explore how the signal intensity varies when the mixing ratio of analytes changes, we performed a series of measurements on single droplets of CA and MA mixture from solutions spanning a range of MA mole fractions, from $x_{MA} = 0.02$ to $x_{MA} = 0.94$. This is shown in **Figure 9A** for single droplets generated from 1-20 g/L total analyte concentration sample solutions (an average across experiments using different mass concentrations is shown). The points show the average of three repeats over different days, and each repeat took the average of 10 individual sequential droplets per data point. The error bars reflect

the standard deviation of 10 % representative of the variability on a droplet-by-droplet basis in the data set.

The slope of the peak area ratio against the molar ratio defines the ionization efficiency, according to:

$$\frac{I_{MA}}{I_{CA}} = \frac{1}{\gamma}\frac{n_{MA}}{n_{CA}} \quad (3)$$

For molar ratios up to ~2 (i.e., 2 molecules of MA to every 1 of CA), the data define a straight line with an R^2 of 0.994, a slope of 0.54 and a standard deviation in the slope of 0.02. This indicates that the relative ionization efficiency is constant over this range with a value of 1.85, in agreement with the determined value from the equimolar mixture in *Section 3.2.1*. When the full range of data are included in the fit, there is some curvature, and a straight line is no longer a good representation of the whole data set shown in the inset of **Figure 9A**. A straight line fit through all the data points varies significantly from the straight line defining just the lower molar ratio points.

The MA peak area as a function of the total peak area is shown in **Figure 9B** and exhibits a curvature as the data approach the limiting points (0,0 and 1,1). This curvature is due to the difference in ionization efficiencies of analytes and accounting for the relative ionization efficiency, via *equation 1*, allows us to calculate the expected mole fraction from the intensity.

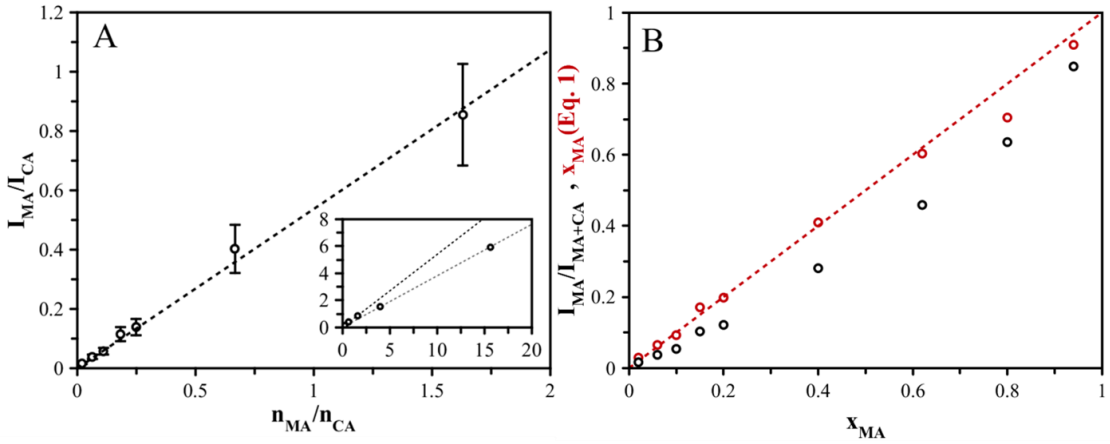

Figure 9: (A) The ratio of maleic acid (MA) to citric acid (CA) peak areas is shown as a function of the molar ratio in the droplet. A linear trend with a slope of 0.54 is observed up to $n_{MA} \setminus n_{CA} \approx 2$, but beyond that some deviation is observed (inset: black dash line shows the fit up to $n_{MA} \setminus n_{CA} \approx 2$ versus a linear fit to all the data shown as a gray dash line). Taking a linear fit to the data up to $n_{MA} \setminus n_{CA} \approx 2$, an ionization efficiency of 1.84 is determined. **(B)** The peak area of MA as a fraction of the total peak area from CA and MS is shown as a function of mole fraction of MA in the droplet (black points). The curvature arises due to the ionization efficiency effects. Accounting for the ionization efficiency using the slope of the data in *Figure 9A* and *equation 3*, the mole fraction can be estimated (red points) using *equation 1*. The 1:1 line is shown as a red dash.

These data exhibit agreement to a 1:1 line, indicating that the mole fraction is determined accurately. The points at higher mole fraction also agree well with the 1:1 line, even though the relative ionization efficiency predicted by these data is much larger. This is a consequence of the choice of parameters and arises due to the much smaller dependence of the peak area ratio on the ionization efficiency when at the extreme ends of the mole fraction range.

3.5. Summary and Conclusions

We have demonstrated several key features of the droplet PS-MS platform that will guide future application of the method for sampling levitated droplets. Firstly, the sensitivity of

the method to oxygenated organic compounds in both positive and negative ion modes ensures that compounds of atmospheric interest and the products from atmospherically relevant reactions (such as ozonolysis and OH-initiated oxidation) can be effectively analyzed using this method. Secondly, we demonstrate high droplet-by-droplet reproducibility (within 10%) and identified key experimental factors that must be constrained to achieve this. When coupling the PS-MS ionization source to an LQ-EDB, the sequential sampling of individual droplets may occur over many minutes or even hours, and it is imperative that the system response over that time be well understood. We have further shown that both internal and external standards can mitigate some variability in the signal. Finally, we have shown that both the absolute signal and the relative signals are effective indicators of abundance, with linearity observed over the entire mass range relevant for levitation studies and over a broad range of composition. Further improvements to the platform may be achieved through the use of different solvents, paper substrate composition and experimental geometry to improve sensitivity or reproducibility.

Although further work with quantitative measures of suspended droplet size are required to fully characterize the technique, we have shown through these measurements that the droplet PS-MS platform will be an effective tool for compositional analysis of levitated picoliter droplets and quantification of changes in their composition due to evaporation or chemical reaction. The coupling of PS-MS with an a linear-quadrupole electrodynamic balance (LQ-EDB) will facilitate experimental interrogations of the evolving chemical composition of levitated droplet samples and allow physical and optical properties to be measured as a function of composition. For this, samples will be drawn from solutions of

model atmospheric compounds or resolubilized laboratory-generated of ambient aerosol material and droplets will be introduced into the LQ-EDB using the microdroplet dispensers described in this work. Direct sampling of aerosol by coalescence of laboratory-generated aerosol into a levitated collection droplet may also be possible.[56] These measurements will be used to characterize the effects of evolving composition due to various atmospheric processes, such as heterogeneous reactions and photochemistry experienced by aerosol in the environment,[57,58] in order to provide a compositionally-resolved understanding of aerosol properties and processes.

3.6. References

(1) Ruehl, C. R.; Davies, J. F.; Wilson, K. R. An Interfacial Mechanism for Cloud Droplet Formation on Organic Aerosols. *Science* **2016**, *351* (6280), 1447–1450. https://doi.org/10.1126/science.aad4889.

(2) Facchini, M. C.; Mircea, M.; Fuzzi, S.; Charlson, R. J. Cloud Albedo Enhancement by Surface-Active Organic Solutes in Growing Droplets. *Nature* **1999**, *401* (6750), 257–259. https://doi.org/10.1038/45758.

(3) Lohmann, U.; Broekhuizen, K.; Leaitch, R.; Shantz, N.; Abbatt, J. How Efficient Is Cloud Droplet Formation of Organic Aerosols? *Geophys. Res. Lett.* **2004**, *31* (5). https://doi.org/10.1029/2003GL018999.

(4) Lambe, A. T.; Cappa, C. D.; Massoli, P.; Onasch, T. B.; Forestieri, S. D.; Martin, A. T.; Cummings, M. J.; Croasdale, D. R.; Brune, W. H.; Worsnop, D. R.; Davidovits, P. Relationship between Oxidation Level and Optical Properties of Secondary Organic Aerosol. *Environ. Sci. Technol.* **2013**, *47* (12), 6349–6357. https://doi.org/10.1021/es401043j.

(5) Moise, T.; Flores, J. M.; Rudich, Y. Optical Properties of Secondary Organic Aerosols and Their Changes by Chemical Processes. *Chem. Rev.* **2015**, *115* (10), 4400–4439. https://doi.org/10.1021/cr5005259.

(6) George, C.; Ammann, M.; D'Anna, B.; Donaldson, D. J.; Nizkorodov, S. A. Heterogeneous Photochemistry in the Atmosphere. *Chem. Rev.* **2015**, *115* (10), 4218–4258. https://doi.org/10.1021/cr500648z.

(7) C. Chapleski, R.; Zhang, Y.; Troya, D.; R. Morris, J. Heterogeneous Chemistry and Reaction Dynamics of the Atmospheric Oxidants, O 3 , NO 3 , and OH, on Organic Surfaces. *Chem. Soc. Rev.* **2016**, *45* (13), 3731–3746. https://doi.org/10.1039/C5CS00375J.

(8) Jang, M.; Carroll, B.; Chandramouli, B.; Kamens, R. M. Particle Growth by Acid-Catalyzed Heterogeneous Reactions of Organic Carbonyls on Preexisting Aerosols. *Environ. Sci. Technol.* **2003**, *37* (17), 3828–3837. https://doi.org/10.1021/es021005u.

(9) Pöschl, U. Atmospheric Aerosols: Composition, Transformation, Climate and Health Effects. *Angew. Chem. Int. Ed.* **2005**, *44* (46), 7520–7540. https://doi.org/10.1002/anie.200501122.

(10) Shiraiwa, M.; Selzle, K.; Pöschl, U. Hazardous Components and Health Effects of Atmospheric Aerosol Particles: Reactive Oxygen Species, Soot, Polycyclic Aromatic Compounds and Allergenic Proteins. *Free Radic. Res.* **2012**, *46* (8), 927–939. https://doi.org/10.3109/10715762.2012.663084.

(11) Isaacman-VanWertz, G.; Massoli, P.; O'Brien, R.; Lim, C.; Franklin, J. P.; Moss, J. A.; Hunter, J. F.; Nowak, J. B.; Canagaratna, M. R.; Misztal, P. K.; Arata, C.; Roscioli, J. R.; Herndon, S. T.; Onasch, T. B.; Lambe, A. T.; Jayne, J. T.; Su, L.; Knopf, D. A.; Goldstein, A. H.; Worsnop, D. R.; Kroll, J. H. Chemical Evolution of Atmospheric Organic Carbon over Multiple Generations of Oxidation. *Nat. Chem.* **2018**, *10* (4), 462–468. https://doi.org/10.1038/s41557-018-0002-2.

(12) Zhang, Q.; Jimenez, J. L.; Canagaratna, M. R.; Allan, J. D.; Coe, H.; Ulbrich, I.; Alfarra, M. R.; Takami, A.; Middlebrook, A. M.; Sun, Y. L.; Dzepina, K.; Dunlea, E.; Docherty, K.; DeCarlo, P. F.; Salcedo, D.; Onasch, T.; Jayne, J. T.; Miyoshi, T.; Shimono, A.; Hatakeyama, S.; Takegawa, N.; Kondo, Y.; Schneider, J.; Drewnick, F.; Borrmann, S.; Weimer, S.; Demerjian, K.; Williams, P.; Bower, K.; Bahreini, R.; Cottrell, L.; Griffin, R. J.; Rautiainen, J.; Sun, J. Y.; Zhang, Y. M.; Worsnop, D. R. Ubiquity and Dominance of Oxygenated Species in Organic Aerosols in Anthropogenically-Influenced Northern Hemisphere Midlatitudes. *Geophys. Res. Lett.* **2007**, *34* (13). https://doi.org/10.1029/2007GL029979.

(13) Jayne, J. T.; Leard, D. C.; Zhang, X.; Davidovits, P.; Smith, K. A.; Kolb, C. E.; Worsnop, D. R. Development of an Aerosol Mass Spectrometer for Size and Composition Analysis of Submicron Particles. *Aerosol Sci. Technol.* **2000**, *33* (1–2), 49–70. https://doi.org/10.1080/027868200410840.

(14) DeCarlo, P. F.; Kimmel, J. R.; Trimborn, A.; Northway, M. J.; Jayne, J. T.; Aiken, A. C.; Gonin, M.; Fuhrer, K.; Horvath, T.; Docherty, K. S.; Worsnop, D. R.; Jimenez, J. L. Field-Deployable, High-Resolution, Time-of-Flight Aerosol Mass Spectrometer. *Anal. Chem.* **2006**, *78* (24), 8281–8289. https://doi.org/10.1021/ac061249n.

(15) Laskin, J.; Laskin, A.; Nizkorodov, S. A. Mass Spectrometry Analysis in Atmospheric Chemistry. *Anal. Chem.* **2018**, *90* (1), 166–189. https://doi.org/10.1021/acs.analchem.7b04249.

(16) Brüggemann, M.; Karu, E.; Stelzer, T.; Hoffmann, T. Real-Time Analysis of Ambient Organic Aerosols Using Aerosol Flowing Atmospheric-Pressure Afterglow Mass Spectrometry (AeroFAPA-MS). *Environ. Sci. Technol.* **2015**, *49* (9), 5571–5578. https://doi.org/10.1021/es506186c.

(17) Hearn, J. D.; Smith, G. D. A Chemical Ionization Mass Spectrometry Method for the Online Analysis of Organic Aerosols. *Anal. Chem.* **2004**, *76* (10), 2820–2826. https://doi.org/10.1021/ac049948s.

(18) Lopez-Hilfiker, F. D.; Mohr, C.; Ehn, M.; Rubach, F.; Kleist, E.; Wildt, J.; Mentel, T. F.; Lutz, A.; Hallquist, M.; Worsnop, D.; Thornton, J. A. A Novel Method for Online Analysis of Gas and Particle Composition: Description and Evaluation of a

Filter Inlet for Gases and AEROsols (FIGAERO). *Atmospheric Meas. Tech.* **2014**, *7* (4), 983–1001. https://doi.org/10.5194/amt-7-983-2014.

(19) Nah, T.; Chan, M.; Leone, S. R.; Wilson, K. R. Real Time in Situ Chemical Characterization of Submicrometer Organic Particles Using Direct Analysis in Real Time-Mass Spectrometry. *Anal. Chem.* **2013**, *85* (4), 2087–2095. https://doi.org/10.1021/ac302560c.

(20) Upton, K. T.; Schilling, K. A.; Beauchamp, J. L. Easily Fabricated Ion Source for Characterizing Mixtures of Organic Compounds by Direct Analysis in Real Time Mass Spectrometry. *Anal. Methods* **2017**, *9* (34), 5065–5074. https://doi.org/10.1039/C7AY00971B.

(21) Gross, J. H. Direct Analysis in Real Time—a Critical Review on DART-MS. *Anal. Bioanal. Chem.* **2014**, *406* (1), 63–80. https://doi.org/10.1007/s00216-013-7316-0.

(22) Brüggemann, M.; Karu, E.; Stelzer, T.; Hoffmann, T. Real-Time Analysis of Ambient Organic Aerosols Using Aerosol Flowing Atmospheric-Pressure Afterglow Mass Spectrometry (AeroFAPA-MS). *Environ. Sci. Technol.* **2015**, *49* (9), 5571–5578. https://doi.org/10.1021/es506186c.

(23) Horan, A. J.; Apsokardu, M. J.; Johnston, M. V. Droplet Assisted Inlet Ionization for Online Analysis of Airborne Nanoparticles. *Anal. Chem.* **2017**, *89* (2), 1059–1062. https://doi.org/10.1021/acs.analchem.6b04718.

(24) Smith, J. D.; Kroll, J. H.; Cappa, C. D.; Che, D. L.; Liu, C. L.; Ahmed, M.; Leone, S. R.; Worsnop, D. R.; Wilson, K. R. The Heterogeneous Reaction of Hydroxyl Radicals with Sub-Micron Squalane Particles: A Model System for Understanding the Oxidative Aging of Ambient Aerosols. *Atmos Chem Phys* **2009**, 14. https://doi.org/10.5194/acp-9-3209-2009.

(25) Bzdek, B. R.; Reid, J. P. Perspective: Aerosol Microphysics: From Molecules to the Chemical Physics of Aerosols. *J. Chem. Phys.* **2017**, *147* (22), 220901. https://doi.org/10.1063/1.5002641.

(26) Krieger, U. K.; Marcolli, C.; Reid, J. P. Exploring the Complexity of Aerosol Particle Properties and Processes Using Single Particle Techniques. *Chem. Soc. Rev.* **2012**, *41* (19), 6631. https://doi.org/10.1039/c2cs35082c.

(27) Chan, M. N.; Choi, M. Y.; Ng, N. L.; Chan, C. K. Hygroscopicity of Water-Soluble Organic Compounds in Atmospheric Aerosols: Amino Acids and Biomass Burning Derived Organic Species. *Environ. Sci. Technol.* **2005**, *39* (6), 1555–1562. https://doi.org/10.1021/es049584l.

(28) Davies, J. F.; Haddrell, A. E.; Rickards, A. M. J.; Reid, J. P. Simultaneous Analysis of the Equilibrium Hygroscopicity and Water Transport Kinetics of Liquid Aerosol. *Anal. Chem.* **2013**, *85* (12), 5819–5826. https://doi.org/10.1021/ac4005502.

(29) Cai, C.; Stewart, D. J.; Reid, J. P.; Zhang, Y.; Ohm, P.; Dutcher, C. S.; Clegg, S. L. Organic Component Vapor Pressures and Hygroscopicities of Aqueous Aerosol Measured by Optical Tweezers. *J. Phys. Chem. A* **2015**, *119* (4), 704–718. https://doi.org/10.1021/jp510525r.

(30) Hosny, N. A.; Fitzgerald, C.; Tong, C.; Kalberer, M.; Kuimova, M. K.; Pope, F. D. Fluorescent Lifetime Imaging of Atmospheric Aerosols: A Direct Probe of Aerosol Viscosity. *Faraday Discuss.* **2013**, *165* (0), 343–356. https://doi.org/10.1039/C3FD00041A.

(31) Price, H. C.; Murray, B. J.; Mattsson, J.; O'Sullivan, D.; Wilson, T. W.; Baustian, K. J.; Benning, L. G. Quantifying Water Diffusion in High-Viscosity and Glassy Aqueous Solutions Using a Raman Isotope Tracer Method. *Atmospheric Chem. Phys.* **2014**, *14* (8), 3817–3830. https://doi.org/10.5194/acp-14-3817-2014.

(32) Bzdek, B. R.; Power, R. M.; Simpson, S. H.; Reid, J. P.; Royall, C. P. Precise, Contactless Measurements of the Surface Tension of Picolitre Aerosol Droplets. *Chem. Sci.* **2016**, *7* (1), 274–285. https://doi.org/10.1039/C5SC03184B.

(33) Power, R. M.; Simpson, S. H.; Reid, J. P.; Hudson, A. J. The Transition from Liquid to Solid-like Behaviour in Ultrahigh Viscosity Aerosol Particles. *Chem. Sci.* **2013**, *4* (6), 2597–2604. https://doi.org/10.1039/C3SC50682G.

(34) Cotterell, M. I.; Willoughby, R. E.; Bzdek, B. R.; Orr-Ewing, A. J.; Reid, J. P. A Complete Parameterisation of the Relative Humidity and Wavelength Dependence of the Refractive Index of Hygroscopic Inorganic Aerosol Particles. *Atmos Chem Phys* **2017**, 15. https://doi.org/10.5194/acp-17-9837-2017.

(35) Gorkowski, K.; Beydoun, H.; Aboff, M.; Walker, J. S.; Reid, J. P.; Sullivan, R. C. Advanced Aerosol Optical Tweezers Chamber Design to Facilitate Phase-Separation and Equilibration Timescale Experiments on Complex Droplets. *Aerosol Sci. Technol.* **2016**, *50*, 1327–1341. https://doi.org/10.1080/02786826.2016.1224317.

(36) Bones, D. L.; Reid, J. P.; Lienhard, D. M.; Krieger, U. K. Comparing the Mechanism of Water Condensation and Evaporation in Glassy Aerosol. *Proc. Natl. Acad. Sci.* **2012**, *109* (29), 11613–11618. https://doi.org/10.1073/pnas.1200691109.

(37) Tracey, P. J.; Vaughn, B. S.; Roberts, B. J.; Poad, B. L. J.; Trevitt, A. J. Rapid Profiling of Laser-Induced Photochemistry in Single Microdroplets Using Mass Spectrometry. *Anal. Chem.* **2014**, *86* (6), 2895–2899. https://doi.org/10.1021/ac403976q.

(38) Huang, Y.; Barraza, K. M.; Kenseth, C. M.; Zhao, R.; Wang, C.; Beauchamp, J. L.; Seinfeld, J. H. Probing the OH Oxidation of Pinonic Acid at the Air–Water Interface Using Field-Induced Droplet Ionization Mass Spectrometry (FIDI-MS). *J. Phys. Chem. A* **2018**, *122* (31), 6445–6456. https://doi.org/10.1021/acs.jpca.8b05353.

(39) Warschat, C.; Stindt, A.; Panne, U.; Riedel, J. Mass Spectrometry of Levitated Droplets by Thermally Unconfined Infrared-Laser Desorption. *Anal. Chem.* **2015**, *87* (16), 8323–8327. https://doi.org/10.1021/acs.analchem.5b01495.

(40) Jacobs, M. I.; Davies, J. F.; Lee, L.; Davis, R. D.; Houle, F.; Wilson, K. R. Exploring Chemistry in Microcompartments Using Guided Droplet Collisions in a Branched Quadrupole Trap Coupled to a Single Droplet, Paper Spray Mass Spectrometer. *Anal. Chem.* **2017**, *89* (22), 12511–12519. https://doi.org/10.1021/acs.analchem.7b03704.

(41) Birdsall, A. W.; Krieger, U. K.; Keutsch, F. N. Electrodynamic Balance–Mass Spectrometry of Single Particles as a New Platform for Atmospheric Chemistry Research. *Atmospheric Meas. Tech.* **2018**, *115194* (1), 33–47. https://doi.org/10.5194/amt-11-33-2018.

(42) Birdsall, A. W.; Hensley, J. C.; Kotowitz, P. S.; Huisman, A. J.; Keutsch, F. N. Single-Particle Experiments Measuring Humidity and Inorganic Salt Effects on Gas-Particle Partitioning of Butenedial. *Atmospheric Chem. Phys. Discuss.* **2019**, 1–26. https://doi.org/10.5194/acp-2019-423.

(43) Espy, R. D.; Muliadi, A. R.; Ouyang, Z.; Cooks, R. G. Spray Mechanism in Paper Spray Ionization. *Int. J. Mass Spectrom.* **2012**, *325–327*, 167–171. https://doi.org/10.1016/j.ijms.2012.06.017.

(44) Wang, H.; Liu, J.; Cooks, R. G.; Ouyang, Z. Paper Spray for Direct Analysis of Complex Mixtures Using Mass Spectrometry. *Angew. Chem.* **2010**, *122* (5), 889–892. https://doi.org/10.1002/ange.200906314.

(45) Liu, J.; Wang, H.; Manicke, N. E.; Lin, J.-M.; Cooks, R. G.; Ouyang, Z. Development, Characterization, and Application of Paper Spray Ionization. *Anal. Chem.* **2010**, *82* (6), 2463–2471. https://doi.org/10.1021/ac902854g.

(46) Riboni, N.; Quaranta, A.; Motwani, H. V.; Österlund, N.; Gräslund, A.; Bianchi, F.; Ilag, L. L. Solvent-Assisted Paper Spray Ionization Mass Spectrometry (SAPSI-MS) for the Analysis of Biomolecules and Biofluids. *Sci. Rep.* **2019**, *9* (1), 10296. https://doi.org/10.1038/s41598-019-45358-x.

(47) Espy, R. D.; Muliadi, A. R.; Ouyang, Z.; Cooks, R. G. Spray Mechanism in Paper Spray Ionization. *Int. J. Mass Spectrom.* **2012**, *325–327*, 167–171. https://doi.org/10.1016/j.ijms.2012.06.017.

(48) Banerjee, S.; Mazumdar, S. Electrospray Ionization Mass Spectrometry: A Technique to Access the Information beyond the Molecular Weight of the Analyte. *Int. J. Anal. Chem.* **2012**, *2012*, 1–40. https://doi.org/10.1155/2012/282574.

(49) Kim, D.; Yim, U. H.; Kim, B.; Cha, S.; Kim, S. Paper Spray Chemical Ionization: Highly Sensitive Ambient Ionization Method for Low- and Nonpolar Aromatic Compounds. *Anal. Chem.* **2017**, *89* (17), 9056–9061. https://doi.org/10.1021/acs.analchem.7b01733.

(50) Davies, J. F. Mass, Charge, and Radius of Droplets in a Linear Quadrupole Electrodynamic Balance. *Aerosol Sci. Technol.* **2019**, *53*, 309–320. https://doi.org/10.1080/02786826.2018.1559921

(51) Yang, Q.; Wang, H.; Maas, J. D.; Chappell, W. J.; Manicke, N. E.; Cooks, R. G.; Ouyang, Z. Paper Spray Ionization Devices for Direct, Biomedical Analysis Using Mass Spectrometry. *Int. J. Mass Spectrom.* **2012**, *312*, 201–207. https://doi.org/10.1016/j.ijms.2011.05.013.

(52) Davies, J. F.; Haddrell, A. E.; Reid, J. P. Time-Resolved Measurements of the Evaporation of Volatile Components from Single Aerosol Droplets. *Aerosol Sci. Technol.* **2011**, *46* (6), 666–677. https://doi.org/10.1080/02786826.2011.652750.

(53) Jimenez, J. L.; Canagaratna, M. R.; Donahue, N. M.; Prevot, A. S. H.; Zhang, Q.; Kroll, J. H.; DeCarlo, P. F.; Allan, J. D.; Coe, H.; Ng, N. L.; Aiken, a C.; Docherty, K. S.; Ulbrich, I. M.; Grieshop, a P.; Robinson, a L.; Duplissy, J.; Smith, J. D.; Wilson, K. R.; Lanz, V. a; Hueglin, C.; Sun, Y. L.; Tian, J.; Laaksonen, A.; Raatikainen, T.; Rautiainen, J.; Vaattovaara, P.; Ehn, M.; Kulmala, M.; Tomlinson, J. M.; Collins, D. R.; Cubison, M. J.; Dunlea, E. J.; Huffman, J. a; Onasch, T. B.; Alfarra, M. R.; Williams, P. I.; Bower, K.; Kondo, Y.; Schneider, J.; Drewnick, F.; Borrmann, S.; Weimer, S.; Demerjian, K.; Salcedo, D.; Cottrell, L.; Griffin, R.; Takami, A.; Miyoshi, T.; Hatakeyama, S.; Shimono, A.; Sun, J. Y.; Zhang, Y. M.; Dzepina, K.; Kimmel, J. R.; Sueper, D.; Jayne, J. T.; Herndon, S. C.; Trimborn, a M.; Williams, L. R.; Wood, E. C.; Middlebrook, a M.; Kolb, C. E.; Baltensperger, U.; Worsnop, D. R. Evolution of Organic Aerosols in the Atmosphere. *Science* **2009**, *326* (5959), 1525–1529. https://doi.org/10.1126/science.1180353.

(54) Kruve, A.; Kaupmees, K. Adduct Formation in ESI/MS by Mobile Phase Additives. *J. Am. Soc. Mass Spectrom.* **2017**, *28* (5), 887–894. https://doi.org/10.1007/s13361-017-1626-y.

(55) Tang, K.; Page, J. S.; Smith, R. D. Charge Competition and the Linear Dynamic Range of Detection in Electrospray Ionization Mass Spectrometry. *J. Am. Soc. Mass Spectrom.* **2004**, *15* (10), 1416–1423. https://doi.org/10.1016/j.jasms.2004.04.034.

(56) Haddrell, A. E.; Miles, R. E. H.; Bzdek, B. R.; Reid, J. P.; Hopkins, R. J.; Walker, J. S. Coalescence Sampling and Analysis of Aerosols Using Aerosol Optical Tweezers. *Anal. Chem.* **2017**, *89*, 2345–2352. https://doi.org/10.1021/acs.analchem.6b03979.

(57) George, C.; Ammann, M.; D'Anna, B.; Donaldson, D. J.; Nizkorodov, S. A. Heterogeneous Photochemistry in the Atmosphere. *Chem. Rev.* **2015**, *115* (10), 4218–4258. https://doi.org/10.1021/cr500648z.

(58) Bzdek, B. R.; Reid, J. P. Perspective: Aerosol Microphysics: From Molecules to the Chemical Physics of Aerosols. *J. Chem. Phys.* **2017**, *147* (22), 220901. https://doi.org/10.1063/1.5002641.

CHAPTER 4

An Open Port Sampling Interface for the Chemical Characterization of Levitated Microparticles

4.1. Abstract

Several studies have reported ionization methods to classify the chemical composition of levitated particles held in an electrodynamic balance using mass spectrometry (MS). These methods range from electrospray-based paper spray (PS) ionization, plasma discharge ionization, and direct analysis in real time (DART) ionization, with each showing advantages and disadvantages. Our recent work demonstrated that PS ionization could yield accurate data for the chemical evolution of mixed component particles undergoing evaporation. However, measurements were performed using an internal standard to account for and correct the inherent variability in the PS ionization source. Here, we explore a new electrospray-based method coupled to particle levitation – the Open Port Sampling Interface (OPSI), which provides many advantages over the PS method, with few disadvantages. In this application note we report experiments in which micron-sized particles, containing analytes such as citric acid, maleic acid and tetraethylene glycol, were levitated and optically probed to determine their size and mass. Subsequent transfer of individual levitated particles into the OPSI allowed for the ionization and mass spectrometry analysis of these particles. We discuss the stability and reproducibility of MS measurements, demonstrate effective quantitation in both positive and negative mode, and

determine the sensitivity of OPSI to a range of analyte mass present in levitated particles. Importantly, we show stability of the OPSI over >6 hours without the need for normalizing signal variations with an internal standard in the sample, demonstrating robust application of OPSI to measurements over extended periods of time.

4.2. Introduction

Single particle levitation experiments have become established methods in aerosol science for characterizing the physical and chemical properties of levitated micron-sized particles.[1–5] Recent developments in coupling single particle levitation with high performance mass spectrometry have produced several methods for transferring and ionizing samples.[3,6–8] Paper spray ionization,[9–11] a heater vaporization platform combined with a corona discharge,[12,13] and a thermal desorption glow discharge ionization method[6] have all been applied to probe the composition of levitated particles. The former is an electrospray method that requires solubilization of the sample in the electrospray ionization (ESI) solvent, while the latter methods require the samples to be vaporized. Although shown to be effective in their respective use cases, these methods suffer limitations, such as limited sensitivity and variability in signal intensity compared to commercially developed ESI sources. Accordingly, many reported measurements have required internal standards to account for such instability and variations in signal intensity over time, which can limit the scope of measurements.

The work presented here demonstrates the analytical performance of a single particle levitation technique, the linear quadrupole electrodynamic balance (LQ-EDB), coupled

with conventional electrospray ionization – mass spectrometry (ESI-MS) via an open port sampling interface (OPSI).[14] An OPSI allows for rapid, high throughput sampling of μL, nL and pL droplets,[15–17] nanometer-sized aerosol particles,[18] single cells,[19] and analytes found on solid surfaces.[20] This OPSI probe allows the LQ-EDB and ESI-MS configurations to be coupled together with minimal instrument modifications. Compared to other single particle ionization methods, OPSI can offer advantages in terms of better sensitivity and reproducibility with minimal variations in integrated peak areas even without the use of internal or external standards. In this work, we briefly review the LQ-EDB platform and describe the application of OPSI in sampling levitated particles via MS for their chemical characterization. We demonstrate effective quantitation in both positive and negative mode for oxygenated samples, stability over extended periods of time, and describe the advantages over other single particle ionization methods.

4.3. Experimental Section

4.3.1. Chemicals and Sample Preparation

Aqueous solutions of citric acid (CA), maleic acid (MA) and tetraethylene glycol (TEG) prepared at various concentrations were used to produce droplets from a microdroplet dispenser (Microfab MJ-ABP-01, 30 μm orifice). The open port sampling interface (OPSI), a co-axial capillary design, collects individual particles ejected out of the LQ-EDB and transfers them to the heated electrospray ionization (H-ESI II) probe of a Q-Exactive Focus Orbitrap mass spectrometer (MS). The OPSI was supplied with a solvent mixture of pure methanol with trans-3-(3-Pyridyl)acrylic acid (meth + TPAA) as an external standard and

connected to an unmodified HESI-II probe (Thermo Fisher) via 254 μm i.d. PEEK tubing. Nitrogen (Technical Grade, 99.97% pure) was used as a nebulizer gas for ionization of sample analytes. The solvent flow rate was varied based on the nebulizer gas pressure and a solvent flow of 50 to 70 μL/min was typically achieved.

4.3.2. Technique Design and Analytical Procedure

The LQ-EDB setup was used to trap and levitate a stack of 5 to 10 micrometer-sized particles, with known initial composition, under controlled environmental conditions. Details on the operation of the LQ-EDB have been previously discussed.[21–24] A nitrogen gas flow of controlled relative humidity (RH) was introduced into LQ-EDB (flow rate of 200 sccm) to control the environmental conditions. The lowermost particle was probed using Mie resonance spectroscopy to determine the size and refractive index (RI) to within 5 nm and 0.005, respectively.[4,25]

Measurements of the composition of the particles were carried out by ejecting them individually from the LQ-EDB to the OPSI. The OPSI acts as an effective sampling platform, consisting of a co-axial capillary design (304 stainless-steel outer tubing, 1.75 mm i.d. × 3.18 mm o.d., and PEEK inner capillary (IDEX PEEK Blue, 254 μm (0.01”) i.d. × 1/32” o.d. × ~25 cm long) and continuously fed with solvent delivered through the annulus region of the tubing by a syringe pump (Chemyx Inc., Fusion 100T model). The solvent creates a reservoir of approximately 1 μL at the top of the vertical capillary as the inner tube is recessed by approximately 0.5 mm, and excess solvent not aspirated into the capillary overflows due to the tapered configuration of outer tubing. The solvent flow rate

and nebulizer gas pressure were balanced to minimize overflow. A schematic illustration of the LQ-EDB-OPSI-MS is shown in **Figure 1**.

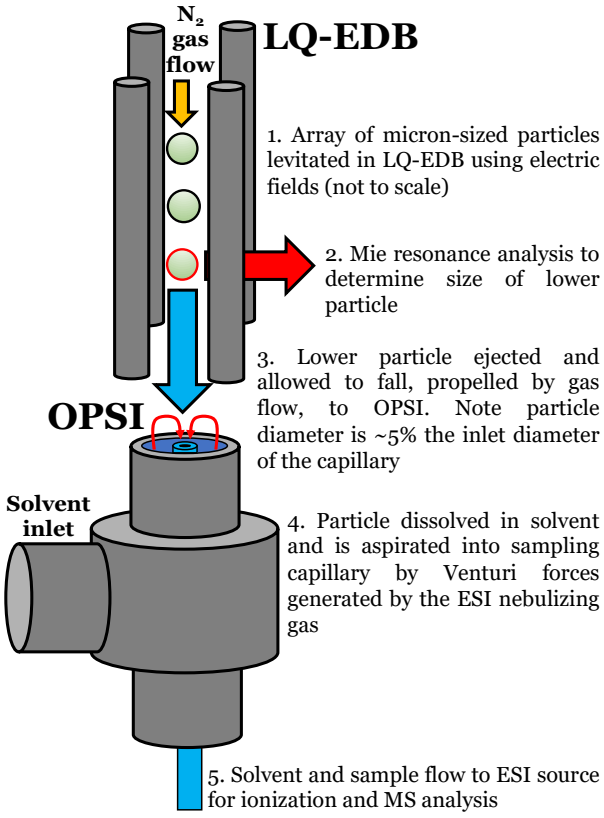

Figure 1: Schematic configuration of the linear quadrupole electrodynamic balance (LQ-EDB) coupled with the open port sampling interface (OPSI) for the compositional analysis using mass spectrometry. The figure is not to scale and is for illustrative purposes only.

The OPSI operational mode was a combination of the "balanced" flow mode and "convex spill over" flow mode that prevents aspiration of air into the solvent flow, which causes instabilities in the ESI function.[14] The OPSI was mounted approx. 2 mm below the LQ-EDB lower outlet and particles were allowed to fall from the trap, propelled by a gas flow, into the reservoir region of the OPSI. The speed of the particles on impact with the OPSI

is estimated to be on the order of 1 – 10 cm / s, based on the volume flow rate of gas (0.2 L / min) and the outlet diameter. Subsequently, particles dissolved in the solvent were transferred by aspiration through the inner capillary of the OPSI into the H-ESI II probe of the MS. This was then followed by similar measurements on subsequent particles in the levitated stack.

4.4. Results and Discussion

4.4.1. Experimental Conditions and Operation Parameters

The MS compositional measurements of levitated microparticles in the size range of 1.5 to 9 μm with various compositions are reported here. The vertical position of the OPSI was chosen to achieve reliable particle capture, and the position of the internal capillary on the sampling end of OPSI and the solvent choice and flow rates were selected based on previous studies.[14] Methanol was determined to be an effective solvent when compared to other solvent options, such as ethanol, chloroform, and water, due to the low viscosity and effective dissolution of analytes. A standard, TPAA, was added to the methanol at very low concentration (approx. 0.2 mg/L) to ensure ESI stability and check for any variations in signal intensity over time. The nebulizing gas pressure supplied to the ESI controls the pressure decrease at the outlet, due to the Venturi effect, which in turn determines the flow rate of solvent. A nebulizing gas flow setting of 30 (with a supply pressure of 80 PSI, leading to a gas flow of up to 6 L min^{-1}) produced solvent flow rates of 50 to 70 μL/min that were stable and reproducible. The time from sample introduction into the 1 μL solvent reservoir at the open-port to detection in the mass spectrometer was approximately 8 s.

According to a previously reported fluid dynamics analysis, the sample dissolves and becomes diluted and stretched out in the inner sampling capillary due to the velocity distribution of the solvent.[26] This leads to a broad detection peak in the mass spectrometer, which for the settings used here was approximately 20 s wide. The ESI was maintained at a spray voltage of 3.00 kV with an inlet capillary temperature of 320 ℃. A comprehensive optimization of all OPSI and ESI parameters was not performed in this work. Duplicate or triplicate measurements of all reported experiments were performed, and representative data sets are shown with error bars to reflect the variation across datasets.

4.4.2. Establishing the Analytical Performance of LQ-EDB-OPSI-MS

4.4.2.1. Signal Stability and Reproducibility

Repeated sampling of individually levitated particles over several hours allows the particle-to-particle variability and long-term stability to be determined. The real-time chronogram of TPAA as an external standard is considered as a tool for visualization of any inconsistencies in the ionization spray of ESI probe which could lead to inconsistent peak shapes and peak areas. For reproducibility, mass spectral signal intensity and related peak areas were compared for similar sized non-volatile particles, namely CA. Reproducibility was observed within a few percent of standard deviation (around 10% of the mean) between individual droplets, with no systematic trend. This level of reproducibility was observed in most experiments, and variations may be attributed to random error sources such as slight variations in solvent flow mode at the reservoir region of OPSI and changes in ESI spray performance due to changes in nebulizing gas pressure

during a measurement. **Figure 2A** shows a chronogram of several droplet deposition events with each peak arising from a single particle generated from a starting solution of 5 g/L CA ejected out of LQ-EDB, sampled by OPSI, and analyzed by ESI-MS. These particles had a radial size of around 5200 nm at 50% RH as determined by Mie resonance spectroscopy.

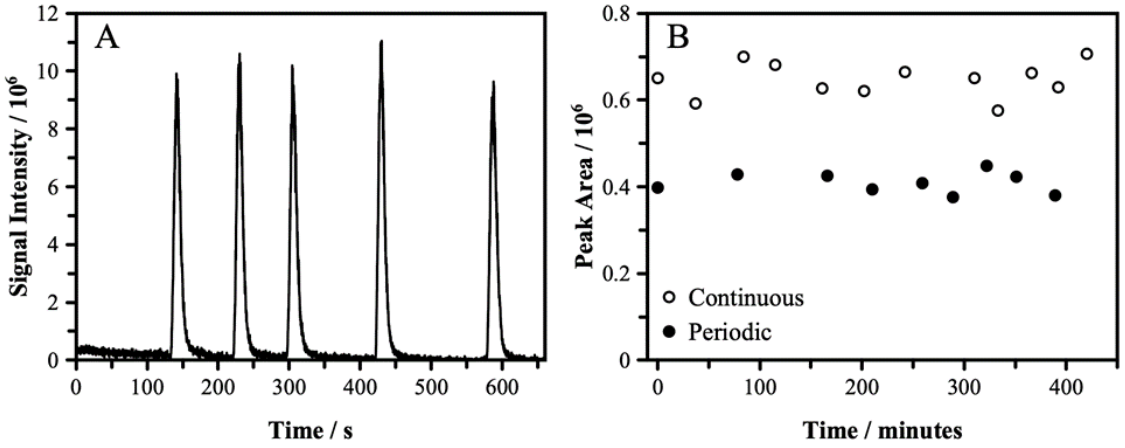

Figure 2: (A) A sequence of five citric acid (CA) particles, with each peak arising from an ejected particle sampled by OPSI probe and delivered to conventional ESI-MS for its compositional analysis. At a solvent flow rate of 50 μL / min, and with signal persisting for ~20 s, the dilution factor of a 5 μm particle is estimated to be on the order of 1 in 10^7. Individual mass spectra can be seen in *Figure 3*. **(B)** Integrated peak areas for the molecular ion for individual CA particles measured over 6 hours. Open circle points represent individual CA particles sampled by OPSI using continuous solvent flow throughout the experiment, whereas solid circle points represent individual CA particles sampled using periodic (on/off) flow of solvent.

To test the feasibility of performing measurements over extended time periods without the need to consume large amounts of gas or solvent, particles were sampled with two different solvent supply configurations over 6 hours: continuous solvent flow and periodic (on/off) solvent flow. In continuous flow, the OPSI and ESI were continuously running for

the entire experiment, while in the periodic configuration, the OPSI and ESI were only enabled for approximately 5 minutes ahead of sampling each particle. **Figure 2B** compares these results and demonstrates that both configurations lead to reproducible and consistent data over a 6-hour period. It should be noted, however, that measurements show differences in the peak area between continuous and periodic sampling that arises due to the difference in the size distributions of the particles. Particles analyzed during continuous sampling were larger, with a mean size of around 4250 nm, as compared to the particles analyzed during periodic sampling with a mean size of around 3800 nm. In addition, these two measurements were performed on different days which may also contribute to some variability in the signal. These day-to-day variations may be due to differences in nebulizing gas pressure, which depends on the supplied pressure, and can change solvent flow and performance of the ESI.

The compositional data was acquired continuously by the mass spectrometer in the scan range of 100-500 m/z, with an ion inject time of up to 100 ms to achieve ACG targets of 10^6. The MS was operated at a resolution of 35,000 and no ion fragmentation was performed as the focus of the reported measurements was on quantitation of known intact molecular species. Individual mass spectra of citric acid (CA), maleic acid (MA) and tetraethylene glycol (TEG) particles sampled by OPSI probe and delivered to conventional ESI-MS for their compositional analysis can be seen in **Figure 3**.

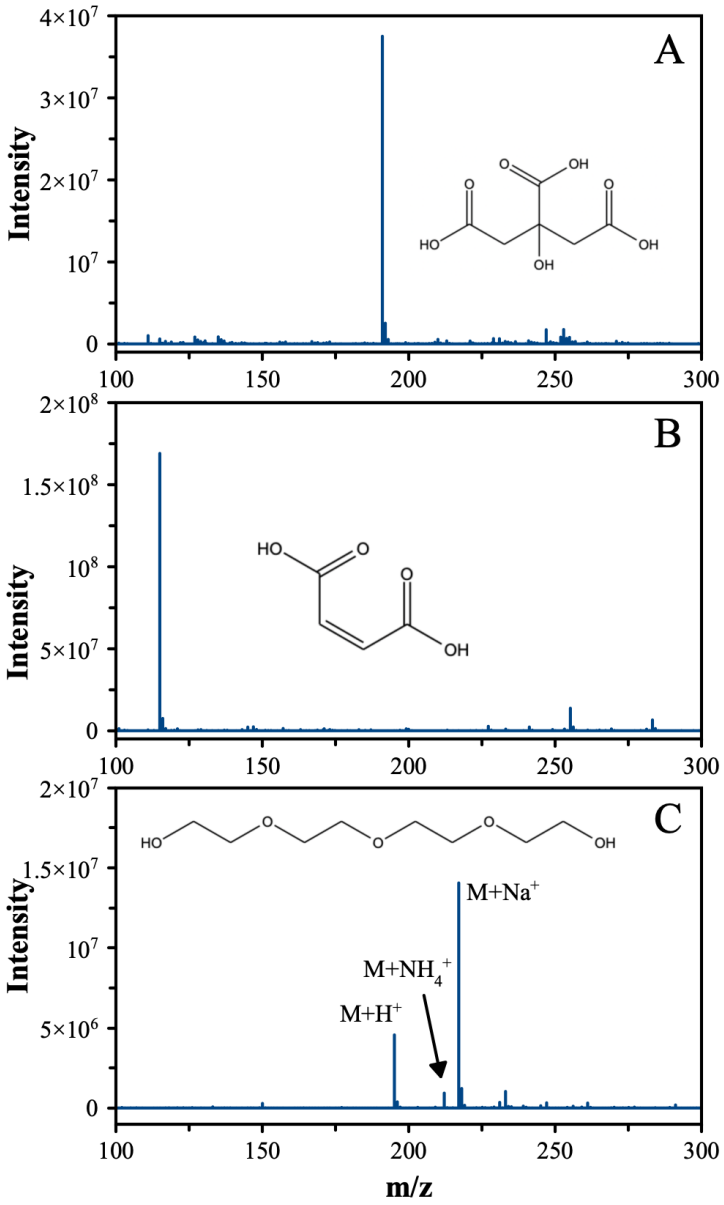

Figure 3: Background corrected mass spectra for a single particle of citric acid (A), maleic acid (B) and tetraethylene glycol (C) sampled by OPSI-MS. The mass spectra correspond to the peak intensity from a single particle of respective sample. Figure A and B are the mass spectra obtained in negative ionization mode of the mass spectrometry while Figure C is the mass spectrum obtained in positive ionization mode of the mass spectrometry. Note that the y-axis has a different range in each spectrum which is based on the abundance of the individual sample particle.

4.4.2.2. Quantitation

Evaporation measurements for particles generated from a 7 g/L TEG starting solution under dry conditions (0% RH) were performed. Due to its high vapor pressure, TEG evaporates on timescales on the order of 1 hour, providing a test of the quantitative capabilities. **Figure 4** shows the compositional evolution in terms of changing relative mass due to the evaporation of TEG from the levitated stack of particles under dry conditions.

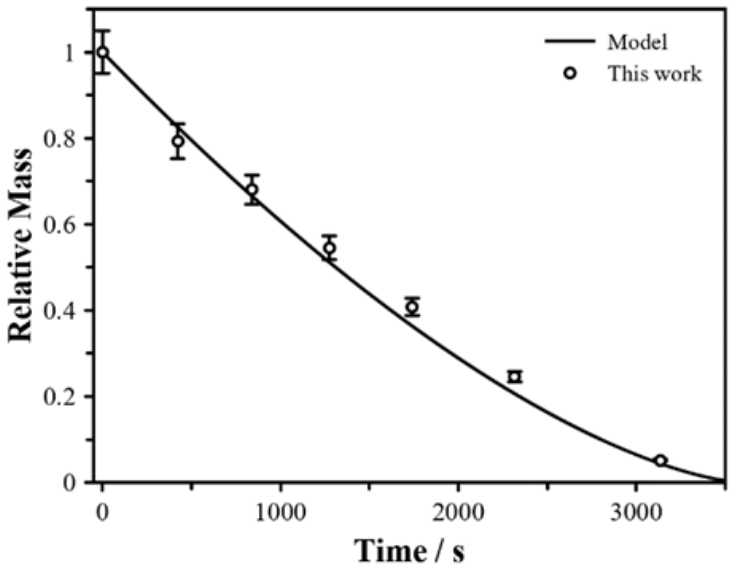

Figure 4: Compositional evolution in terms of relative mass for consecutive tetraethylene glycol (TEG) particles evaporating under dry conditions (0% RH). The compositional analysis was carried out by the mass spectrometer. The solid line shows the data output from model simulation while the open circle points correspond to the experimental observation and show the relative analyte mass calculated from the integrated peak intensities, as described in the text. Error bars indicate a ±5% uncertainty.

The relative mass is defined as the integrated signal intensity of each particle ratioed against the integrated signal intensity for the first particle sampled. The corresponding size

evolution of these levitated particles is shown in **Figure 5**. TEG evaporation follows the expected trend for the steady-state evaporation of a single component, which may be described in terms of the particle size and the vapor pressure of the evaporating species.

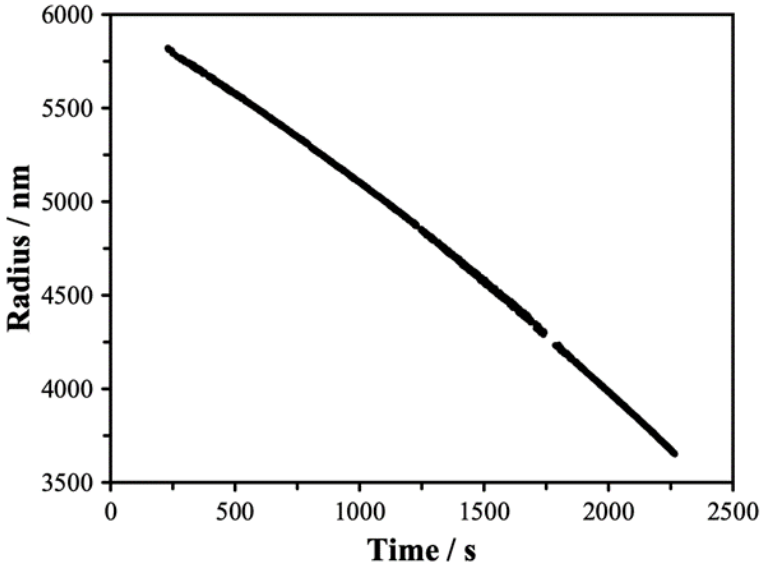

Figure 5: Size evolution of an evaporating tetraethylene glycol particle in dry conditions as measured by the Mie resonance spectrometer. Plot is made up of 8 similar sized particles that were introduced into the trap at t = 0 s. Individual particles were ejected and sampled by OPSI-MS at times indicated in Figure 3.

The measurements were compared against evaporation model predictions using a gas-phase diffusion limited mass flux framework and show close agreement. The details related to the evaporation model are described in our previous publication.[11] Further measurements for TEG evaporation were carried out at different RH conditions, shown in **Figure 6**, with a clear slowing of the evaporation rate at high RH due to the reduced chemical activity of the evaporating species.

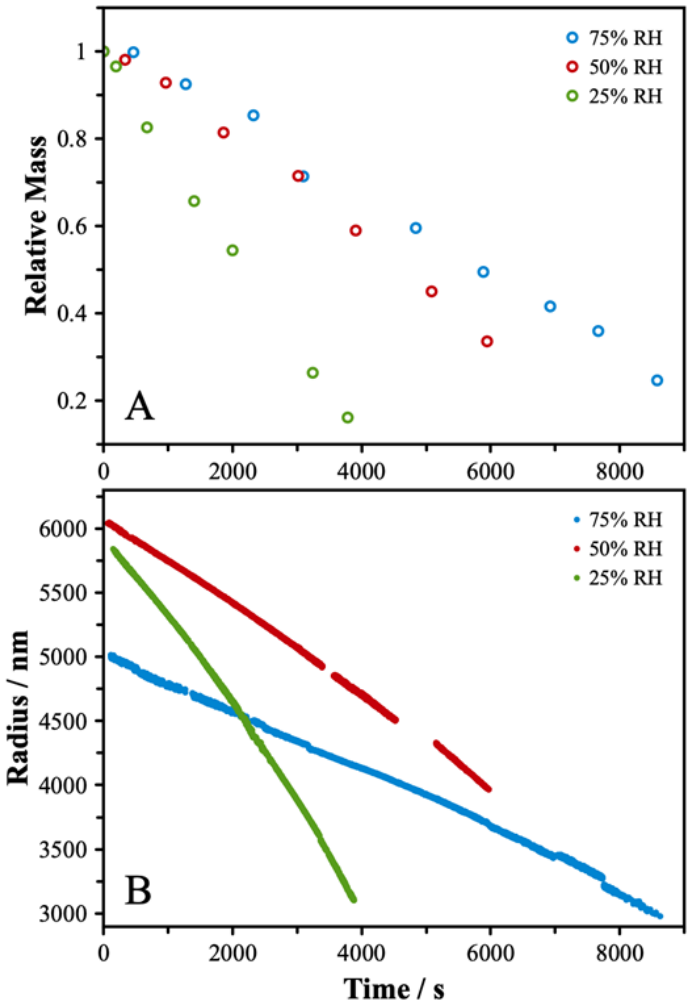

Figure 6: (A) Compositional evolution of evaporating tetraethylene glycol (TEG) particles evaporating in a range of RH conditions. The compositional analysis was carried out by the mass spectrometer. **(B)** Size evolution of evaporating tetraethylene glycol particles evaporating in a range of RH conditions as measured by the Mie resonance spectrometer.

To further explore the application of OPSI as a sampling probe for the quantitation of analyte in particles in both negative and positive ionization mode of MS, we show the integrated signal as a function of analyte mass in **Figure 7**.

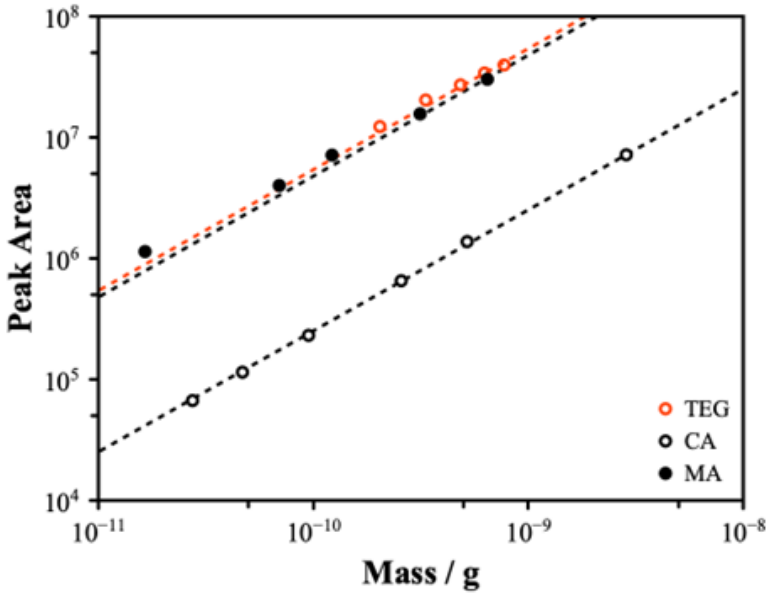

Figure 7: Integrated peak areas for CA, MA, and TEG single particles with the mass derived from the size of the particles as measured using Mie resonance spectroscopy. The dashed lines indicate linear fits constrained to a zero y-intercept.

We observe high signal (relative to the background) for CA, MA, and TEG particles with analyte masses approaching 10 pg and a clear linear dependence of their respective peak areas on the mass of the analyte. Representative mass spectra can be found in the **Figure 8** which shows artifacts in the background due to standard. The full mass range explored for these chemical species establish linearity over 1-2 orders of magnitude, which is promising for the study of evolving analyte compositions in levitated particles undergoing-physicochemical transformations.

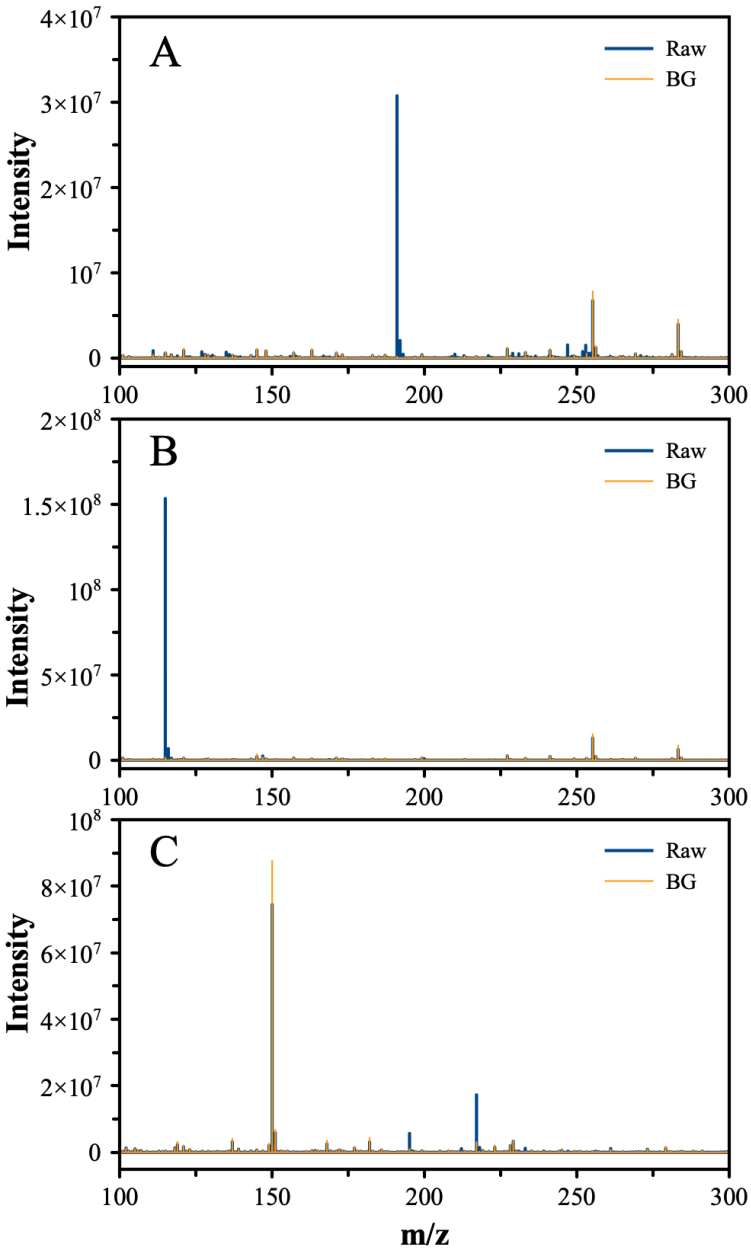

Figure 8: Background and raw mass spectra for a single particle of citric acid (A), maleic acid (B) and tetraethylene glycol (C) sampled by OPSI-MS. Large background peaks in (C) arise from internal standard added to the ESI solution. The mass spectra correspond to the peak intensity from a single particle of respective sample. Figure A and B are the mass spectra obtained in negative ionization mode of the mass spectrometry while Figure C is the mass spectrum obtained in positive ionization mode of the mass spectrometry. Note that the y-axis has a different range in each spectrum which is based on the abundance of the individual sample particle.

4.5. Summary and Conclusions

Our results demonstrate effective and accurate quantitation of levitated microparticles using the LQ-EDB-OPSI-MS approach. The open port sampling interface (OPSI) is a robust setup for sampling of particles ejected out of LQ-EDB into the mass spectrometer to study their chemical composition. It allows for fully reliable particle capture from LQ-EDB with appropriate positioning of the OPSI inlet underneath the outlet of the LQ-EDB, and well-controlled dilution of the entrained analytes due to constant supply of solvent. The ejected particles are rapidly solubilized in solvent and do not directly interact with any component of the OPSI. This contrasts with other single particle sampling methods, such as paper spray, in which the particles are deposited on a solid substrate ahead of either dissolution or vaporization. This reduces the risk of sampling artefacts in the compositional analysis. Furthermore, due to the advanced technology available in commercial ionization sources, the OPSI-MS method is more stable and reliable than the custom interfaces previously used (although it should be made clear that the OPSI interface itself is constructed on-site). Unlike in PS, for example, the ionization step in our reported OPSI-MS method is fully enclosed within the commercial HESI-II probe, improving stability and safety and allowing for optimization in conditions, such as temperature, that are not possible with the open nature of PS.

Compared to our previous work using paper spray ionization to sample levitated particles,[9,11] an additional advantage of the OPSI method is that an internal standard is not required to normalize mass spectral intensity data. Indeed, the reported evaporation trend for pure tetraethylene glycol was derived from the raw mass spectral signal, in contrast to

the normalized data we reported previously.[11] These data demonstrate that the OPSI-MS interface is stable and reliable, allowing measurements to be performed on samples in the absence of added standard compounds. This expands the scope of possible measurements and will allow chemical changes in levitated particles to be explored without perturbation of the system through direct or indirect reactions with a standard. An external standard (TPAA) in the solvent was used as a means of verifying ESI stability, but it was not required for any of the compositional analysis steps described herein.

Overall, the coupling of OPSI-MS with LQ-EDB allows for a more robust, reliable, and safer chemical characterization platform than our previously reported paper spray ionization method and yields similar or better results in terms of stability and quantitation. Importantly, long term stability is observed without the need for an internal standard, permitting a broader range of measurements that require extended time periods, such as those exploring heterogeneous reactions in levitated particles.

4.6. References

(1) Davis, E. J. A History of Single Aerosol Particle Levitation. *Aerosol Sci Technol* **1997**, *26* (3), 212–254. https://doi.org/10.1080/02786829708965426.

(2) Krieger, U. K.; Marcolli, C.; Reid, J. P. Exploring the Complexity of Aerosol Particle Properties and Processes Using Single Particle Techniques. *Chem Soc Rev* **2012**, *41* (19), 6631–6662. https://doi.org/10.1039/c2cs35082c.

(3) Birdsall, A. W.; Krieger, U. K.; Keutsch, F. N. Electrodynamic Balance–Mass Spectrometry of Single Particles as a New Platform for Atmospheric Chemistry Research. *Atmospheric Meas. Tech.* **2018**, *11* (1), 33–47. https://doi.org/10.5194/amt-11-33-2018.

(4) Bain, A. Determining the Size and Refractive Index of Single Aerosol Particles Using Angular Light Scattering and Mie Resonances. **2018**, 10. https://doi.org/10.1016/j.jqsrt.2018.09.026.

(5) Bzdek, B. R.; Pennington, M. R.; Johnston, M. V. Single Particle Chemical Analysis of Ambient Ultrafine Aerosol: A Review. *J. Aerosol Sci.* **2012**, *52*, 109–120. https://doi.org/10.1016/j.jaerosci.2012.05.001.

(6) Willis, M. D.; Rovelli, G.; Wilson, K. R. Combining Mass Spectrometry of Picoliter Samples with a Multicompartment Electrodynamic Trap for Probing the Chemistry of Droplet Arrays. *Anal. Chem.* **2020**. https://doi.org/10.1021/acs.analchem.0c02343.

(7) Kaur Kohli, R.; Davies, J. F. Paper Spray Mass Spectrometry for the Analysis of Picoliter Droplets. *The Analyst* **2020**, *145* (7), 2639–2648. https://doi.org/10.1039/C9AN02534K.

(8) Warschat, C.; Stindt, A.; Panne, U.; Riedel, J. Mass Spectrometry of Levitated Droplets by Thermally Unconfined Infrared-Laser Desorption. *Anal. Chem.* **2015**, *87* (16), 8323–8327. https://doi.org/10.1021/acs.analchem.5b01495.

(9) Kaur Kohli, R.; Davies, J. F. Paper Spray Mass Spectrometry for the Analysis of Picoliter Droplets. *Analyst* **2020**, *145*, 2639–2648. https://doi.org/10.1039/C9AN02534K.

(10) Jacobs, M. I.; Davies, J. F.; Lee, L.; Davis, R. D.; Houle, F.; Wilson, K. R. Exploring Chemistry in Microcompartments Using Guided Droplet Collisions in a Branched Quadrupole Trap Coupled to a Single Droplet, Paper Spray Mass Spectrometer. *Anal. Chem.* **2017**, *89* (22), 12511–12519. https://doi.org/10.1021/acs.analchem.7b03704.

(11) Kaur Kohli, R.; Davies, J. F. Measuring the Chemical Evolution of Levitated Particles: A Study on the Evaporation of Multicomponent Organic Aerosol. *Anal. Chem.* **2021**, *93* (36), 12472–12479. https://doi.org/10.1021/acs.analchem.1c02890.

(12) Birdsall, A. W.; Hensley, J. C.; Kotowitz, P. S.; Huisman, A. J.; Keutsch, F. N. Single-Particle Experiments Measuring Humidity and Inorganic Salt Effects on Gas-Particle Partitioning of Butenedial. *Atmospheric Chem. Phys. Discuss.* **2019**, 1–26. https://doi.org/10.5194/acp-2019-423.

(13) Birdsall, A. W.; Krieger, U. K.; Keutsch, F. N. Electrodynamic Balance–Mass Spectrometry of Single Particles as a New Platform for Atmospheric Chemistry Research. *Atmospheric Meas. Tech.* **2018**, *115194* (1), 33–47. https://doi.org/10.5194/amt-11-33-2018.

(14) Van Berkel, G. J.; Kertesz, V. An Open Port Sampling Interface for Liquid Introduction Atmospheric Pressure Ionization Mass Spectrometry. *Rapid Commun. Mass Spectrom.* **2015**, *29* (19), 1749–1756. https://doi.org/10.1002/rcm.7274.

(15) Van Berkel, G. J.; Kertesz, V.; Orcutt, M.; Bentley, A.; Glick, J.; Flarakos, J. Combined Falling Drop/Open Port Sampling Interface System for Automated Flow Injection Mass Spectrometry. *Anal. Chem.* **2017**, *89* (22), 12578–12586. https://doi.org/10.1021/acs.analchem.7b03899.

(16) Liu, C.; Van Berkel, G. J.; Cox, D. M.; Covey, T. R. Operational Modes and Speed Considerations of an Acoustic Droplet Dispenser for Mass Spectrometry. *Anal. Chem.* **2020**, *92* (24), 15818–15826. https://doi.org/10.1021/acs.analchem.0c02999.

(17) Van Berkel, G. J.; Kertesz, V.; Boeltz, H. Immediate Drop on Demand Technology (I-DOT) Coupled with Mass Spectrometry via an Open Port Sampling Interface. *Bioanalysis* **2017**, *9* (21), 1667–1679. https://doi.org/10.4155/bio-2017-0104.

(18) Swanson, K. D.; Worth, A. L.; Glish, G. L. Use of an Open Port Sampling Interface Coupled to Electrospray Ionization for the On-Line Analysis of Organic Aerosol Particles. *J. Am. Soc. Mass Spectrom.* **2018**, *29* (2), 297–303. https://doi.org/10.1007/s13361-017-1776-y.

(19) Cahill, J. F.; Riba, J.; Kertesz, V. Rapid, Untargeted Chemical Profiling of Single Cells in Their Native Environment. *Anal. Chem.* **2019**, *91* (9), 6118–6126. https://doi.org/10.1021/acs.analchem.9b00680.

(20) Walton, C. L.; Kertesz, V.; Cahill, J. F. Design and Evaluation of a Tethered, Open Port Sampling Interface for Liquid Extraction-Mass Spectrometry Chemical Analysis. *J. Am. Soc. Mass Spectrom.* **2021**, *32* (1), 198–205. https://doi.org/10.1021/jasms.0c00268.

(21) Price, C. L.; Bain, A.; Wallace, B. J.; Preston, T. C.; Davies, J. F. Simultaneous Retrieval of the Size and Refractive Index of Suspended Droplets in a Linear Quadrupole Electrodynamic Balance. *J. Phys. Chem. A* **2020**, *124* (9), 1811–1820. https://doi.org/10.1021/acs.jpca.9b10748.

(22) Davies, J. F. Mass, Charge, and Radius of Droplets in a Linear Quadrupole Electrodynamic Balance. *Aerosol Sci. Technol.* **2019**, *53*, 309–320. https://doi.org/10.1080/02786826.2018.1559921.

(23) Hart, M. B.; Sivaprakasam, V.; Eversole, J. D.; Johnson, L. J.; Czege, J. Optical Measurements from Single Levitated Particles Using a Linear Electrodynamic Quadrupole Trap. *Appl. Opt.* **2015**, *54* (31), F174. https://doi.org/10.1364/AO.54.00F174.

(24) Berkemeier, T.; Mishra, A.; Mattei, C.; Huisman, A. J.; Krieger, U. K.; Pöschl, U. Ozonolysis of Oleic Acid Aerosol Revisited: Multiphase Chemical Kinetics and Reaction Mechanisms. *ACS Earth Space Chem.* **2021**, 11. https://doi.org/10.1021/acsearthspacechem.1c00232.

(25) Preston, T. C.; Reid, J. P. Accurate and Efficient Determination of the Radius, Refractive Index, and Dispersion of Weakly Absorbing Spherical Particle Using Whispering Gallery Modes. *J. Opt. Soc. Am. B* **2013**, *30* (8), 2113–2122. https://doi.org/10.1364/josab.30.002113.

(26) Liu, C.; Van Berkel, G. J.; Kovarik, P.; Perot, J. B.; Inguva, V.; Covey, T. R. Fluid Dynamics of the Open Port Interface for High-Speed Nanoliter Volume Sampling Mass Spectrometry. *Anal. Chem.* **2021**, *93* (24), 8559–8567. https://doi.org/10.1021/acs.analchem.1c01312.

CHAPTER 5

Measuring the Chemical Evolution of Levitated Particles: A Study on the Evaporation of Multicomponent Organic Aerosol

5.1. Abstract

Single particle levitation methods provide an effective platform for probing the physical properties of atmospheric aerosol via micrometer sized particles. Until recently, chemical composition measurements on levitated particles were limited to spectroscopy, yielding only basic chemical information. Here, we describe, benchmark, and discuss the applications of an approach for probing the physical properties and chemical composition of single levitated particles using high resolution mass spectrometry. Using a linear quadrupole electrodynamic balance (LQ-EDB) coupled to paper spray mass spectrometry (PS-MS), we report accurate measurements of the evolving size within 5 nm (using broadband light scattering) and relative composition (using mass spectrometry) of evaporating multicomponent levitated particles in real-time. Measurements of the evaporation dynamics of semi-volatile organic particles containing a range of n-ethylene glycols (n = 3, 4 and 6) in various binary and ternary mixtures were made under dry conditions and compared with predictions from a gas-phase diffusion evaporation model. Under assumptions of ideal mixing, excellent agreement for both size and composition evolution between measurements and model were obtained for these mixtures. At increased relative humidity (RH), the presence of water in particles causes the assumption of ideality

to break down, and the evaporative mass flux becomes a function of the mole fraction and activity coefficient. Through compositionally-resolved evaporation measurements and thermodynamic models, we characterize the activity of organic components in multicomponent particles. Our results demonstrate that the LQ-EDB-MS platform can identify time-dependent size and compositional changes with high precision and reproducibility, yielding an effective methodology for future studies on chemical aging and gas-particle partitioning in suspended particles.

5.2. Introduction

Atmospheric aerosol strongly influence climate, air quality and human health.[1–4] The extent of their atmospheric and environmental effects depends on the physical, chemical, and optical properties of the constituent aerosol particles.[5] Particles exhibit a wide range of characteristics that depend on composition, which spans a broad range of organic and inorganic components,[6] and local environmental conditions, such as humidity and temperature.[5,7] Under the oxidizing conditions of the atmosphere, the chemical composition of aerosol particles is continuously evolving, due to evaporation and condensation of semi-volatile species, photochemical reactions involving sunlight, and heterogeneous reactions with ozone and other reactive gas-phase species.[6,8–10] Thus, composition-dependent properties of aerosol particles, such as their hygroscopicity, phase state, vapor pressure, and refractive index, will vary over time.[11–13] Characterizing and understanding the evolution of these properties is crucial to predict the role and impacts of aerosol in the atmosphere.[14–16]

Laboratory-based techniques have long been employed to explore the formation and evolving composition of aerosol under atmospheric conditions. Environmental chambers, tank reactors and flow-tubes have been effectively coupled with various advanced analytical methods to characterize size distributions and chemical composition in aerosol particle ensembles.[17–21] Mass spectrometry (MS) methods are most commonly adopted to yield composition data using a variety of ionization methods and MS configurations.[22–25] While electron impact ionization is commonly used in aerosol mass spectrometry,[26–29] atmospheric pressure ionization methods using electrospray and plasma discharge ionization are becoming more common, providing increased molecular detail.[30–33] These ensemble methods can provide detailed insights into reaction pathways and kinetics and allow for improved predictions of aerosol composition in climate models.[34–38] Characterizing the physical properties of aerosol can be more challenging, requiring specialized experimental platforms to probe volatility, hygroscopicity, optical properties etc.[39–41] Other physical properties, such as particle viscosity, surface tension, hygroscopicity, and phase morphology, cannot be easily probed using the ensemble methods.

Alternative methods to characterize the physical properties of aerosol under controlled laboratory conditions have incorporated single-particle techniques, such as acoustic levitation, optical trapping and the electrodynamic balance.[42–46] Unlike ensemble measurements, single-particle techniques reduce the complexity of the aerosol to a single particle, and allow direct measurements of the properties of individual levitated particles using light scattering methods.[47–49] While levitated particles are generally larger than those

found directly in the atmosphere, many detailed insights on the properties and processes of atmospheric aerosol can be derived from measurements on micron-sized particles, such as hygroscopicity, pH, morphology, phase transitions, viscosity, surface tension, vapor pressures, chemical activity, and optical properties.[50–56] Several studies have also characterized reactive transformations of levitated particles, typically using Raman spectroscopy to probe changes in the abundance of certain functional groups.[57–59] However, due to a lack of suitable chemical analysis methods for molecular identification, single particle methods are often limited to characterizing simplified model systems with known chemical compositions.

Recently, several studies have reported combined single particle mass spectrometry approaches, with Jacobs et al.[60] and Willis et al.[61] describing the use of paper spray (PS) ionization and Birdsall et al.[62,63] discussing a plasma ionization method. These combined approaches allow the physical characterization methods developed in single particle levitation experiments to correlate with chemical composition, allowing samples of arbitrary and evolving composition to be probed. Both Willis et al. [61] and Birdsall et al.[62] report chemical changes in single levitated particles, for the reaction of maleic acid with ozone and for the evaporation of multicomponent organic droplets, respectively. These studies show the use of single particle MS to explore the evolving composition of levitated particles, but challenges remain in obtaining and validating accurate composition data for chemically evolving systems.

In our earlier work, we characterized the quantitative and qualitative nature of PS for direct sampling of picoliter droplets, showing that effective quantitation could be achieved.[64] Here, we demonstrate that similar levels of quantitative accuracy and precision can be achieved using PS to sample levitated particles undergoing chemical change. A linear quadrupole electrodynamic balance (LQ-EDB) was coupled with paper spray mass spectrometry (PS-MS) to probe the evaporation of low molecular weight n-ethylene glycols (3-EG and 4-EG) in single levitated aerosol particles. We report measurements on the evaporation of binary and ternary mixtures of glycols across varying compositions in particles under dry and humid (25, 50, 75% RH) conditions, in measurements analogous to those reported by Birdsall et al.[62] We additionally demonstrate the accuracy and precision of our composition measurements by comparison to the measured size evolution obtained using Mie resonance spectroscopy.[65] We also compare these results to predictions from an evaporation model and demonstrate that under assumptions of ideal mixing, our measured and predicted evaporation results agree within uncertainty. We go on to explore the influence of RH on the evaporation of multicomponent particles, using a combination of measured data and thermodynamic predictions to calculate the activity coefficients of n-EG molecules in aqueous solutions. These measurements exemplify the application of this method for probing volatility and vapor pressures of semi-volatile components in complex organic mixtures.

5.3. Experimental Section

5.3.1. Chemicals and Sample Preparation

Aqueous binary or ternary solutions of triethylene glycol (3-EG, Sigma-Aldrich, ≥99% purity) and tetraethylene glycol (4-EG, Sigma-Aldrich, 99% purity) with hexaethylene glycol (6-EG, Sigma-Aldrich, 97% purity) were prepared at known mass ratios and total aqueous concentrations in the range 10 – 15 g/L. The starting concentration only affects the size of the particle, and the aqueous concentration of the levitated particle is controlled by the environmental relative humidity (RH). Droplets with an initial diameter of approximately 50 μm were generated either individually or in burst mode using a microdroplet dispenser (Microfab MJ-ABP-01, 30 μm orifice) powered by an in-house constructed pulse generator using a 30 μs square pulse with up to 50 V peak voltage, controlled by a DAQ card and LabVIEW software.

Mass spectrometry measurements of particle composition were performed using a paper spray ionization source supplied with a 50% v/v mixture of methanol (Fisher Chemical, 0.2 micron filtered) and chloroform (Fisher Chemical, approx. 0.75% ethanol as preservative). This composition has been previously established to be effective for use in paper spray and we performed no further optimization of the solvent mix.[64] The paper spray ionization substrate was a triangular piece of chromatography paper (Whatman, 0.18 mm thickness).

5.3.2. Technique Setup and Analytical Procedure

5.3.2.1. Particle Levitation

A linear quadrupole electrodynamic balance (LQ-EDB) was used to levitate a stack of micrometer-sized mixed n-EG particles under controlled environmental conditions (**Figure 1**). The LQ-EDB consists of four stainless steel rods with an applied AC voltage in a quadrupole configuration (500 to 1000 V at 300 to 1000 Hz). Details of the fundamental principles of this technique have been previously discussed.[46,60,66] Multiple droplets of known initial composition were generated and given a charge due to the presence of an induction electrode at 200 to 500 V. The polarity of the droplets was adjusted as necessary to ensure deposition on the paper spray source, as described later. The small amount of charge, on the order of 10 fC, is not expected to influence the measured evaporation dynamics at the size range explored in this work.[46,67] An array of charged droplets was trapped and confined along the central axis of the LQ-EDB. A DC voltage was applied to a disc electrode to balance the net vertical forces acting upon the droplet stack (including their weight and drag forces). A nitrogen gas flow of controlled relative humidity (0 to 75% RH) was introduced into the chamber at 200 sccm to control the environmental conditions leading to the evaporation of excess water to equilibrate the particles with the RH. The temperature inside the chamber was maintained at the ambient laboratory conditions (~293 K). A 532 nm laser (Thorlabs CPS532, 5 mW) was used to illuminate the levitated particles for visual verification of the number and stability of the stack. The lowermost particle was additionally illuminated with a red LED (Thorlabs M660L4) and its light scattering was imaged by a CMOS camera (Thorlabs CS165MU). A PID feedback between particle

position and the DC voltage maintained the sample in a constant position. Scattered light from the lowermost particle was also sampled into a spectrometer (Ocean Insight HR4000+ with a 1200 mm^{-1} grating operating over 600 – 700 nm) for Mie resonance spectroscopy.

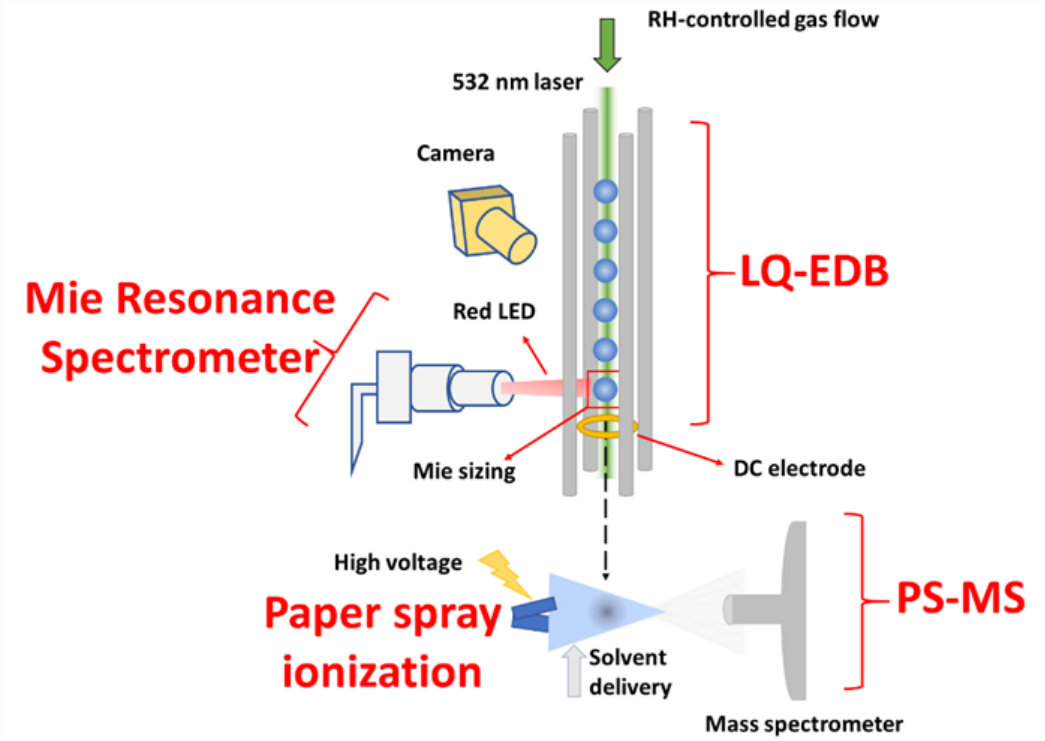

Figure 1: Schematic configuration of the linear quadrupole electrodynamic balance (LQ-EDB) coupled with paper-spray mass spectrometer (PS-MS) for studying physicochemical trans-formations on single levitated particles. A stack of 5 to 10 particles is levitated in the LQ-EDB, and the lowermost particle is probed using Mie resonance spectroscopy. The same particle is then ejected to the paper spray platform for sampling in the mass spectrometer for compositional analysis. This is followed by periodic measurements of subsequent particles in the levitated stack.

5.3.2.2. Mie Resonance Spectroscopy

A typical backscattered light spectrum produced by illumination of a particle with broadband red light is shown in **Figure 2**. For spherical particles, the spectra show sharp peaks corresponding to wavelengths that are internally resonant in the spherical cavity of

the particle. The wavelength position of these peaks is used to determine the size and refractive index using the algorithms of Preston and Reid, discussed in our earlier work.[65,68] Briefly, a library of peak positions is generated for size and RI combinations using Mie theory, and a least-squares minimization is performed to find the combination that best resembles the measured peaks. We additionally generate a full simulation of the spectrum using Mie theory in order to validate results and ensure the best-fit size and RI reproduce the features of the measured spectra. Using this approach, the size is determined with an accuracy of ±5 nm and the RI within an uncertainty of 0.001 to 0.005, depending on the number and type of resonance peaks in the spectrum.

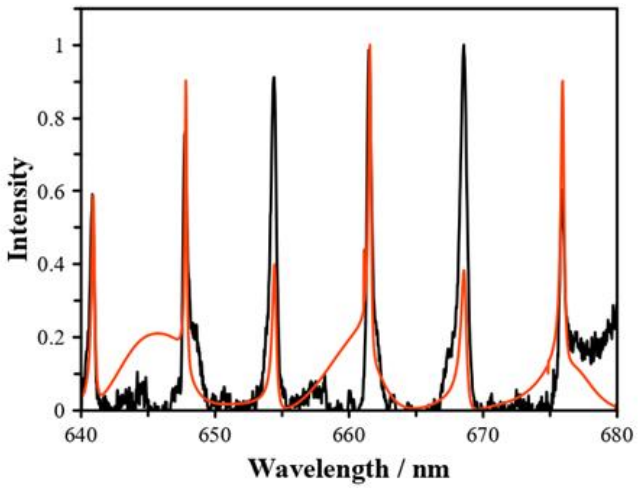

Figure 2: Mie resonance spectrum for a 3655 nm (radius) particle with an RI of 1.468 at a wavelength of 589 nm, as determined from the peak positions. The black line shows the intensity-normalized experimental spectrum, and the red line shows predicted spectrum using Mie theory.

5.3.2.3. Paper Spray Mass Spectrometry

Composition measurements were carried out using a Q Exactive Focus Orbitrap Mass Spectrometer (MS, ThermoFisher, USA) operated at a 35000 resolution and 100 ms

maximum ion injection time. Samples were ionized using an in-house built paper spray ionization source. A detailed description of this technique has been discussed in our earlier work and a brief summary is presented here.[64,69] A triangular piece of chromatography paper was attached to a stainless steel clip maintained at 3000 – 5000 V by a high voltage supply (Stanford Research Systems P350) while a methanol-chloroform solvent mixture was continuously supplied at 20 μL min^{-1} by a Chemyx Inc., Fusion 100T model syringe pump. The paper substrate was continuously saturated with solvent and an electrospray directed towards MS inlet was produced from its tip (**Figure 1**).

During experiments, individual levitated particles were ejected out of LQ-EDB by rapid manipulation of the DC balancing voltage, falling under gravity and being propelled by the nitrogen gas flow down the axis of the rods and out of the bottom of the chamber. The paper spray source was positioned just below the chamber and individual particles were collected onto the surface by direct impaction. Following impaction, individual particles were solubilized by solvent and eventually sprayed from the PS tip in an electrospray plume. Typical electrospray processes (evaporation and breakup of charged droplets) lead to ionization of sample and ions were transferred into the MS for chemical analysis. For this work, the MS was operated in positive polarity to detect adducts (H^+, Na^+, and NH_4^+) of the PEGs in the range of 100-400 m/z. **Figure 3** shows a typical mass chromatogram of the n-EGs, namely triethylene glycol (3-EG), tetraethylene glycol (4-EG) and hexaethylene glycol (6-EG).

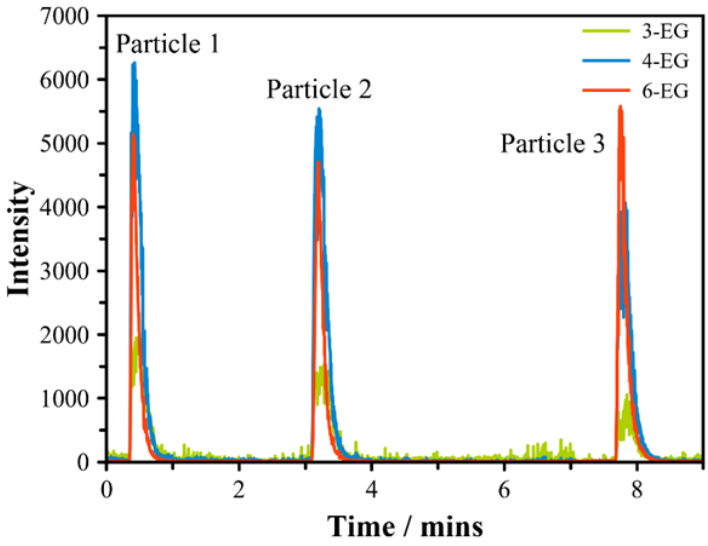

Figure 3: Mass chromatogram showing the $M+Na^+$ ion intensity for each n-EG compound (3-EG, 4-EG and 6-EG) in three evaporating levitated ternary particles ejected for PS-MS analysis at 0.5 mins, 3 mins, and 7.5 mins. The peak intensities corresponding to the 3-EG and 4-EG components decrease as a result of their evaporation from the particles while the peak intensity of 6-EG component increases due to its enhanced abundance with time.

Mass spectra were initially analyzed using Xcalibur 4.1 software (ThermoFisher Scientific) and chromatograms of the peaks were exported for further processing using data analysis software (MagicPlot Pro 2.8.2). The compositional evolution in evaporating particles is determined in terms of the mass ratio changes of the respective analytes (3- or 4-EG) with respect to the internal standard (6-EG). To achieve this, the mass spectra associated with each analyte in a particle were analyzed as follows in order to calculate the mass ratio of 3- or 4-EG relative to 6-EG. Corresponding mass spectra for the particle signal and background, associated with an individual particle consisting of 3-EG, 4-EG and 6-EG, are shown in **Figure 4**.

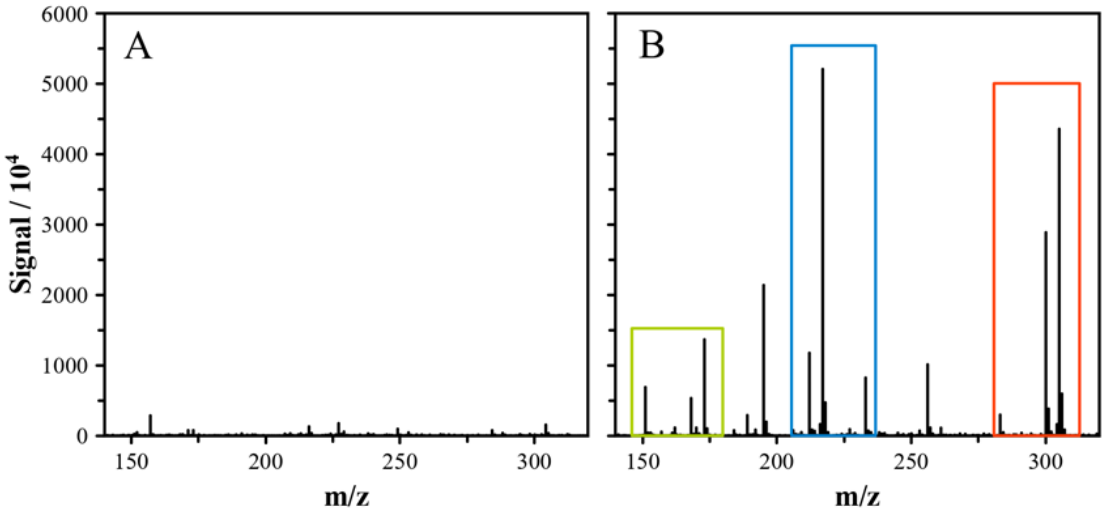

Figure 4: (A) Background mass spectrum recorded prior to particle sampling. **(B)** Mass spectrum recorded at the peak of particle signal for a ternary mixture of 3, 4, and 6-EG, indicated by green, blue and red boxes, respectively.

The integrated peak areas for the three dominant ions relating to each component (H^+, Na^+, and $NH4^+$ adducts of respective n-EGs) were found. The peak area from each ion for 3-EG and 4-EG was divided by the respective peak area from 6-EG for normalization. Then, the normalized peak area for each ion was divided by the normalized peak area at the start of the measurement corresponding to first particle. The average from all three ions was found. Finally, the averaged normalized peak areas corresponding to each sampled droplet were multiplied by the known starting mass ratio resulting in a measure of the mass ratio at every subsequent time. These steps inherently account for ionization efficiency differences in the system.

In order to mitigate particle-to-particle variability due to temporal variability in the PS ionization source, an internal standard of 6-EG was used for all measurements. 6-EG is effective as a standard due to its similarity to the other components of interest, and its low

vapor pressure means that it may be considered non-volatile on the timescales of our measurements.[63] We verified the negligible evaporation (< 1% of particle size) of 6-EG by measuring its evaporation rate in a pure 6-EG particle over around 2 hours (**Figure 5**). Since the evaporation of 3-EG and 4-EG particles took on the order of 500 – 8000 s depending on the RH conditions, changes in the amount of 6-EG will have a negligible impact on measurements.

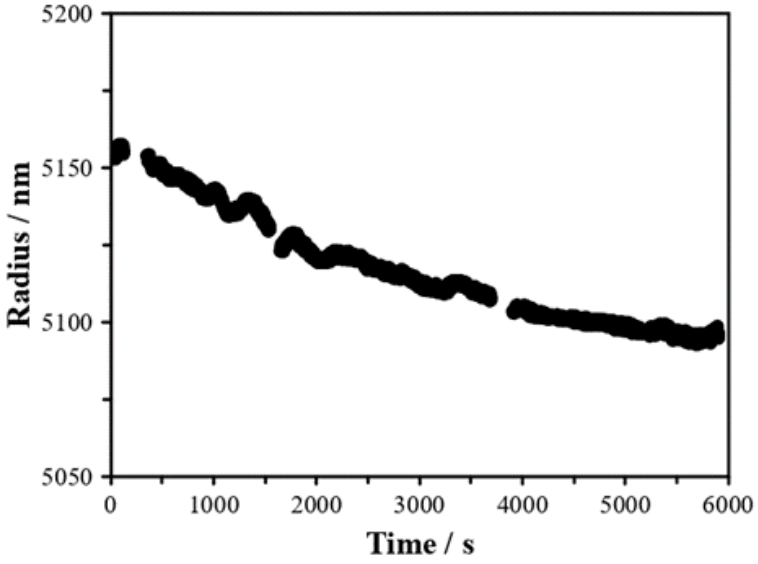

Figure 5: Evaporation of a pure hexaethylene glycol (6-EG) particle under dry conditions.

5.3.2.4. Errors and Uncertainty

Accurate and precise measurements of size and refractive index (RI) using Mie resonance spectroscopy are obtained, with a typical uncertainty of ±5 nm and ±0.002 respectively. For the sizing data reported in this manuscript, the uncertainty is smaller than the size of the points used in the respective plots. For composition measurements using mass spectrometry, we propagate the uncertainty in peak areas to the mass ratio using a standard

combination of errors approach. An uncertainty of around 10% in the normalized peak area is observed due to particle to particle sampling variability.[64] Since measured MS signals for individual components (3-EG and 4-EG) are normalized against an internal standard and then scaled by the signal at the start of the measurement, the uncertainty in the mass ratio reported is the combination of errors from multiple measurements. It should be noted that, although the error in peak areas is random, by scaling the signal by the first data point, a systematic uncertainty is introduced. A total uncertainty of 17% in mass ratios is shown in all plots of composition to reflect the resulting error in mass ratios. Other sources of error, such as the exact starting composition and the extrapolation to get initial size, are not considered but may contribute to a further systematic error in the results.

5.4. Results and Discussion

The size and composition of evaporating particles containing mixtures of n-ethylene glycols are reported here. In each set of measurements, a stack of 5-10 particles was levitated in the LQ-EDB and the size and RI of the lower particle in the stack was probed continuously using Mie resonance spectroscopy. The chemical composition of the same lower particle was determined by ejection from the chamber to the MS sampling region. After each particle was ejected and probed using MS, the next particle in the stack was lowered into the illuminated position for Mie resonance spectroscopy and sizing and RI analysis. To facilitate an understanding of the evolution of the particles undergoing chemical changes, the continuous size evolution of the particles was recorded over the measurements. All measurements were compared against model predictions, and these are

indicated in the respective figures. Measurements of all compositions were performed in duplicate or triplicate and representative datasets are shown. A summary of the measurements and environmental conditions is shown in **Table 1**, including the starting mass ratios for each mixture.

Table 1: Experimental conditions, such as RH, temperature, and, starting n-EG mass ratios and water mole fractions, for measurements reported in this study. The mole fractions of water are estimated using AIOMFAC predictions for single component aqueous solutions and ZSR mixing rules, as described in the text.

Composition	RH (%)	T / K	Starting EG mass ratios			Starting water mole fraction (x_w)
			3-EG	**4-EG**	**6-EG**	
Binary (Dry conditions)						
3-EG:6-EG	0	293	3	-	1	-
4-EG:6-EG	0	293	-	2	1	-
Ternary (Dry conditions)						
3-EG:4-EG:6-EG	0	293	3	2	1	-
Binary (Humid conditions)						
3-EG:6-EG	25	293	3	-	1	0.44
4-EG:6-EG	25	293	-	2	1	0.46
3-EG:6-EG	50	293	3	-	1	0.63
4-EG:6-EG	50	293	-	2	1	0.65
3-EG:6-EG	75	293	3	-	1	0.77
4-EG:6-EG	75	293	-	2	1	0.78

5.4.1. Evaporation Under Dry Conditions

Measurements under dry conditions (0% RH) were performed for the binary mixtures of 3-EG and 4-EG with 6-EG, respectively, and the ternary mixtures containing all three chemical compounds.

5.4.1.1. Analysis of Binary Particles

Figure 6 shows the size and composition evolution for the evaporation of 3-EG from binary particles. The size evolution follows the expected trend for a binary mixture, slowing as the fraction of the evaporating component decreases. The size plateaus at around 1000 s when all of the 3-EG has evaporated, leaving a particle containing pure 6-EG, which evaporates over timescales of many hours. **Figure 6A** reflects the sequential size trend exhibited by all the particles in the measurement.

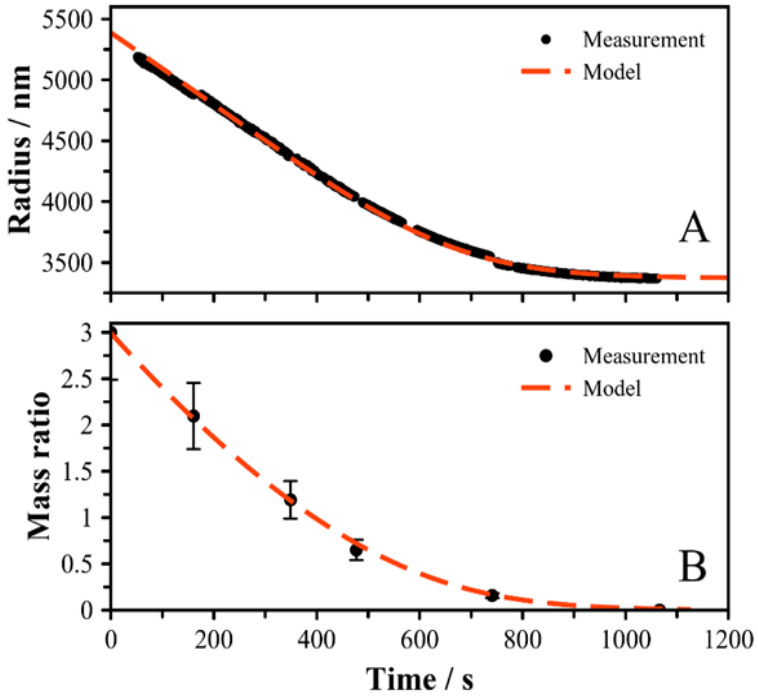

Figure 6: (A) Size evolution of consecutive binary 3-EG particles evaporating in the levitated particle stack under dry conditions. The trend in the size evolution was obtained with the help of Mie resonance spectroscopy. The time of ejection of each particle corresponds to the points in panel B. **(B)** Mass ratio of 3-EG relative to 6-EG, calculated from the PS-MS signal as described in the *Experimental Section*, during evaporation. In both plots, individual black points correspond to the experimental observations, and the red dashed line is the model prediction, as described in the *Experimental Section*.

Slight jumps in size are apparent at the times when the lower particle is ejected to the MS for chemical analysis and reflects a new particle moving into position for sizing. The starting size of all the particles is estimated to have been within approx. 50 nm based on the close agreement of sizing between consecutive particles. The chemical evolution of the particles is shown in **Figure 6B**. With a starting mass ratio of 3:1 between 3-EG and 6-EG, the subsequent particle measurements show a decrease in the relative amount of 3-EG to 6-EG, consistent with the evaporation of 3-EG. After ~1000 s, no measurable signal for 3-EG was detected above the noise level. The time evolution of the size and composition agree closely.

To verify that the measured compositional evolution is consistent with the evolving size, an evaporation model was developed to predict both the changing size and composition. The model was based on the gas-phase diffusion limited multicomponent evaporation to simulate measured data and validate the experimental results. Mixtures were assumed to behave ideally under dry conditions, gas phase diffusion coefficients were taken from Krieger et al.,[70] and pure component vapor pressures under the experimental conditions used in this study were taken from Price et al.[65] For multicomponent evaporation in the absence of water, a straightforward mass flux model was used to determine the evolution of each component, as well as the change in the size of the particle assuming a volume-additive density. *equation 1* was used to calculate the mass flux of each species, with a given starting composition and particle size. The total mass flux is the sum of the flux of each species, given by:

$$\frac{dm}{dt} = \sum_i \frac{dm_i}{dt} = -\sum_i \frac{4\pi a M_i D_i}{RT} p_{i,a} \qquad (1)$$

where m_i is the mass of species i with molecular mass M_i and density ρ_i, a is the radius of the particle, and $p_{i,a}$ is the vapor pressure of i in the mixture, determined from $p_{i,a} = a_i p_i^\circ$ with the activity a_i set equal to the mole fraction x_i, and pure component vapor pressure p_i°. The starting particle size and composition was input to the model, and the mass flux was determined and used to update the size and composition at each time step. For the simulations reported here, the time step was chosen to be 1 s, with little impact on the model output for longer or shorter times.

For evaporation under elevated RH conditions, the particles contain additional water, reducing the activity of each of the evaporating components. From measurements and thermodynamic models of n-EG systems,[71,72] an aqueous solution does not behave ideally, and we must scale the mole fraction by the activity coefficient in order to correctly predict the amount of water and the evaporation dynamics. The Aerosol Inorganic–Organic Mixtures Functional groups Activity Coefficients (AIOMFAC)[73,74] model was used to predict the mole fraction of water and the mole fraction of organic (x_i) in individual aqueous solutions of each glycol of interest as a function of RH using a group contribution approach (**Figure 7**).

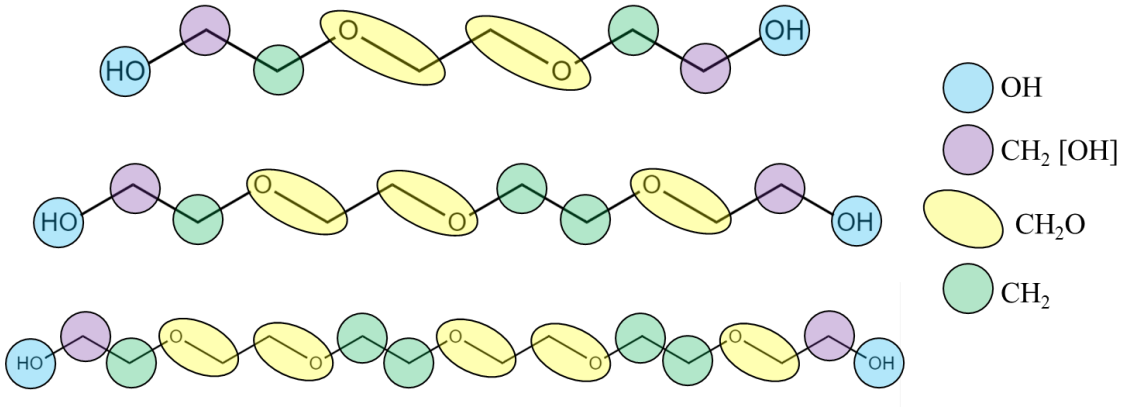

Figure 7: Functional group breakdown of 3-EG, 4-EG, and 6-EG (top to bottom) used in the AIOMFAC predictions described in the text. Some ambiguity on assignment of alkyl groups next to ethers may lead to some errors, but minimal differences were observed in the model output.

Using Zdanovskii-Stokes-Robinson (ZSR) mixing rules, we can estimate the total amount of water in a binary or ternary aqueous solution based on the amount of water associated with each component, allowing us to derive $x_{i,a}$, the mole fraction of i in the particle including all other components. The full mass flux equation becomes:

$$\frac{dm}{dt} = -\sum_i \frac{4\pi a M_i D_i}{RT} \gamma_i x_{i,a} p_i^\circ \times \frac{x_i M_i + (1-x_i) M_w}{x_i} \qquad (2)$$

where the additional term in the fraction accounts for the water that is lost along with species i. A more detailed derivation of this expression is provided below. The activity coefficient, γ_i, is determined from the measurements reported here.

Explanation of Equation 2:

With the additional presence of water, the mass flux equation for a single component remains the same:

$$\frac{dm_i}{dt} = -\frac{4\pi a M_i D_i}{RT} p_{i,a}$$

with $p_{i,a} = p_i^\circ a_i$, where a_i is the activity of i in the droplet. The measured particle evaporation includes the loss of i as well as the water associated with i. Thus, we can write the change in particle mass as:

$$\frac{dm}{dt} = -\frac{dm_i}{dt} \times \frac{1}{w_i}$$

where $w_i = \frac{m_i}{m_i + m_w}$ is the mass fraction of i. The mass fraction and mole fraction are related by:

$$w_i = \frac{x_i M_i}{x_i M_i + (1 - x_i) M_w}$$

Thus, we can express the evaporation rate of the droplet as:

$$\frac{dm}{dt} = -\frac{4\pi a M_i D_i}{RT} \gamma_i x_{i,a} p_i^\circ \times \frac{x_{i,a} M_i + \left(1 - x_{i,a}\right) M_w}{x_{i,a}}$$

For the multicomponent case, we sum the individual components:

$$\frac{dm}{dt} = -\sum_i \frac{4\pi a M_i D_i}{RT} \gamma_i x_{i,a} p_i^\circ \times \frac{x_i M_i + (1 - x_i) M_w}{x_i}$$

It should be noted here that x_i and $x_{i,a}$ are no longer interchangeable, as was the case in the single component derivation. Instead, x_i refers to the mole fraction of i with respect to the amount of water associated with i – that is to say that it considers only the water in the droplet that is present due to the presence of i – this utilized the Zdanovskii-Stokes-Robinson mixing rule. The mole fraction of i ($x_{i,a}$) considers all species present in the

particle, including other solutes and water. The relevant physicochemical properties of the n-EG species used in the model are shown in **Table 2**.

Table 2: Physicochemical properties of the n-EG molecules studied. The vapor pressure is taken from Price et al.,[65] the gas phase diffusion coefficients from Krieger et al.,[70] and the activity coefficients at each RH are determined from the measurements, as described in the text. x_i is the mole fraction of i when a particle containing pure i is exposed to a specific RH, as determined from AIOMFAC and explained in greater detail in the text.

	Molecular mass / g mol^{-1}	**Density / kg m^{-3}**	**Vapor pressure / Pa**	**Gas phase diffusivity / m^2 s^{-1}**	**x_i; γ at 25% RH**	**x_i; γ at 50% RH**	**x_i; γ at 75% RH**
3-EG	150	1100	5.10×10^{-2}	5.95×10^{-6}	0.575; 1.38±0.02	0.383; 1.25±0.02	0.237; 1.12±0.02
4-EG	194	1125	1.26×10^{-3}	5.10×10^{-6}	0.546 1.40±0.02	0.358; 1.28±0.02	0.224; 1.15±0.02
6-EG	282	1127	3.15×10^{-5}	4.26×10^{-6}	0.507; N/A	0.323; N/A	0.202; N/A

The predicted size and composition evolution from the model are compared to the observations in *Figure 6*. The starting size was extrapolated back to t = 0, as the size of the first particle was not measured. Using the vapor pressures of pure n-EG species measured by Price et al.[65] from size measurements of evaporating single component particles, the model predictions yield a size evolution that closely agree with the measured data. The complementary predictions of the composition evolution also agree with the measured composition within uncertainty across the whole measurement. The excellent agreement between size, composition and modelled data demonstrates effective and accurate quantitation of evolving composition using the combined LQ-EDB-MS. Similar results for evaporation of 4-EG in terms of size and chemical composition are shown in **Figure 8**.

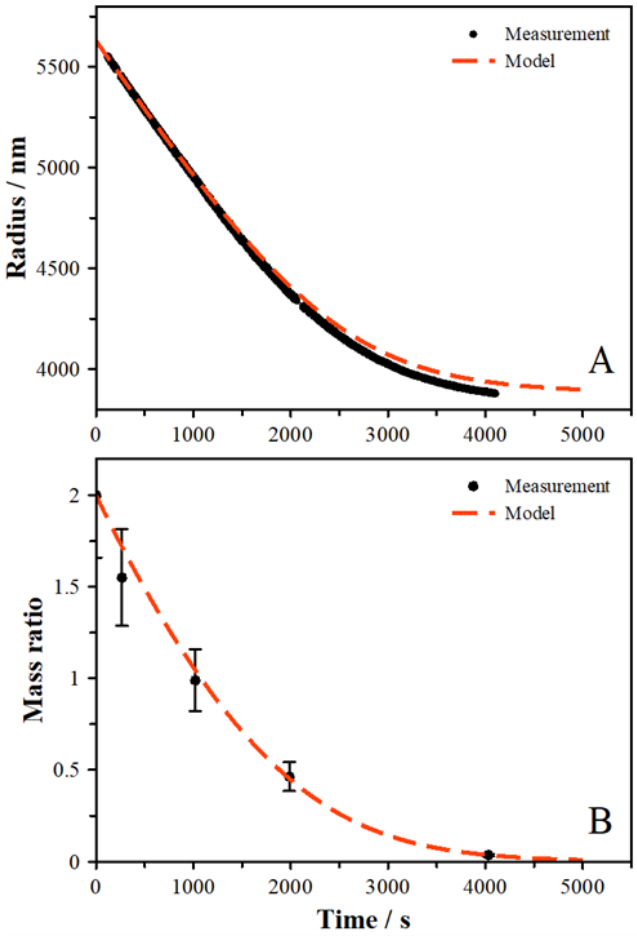

Figure 8: (A) Size evolution of consecutive binary 4-EG particles evaporating in the levitated particle stack under dry conditions. **(B)** Mass ratio of 4-EG relative to 6-EG for particles undergoing evaporation, calculated as described in the *Experimental Section*. In both plots, individual black points correspond to the experimental observations, and the red dashed line is the model prediction, as described in the *Experimental Section*.

The evaporation times for 4-EG particles under dry conditions, as shown in **Figure 8A**, are considerably longer than those for 3-EG, as expected based on the reduced vapor pressure of the higher molecular weight 4-EG. The size evolution due to 4-EG evaporation follows the expected trend, following the same behavior as the 3-EG mixtures and reaching a plateau in size when only 6-EG remains in the particle. **Figure 8B** shows the chemical evolution of particles due to the evaporation of 4-EG.

The model predictions for this mixture, determined in the same way as for the 3-EG binary case, shows good agreement with both the size and composition. The final size predicted by the model is a slight over-prediction compared to the measurements. This may be attributed to the uncertainty in the exact starting composition and size, which can lead to small discrepancies in the predicted final size, or slight variations in the size of successive particles. The rate of evaporation, indicated by the slope of the radius versus time, agrees well with model predictions. The composition data agrees with the prediction within the uncertainty, and shows no detectible 4-EG signal after approximately 4000 s.

5.4.1.2. Analysis of Ternary Particles

To explore the influence of increased chemical complexity on multicomponent evaporation, a ternary mixture was prepared and sampled under dry conditions. The size evolution during the evaporation of 3-EG and 4-EG from ternary particles is shown in **Figure 9A**. The initial evaporation rate is dominated by the more rapid evaporation of 3-EG up to approximately 1100 s, followed by a slower rate of evaporation dominated by the 4-EG. As before, the size plateaus when all of the 3-EG and 4-EG has evaporated, leaving a particle containing pure 6-EG. The evaporation model was again used to predict the evaporation process for this mixture, and in this case both semi-volatile species (3-EG and 4-EG) are incorporated in the mass flux equations. Overall, the model functions as before, although now with a more complex change in composition over time. The predicted size evolution from the evaporation model agrees well with the measurements. We can further

verify these predictions by decoupling the evaporation of individual species in terms of their chemical composition using the MS data as shown in **Figure 9B**.

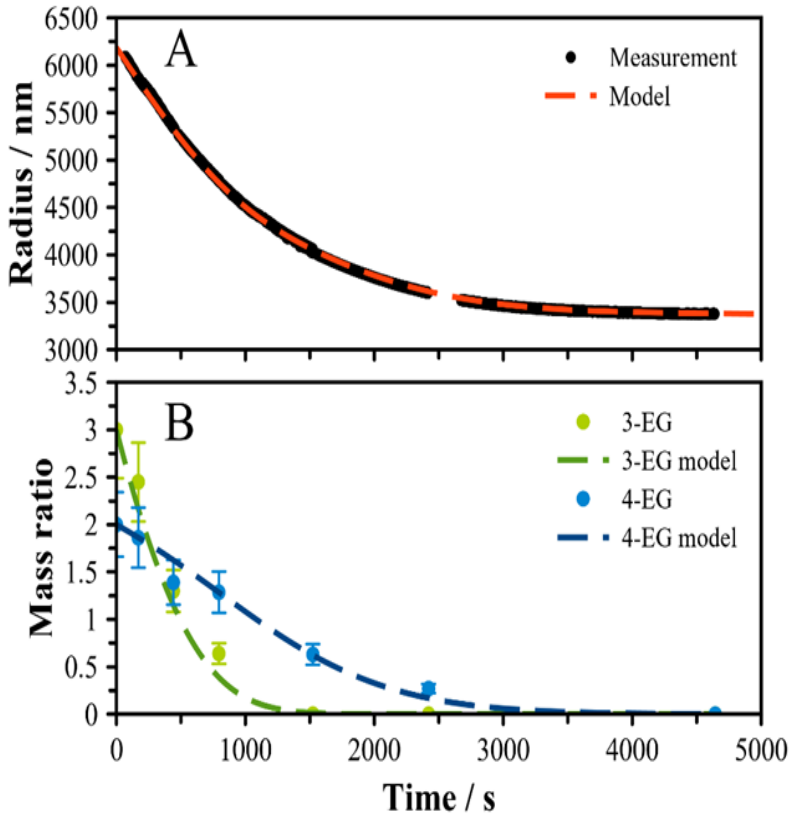

Figure 9: (A) Size evolution of consecutive ternary 3-EG and 4-EG particles evaporating in the levitated particle stack under dry conditions. The trend in the size evolution was obtained with the help of Mie resonance spectroscopy. Individual black points correspond to the experimental observations, and the red dashed line is the model prediction. **(B)** Mass ratios of 3-EG and 4-EG relative to the internal standard (6-EG). 3-EG is shown in green and 4-EG is shown in blue, with their respective model predictions given by dashed lines of the same colors.

The changes in the relative abundance of individual species (3-EG and 4-EG) in these multicomponent mixture particles were resolved in terms of their respective mass ratios to 6-EG. The 3-EG and 4-EG components in the initial particle had a starting mass ratio fixed at 3 and 2, respectively, which decrease to zero over the evaporation measurements. The

measured abundance shows two very clear timescales for the loss of individual species, with excellent agreement to predicted changes using the evaporation model.

5.4.2. Evaporation Under Humid Conditions

n-Ethylene glycol molecules are hygroscopic and under elevated humidity conditions will exist in equilibrium with water as an aqueous solution. Aqueous particles containing n-EG will evaporate over extended timescales due to the reduced activity of evaporating species brought about by the addition of water. Assumptions of ideality in aqueous solutions break down, as evidenced by previous hygroscopic growth measurements on individual n-EG components and thermodynamic modelling.[72] In an ideal solution, the activity of water in the solution, set by the relative humidity, will equal the mole fraction of water in the mixture. In real solutions of n-EG, the mole fraction of water is higher than predicted by ideality for most of the RH range, indicating the activity coefficient of water to be less than 1.

Table 1 shows the expected mole fraction of water in individual particles exposed to a range of RH conditions as predicted by the AIOMFAC model – these have been verified by experiments and shown to be accurate for the pure component cases.[71,72] These predictions allow the aqueous composition of mixtures to be estimated using the Zdanovskii-Stokes-Robinson (ZSR) mixing rule, which equates the sum of the water content in a mixture as the sum of the water content associated with each individual components at the same humidity. The AIOMFAC model may also be used to predict the water content of the mixtures, however it was not possible to incorporate these predictions

into the evaporation model for a continuously changing composition. Instead, the ZSR relation was compared to AIOMFAC for the initial compositions, showing agreement in the predicted water mole fraction to two decimal places. In addition to the non-ideality effect on the composition of the mixtures, non-ideality may also influence the evaporation rate of n-EG molecules based on their activity coefficients. In this section, we describe the evaporation of binary particles under three humidity conditions (25%, 50% and 75% RH) and use the evaporation model to determine the activity coefficients of n-EG at each RH. All measurements were carried out in the same manner as described earlier, and changes to the model are described subsequently.

Figure 10 shows the size and composition evolution of binary particles during the evaporation of 3-EG at varying RH conditions. The size evolution is shown in **Figure 10A** and exhibits a trend towards slower evaporation as the RH is increased. At elevated RH, due to the presence of water, measured changes in size arise due to loss of both evaporating organic molecules and the water associated with them. The evolution of n-EG composition is shown in **Figure 10B** for the mass ratio of 3-EG normalized against 6-EG. In these data, the effect of water on the loss of the organic species is observed, and the trend to slower loss of 3-EG with increasing RH is clear.

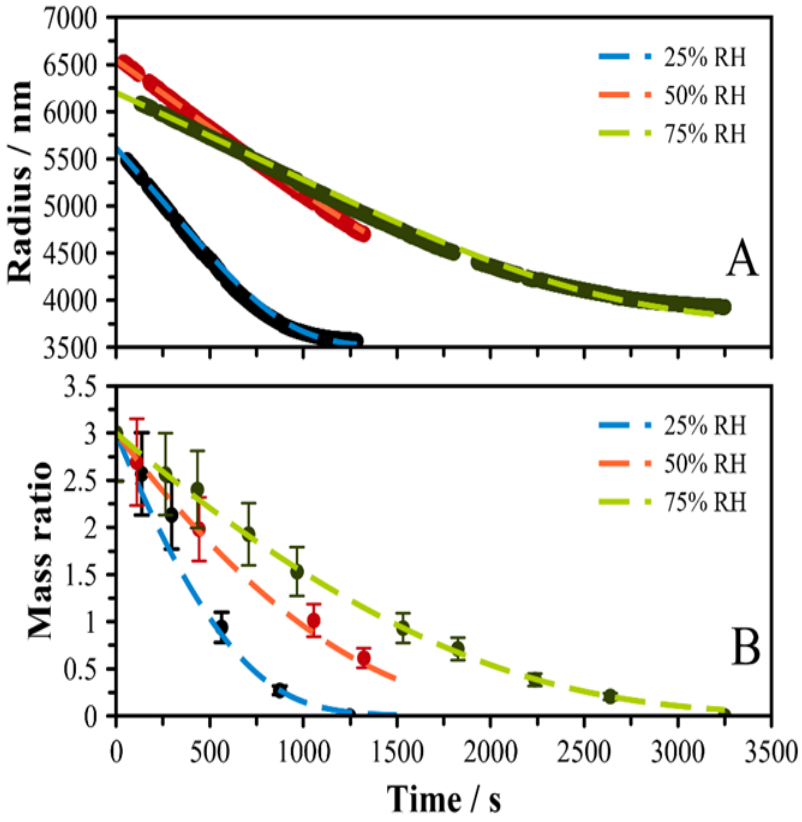

Figure 10: (A) Size evolution of consecutive binary 3-EG particles evaporating under 25, 50, and 75% RH conditions. **(B)** Composition evolution of 3-EG relative to the internal standard (6-EG) during evaporation under each RH. Model predictions are shown by dashed lines in both panels and use the activity coefficients reported in *Table 2*.

Figure 11 shows analogous measurements for binary 4-EG particles, with the same trends observed at different RH. The 4-EG evaporation extends to longer timescales as compared to 3-EG evaporation due to the lower vapor pressure of 4-EG. In order to interpret how aqueous particles are behaving in this system, it is first necessary to estimate the amount of water associated with the particle. Considering the case of 3-EG:6-EG sample particles and using the AIOMFAC model for individual n-EG species, we can estimate the amount of water associated with 3-EG and 6-EG in order to estimate the total water content as a function of RH (*refer Table 1*).

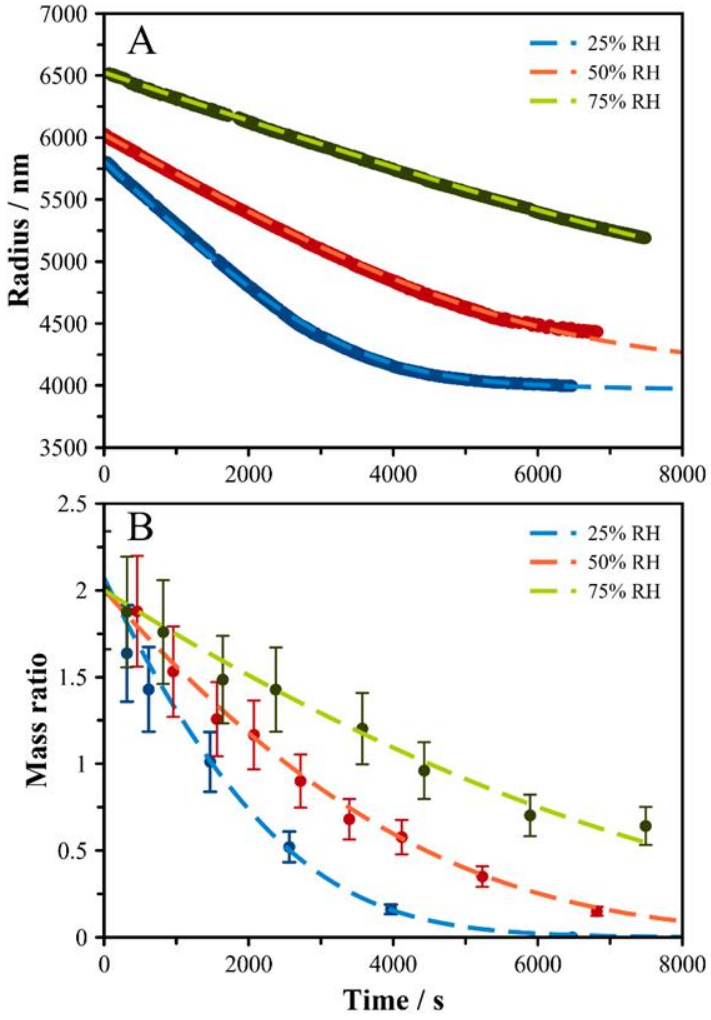

Figure 11: (A) Size evolution of consecutive binary 4-EG particles evaporating under 25, 50, and 75% RH conditions **(B)** Composition evolution of 4-EG relative to the internal standard (6-EG) during evaporation under each RH. Model predictions are shown by dashed lines in both panels and use the activity coefficients reported in *Table 2*.

Based on predictions from AIOMFAC and using ZSR mixing rules, the mole fraction of water is 0.44, 0.63, and 0.77 at the start of these measurements for 25, 50 and 75% RH respectively. As the evaporation progresses, the water mole fraction will change as the particle becomes depleted of 3-EG. The final composition after evaporation represents an aqueous particle of 6-EG, with water mole fractions of water of 0.49, 0.68, and 0.80. From

these data, we estimate the mole fraction of 3-EG in the evaporating particle and calculate the mass flux of organic molecules and the associated water using *equation 2*. If we assume that the activity coefficient of evaporating molecules is 1, the evaporation rate is underpredicted, as seen from both the size and composition evolution of the system (**Figure 12**).

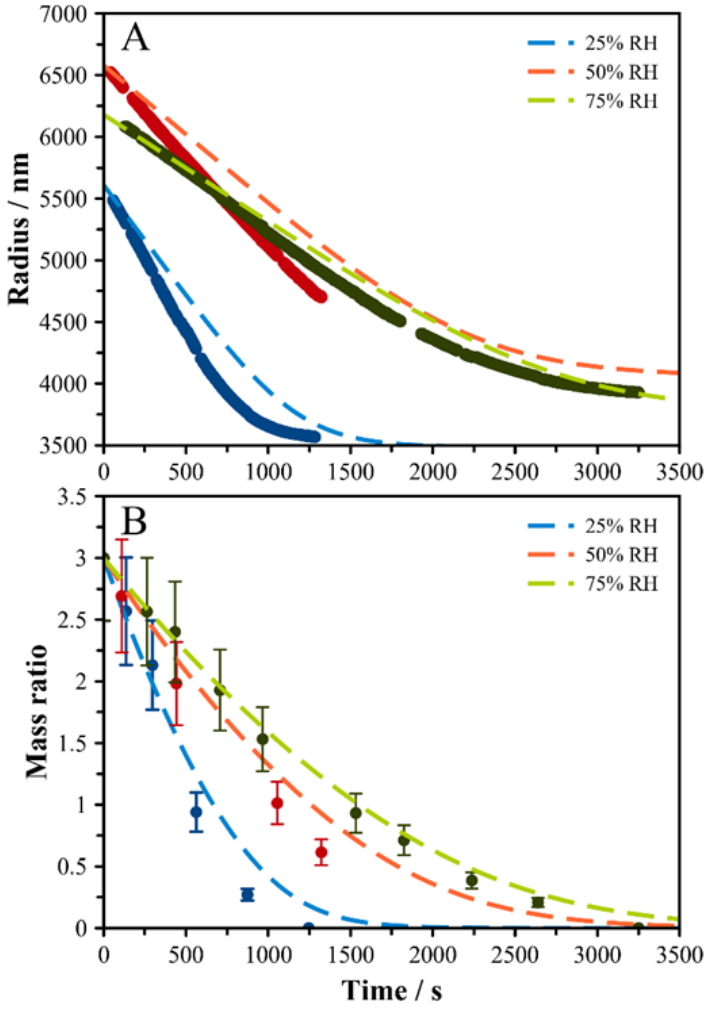

Figure 12: (A) Size evolution of consecutive binary 3-EG particles evaporating under 25, 50, and 75% RH conditions **(B)** Composition evolution of 3-EG relative to the internal standard (6-EG) during evaporation under each RH. Model predictions are shown by dashed lines in both panels assuming an activity coefficient of 1.

Instead, the activity coefficient was found by varying its value to achieve the best agreement between predicted and measured data. When the best fit value is obtained, both the size and composition predictions agree closely with the measured data. This process was repeated for 4-EG:6-EG particles, and the activity coefficients of both systems are shown in *Table 2*. Using the size data, the uncertainty in activity coefficient is on the order of ± 2-3% given the precision of the size information. It is important to note that, although this process has been applied in the case of binary systems, the procedure may be generalized to multicomponent systems. In these cases, the activity of evaporating species may be deduced from the composition change of each component. In the binary cases presented here, this leads to the same values for the activity coefficients, but with a larger uncertainty (of approximately ±10%) due to the larger uncertainty in the MS data.

5.5. Summary and Conclusions

Through measurements of the evaporation of binary and ternary n-EG particles levitated in a LQ-EDB, we have demonstrated the accuracy and precision of compositional measurements using a paper spray ionization source coupled to a high-resolution mass spectrometer. This experimental platform improves upon other similar methods by combining quantitative composition measurements using MS with robust particle sizing using Mie resonance spectroscopy, and allowing for multiple particles to be levitated in a stack, with individual particles sampled consecutively over extended time periods.[61,62] Both size and composition evolution follow the expected trend for binary and ternary mixtures when compared against model predictions incorporating single component vapor

pressures and ideal mixing rules under dry conditions. The agreement observed across size, composition, and their respective modelled data provides robust validation for the methods described herein. Experiments were performed on the evaporating particles across a range of timescales. This allows a robust assessment of the quality of compositional data collected over a longer time period, with larger time steps between particle samplings. This is an important facet of particle levitation measurements, as they often are performed over several hours.

Under elevated RH, we encounter conditions where the levitated particles do not exhibit ideal mixing. This is a commonplace among atmospheric aerosol particles that conditions a wide range of chemical species. The measurements reported here demonstrate that the individual activity coefficients of semi-volatile species in complex organic mixtures may be derived through compositionally-resolved evaporation measurements, with significant advantages for understanding gas-particle partitioning in the atmosphere. Overall, the measurements described here illustrate the broad capabilities of a combined particle levitation and mass spectrometry approach for characterizing evolving chemical systems.

5.6. References

(1) Pöschl, U. Atmospheric Aerosols: Composition, Transformation, Climate and Health Effects. *Angew. Chem. Int. Ed.* **2005**, *44* (46), 7520–7540. https://doi.org/10.1002/anie.200501122.

(2) Ruehl, C. R.; Davies, J. F.; Wilson, K. R. An Interfacial Mechanism for Cloud Droplet Formation on Organic Aerosols. *Science* **2016**, *351* (6280), 1447–1450. https://doi.org/10.1126/science.aad4889.

(3) Menon, S.; Unger, N.; Koch, D.; Francis, J.; Garrett, T.; Sednev, I.; Shindell, D.; Streets, D. Aerosol Climate Effects and Air Quality Impacts from 1980 to 2030. *Environ. Res. Lett.* **2008**, 3 (2). https://doi.org/10.1088/1748-9326/3/2/024004.

(4) Shiraiwa, M.; Ueda, K.; Pozzer, A.; Lammel, G.; Kampf, C. J.; Fushimi, A.; Enami, S.; Arangio, A. M.; Fröhlich-Nowoisky, J.; Fujitani, Y.; Furuyama, A.; Lakey, P. S. J.; Lelieveld, J.; Lucas, K.; Morino, Y.; Pöschl, U.; Takahama, S.; Takami, A.; Tong, H.; Weber, B.; Yoshino, A.; Sato, K. Aerosol Health Effects from Molecular to Global Scales. *Environ. Sci. Technol.* **2017**, *51* (23), 13545–13567. https://doi.org/10.1021/acs.est.7b04417.

(5) Bzdek, B. R.; Reid, J. P. Perspective: Aerosol Microphysics: From Molecules to the Chemical Physics of Aerosols. *J. Chem. Phys.* **2017**, *147* (22), 220901-1–220901-17. https://doi.org/10.1063/1.5002641.

(6) Jimenez, J. L.; Canagaratna, M. R.; Donahue, N. M.; Prevot, A. S. H.; Zhang, Q.; Kroll, J. H.; DeCarlo, P. F.; Allan, J. D.; Coe, H.; Ng, N. L.; Aiken, a C.; Docherty, K. S.; Ulbrich, I. M.; Grieshop, a P.; Robinson, a L.; Duplissy, J.; Smith, J. D.; Wilson, K. R.; Lanz, V. a; Hueglin, C.; Sun, Y. L.; Tian, J.; Laaksonen, A.; Raatikainen, T.; Rautiainen, J.; Vaattovaara, P.; Ehn, M.; Kulmala, M.; Tomlinson, J. M.; Collins, D. R.; Cubison, M. J.; Dunlea, E. J.; Huffman, J. a; Onasch, T. B.; Alfarra, M. R.; Williams, P. I.; Bower, K.; Kondo, Y.; Schneider, J.; Drewnick, F.; Borrmann, S.; Weimer, S.; Demerjian, K.; Salcedo, D.; Cottrell, L.; Griffin, R.; Takami, A.; Miyoshi, T.; Hatakeyama, S.; Shimono, A.; Sun, J. Y.; Zhang, Y. M.; Dzepina, K.; Kimmel, J. R.; Sueper, D.; Jayne, J. T.; Herndon, S. C.; Trimborn, a M.; Williams, L. R.; Wood, E. C.; Middlebrook, a M.; Kolb, C. E.; Baltensperger, U.; Worsnop, D. R. Evolution of Organic Aerosols in the Atmosphere. *Science* **2009**, *326* (5959), 1525–1529. https://doi.org/10.1126/science.1180353.

(7) Randriamiarisoa, H.; Chazette, P.; Couvert, P.; Sanak, J.; Megie, G. Relative Humidity Impact on Aerosol Parameters in a Paris Suburban Area. *Atmos. Chem. Phys.* **2006**, *6* (5), 1389–1407. *https://doi.org/10.5194/acp-6-1389-2006.*

(8) Isaacman-VanWertz, G.; Massoli, P.; O'Brien, R.; Lim, C.; Franklin, J. P.; Moss, J. A.; Hunter, J. F.; Nowak, J. B.; Canagaratna, M. R.; Misztal, P. K.; Arata, C.; Roscioli, J. R.; Herndon, S. T.; Onasch, T. B.; Lambe, A. T.; Jayne, J. T.; Su, L.; Knopf, D. A.; Goldstein, A. H.; Worsnop, D. R.; Kroll, J. H. Chemical Evolution of Atmospheric Organic Carbon over Multiple Generations of Oxidation. *Nat. Chem.* **2018**, *10* (4), 462–468. https://doi.org/10.1038/s41557-018-0002-2.

(9) George, C.; Ammann, M.; D'Anna, B.; Donaldson, D. J.; Nizkorodov, S. A. Heterogeneous Photochemistry in the Atmosphere. *Chem. Rev.* **2015**, *115* (10), 4218–4258. https://doi.org/10.1021/cr500648z.

(10) Chapleski, R. C.; Zhang, Y.; Troya, D.; Morris, J. R. Heterogeneous Chemistry and Reaction Dynamics of the Atmospheric Oxidants, O_3, NO_3, and OH, on Organic Surfaces. *Chem. Soc. Rev.* **2016**, *45* (13), 3731–3746. https://doi.org/10.1039/C5CS00375J.

(11) Wilson, K. R.; Smith, J. D.; Kessler, S. H.; Kroll, J. H. The Statistical Evolution of Multiple Generations of Oxidation Products in the Photochemical Aging of Chemically Reduced Organic Aerosol. Phys. Chem. Chem. Phys. **2012**, *14* (4), 1468–1479. https://doi.org/10.1039/c1cp22716e.

(12) Lambe, A. T.; Cappa, C. D.; Massoli, P.; Onasch, T. B.; Forestieri, S. D.; Martin, A.; T., er; Cummings, M. J.; Croasdale, D. R.; Brune, W. H.; Worsnop, D. R.; Davidovits, P. Relationship between Oxidation Level and Optical Properties of Secondary Organic Aerosol. *Environ. Sci. Technol.* **2013**, *47* (12), 6349–6357. https://doi.org/10.1021/es401043j.

(13) Donahue, N. M.; Robinson, A. L.; Trump, E. R.; Riipinen, I.; Kroll, J. H. Volatility and Aging of Atmospheric Organic Aerosol. *Atmospheric and Aerosol Chemistry*. McNeill, V. F., Ariya, P. A., Eds.; *Top. Curr. Chem.* **2014**, 339, 97–143. https://doi.org/10.1007/128_2012_355.

(14) Facchini, M. C.; Mircea, M.; Fuzzi, S.; Charlson, R. J. Cloud Albedo Enhancement by Surface-Active Organic Solutes in Growing Droplets. *Nature* **1999**, *401* (6750), 257–259. https://doi.org/10.1038/45758.

(15) Shiraiwa, M.; Selzle, K.; Pöschl, U. Hazardous Components and Health Effects of Atmospheric Aerosol Particles: Reactive Oxygen Species, Soot, Polycyclic Aromatic Compounds and Allergenic Proteins. *Free Radic. Res.* **2012**, *46* (8), 927–939. https://doi.org/10.3109/10715762.2012.663084.

(16) Finlayson-Pitts, B. J. Tropospheric Air Pollution: Ozone, Airborne Toxics, Polycyclic Aromatic Hydrocarbons, and Particles. *Science* **1997**, *276* (5315), 1045–1051. https://doi.org/10.1126/science.276.5315.1045.

(17) Carter, W.; Cockeriii, D.; Fitz, D.; Malkina, I.; Bumiller, K.; Sauer, C.; Pisano, J.; Bufalino, C.; Song, C. A New Environmental Chamber for Evaluation of Gas-Phase Chemical Mechanisms and Secondary Aerosol Formation. *Atmos. Environ.* **2005**, *39* (40), 7768–7788. https://doi.org/10.1016/j.atmosenv.2005.08.040.

(18) Zhang, X.; Cappa, C. D.; Jathar, S. H.; McVay, R. C.; Ensberg, J. J.; Kleeman, M. J.; Seinfeld, J. H. Influence of Vapor Wall Loss in Laboratory Chambers on Yields of Secondary Organic Aerosol. *Proc. Natl. Acad. Sci. U.S.A.* **2014**, *111* (16), 5802–5807. https://doi.org/10.1073/pnas.1404727111.

(19) Che, D. L.; Smith, J. D.; Leone, S. R.; Ahmed, M.; Wilson, K. R. Quantifying the Reactive Uptake of OH by Organic Aerosols in a Continuous Flow Stirred Tank Reactor. *Phys. Chem. Chem. Phys.* **2009**, *11* (36), 7885-7895. https://doi.org/10.1039/B904418C.

(20) Houle, F. A.; Wiegel, A. A.; Wilson, K. R. Predicting Aerosol Reactivity Across Scales: From the Laboratory to the Atmosphere. *Environ. Sci. Technol.* **2018**, *52* (23), 13774–13781. https://doi.org/10.1021/acs.est.8b04688.

(21) Friebel, F.; Mensah, A. A. Aging Aerosol in a Well-Mixed Continuous-Flow Tank Reactor: An Introduction of the Activation Time Distribution. *Atmos. Meas. Tech.* **2019**, 12 (5), 2647–2663. https://doi.org/10.5194/amt-12-2647-2019.

(22) Hearn, J. D.; Smith, G. D. A Chemical Ionization Mass Spectrometry Method for the Online Analysis of Organic Aerosols. *Anal. Chem.* **2004**, *76* (10), 2820–2826. https://doi.org/10.1021/ac049948s.

(23) Pratt, K. A.; Prather, K. A. Mass Spectrometry of Atmospheric Aerosols—Recent Developments and Applications. Part I: Off-line Mass Spectrometry Techniques. *Mass Spectrom. Rev.* **2012**, *31*, 1–16. https://doi.org/10.1002/mas.20322.

(24) Pratt, K. A.; Prather, K. A. Mass Spectrometry of Atmospheric Aerosols—Recent Developments and Applications. Part II: On-line Mass Spectrometry Techniques. *Mass Spectrom. Rev.* **2012**, *31*, 17–48. https://doi.org/10.1002/mas.20330.

(25) Noble, C. A.; Prather, K. A. Real-time Single Particle Mass Spectrometry: A Historical Review of a Quarter Century of the Chemical Analysis of Aerosols. *Mass Spectrom. Rev.* **2000**, *19* (4), 248–74. https://doi.org/10.1002/1098-2787(200007).

(26) Jayne, J. T.; Leard, D. C.; Zhang, X.; Davidovits, P.; Smith, K. A.; Kolb, C. E.; Worsnop, D. R. Development of an Aerosol Mass Spectrometer for Size and Composition Analysis of Submicron Particles. *Aerosol Sci Technol.* **2000**, *33* (1–2), 49–70. https://doi.org/10.1080/027868200410840.

(27) DeCarlo, P. F.; Kimmel, J. R.; Trimborn, A.; Northway, M. J.; Jayne, J. T.; Aiken, A. C.; Gonin, M.; Fuhrer, K.; Horvath, T.; Docherty, K. S.; Worsnop, D. R.; Jimenez, J. L. Field-Deployable, High-Resolution Time-of-Flight Aerosol Mass Spectrometer. *Anal. Chem.* **2006**, *78* (24), 8281–8289. https://doi.org/10.1021/ac061249n.

(28) Lanz, V. A.; Prevot, A. S. H.; Alfarra, M. R.; Weimer, S.; Mohr, C.; DeCarlo, P. F.; Gianini, M. F. D.; Hueglin, C.; Schneider, J.; Favez, O.; D'Anna, B.; George, C.; Baltensperger, U.; Institut, P. S. Characterization of Aerosol Chemical Composition with Aerosol Mass Spectrometry in Central Europe: An Overview. *Atmos. Chem. Phys.* **2010**, *10* (21), 10453–10471. https://doi.org/10.5194/acp-10-10453-2010.

(29) Nash, D. G.; Baer, T.; Johnston, M. V. Aerosol Mass Spectrometry: An Introductory Review. *Int. J. Mass Spectrom.* **2006**, *258* (1–3), 2–12. https://doi.org/10.1016/j.ijms.2006.09.017.

(30) Nah, T.; Chan, M.; Leone, S. R.; Wilson, K. R. Real Time in Situ Chemical Characterization of Submicrometer Organic Particles Using Direct Analysis in Real Time-Mass Spectrometry. *Anal. Chem.* **2013**, *85* (4), 2087–2095. https://doi.org/10.1021/ac302560c.

(31) Swanson, K. D.; Worth, A. L.; Glish, G. L. Use of an Open Port Sampling Interface Coupled to Electrospray Ionization for the On-Line Analysis of Organic Aerosol Particles. *J. Am. Soc. Mass Spectrom.* **2018**, *29* (2), 297–303. https://doi.org/10.1007/s13361-017-1776-y.

(32) Johnston, M. V.; Kerecman, D. Molecular Characterization of Atmospheric Organic Aerosol by Mass Spectrometry. *Annu. Rev. Anal. Chem.* **2016**, *12* (1), 1–28. https://doi.org/10.1146/annurev-anchem-061516-045135.

(33) Apsokardu, M. J.; Kerecman, D. E.; Johnston, M. V. Ion Formation in Droplet-Assisted Ionization. *Rapid Commun. Mass Spectrom.* **2018**, *35* (S1), 1–7. https://doi.org/10.1002/rcm.8227.

(34) Lim, Y. B.; Ziemann, P. J. Products and Mechanism of Secondary Organic Aerosol Formation from Reactions of N-Alkanes with OH Radicals in the Presence of NOx. *Environ. Sci. Technol.* **2005**, *39* (23), 9229–9236. https://doi.org/10.1021/es051447g.

(35) Kroll, J. H.; Chan, A. W. H.; Ng, N. L.; Flagan, R. C.; Seinfeld, J. H. Reactions of Semivolatile Organics and Their Effects on Secondary Organic Aerosol Formation. *Environ. Sci. Technol.* **2007**, *41* (10), 3545–3550. https://doi.org/10.1021/es062059x.

(36) Ziemann, P. J. Kinetics, Products, and Mechanisms of Secondary Organic Aerosol Formation. *Chem. Soc. Rev.* **2012**, *41* (19), 6582–6605. https://doi.org/10.1039/C2CS35122F.

(37) Kanakidou, M.; Seinfeld, J. H.; Pandis, S. N.; Barnes, I.; Dentener, F. J.; Facchini, M. C. Organic Aerosol and Global Climate Modelling: A Review. *Atmos. Chem. Phys.* **2005**, *5* (4), 1053–1123. https://doi.org/10.5194/acp-5-1053-2005.

(38) Poschl, U.; Rudich, Y.; Ammann, M. Kinetic Model Framework for Aerosol and Cloud Surface Chemistry and Gas-Particle Interactions – Part 1: General Equations, Parameters, and Terminology. *Atmos. Chem. Phys.* **2007**, *7* (23), 5989–6023. https://doi.org/10.5194/acp-7-5989-2007.

(39) Tang, M.; Chan, C. K.; Li, Y. J.; Su, H.; Ma, Q.; Wu, Z.; Zhang, G.; Wang, Z.; Ge, M.; Hu, M.; He, H.; Wang, X. A Review of Experimental Techniques for Aerosol Hygroscopicity Studies. *Atmos. Chem. Phys.* **2019**, *19* (19), 12631–12686. https://doi.org/10.5194/acp-19-12631-2019.

(40) Huffman, J. A.; Docherty, K. S.; Mohr, C.; Cubison, M. J.; Ulbrich, I. M.; Ziemann, P. J.; Onasch, T. B.; Jimenez, J. L. Chemically-Resolved Volatility Measurements of Organic Aerosol from Different Sources. *Environ. Sci. Technol.* **2009**, *43* (14), 5351–5357. https://doi.org/10.1021/es803539d.

(41) Moise, T.; Flores, J. M.; Rudich, Y. Optical Properties of Secondary Organic Aerosols and Their Changes by Chemical Processes. *Chem. Rev.* **2015**, *115* (10), 4400–4439. https://doi.org/10.1021/cr5005259.

(42) Krieger, U. K.; Marcolli, C.; Reid, J. P. Exploring the Complexity of Aerosol Particle Properties and Processes Using Single Particle Techniques. *Chem. Soc. Rev.* **2012**, *41* (19), 6631–6662. https://doi.org/10.1039/c2cs35082c.

(43) Knox, K. J.; Reid, J. P. Ultrasensitive Absorption Spectroscopy of Optically-Trapped Aerosol Droplets. J. Phys. Chem. A 2008, 112 (42), 10439–10441. https://doi.org/10.1021/jp807418g.

(44) Mitchem, L.; Reid, J. P. Optical Manipulation and Characterisation of Aerosol Particles Using a Single-Beam Gradient Force Optical Trap. *Chem. Soc. Rev.* **2008**, *37* (4), 756–769. https://doi.org/10.1039/b609713h.

(45) Richards, D. S.; Trobaugh, K. L.; Hajek-Herrera, J.; Davis, R. D. Dual-Balance Electrodynamic Trap as a Microanalytical Tool for Identifying Gel Transitions and Viscous Properties of Levitated Aerosol Particles. *Anal. Chem.* **2020**, *92* (4), 3086–3094. https://doi.org/10.1021/acs.analchem.9b04487.

(46) Davies, J. F. Mass, Charge, and Radius of Droplets in a Linear Quadrupole Electrodynamic Balance. *Aerosol Sci Technol.* **2019**, *53* (3), 309–320. https://doi.org/10.1080/02786826.2018.1559921.

(47) Cotterell, M. I.; Willoughby, R. E.; Bzdek, B. R.; Orr-Ewing, A. J.; Reid, J. P. A Complete Parameterisation of the Relative Humidity and Wavelength Dependence of the Refractive Index of Hygroscopic Inorganic Aerosol Particles. *Atmos. Chem. Phys.* **2017**, *17* (16), 9837–9851. https://doi.org/10.5194/acp-17-9837-2017.

(48) Bain, A. Determining the Size and Refractive Index of Single Aerosol Particles Using Angular Light Scattering and Mie Resonances. *J. Quant. Spectrosc. Radiat. Transf.* **2018**, *221*, 61–70. https://doi.org/10.1016/j.jqsrt.2018.09.026.

(49) Preston, T. C.; Reid, J. P. Determining the Size and Refractive Index of Microspheres Using the Mode Assignments from Mie Resonances. *J. Opt. Soc. Am. A* **2015**, *32* (11), 2210–2217. https://doi.org/10.1364/JOSAA.32.002210.

(50) Bzdek, B. R.; Power, R. M.; Simpson, S. H.; Reid, J. P.; Royall, C. P. Precise, Contactless Measurements of the Surface Tension of Picolitre Aerosol Droplets. *Chem. Sci.* **2016**, *7* (1), 274–285. https://doi.org/10.1039/C5SC03184B.

(51) Steimer, S. S.; Krieger, U. K.; Peter, T. Electrodynamic Balance Measurements of Thermodynamic, Kinetic, and Optical Aerosol Properties Inaccessible to Bulk Methods. *Atmos. Meas. Tech.* **2015**, *8* (6), 2397–2408. https://doi.org/10.5194/amt-8-2397-2015.

(52) Davies, J. F.; Haddrell, A. E.; Rickards, A. M. J.; Reid, J. P. Simultaneous Analysis of the Equilibrium Hygroscopicity and Water Transport Kinetics of Liquid Aerosol. *Anal. Chem.* **2013**, *85* (12), 5819–5826. https://doi.org/10.1021/ac4005502.

(53) Power, R. M.; Burnham, D. R.; Reid, J. P. Toward Optical-Tweezers-Based Force Microscopy for Airborne Microparticles. *Appl. Opt.* **2014**, *53* (36), 8522–8534. https://doi.org/10.1364/ao.53.008522.

(54) Cohen, L.; Quant, M. I.; Donaldson, D. J. Real-Time Measurements of PH Changes in Single, Acoustically Levitated Droplets Due to Atmospheric Multiphase Chemistry. *ACS Earth Space Chem.* **2020**, *4* (6), 854–861. https://doi.org/10.1021/acsearthspacechem.0c00041.

(55) Bain, A.; Preston, T. C. The Wavelength-Dependent Optical Properties of Weakly Absorbing Aqueous Aerosol Particles. *Chem. Commun.* **2020**, *56* (63), 8928–8931. https://doi.org/10.1039/D0CC02737E.

(56) Davis, R. D.; Lance, S.; Gordon, J. A.; Tolbert, M. A. Long Working-Distance Optical Trap for in Situ Analysis of Contact-Induced Phase Transformations. *Anal. Chem.* **2015**, *87* (12), 6186–6194. https://doi.org/10.1021/acs.analchem.5b00809.

(57) Lee, A. K. Y.; Chan, C. K. Single Particle Raman Spectroscopy for Investigating Atmospheric Heterogeneous Reactions of Organic Aerosols. Atmos. Environ. **2007**, *41* (22), 4611–4621. https://doi.org/10.1016/j.atmosenv.2007.03.040.

(58) Kang, L.; Xu, P.; Zhang, B.; Tsai, H.; Han, X.; Wang, H.-L. Laser Wavelength- and Power-Dependent Plasmon-Driven Chemical Reactions Monitored Using Single Particle Surface Enhanced Raman Spectroscopy. *Chem. Commun.* **2013**, *49* (33), 3389–3391. https://doi.org/10.1039/C3CC40732B.

(59) Lee, A. K. Y.; Ling, T. Y.; Chan, C. K. Understanding Hygroscopic Growth and Phase Transformation of Aerosols Using Single Particle Raman Spectroscopy in an Electrodynamic Balance. *Faraday Discuss.* **2008**, *137*, 245–263. https://doi.org/10.1039/B704580H.

(60) Jacobs, M. I.; Davies, J. F.; Lee, L.; Davis, R. D.; Houle, F.; Wilson, K. R. Exploring Chemistry in Microcompartments Using Guided Droplet Collisions in a Branched Quadrupole Trap Coupled to a Single Droplet, Paper Spray Mass Spectrometer. *Anal. Chem.* **2017**, *89* (22), 12511–12519. https://doi.org/10.1021/acs.analchem.7b03704.

(61) Willis, M. D.; Rovelli, G.; Wilson, K. R. Combining Mass Spectrometry of Picoliter Samples with a Multicompartment Electrodynamic Trap for Probing the Chemistry of Droplet Arrays. *Anal. Chem.* **2020**, *92* (17), 11943–11952. https://doi.org/10.1021/acs.analchem.0c02343.

(62) Birdsall, A. W.; Krieger, U. K.; Keutsch, F. N. Electrodynamic Balance–Mass Spectrometry of Single Particles as a New Platform for Atmospheric Chemistry Research. *Atmos. Meas. Tech.* **2018**, *11* (1), 33–47. https://doi.org/10.5194/amt-11-33-2018.

(63) Birdsall, A. W.; Hensley, J. C.; Kotowitz, P. S.; Huisman, A. J.; Keutsch, F. N. Single-Particle Experiments Measuring Humidity and Inorganic Salt Effects on Gas-Particle Partitioning of Butenedial. *Atmos. Chem. Phys.* **2019**, *19* (22), 14195–14209. https://doi.org/10.5194/acp-19-14195-2019.

(64) Kaur Kohli, R.; Davies, J. F. Paper Spray Mass Spectrometry for the Analysis of Picoliter Droplets. *Analyst* **2020**, *145* (7), 2639–2648. https://doi.org/10.1039/C9AN02534K.

(65) Price, C. L.; Bain, A.; Wallace, B. J.; Preston, T. C.; Davies, J. F. Simultaneous Retrieval of the Size and Refractive Index of Suspended Droplets in a Linear Quadrupole Electrodynamic Balance. *J. Phys. Chem.* **2020**, *124* (9), 1811–1820. https://doi.org/10.1021/acs.jpca.9b10748.

(66) Hart, M. B.; Sivaprakasam, V.; Eversole, J. D.; Johnson, L. J.; Czege, J. Optical Measurements from Single Levitated Particles Using a Linear Electrodynamic Quadrupole Trap. *Appl. Opt.* **2015**, *54* (31), F174–F181. https://doi.org/10.1364/AO.54.00F174.

(67) Nielsen, J. K.; Maus, C.; Rzesanke, D.; Leisner, T. Charge Induced Stability of Water Droplets in Subsaturated Environment. *Atmos. Chem. Phys.* **2011**, *11* (5), 2031–2037. https://doi.org/10.5194/acp-11-2031-2011.

(68) Preston, T. C.; Reid, J. P. Accurate and Efficient Determination of the Radius, Refractive Index, and Dispersion of Weakly Absorbing Spherical Particle Using Whispering Gallery Modes. *J. Opt. Soc. Am. B.* **2013**, *30* (8), 2113–2122. https://doi.org/10.1364/josab.30.002113.

(69) Espy, R. D.; Muliadi, A. R.; Ouyang, Z.; Cooks, R. G. Spray Mechanism in Paper Spray Ionization. *Int. J. Mass Spectrom.* **2012**, *325–327*, 167–171. https://doi.org/10.1016/j.ijms.2012.06.017.

(70) Choczynski, J. M.; Kaur Kohli, R.; Sheldon, C. S.; Price, C. L.; Davies, J. F. A Dual-Droplet Approach for Measuring the Hygroscopicity of Aqueous Aerosol. *Atmos. Meas. Tech. Discuss.* **2021**, *14* (7), 5001–5013. https://doi.org/10.5194/amt-14-5001-2021.

(71) Herskowitz, M.; Gottlieb, M. Vapor-Liquid Equilibrium in Aqueous Solutions of Various Glycols and Poly(Ethylene Glycols). *J. Chem. Eng. Data* **1985**, *30* (2), 233–234. https://doi.org/10.1021/je00040a033.

(72) Krieger, U. K.; Siegrist, F.; Marcolli, C.; Emanuelsson, E. U.; Gøbel, F. M.; Bilde, M.; Marsh, A.; Reid, J. P.; Huisman, A. J.; Riipinen, I.; Hyttinen, N.; Myllys, N.; Kurtén, T.; Bannan, T.; Percival, C. J.; Topping, D. A Reference Data Set for Validating Vapor Pressure Measurement Techniques: Homologous Series of Polyethylene Glycols. *Atmos. Meas. Tech.* **2018**, *11* (1), 49–63. https://doi.org/10.5194/amt-11-49-2018.c.

CHAPTER 6

Connecting the Phase State and Volatility of Single and Binary Component Dicarboxylic Acid Particles at Elevated Temperatures

6.1. Abstract

The gas-particle partitioning of semi-volatile organic molecules has broad applications across a range of scientific disciplines, with significant impacts in atmospheric chemistry for regulating the evolving composition of aerosol particles. Vapor partitioning depends on the molecular interactions and phase state of the condensed material and shows a well-established dependence on temperature. The phase state exhibited by the organic material in particles is not always well-defined, and many examples can be found for the formation of amorphous super-cooled liquid states rather than crystalline solids. This can modify the thermodynamics and kinetics of evaporation leading to significant changes to vapor equilibrium processes. Here, we explore the influence of phase state on the evaporation dynamics of a series of straight-chain dicarboxylic acids and their binary component mixtures across a range of above-ambient temperatures. For this, particles consisting of respective pure and mixed dicarboxylic acid compositions were studied at chosen temperatures. These diacid molecules show an odd/even alteration in some of their properties based on the number of carbon atoms that may be connected to their phase state under dry conditions. Using a newly developed linear-quadrupole electrodynamic balance, we levitate single particles containing the sample and expose them to dry conditions across

a range of temperatures (ambient to ~350 K). The rate of evaporation measured from the change in the size or relative mass, was utilized to derive the vapor pressures and associated enthalpy of vaporization. Single component diacids were studied using Mie resonance spectroscopy data, which allows for unambiguous identification of the phase of the particles (crystalline vs amorphous). The identification of phase state further allows the vapor equilibrium properties to be attributed to a particular state associated with the particle. Binary component diacid mixtures[†] were primarily studied using mass spectrometry to determine changes in the chemical composition to understanding the evaporation dynamics of each component. This work highlights a new and specialized experimental method for characterizing the vapor pressures of low volatility substances and extends the temperature range of available data for the vapor pressure of terminal dicarboxylic acids. These measurements for pure component particles show that they can exist in both crystalline and super-cooled liquid states at elevated temperatures and provide a direct comparison between super-cooled and crystal phases. For binary component particles, these measurements show that they retain a crystalline phase state under all experimental conditions.

6.2. Introduction

The partitioning of organic molecules between vapor and condensed phases is important in a wide range of scientific disciplines. In the atmosphere, gas phase oxidation leads to the production of semi-volatile and low volatility compounds that contribute to the

[†]The term “Binary component diacid mixture” is also referred as “Diacid mixture” throughout the chapter.

formation of secondary organic aerosol.[1] Further evaporation and condensation of semi-volatile organic molecules drives changes in the chemical composition and size distribution of these aerosol particles over time.[2–4] In indoor environments, the vaporization of semi-volatile organics from solvents, paints, and cooking oils (so-called volatile chemical products) plays an important role in regulating air quality.[5,6] In engineering, the vaporization of fuel is a necessary step in the process of combustion, and the evaporation of components found in lubricating and cooling oils affects their long-term function.[7–10] The vapor pressure of volatile and semi-volatile compounds plays an important role in the function, characterization, and environmental impacts of these systems.

The vapor pressure is a thermodynamic quantity derived from the equilibrium pressure of a compound in the gas phase above a pure condensed phase of that substance. In mixtures of organic substances, the effective vapor pressure of each component varies with its mole fraction and chemical activity, which may be measured or derived from theory.[11] Additional complicating factors arise when both intra- and inter-molecular interactions are possible between the condensed phase species. In the homologous series of terminal dicarboxylic acids (malonic, succinic, glutaric, adipic acid, and so on), a distinct odd-even alteration of properties, such as solubility and melting point, with the number of carbon atoms is observed.[11–14] This is attributed to the ways in which the even and odd molecules, respectively, can arrange and form intra- and inter-molecular hydrogen bonds in solution. These interactions change the thermodynamics of various transformations, such as melting, dissolution etc., and result in condensed phases that do not always tend to the thermodynamic equilibrium (crystalline) state under ambient conditions, instead forming

amorphous super-cooled liquids.[15] In the atmosphere, such interactions between organic molecules that span a wide range of chemical functionalities may lead to particles that exhibit vapor pressures that are much lower than expected.[16] Deriving an improved understanding of how physical state and vapor pressure are connected will allow us to better predict the chemical evolution of complex systems.

Many studies have explored the vapor pressure, and specifically the vapor pressure of the diacids, using various laboratory techniques such as tandem differential mobility analysis,[17–20] Knudsen effusion mass spectrometry,[21] thermal desorption mass spectrometry,[22,23] and single particle methods, including optical tweezers and the electrodynamic balance (EDB).[12] There is over an order of magnitude variability in the reported vapor pressures, attributed both to the range of methods as well as the physical state the samples can adopt (see Soonsin et al.[24] and Bilde et al.[11] for a compilation of measured values). Although some of these previous studies identified and compared amorphous super-cooled liquid and crystalline solid states, measurements were limited to below or slightly above ambient conditions (up to 303 K). While these are most relevant for the atmosphere, they limit a more fundamental exploration of the role of temperature in regulating phase state and the associated vapor partitioning properties. Through measurements on crystal and amorphous states, and saturated solutions, it has been identified that odd-numbered carbon chains, in particular, can form anhydrous condensed phase states that exhibit thermodynamic properties consistent with either crystalline or amorphous behavior, with the former being the most thermodynamically stable state of the material.[12,15,17,18]

In this work, we explore the temperature dependence of the vapor pressure of a series of dicarboxylic acids and their binary component mixtures, specifically addressing the high temperature behavior of these systems. As the temperature increases and the melting point is approached, it is expected that the thermodynamic behavior of the condensed phases, whether amorphous or crystalline, will converge. Here, we use single particles levitated in a linear-quadrupole electrodynamic balance (LQ-EDB) and measure the rate of evaporation under dry conditions using either the change in size, relative mass or chemical composition. Using optical methods, we determine whether the particle is crystalline or amorphous and attribute measured properties with the phase state of the sample. From these data we determine the enthalpy of vaporization and/or enthalpy of sublimation and compare our results with previously reported values. Mass spectrometry analysis is carried out on diacid mixtures for evaluating the chemical composition of the particles. Our measurements extend the range of available vapor pressure data and bridge a dearth of measurements in the temperature range from 293 K to ~350 K for amorphous phase states. The reported values of amorphous state vapor pressures do not require corrections for the activity of the evaporating species in a saturated solution, as in the case with some previous work, as measurements are conducted under dry conditions. Additionally, particles with both phase states were produced for single dicarboxylic component particles while only crystalline solid particles could be produced for binary component dicarboxylic acids under identical experimental procedures. Thus, our work allows for direct comparisons between amorphous and solid phases under the same environmental and experimental configuration.

6.3. Experimental Section

6.3.1. Chemicals and Sample Preparation

The chemicals in this study were used without further purification. Aqueous solutions for single component dicarboxylic acids were prepared from a series of dicarboxylic acid compounds, including malonic acid (MA, Sigma-Aldrich, 99% purity), succinic acid (SA, Sigma-Aldrich, ≥ 97 % purity), glutaric acid (GA, Sigma-Aldrich, 99 % purity) and adipic acid (AA, Sigma-Aldrich, ≥ 99.5 % purity). Solutions were prepared at concentrations from 6 to 8 g/L, except for malonic acid which was prepared at a concentration of 20 g/L to generate larger particles due to an observed rapid initial evaporation period. Aqueous mixtures for the binary component dicarboxylic acids of malonic and succinic acid, succinic and glutaric acid, and glutaric and adipic acid, were prepared similarly at equimolar concentrations from 6 to 8 g/L. The concentration dictates the size of the resulting particle and does not further impact measurements. For each solution, the compound was weighed and dissolved in HPLC grade water (Fisher Chemical) and stored in a pre-cleaned plastic vial. To generate samples for levitation, up to 12 μL of each solution was transferred into a microdroplet dispenser (Microfab MJ-ABP-01, 30 µm orifice) and droplets on the order of 50 μm in diameter were introduced into the LQ-EDB. Excess water evaporated and the particles attained an equilibrium (or metastable) state with respect to gas phase water.

The measurements on the diacid mixtures were done on the LQ-EDB coupled to a mass spectrometer (MS) using an open port sampling interface (OPSI). A continuous solvent

mixture of pure methanol with trans-3-(3-Pyridyl)acrylic acid (meth + TPAA) was supplied to the OPSI as an external standard to check for the ESI spray quality and stability. The OPSI probe was connected to an unmodified heated electrospray ionization (ESI) needle of the MS for ionization.

6.3.2. Technique Setup and Analytical Procedure

The LQ-EDB used in this study was based on the configurations described in our previous work, with minor modifications to allow the temperature to be controlled above ambient conditions using heating cartridges.[25] A succinct summary of the operation is described here. Droplets were generated by the microdroplet dispenser in the presence of an induction electrode (130 to 500 V) creating a net charge of 10 to 100 fC on the resulting droplet as it entered the LQ-EDB.[26] A 532 nm laser (Thorlabs CPS532, 5 mW) was used to illuminate the droplets for visual verification as they enter the trap. The trap consists of 4 stainless steel rods in a quadrupole arrangement with paired out-of-phase AC voltages applied in a diagonal manner, generating an electric field that confines the droplet to the central axis. A disc electrode with an applied DC voltage of 30 to 300 V in the center of the LQ-EDB creates a repulsive electrostatic force that balances net forces on the droplet and maintains the droplet in a fixed vertical position throughout the experiment. A CMOS camera (Thorlabs CS165MU) was used to visualize the droplet and stabilize the position of the droplet by changing the DC voltage through a PID feedback loop with the help of the LabVIEW software.

To monitor evaporation as a function of temperature, a temperature between 303 K and 353 K was set using a Digi-Sense PID temperature controller (TC5000) coupled with four 2” cartridge heaters (1/8” diameter, McMaster-Carr 8376T27) inserted symmetrically around the particle trapping location running through the walls of the chamber. The temperature was measured with a thermistor embedded in the chamber wall, which measures a slightly higher temperature than within the chamber. This discrepancy was accounted for in the calibration, as described later. The LQ-EDB was heated for 30 minutes for the lower temperatures (303 K to 323 K) and up to 1.5 hours for the higher temperatures (333 K to 353 K) to ensure thermal equilibrium throughout the chamber ahead of experiments. Experiments were carried out under dry conditions and performed over 100’s to 1000’s of seconds to ensure sufficient evaporation occurred to determine evaporation rates accurately. Single component measurements were conducted on a single particle whereas the diacid mixture measurements were done on a levitated stack consisting of 7 – 10 particles.

For single component dicarboxylic acids, LQ-EDB setup was coupled with the Mie resonance spectroscopy (MRS) which allows to probe the particle in real-time to determine its morphology, size and refractive index (RI). For diacid mixtures, compositional analysis was carried out by ejecting each lowermost particle out of the LQ-EDB trap at specific interval of time and is effectively transferred to MS via an OPSI. The transfer of the lowermost particle to OPSI platform was assisted with a supply of dry nitrogen gas which was introduced at the top of the chamber.

6.3.3. Mie Resonance Spectroscopy

The LQ-EDB trap was coupled with a broadband red LED (Thorlabs M660L4) to measure the evolving properties (size and refractive index) of spherical particles using Mie resonance spectroscopy (MRS). Broadband light was focused onto the levitated particle in the LQ-EDB and the back-scattered light from the particle was collected and introduced to a spectrometer (Ocean Insight HR4000) with resolution of 0.47 nm. Particles that have a spherical morphology can act as an efficient optical cavity in which light of specific wavelengths can become resonant.[25] This gives rise to morphology dependent resonances (MDRs) across the illuminated range of the spectrum (640 to 680 nm) and appear in the measured spectra as sharp peaks in intensity. Spectra were collected at 1 Hz with an exposure time of 1 s and analyzed offline to determine the center wavelength of each peak. The wavelength positions were delivered to the MRFIT sizing algorithm of Preston and Reid,[26] embedded in a LabVIEW graphical user interface, and the radius and wavelength-dependent RI of the particle were determined through a least-squares minimization procedure in comparison to Mie theory predictions of peak positions.[26] To validate the results, full Mie theory simulations were generated using the output size and RI using the code of Bohren and Huffman[27] and the resulting spectra were visually compared against experimental spectra. Sizing results were validated by the comparisons between peak widths and positions in the measured and simulated spectra. Particles in this study ranged between 3 to 10 μm and this size range was chosen because the particles smaller than 3 μm lack sufficient spectral information to determine the size, while particles larger than 10 μm exhibit complex spectra resulting in several low-error solutions, yielding imprecise results.

All particles in this study that remained spherical under the experimental conditions were analyzed using this method. However, due to the solid phase state adopted by some particles, not all samples remained spherical and lacked the spectral information required for sizing. For such cases, an electrostatic analysis was used to determine any changes in particle mass during evaporation.

6.3.4. Electrostatic Analysis

While generally superseded by more accurate optical methods, the electrostatic analysis of particles using an EDB to determine relative mass changes has been long established. In the absence of an air flow in the chamber, the only force acting on the particle is gravity, therefore the balancing voltage (DC) is directly proportional to the mass of the particle present, as shown in *equation 1*:[28]

$$mg = \frac{qV_{DC}C}{z} \quad (1)$$

where m is the mass of the particle, g is the acceleration due to gravity, q is the charge on the particle, V_{DC} is the balancing voltage, C is the geometrical constant that accounts for the effect of electrode geometry on the electric field, and z is the vertical distance from the DC electrode to the particle.

Both q and C are assumed to be constant for a particle at a fixed z above the electrode, so the DC varies linearly with the particle mass. Therefore, tracking the changes in DC voltage yields an estimation of decrease in relative mass of the particle due to its evaporation, which was used to derive vapor pressure along with an estimated starting size.

6.3.5. Mass Spectrometry Analysis

Quantitative measurements for the binary component equimolar mixtures were performed for individual particles in the levitated stack. Each lowermost particle is ejected out of the high temperature linear quadrupole electrodynamic balance (LQ-EDB) to fall in the open port sampling interface (OPSI) where is dissolves in a continuous solvent supply (methanol + TPAA) and is delivered to the heated electrospray ionization (ESI) probe of the Orbitrap mass spectrometry (MS). It is assumed that particles were initially of a uniform size allowing effective quantitation of the semi-volatile diacid species throughout the time period of evaporation transformation. A detailed description of the LQ-EDB setup coupled with MS for conducting experiments on a levitated stack of particles is discussed in our previous work.[44,45] For this work, the MS was operated in the negative polarity, a resolution of 35000 and maximum inject ion inject time of 100 ms. The peaks of the diacid signals of interest in the mass spectra were detected as $(M\text{-}H^{+})^{-}$ adducts in the range of 60 – 400 m/z. The resulting mass spectra were analyzed initially using the Xcalibur 4.1 software which were analyzed further to study the extracted ion chronograms using the MagicPlot Pro 2.8.2. software (*refer Section 5.3.2.3*).

A representative mass spectrum for the binary component equimolar mixture of succinic acid and glutaric acid is shown in **Figure 1A.** A chronogram associated with the glutaric acid component in the binary mixture for 2 consecutive particles is presented in **Figure 1B**. Each peak arises from an individual levitated particle of the diacids mixture sampled via OPSI and analyzed by ESI-MS. A decrease in both the peak intensity and peak area depicts

the evaporation of the glutaric acid component. A similar chronogram was also obtained for the succinic acid (SA) component in the diacids mixture particles but not shown here.

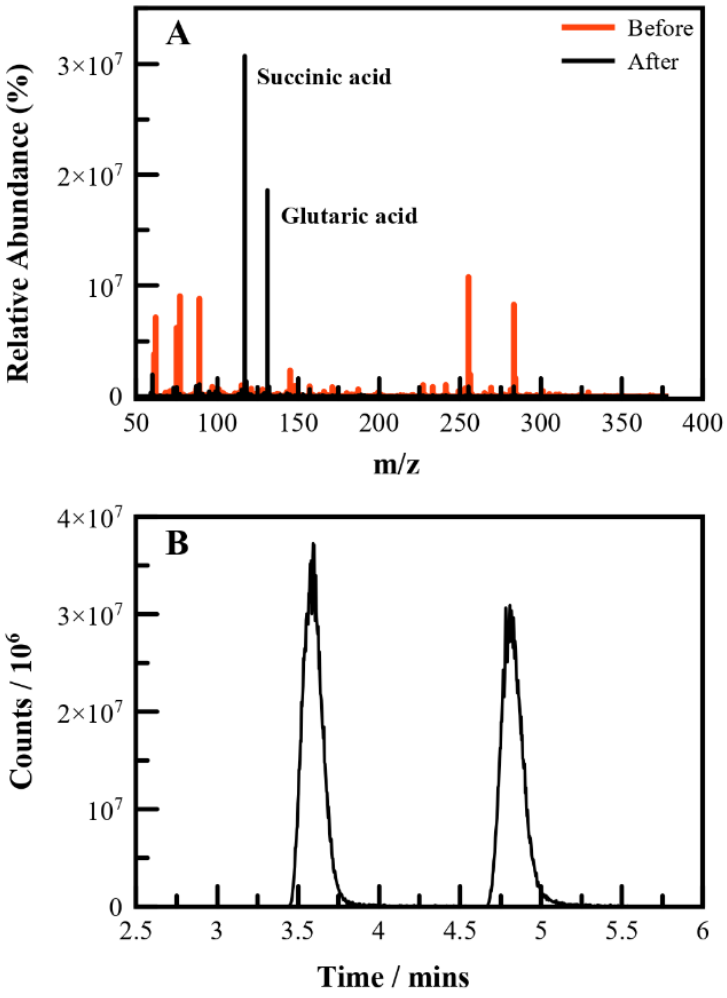

Figure 1: (A) Mass spectra recorded for a binary mixture of succinic acid and glutaric acid. Red data represents the mass spectrum recorded prior (background) to particle sampling whereas black data represents the background subtracted mass spectra of the chemical species recorded during MS analysis of particle composition. Note that the y-axis corresponds to the relative abundance of each acid in the same particle. **(B)** Extracted ion chronogram of the peaks corresponding to glutaric acid present in a mixture with succinic acid. The counts correspond to the intensity of the molecular ion peak relating to the glutaric acid. The intensity decreases with time as a result of the evaporation of the glutaric acid from the particles.

6.3.6. Evaporation Model

A steady-state isothermal evaporation model was used to relate the measured evaporation rate of diacid components to their vapor pressure. Continuum regime kinetics were applied due to the large size of the particle relative to the mean free path of the evaporating molecules, which gives a Knuden number of ~0.01.[29] For a general system containing multiple components with index *i*, the mass flux from a particle of radius *a* is related to the vapor pressure, $p_{i,a}$, through *equation 2*:

$$\frac{dm_i}{dt} = \frac{4\pi a M_i D_i}{RT}\left(p_{i,\infty} - p_{i,a}\right) \qquad (2)$$

where m_i is the mass of component *i* in the droplet, M_i is the molecular mass of *i*, D_i is the gas-phase diffusion coefficient, *R* is the gas constant, *T* is the temperature, $p_{i,\infty}$ is the environmental partial pressure of *i* , and $p_{i,a}$ is the partial pressure of *i* at the surface of the particle. For the single component diacids, $p_{i,\infty}$ is maintained at the zero, and $p_{i,a}$ represents the pure component vapor pressure of the chemical species.

To derive the vapor pressure using *equation 2*, the density, gas-phase diffusion coefficient and molecular mass of the species of interest are needed. The diffusion coefficient values as a function of temperature were derived for SA, GA, MA and AA using the Chapman-Enskog approach, as shown below in *equation 3*:

$$D_i = 0.0018583\sqrt{T^3\left[\frac{1}{M_i} + \frac{1}{M_{N_2}}\right]}\frac{1}{P\sigma_{i,N_2}^2\Omega_{i,N_2}} \qquad (3)$$

where M_i and M_{N_2} are the molecular masses of component *i* and N_2 respectively, *P* is the gas pressure in atm, σ_{i,N_2} is the binary collision diameter, with $\sigma_{i,N_2} = \frac{1}{2}(\sigma_i + \sigma_{N_2})$, and Ω_{i,N_2} is the collision integral which was determined using the tabulated values presented by Bird et al.[30] and the parameterization of Neufeld et al.[31]

The values necessary for performing the above calculations are provided in **Table 1**. This approach is generally considered to yield gas phase diffusion values that are accurate to within 5%, although some discrepancies up to 13% have been observed,[32] and allows the temperature dependence to be determined.

Table 1. Values for the collision diameter (σ**)** and collision integral (Ω) used to calculate the diffusion coefficient (D_i) for all compounds (MA, SA, GA, AA). See references in the main text.

Compound, *i*	**M_i / g mol^{-1}**	**σ_i / Å**	**$\Omega_{i,N2}$ (298K)**	**$\sigma_{i,N2}$ / Å**	**D_i x 10^{-6} / m^2 s^{-1} (298K)**
Nitrogen	28.00	3.798		3.798	
Malonic Acid	104.06	5.33	1.400	4.564	6.8039
Succinic Acid	118.09	5.69	1.400	4.744	6.0449
Glutaric Acid	132.12	6.01	1.440	4.904	5.8637
Adipic Acid	146.14	6.30	1.375	5.049	5.3872

If the absolute size of the particle is known, as with measurements on spherical particles, and $p_{i,\infty} = 0$, *equation 2* may be re-written as:

$$\frac{da^2}{dt} = \frac{-2M_i D_i p_{i,a}}{\rho RT} \qquad (4)$$

where ρ is the density of the particle. This may be rearranged to solve for $p_{i,a}$ from the measured rate of change of the radius-squared with time. For measurements where the radius was not directly measured, as in the case of non-spherical solid particles, an estimate of the initial radius was required and a subsequent numerical simulation of the evolving mass using *equation 2* was performed. The model generates an output of mass versus time, which was normalized to the starting value and compared against the experimental normalized V_{DC} data. The value of $p_{i,a}$ was varied in order to achieve agreement between the measured and modelled evaporation trends.

6.4. Results and Discussion

6.4.1. In-Situ Temperature Calibration

To characterize vapor pressures as a function of temperature, a reliable measurement of temperature was required. A thermocouple in the aluminum chamber wall of the LQ-EDB was used to control the heater output, but the exact temperature experienced by a levitated particle is lower than in the walls due to the low thermal conductivity of air in the chamber. In this work, we used the evaporation rate of a well-characterized chemical compound (glycerol) to solve *equation 2* for T, with a known value of $p_{i,a}$. The temperature dependent vapor pressure of glycerol was determined from an empirical expression:

$$\ln\left(p_{i,a} \,/\, kPa\right) = A \times \ln(T) + \frac{B}{T} + C + D \times T^2 \quad (5)$$

with coefficients $A = -2.12586 \times 10^{1}$, $B = 1.67263 \times 10^{4}$, $C = 1.65510 \times 10^{2}$ and $D = 1.10048 \times 10^{-5}$ taken from the CHERIC database. In previous measurements at room temperature, this relation has been shown to be accurate.[33]

Measurements were made on the size-evolution of glycerol particles trapped at a range of temperatures, from 293 to 333 K, and the evaporation rate of the particle was determined under dry conditions to avoid the complicating effects of water uptake. **Figure 2A** shows the radius evolution of three particles at three different temperatures. To compare the influence of temperature alone on the evaporation rate, the size must be factored out. When integrating *equation 4*, one arrives at the expression:

$$a^2 = kt + a_0^2 \qquad (6)$$

where a_0 is the starting size and *k* is the evaporation rate given by:

$$k = \frac{-2M_i D_i p_{i,a}}{\rho RT} \qquad (7)$$

We can rearrange *equation 6* to:

$$\frac{a^2}{a_0^2} = \frac{k}{a_0^2} t + 1 \qquad (8)$$

and, thus, a plot of $\frac{a^2}{a_0^2}$ versus $\frac{t}{a_0^2}$ will yield a straight line that depends only on *k*. **Figure 2B** shows this relationship and leads to straight line plots that vary only due to the temperature, giving a clear indication of the influence of temperature on the evaporation rate.

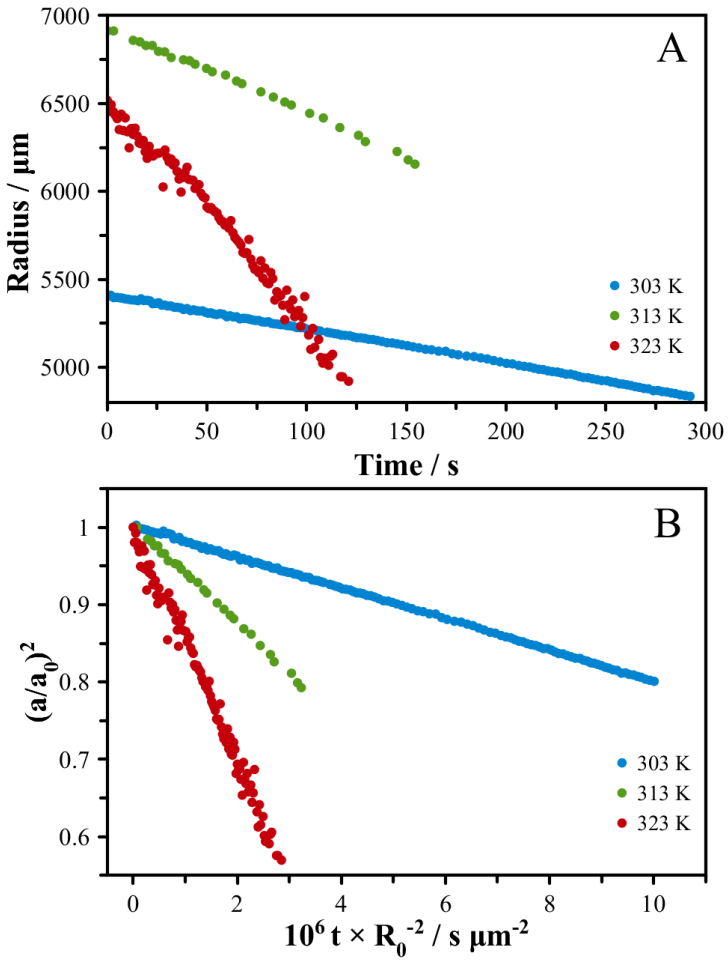

Figure 2: (A) Radius evolution of glycerol particles at temperatures from 303 – 323 K using MRS. **(B)** Temperature dependence on evaporation with influence of size omitted.

From these data and the parameterized vapor pressure (*equation 5*), the temperature was determined by solving *equation 4* and yielded a linear dependence of the calculated temperature as a function of the set-point temperature (**Figure 3A**). The uncertainty in the calculated T of $\pm$1 K is determined from a $\pm$10% uncertainty in the value of D_i (for glycerol) and does not consider any uncertainty in the values of $p_{i,a}$. **Figure 3A** shows good agreement between the set and calculated temperature of the trap, with a small negative deviation of the trap temperature form the set temperature, as expected based on

thermal conductivity and heat loss to the environment. A comparison of the vapor pressure derived using the evolving mass of the particle in an electrostatic analysis yielded values that agreed within 10%.

Further temperature calibration to higher temperatures was not possible using glycerol due to the rapid rate of evaporation and the inability for the MDR's to be resolved due to the rapid change in particle size. Instead, measurements were performed on another semi-volatile organic molecule, 1,2,6-hexanetriol, at up to 347 K, with a vapor pressure 50 × lower than glycerol at room temperature. This system was chosen as there are literature sources against which the results can be compared. The vapor pressure measured as a function of temperature is shown in **Figure 3B**.

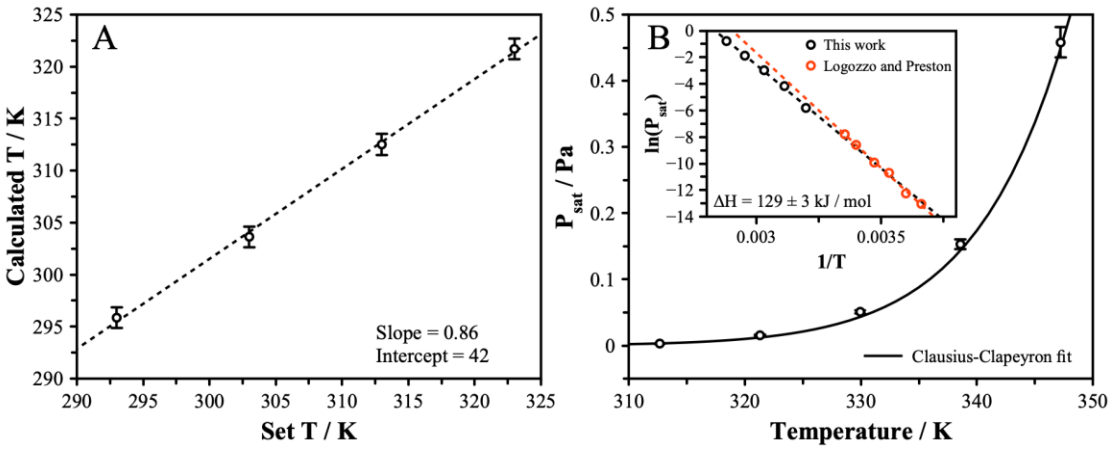

Figure 3: (A) The evaporation of a glycerol particle was used to derive the temperature in the LQ-EDB using Mie resonance spectroscopy. Determination of the actual temperature inside the LQ-EDB using the linear relationship between calculated and set temperature. **(B)** The vapor pressure trend of 1,2,6-hexanetriol is shown as a function of temperature for our data and that of Logozzo and Preston.[34] Figure inset shows the calculated value for the enthalpy of vaporization of 1,2,6-hexanetriol using the linear slope of $\log_e(P_{sat})$ versus 1/T for our data. See text for a discussion of the connection with the data reported by Logozzo and Preston.[34]

These data agree well with the low temperature measurements of Logozzo and Preston,[34] and yield an estimate for the enthalpy of vaporization to be $\Delta H^{\circ} = 129 \pm 3$ kJ / mol. Compared to the value obtained from the Logozzo and Preston data of 144 kJ / mol (note the value reported in the original manuscript was incorrectly stated to be 154 kJ /mol), it is clear that measurements over a large range of temperatures are required for accurately constraining the enthalpy. When combining both datasets, we arrive at a value of 130 ± 2 kJ /mol. Note that the uncertainty quoted reflects an error in the linear fit and does not account for systematic errors in any parameters.

6.4.2. Morphology and Vapor Pressure of Single Component Particles

The vapor pressures of all four diacids were determined by conducting evaporation measurements at temperatures varying from 303 to 353 K in increments of 10 K. The odd/even alteration in carbon number of these diacids influence their morphologies, and dry particles exist as either amorphous super-cooled liquid or crystalline solid particles. Adipic acid ($n_C = 6$) and succinic acid ($n_C = 4$) samples were both observed to consistently form a solid, non-spherical particle morphology under dry conditions, indicating these systems effloresced to a crystalline solid state. Glutaric acid and malonic acid were observed to randomly form either solid, non-spherical particles or spherical, amorphous super-cooled liquid particles following trapping. The morphology affects the rate of evaporation resulting in differences in their vapor pressures corresponding to the different enthalpies of the super-cooled and crystalline states. In all cases, the amorphous super-cooled liquids showed larger vapor pressures than their crystalline counterparts. A

summary of the morphologies adopted by particles across a range of temperatures is shown in the **Table 2**. Although various factors were explored to explain the formation of crystalline versus amorphous states in these particles, no consistent explanation was determined. Instead, the process is likely stochastic in nature, with molecular diffusion playing a determining role in whether the particle achieves a thermodynamic equilibrium state. We discuss the results and dynamics of each diacid in the following sections.

Table 2: Summary of particle morphology at each temperature for each diacid as determined by Mie resonance spectroscopy. 'C' represents crystalline morphology whereas 'A' represents amorphous morphology. Note that Mie resonance sizing was performed for only amorphous particles, whereas electrostatic analysis was performed for both amorphous and crystalline particles.

Diacid	**Carbon #**	**Temperature / K**					
		303	313	323	333	343	353
Malonic Acid (MA)	3	C / A	C / A	A	A	A	A
Succinic Acid (SA)	4	C	C	C	C	C	C
Glutaric Acid (GA)	5	C / A	C / A	C / A	C / A	C / A	C / A
Adipic Acid (AA)	6	C	C	C	C	C	C

6.4.2.1. Succinic Acid

Succinic acid particles were observed to form a solid crystalline phase on drying, indicated by the complete loss of structure in the broadband light scattering spectra. The temperature dependence on the evaporation rates of SA particles was investigated across 303 to 353 K and the vapor pressures were determined at these temperatures. Due to the crystalline state, the electrostatic method was used to derive vapor pressures, with the size estimated by the starting solution concentration. The vapor pressure increases with

temperature, as depicted in **Figure 4A**, where each open circle is the average of at least three evaporation measurements performed at a specific temperature, with error bars depicting the standard deviation in derived vapor pressure. The origin of the ~10% uncertainty comes from environmental factors in the trap, such as small changes in RH and temperature that affect the conditions experienced by the particle, and particle shape effects. The surface area to volume ratio determines the rate of evaporation and it is assumed in the analysis of these measurements that the particle adopts a spherical morphology. Because it is not the case, there is an absolute uncertainty based on the shape factor and a random error that arises from the different shape factors arising due to the morphology adopted by the particle.

The calculated vapor pressure ranged from 8.9×10^{-5} to 3.7×10^{-2} Pa from 303 to 353 K, respectively. Literature data of the vapor pressure at 298 K report values in the range 3.9×10^{-5} to 1.5×10^{-3} Pa, compared to our extrapolated value of 2.2×10^{-5} Pa.[20,22,35,36] The vapor pressure at 298 K in this study shows agreement within the range of literature values. In their compilation of data at 298 K, Bilde et al.[11] find a best value of $7.7^{+5}_{-3} \times 10^{-5}$ Pa for the solid-state vapor pressure, which is higher than our value. However, the spread in values for this system are large and our measurements fall within the reported ranges. Indeed, Soonsin et al.[15] showed that the evaporation of SA particles shows two vapor pressures indicating two possible crystal arrangements. The first of which contained enclosed water and amorphous portions, while the second arrangement was due to the loss of enclosed water and the further crystallization of the amorphous portions.[11,15]

The temperature dependence of the vapor pressure allows us to establish a value for the enthalpy of sublimation of succinic acid. Using the Clausius-Clapeyron equation in conjunction with experimental vapor pressures, the enthalpy of sublimation was found to be 134 ± 9 kJ/mol, as shown in **Figure 4A**, which is comparable to the value reported by Cappa et al.[22] of 128 kJ/mol but is lower than the literature average reported by Bilde et al. of 115±15 kJ/mol.[11]

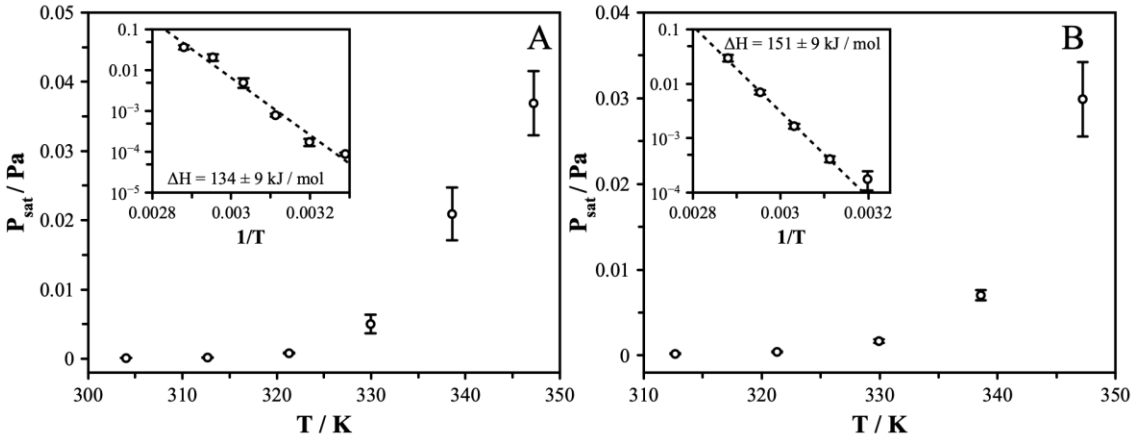

Figure 4: The experimentally determined vapor pressure as a function of temperature using the MRS for: **(A)** Succinic acid, and **(B)** Adipic acid. Inset figures show Clausius-Clapeyron plots (note that the y-axis is represented with $\log_{10}$ rather than $\log_e$) along with the enthalpy of sublimation derived from the linear slope of $\log_e(P_{sat})$ and 1/T. Error bars represent the standard deviation in the vapor pressure values for repeat measurement at each temperature.

6.4.2.2. Adipic Acid

Adipic acid follows a similar trend to succinic acid as the next even-number diacid in the homologous series. Again, due to its crystalline morphology we used the electrostatic analysis approach to determine vapor pressure and measured vapor pressures in the range of 4.50 x 10^{-5} Pa to 2.8 x 10^{-2} Pa for 303 to 353 K, respectively. In this system, low

temperature measurements deviate to slightly higher vapor pressures than expected based on a linear fit of $\log_e(P_{sat})$ versus inverse temperature, as dictated by the Clausius-Clapeyron relation. Higher temperature measurements were closer to the expected trend and are discussed here.

The temperature dependence of vapor pressure of AA, as depicted in **Figure 4B**, shows a similar trend to SA, but is comparatively lower due to the differences in molecular structure and weight. Literature vapor pressures are found in the wide range of 6.0 x 10^{-6} Pa to 2.8 x 10^{-4} at a temperature of 298 K.[21,35] Extrapolating our data to this temperature using the Clausius-Clapeyron equation yields an estimated value of 1.4 x 10^{-5} Pa which is within the literature value range and agrees well with the best estimate compiled by Bilde et al. of $1.9^{+1.4}_{-0.8}$ x 10^{-5} Pa.[11] Direct measurements under room temperature conditions are challenging due to the very slow change in the particle size and the relatively low precision of the electrostatic measurements compared to optical measurements of size. The enthalpy of sublimation for AA was determined to be 129 ± 9 kJ / mol, falling lower than the values reported by Cappa et al.[22] but within the range of values reported by Bilde et al.[11]

6.4.2.3. Glutaric Acid

Glutaric acid particles were encountered in both spherical amorphous states and non-spherical crystalline states across all temperatures. It is not clear what factors control the final morphology of these particles. Slow drying by controlling the RH, temperature changes, and particle size were not found to strongly impact the formation of one phase over another. At high temperatures (333 K to 343 K), amorphous particles were

consistently observed, perhaps due to the system being closer to the melting temperature or experiencing more rapid drying. To generate the non-spherical crystalline particles to probe under these conditions, particles were trapped at lower temperatures, where non-spherical particle formation was more typically observed. A general observation pointed to freshly made glutaric acid stock solutions producing non-spherical particles, while older solutions produced more spherical particles. This was a purely empirical observation, and we have no explanation for its origin. No changes in the solution were expected and no exposure to either the light or ambient gas phase reactants was possible that might cause chemical changes.

One hypothesis, unsubstantiated by literature or experiment, points to dimers or small clusters remaining stable in solution for extended times that can nucleate a crystal phase. These clusters breakdown over time as they become fully solubilized. This explanation requires a very slow kinetic process to drive changes in the solution over time and efforts to test this theory by sonicating and heating the solution did not yield any differences in behavior. At this point, we conclude that formation of a solid crystalline phase is a stochastic process and may involve multiple steps due to the formation of polymorphs in glutaric acid resulting in a highly non-linear dependence of particle phase on many different properties and processes.

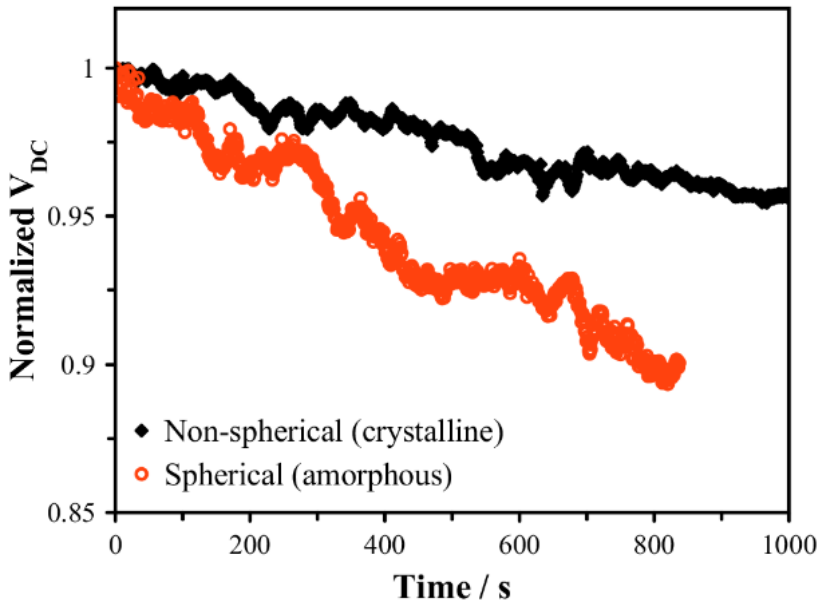

Figure 5: Comparison of the normalized DC voltage from a non-spherical (black) and spherical (red) glutaric acid particle as derived from the respective electrostatic analysis. Over the same period, spherical particles evaporate much quicker than their non-spherical counterpart which can be attributed to the differences in their morphologies as described in the text.

For the purposes of this work, we accept that samples were generated with either crystalline or amorphous character and analyze the behavior of these systems accordingly. A direct comparison of the slope of the DC voltage of a spherical versus a non-spherical particle is shown in **Figure 5** showing that a spherical particle evaporates considerably faster than the non-spherical particle.

The particles are easily segregated into spherical and non-spherical by comparing the Mie resonance spectra, clearly showing the different morphologies, as seen in **Figure 6**.

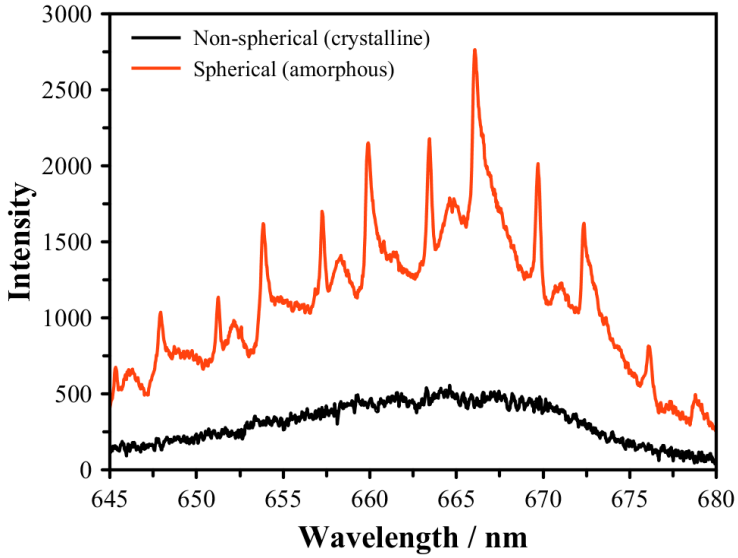

Figure 6: Comparison of Mie resonance spectra for a non-spherical (back) and spherical (red) glutaric acid particle. Absence of sharp peaks in the Mie resonance spectrum indicates a non-spherical particle.

In the case of the non-spherical particles, the electrostatic analysis method was applied to determine the vapor pressure as a function of temperature, shown in **Figure 7A**. At 298K, the value we determine was 4.4 x 10^{-5} Pa, which is on the low end of the literature data compiled and reported by Bilde et al.,[11] with a literature average value for the crystal state to be $1.7^{+1.5}_{-0.8}$ x 10^{-4} Pa (**Figure 7B**). From a Clausius-Clapeyron analysis, the enthalpy of sublimation was determined to be 154±9 kJ / mol. This is higher than many literature values and the vapor pressure values measured here were considerably lower, indicating that a more stable state was measured in these experiments. As reported by Yeung et al.,[37] GA has two crystalline forms with different thermal stabilities. At lower temperatures the β-form is stable while the α-form is found to be stable at higher temperatures. The energy difference between the crystal polymorphs is on the order of 2 kJ / mol and it is not possible to distinguish the difference based on the enthalpy of sublimation alone.[38]

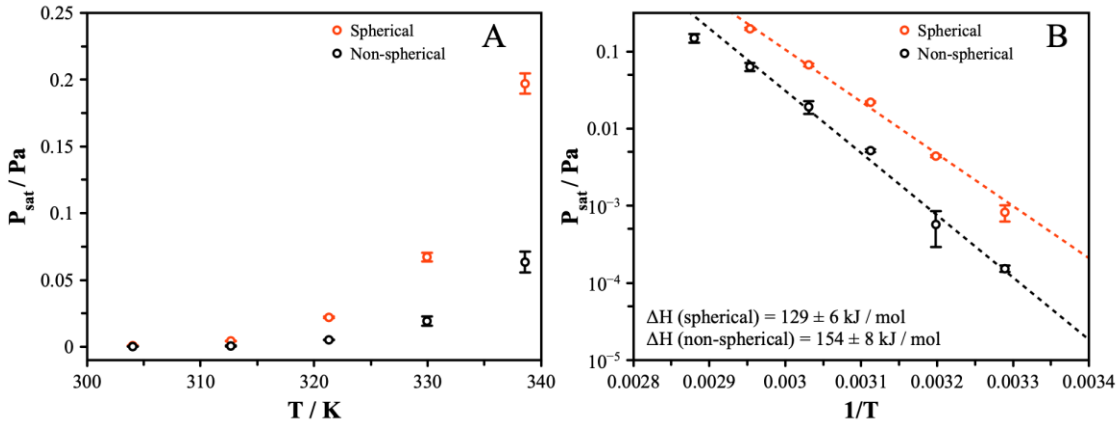

Figure 7: (A) Comparison between the derived vapor pressures for both spherical (red) and non-spherical (black) glutaric acid particles. The non-spherical vapor pressures were consistently lower than the spherical particle vapor pressures across all temperatures due to the differences in morphology. **(B)** The enthalpy of sublimation for both spherical and non-spherical morphologies of glutaric acid was calculated using the linear relationship between $\log_e P_{sat}$ and 1/T. Again, non-spherical enthalpies were lower at each temperature compared to spherical particles and error bars represent their respective standard deviation in the vapor pressure values for different measurement trials at each temperature.

For spherical particles, the size evolution was analyzed using Mie theory, and yielded vapor pressures that were considerably higher. These are shown in *Figure 7A* and reveal values that are around 5× higher than the solid particles. At 298K, the vapor pressure is estimated to be 4.6×10^{-4} Pa, which is lower than the value reported by Bilde et al. of $1.0^{+0.3}_{-0.2} \times 10^{-3}$Pa but falls within the broad range of values in the literature.[11] The enthalpy of vaporization here was found to be 129 ± 6 kJ / mol, in agreement with literature values, but falling above the literature average compiled by Bilde et al.[11,20,22,35,36] The difference in the enthalpy between our measured solid and super-cooled states is on the same order as values for the enthalpy of fusion of glutaric acid, indicating that the amorphous phase is consistent with the super-cooled liquid.[38]

6.4.2.4. Malonic Acid

Malonic acid (MA) , like glutaric acid (GA), is an odd-numbered dicarboxylic acid and showed both amorphous and crystalline character. The crystalline phase was only observed at 303 and 313 K, and vapor pressures at these temperatures were determined using electrostatic analysis to be on the order of 5.5 x 10^{-5} and 2.3 x 10^{-4} Pa, respectively. A full Clausius-Clapeyron analysis was not performed due to the limited data available as a function of temperature. As with the case of glutaric acid, the vapor pressures for the crystalline particles were around an order of magnitude lower than the amorphous particles. For MA, the evaporation of amorphous particles presented some interesting observations. **Figure 8** shows the radius evolution of a single particle held at 333 K.

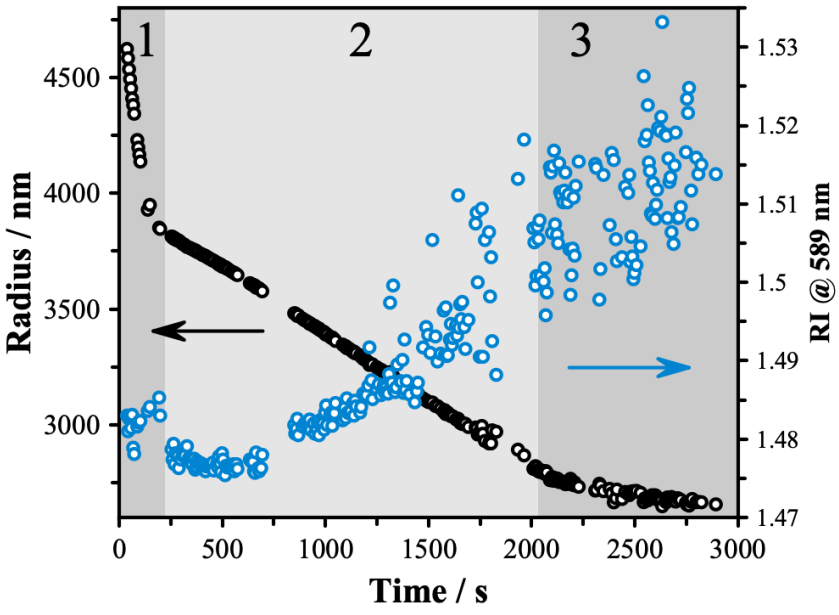

Figure 8: The evaporation of malonic acid over 3000s showed an evolution in both the radius and refractive index (RI) as described by the Mie resonance spectroscopy. Three distinct slopes were observed which are marked by the shaded region. This also corresponds to a simultaneous increase in RI over the course of the measurement.

It is clear from the above plot that there are multiple distinct slopes in the data, indicating possible phase transitions that lead to reduced vapor pressure and evaporation rate. This change in slope was observed from the radius data, derived from Mie resonance spectroscopy, and the electrostatic data. At 333 K temperature, three slopes were identified, but the data begins to break down, as seen in Figure 8. This was due to a degradation of the spectra and the small absolute size of the particle.

To confirm the purity of the compound, the composition of the starting solution was probed using electrospray ionization mass spectrometry (Q Exactive Focus Orbitrap MS) in both positive and negative ionization modes. A prominent peak was observed at m/z consistent with the singly deprotonated parent compound, and lack of any significant peaks above the background confirms that sample was not measurably contaminated. During the evaporation, the refractive index was observed to change in conjunction with the size. The RI depends on many factors, such as composition, density, and temperature. Given that the composition was pure, and the temperature was constant, the change in RI may indicate a change in the particle phase to one with a higher density. It should be noted, however, that there is a larger uncertainty in the RI than the radius, and this is apparent as the scatter in the RI increases significantly. An analysis of the two slopes (1 and 2, indicated in *Figure 8*) and the resulting estimates of the vapor pressure from each of the slopes is shown in **Figure 9A and 9B**.

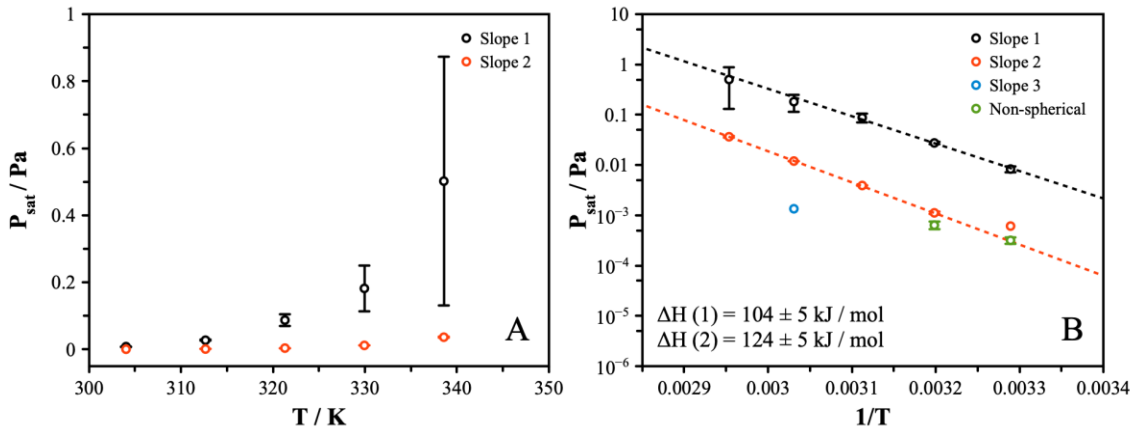

Figure 9: (A) A comparison of the derived vapor pressure for the first (black) and second (red) slopes observed during the evaporation of MA. The second slope vapor pressure is lower than the first slope due to their difference in evaporation rate. **(B)** Relationship between $\log_e(P_{sat})$ and 1/T for four different phases attributed to three distinct MA polymorphs (black, red, and blue) and the MA solid phase (green). The corresponding enthalpy of vaporization was derived for both slopes 1 and 2 using the method previously discussed.

Extrapolating to 298 K, the vapor pressures predicted from slope 1 and slope 2, respectively, are 0.004 and 1.3 x 10^{-4}. Data from slope 1 indicate a higher vapor pressure than the super-cooled value compiled by Bilde et al.[11] ($6.2^{+3.2}_{-2.1} \times 10^{-4}$ Pa) that were extrapolated from measurements on aqueous solutions, while much close agreement is observed for slope 2 when compared against the reported solid vapor pressure ($1.7^{+1.1}_{-0.7} \times 10^{-4}$ Pa). Both slopes show a temperature dependence as expected from the Clausius-Clapeyron equation, with a ~20 kJ /mol difference in the estimated enthalpy of vaporization (104 ± 5 kJ /mol versus 124±5 kJ /mol for amorphous super-cooled and solid-state crystal phases, respectively). This change in enthalpy is around the difference observed between amorphous and crystalline glutaric acid, but falls slightly lower than literature data for the enthalpy of fusion (of 23 kJ / mol).[39] This indicates that over the

course of measurement, the sample may be undergoing a phase transition. Indeed, the Mie spectra show clear peaks initially, indicating that the particle remains spherical. Over time, during slope 2, the peaks in the spectra become less well resolved, as evidenced by the degradation of the spectra resulting in increased scatter in the radius and RI output, indicating that the particle tends towards a non-spherical morphology. The values of vapor pressure for slope 2 are slightly higher than the values reported on particles that were crystalline from the start of the measurement, indicating the particle may be a mix of crystalline and amorphous during this regime. Slope 3 in *Figure 8* was only observed in limited cases, and due to the small size of the particle at this point, the estimated vapor pressure using these data is not reliable, falling significantly below the other data. However, it is likely that this represents the fully crystalline state with the amorphous contribution having been eliminated.

Several factors may be contributing to these observations. The existence of many malonic acid polymorphs likely gives rise to the transitions between phases during the measurement.[40] While the stability and thermodynamics of up to five polymorphs have been explored in the solid state, it is not known what forms will be available to levitated particles prepared following rapid drying from aqueous solution droplets, as is the case here. Additionally, malonic acid can undergo a keto-enol tautomerization in aqueous solution. Recent work indicates this is accelerated in droplets; however, the timescales are still on the order of hundreds to thousands of seconds, with the rate slowing at lower RH.[41] Given our droplets experience rapid drying immediately after generation, it is likely that the keto-enol ratio will be dictated by the conditions in the dilute starting solution. The

equilibrium constant strongly favors the keto-form and, thus, we assume that our sample particles are primarily consisting of this tautomer.[42]

6.4.3. Morphology and Composition of Binary Component Particles

To characterize the evaporation dynamics of levitated particles containing mixtures of dicarboxylic acids, both Mie resonance spectroscopy (MRS) and mass spectroscopy (MS) measurements were utilized to characterize their morphology and compositional evolution, respectively. We study the effect of mixture compositions on the evaporation kinetics under dry conditions by characterizing the change in the MS peak areas associated with the levitated droplets throughout the transformation timescale. For this, we focus on the three binary diacid compositions, namely, malonic acid (MA) and succinic acid (SA), succinic acid (SA) and glutaric acid (GA), and glutaric acid (GA) and adipic acid (AA). These measurements were carried out on trapped particles at a range of temperatures, from 40 °C (313 K) to 80 °C (353 K). We additionally explore the influence of the carbon chain and odd/even alteration on physicochemical characteristics due to intra- and inter-molecular interactions between the organic molecules. These experimental studies help in determining the vapor pressure and evaporation dynamics as a function of composition and temperature in case of semi-volatile organic mixture compositions.

6.4.3.1. Malonic Acid and Succinic Acid Mixture

The evaporation rate of malonic acid and succinic acid mixture (MA+SA) under dry conditions is dominated by the more rapid evaporation of MA than SA at all five chosen

temperatures. A comparison of the evolving chemical composition associated with individual components due to the evaporation of levitated particles is shown in **Figure 10**. The difference in the evaporation rates of MA and SA becomes less prominent around the highest achievable temperature. It can be attributed to the fact that the more rapidly evaporating component was already partially evaporated by the time the first measurement was made, lowering its mole fraction in the particle. For the MA+SA mixture, the MS measurements reveal that MA showed half the ionization efficiency than SA.

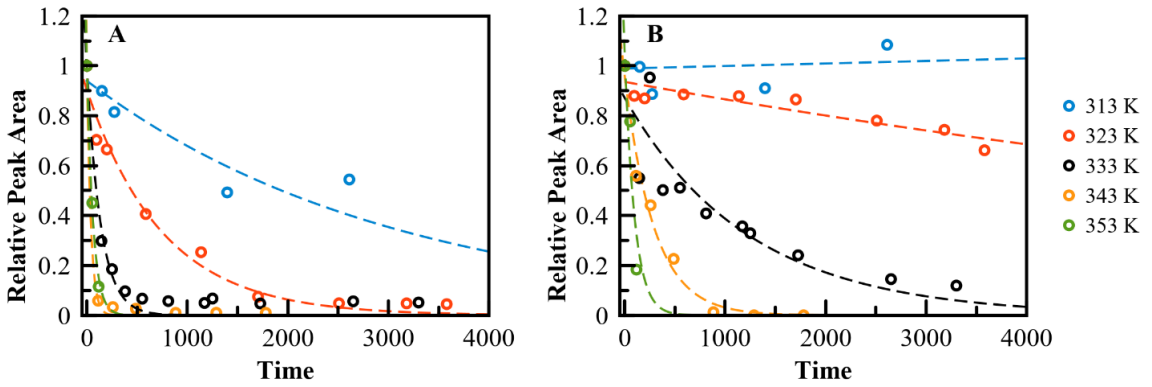

Figure 10: (A) The MS compositional evolution of malonic acid (MA) due to its evaporation in the levitated particle stack under dry conditions. **(B)** The compositional evolution of succinic acid (SA) due to its evaporation in the levitated particle stack under dry conditions. In both plots, the color-coded data points represent the evaporation trends at specific temperatures as listed on the right side of the figures. The fit to the data points serves as a guide for the eye and is shown by the dashed lines corresponding to respective data points having same color coding.

An analysis of the phase state and morphology was also carried out. The spectra generated by the MRS indicated the formation of only crystalline phase states due to the absence of sharp peaks associated with spherical amorphous particles. The crystalline phase state was exclusively observed at all temperatures which is contrary to observations

of both amorphous and crystalline phase states exhibited by pure MA. The transformation of the MA phase state is a consequence of the influence of even-numbered molecules of SA resulting in inter-molecular interactions that allow for efficient packing of the molecules and a strong thermodynamic preference towards a crystalline state. This may further have implications in lowering the effective vapor pressure of MA due to its crystalline phase state in the binary component diacid mixture.

6.4.3.2. Succinic Acid and Glutaric Acid Mixture

Figure 11 shows the evolution in the chemical composition associated with the individual components present in the succinic acid and glutaric acid mixture (SA+GA). The evaporation dynamics is dominated by the more rapid evaporation of GA than SA at all four temperatures (except highest temperature). This is attributed due to the odd-numbered molecules present in GA having a higher vapor pressure than even-numbered molecules of SA, as discussed in the pure component case. Additionally, a similar trend as with the MA+SA, was observed for this mixture in which the interactions between the functional groups of the SA and GA molecules influence the phase state of GA. Contrary to both amorphous and crystalline phase states exhibited by GA in pure component particles, the binary mixture particles containing GA showed only the crystalline phase state. This was evidenced by the absence of sharp peaks in the spectra generated by MRS which confirmed the presence of crystalline phase state.

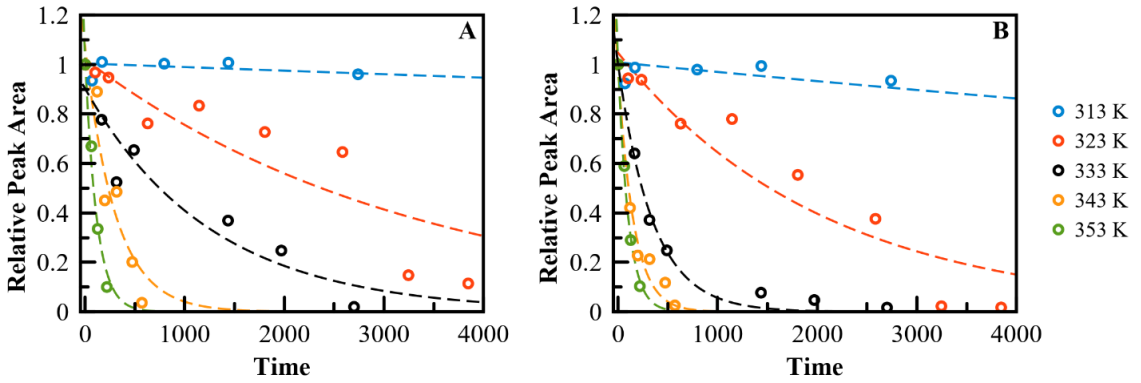

Figure 11: (A) The MS compositional evolution of succinic acid (SA) due to its evaporation in the levitated particle stack under dry conditions. **(B)** The compositional evolution of glutaric acid (GA) due to its evaporation in the levitated particle stack under dry conditions. In both plots, the color-coded data points represent the evaporation trends at specific temperatures as listed on the right side of the figures. The fit to the data points serves as a guide for the eye and is shown by the dashed lines corresponding to respective data points having same color coding.

6.4.3.3. Glutaric Acid and Adipic Acid Mixture

Another mixture of binary diacid components composed of glutaric acid (GA) and adipic acid (AA) was explored to understand if it follows the similar trend observed in the other two mixtures. AA being the biggest molecule out of the studied diacids has a tendency to evaporate the slowest due to its low vapor pressure. Similar to previous observations, GA evaporates much faster as compared to AA in its GA+AA binary mixture due to high effective vapor pressure of GA. Additional comparisons of the GA gas-phase partitioning between different mixtures yield that GA evaporates faster when present with SA than AA at lower temperatures.

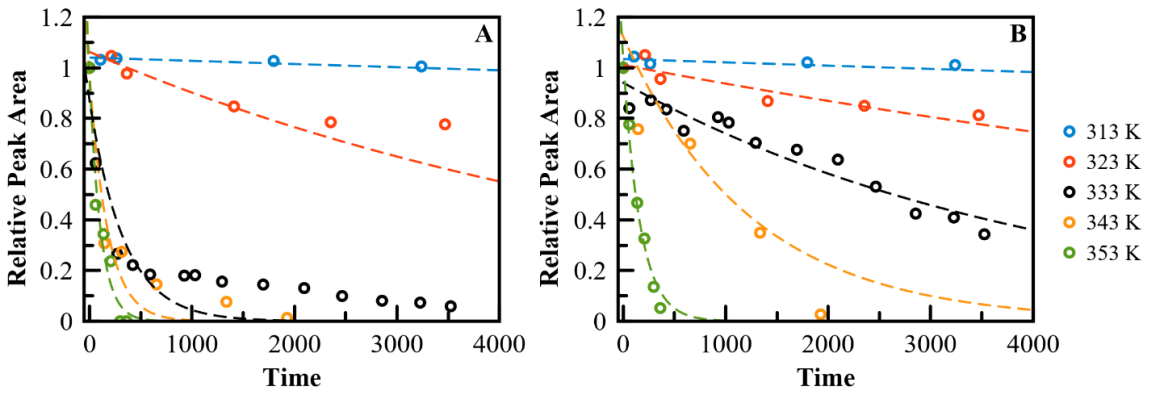

Figure 12: (A) The MS compositional evolution of glutaric acid (GA) due to its evaporation in the levitated particle stack under dry conditions. **(B)** The compositional evolution of adipic acid (AA) due to its evaporation in the levitated particle stack under dry conditions. In both plots, the color-coded data points represent the evaporation trends at specific temperatures as listed on the right side of the figures. The fit to the data points serves as a guide for the eye and is shown by the dashed lines corresponding to respective data points having same color coding.

6.5. Summary and Conclusions

We report measurements on the rate of evaporation of particles levitated in a linear quadrupole electrodynamic balance at elevated temperatures and derive the vapor pressure of pure component dicarboxylic acids. We rely on mass spectrometry analysis for measuring the evaporation dynamics of individual components present in the binary component dicarboxylic acid mixtures. Through analysis of the physical state adopted by the particles in our measurements, we explore the connection between the vapor pressure and the formation of amorphous or crystalline phase states. We have reported vapor pressure explorations for the pure and mixed dicarboxylic acid molecules across a range of temperatures (up to ~350 K) previously unexplored in the literature for levitated particles. To aid comparisons, we have reproduced our values for the vapor pressure at 298 K and

enthalpies for the pure component diacids, along with literature data, in **Table 3**.

Table 3: Summary of all data corresponding to the measurements and relevant literature. Literature values were obtained from Bilde et al.[11] from their comprehensive analysis and averaging of literature data. We refer readers to the reference contained therein for original sources.

Species	P_{sat} **(298 K) / Pa**	ΔH **/ kJ mol^{-1}**	P_{sat} **(298 K) / Pa Lit.**	ΔH **/ kJ mol^{-1} Lit.**
Malonic acid (amorphous)	$4.0\pm0.4 \times 10^{-3}$	104 ± 5	$6.2^{+3.2}_{-2.1} \times 10^{-4}$	115 ± 22
Malonic acid (crystalline)	$1.3\pm0.2 \times 10^{-4}$	124 ± 5	$1.7^{+1.1}_{-0.7} \times 10^{-4}$	111 ± 15
Succinic acid	$2.2\pm0.2 \times 10^{-5}$	134 ± 9	$7.7^{+5}_{-3} \times 10^{-5}$	115 ± 15
Glutaric acid (amorphous)	$4.6\pm0.3 \times 10^{-4}$	129 ± 6	$1.0^{+0.3}_{-0.2} \times 10^{-3}$	100 ± 5
Glutaric acid (crystalline)	$4.4\pm0.4 \times 10^{-5}$	154 ± 8	$1.7^{+1.5}_{-0.8} \times 10^{-4}$	130 ± 11
Adipic acid	$1.4\pm0.1 \times 10^{-5}$	129 ± 9	$1.9^{+1.4}_{-0.8} \times 10^{-5}$	131 ± 18

The literature data, taken from the meta-analysis of Bilde et al.[11], represent averages of many experimental datasets spanning a varied range of temperatures and, while some of our data falls outside the compiled averages, the same trends are observed with respect to the influence of phase, molecular size and temperature.

As expected, an odd/even alteration in physical state was observed with changing number of carbon atoms. Even-number molecules, which are known to exhibit lower solubility, were observed to form the crystalline phase under all conditions, as evidenced by the loss of spectral features in the Mie resonance spectra. Odd-numbered molecules were observed to randomly form either the crystalline phase or an amorphous super-cooled liquid phase. While it was not possible to control the phase state adopted by the particle, unambiguous identification of the phase state was inferred from the persistence of resonance peaks in the spectra (amorphous) or the loss of structure features typical of crystallization (solid). These measurements allow for a direct comparison of the effect of phase state using particles generated and manipulated in the same experimental procedures.

Consistent with previous studies that compile measurements from multiple techniques to achieve a comparison between amorphous and solid phase states, we show that crystal phase state vapor pressures are on the order of 4× to 10× lower than their amorphous counterparts. These measurements also allowed both the enthalpy of vaporization and sublimation for the compounds of interest to be determined, with values generally consistent with previous estimates derived from low temperature measurements. The differences observed between the crystalline and super-cooled liquid states were consistent with the enthalpy of fusion, validating assertions of the ascribed phase state. In the case of malonic acid, abrupt changes in the evaporation rate were observed, indicating a change of phase over the course of the measurement. This was not observed in glutaric acid and may be attributed to the greater mobility of malonic acid molecules due to the smaller size.

A unique influence on the phase states is exhibited by the individual diacid components present in binary mixtures. Due to these differing vapor pressures, the chemical composition evolves continuously as more volatile species evaporate. Previous studies to predict the gas-particle partitioning of semi-volatile species lack the detail required for precise evaluations of the evolving chemical composition. These diacid mixtures show both the intramolecular and intermolecular interactions due to the presence of the carboxylic acid functional groups which results in a deviation from ideality. The resulting non-ideality introduces complicating factors, such as the alteration of activity coefficients with carbon-number and the particle physical state, which influences evaporation dynamics. Contrary to pure components in which odd-number molecules exhibited both amorphous and crystalline phase states, the binary mixtures of these odd-number molecules exhibited only crystalline morphologies at all temperatures with no exceptions. Additionally, such deviations lead to changes in the evaporation kinetics associated with individual components, however, the general trend of even-number molecules exhibiting higher vapor pressure due to efficient packing of the molecules (as observed in pure component measurements) still hold true for mixture compositions. Further analysis of binary component mixtures will reveal how the composition affects the effective vapor pressure of organic compounds in binary mixtures. The utilization of the modelling measurements can help in predicting the variations in the values of the effective vapor pressure associated with the individual components and the influence of composition and phase on the effective vapor pressures.

Compared to the extensive previous literature exploring these systems, summarized in the previously cited review by Bilde et al.,[11] this work provides evidence that the amorphous phase states of these compounds, previously shown only at room temperature and below, persist at elevated temperatures up the maximum accessible temperature of our methods. A convergence of the phase state is expected as the melting point is approached, the persistence of amorphous phases at high temperature provides an opportunity to measure vapor pressure across a broad range of temperatures. While the presence of amorphous phase states is true for single (pure) component dicarboxylic acids, the binary component dicarboxylic acid mixtures showed the existence of only crystalline phase states at all the temperatures considered for the experimental measurements. This allows for improved estimates of the vapor pressure at low temperatures relevant to the atmosphere, as discussed in the following section.

6.5.1. Atmospheric Relevance

Although these measurements were performed for sample particles at elevated temperatures, the thermodynamic data are well described using a simple Clausius-Clapeyron equation. This allows vapor pressure to be estimated at low temperatures through a linear extrapolation of $\log_e(P_{sat})$ versus inverse temperature. We have demonstrated several important factors in this work that will inform future studies on the vapor pressure and volatility of atmospheric samples. Firstly, at least in the cases explored here, amorphous super-cooled liquid phases persist even at elevated temperatures, indicating that volatility basis sets derived from thermal desorption methods for SOA

samples should yield similar results to isothermal measurements.[43] Secondly, using isothermal measurements above ambient temperatures, we can establish and estimate vapor pressure for low volatility species that would otherwise evaporate too slowly under ambient conditions. This allows a methodology for establishing vapor pressures and volatilities for low and extremely low volatility organic compounds.

However, given the chemical complexity of atmospheric aerosol particles, binary mixtures of the dicarboxylic acids were also studied as it is unclear how informative any pure component measurements are for estimating the vapor pressure of individual component in mixtures. When the phase state is taken as an additional complicating factor, single valued vapor pressures are not sufficient to fully describe the behavior of these systems. Furthermore, the phase states adopted by the particles containing mixtures of odd and even numbered acids were explored, and the thermodynamics that describe volatilization of species in complex atmospheric particles is even less well-constrained.

Thus, we coupled the high temperature LQ-EDB to a high-resolution mass spectrometer to perform a compositional analysis of complex mixtures as they undergo evaporation.[44–46] This facilitates a molecularly-resolved understanding of the chemical evolution and connect the experimental findings to the physical and thermodynamic properties of the complex organic mixtures present in the atmospheric aerosol particles.

6.6. References

(1) Hallquist, M.; Wenger, J. C.; Baltensperger, U.; Rudich, Y.; Simpson, D.; Claeys, M.; Dommen, J.; Donahue, N. M.; George, C.; Goldstein, A. H.; Hamilton, J. F.; Herrmann, H.; Hoffmann, T.; Iinuma, Y.; Jang, M.; Jenkin, M. E.; Jimenez, J. L.; Kiendler-Scharr, A.; Seinfeld, J. H.; Surratt, J. D.; Szmigielski, R.; Wildt, J. The Formation, Properties and Impact of Secondary Organic Aerosol: Current and Emerging Issues. *Atmospheric Chem. Phys.* **2009**, *9* (14), 5155–5236. https://doi.org/10.5194/acp-9-5155-2009.

(2) Bilde, M.; Pandis, S. N. Evaporation Rates and Vapor Pressures of Individual Aerosol Species Formed in the Atmospheric Oxidation of α- and β-Pinene. *Environ. Sci. Technol.* **2001**, *35* (16), 3344–3349. https://doi.org/10.1021/es001946b.

(3) D'Ambro, E. L.; Schobesberger, S.; Zaveri, R. A.; Shilling, J. E.; Lee, B. H.; Lopez-Hilfiker, F. D.; Mohr, C.; Thornton, J. A. Isothermal Evaporation of α-Pinene Ozonolysis SOA: Volatility, Phase State, and Oligomeric Composition. *ACS Earth Space Chem.* **2018**, *2* (10), 1058–1067. https://doi.org/10.1021/acsearthspacechem.8b00084.

(4) Donahue, N. M.; Robinson, A. L.; Trump, E. R.; Riipinen, I.; Kroll, J. H. Volatility and Aging of Atmospheric Organic Aerosol. *Atmos. Aerosol Chem*. McNeill, V. F., Ariya, P. A., Eds.; *Top. Curr. Chem.* **2014**, *339*, 97–143. https://doi.org/10.1007/128_2012_355.

(5) McDonald, B. C.; de Gouw, J. A.; Gilman, J. B.; Jathar, S. H.; Akherati, A.; Cappa, C. D.; Jimenez, J. L.; Lee-Taylor, J.; Hayes, P. L.; McKeen, S. A.; Goldstein, A. H.; Harley, R. A.; Frost, G. J.; Roberts, J. M.; Ryerson, T. B.; Trainer, M. Volatile Chemical Products Emerging as Largest Petrochemical Source of Urban Organic Emissions. *Science* **2018**, *359* (6377), 760–764. https://doi.org/10.1126/science.aaq0524.

(6) Qin, M.; Murphy, B. N.; Isaacs, K. K.; McDonald, B. C.; Lu, Q.; McKeen, S. A.; Koval, L.; Robinson, A. L.; Efstathiou, C.; Allen, C.; Pye, H. O. T. Criteria Pollutant Impacts of Volatile Chemical Products Informed by Near-Field Modelling. *Nat. Sustain.* **2021**, *4* (2), 129–137. https://doi.org/10.1038/s41893-020-00614-1.

(7) Yilmaz, E.; Tian, T.; Wong, V. W.; Heywood, J. B. An Experimental and Theoretical Study of the Contribution of Oil Evaporation to Oil Consumption. *SAE Trans.* **2002**, *111* (4), 1182–1193. https://doi.org/10.4271/2002-01-2684.

(8) Gough, M. A.; Rowland, S. J. Characterization of Unresolved Complex Mixtures of Hydrocarbons in Petroleum. *Nature* **1990**, *344*, 648–650. https://doi.org/10.1038/344648a0.

(9) Gough, M.; Rowland, S. Characterization of Unresolved Complex Mixtures of Hydrocarbons from Lubricating Oil Feedstocks. *Energy Fuels* **1991**, *5* (6), 869–874. https://doi.org/10.1021/ef00030a016.

(10) Ravikumar, V.; Senthilkumar, D.; Solaimuthu, C. Evaporation Rate and Engine Performance Analysis of Coated Diesel Engine Using Raphanus Sativus Biodiesel and Its Diesel Blends. *Int. J. Ambient Energy* **2015**, *38* (2), 1–7. https://doi.org/10.1080/01430750.2015.1086673.

(11) Bilde, M.; Barsanti, K.; Booth, M.; Cappa, C. D.; Donahue, N. M.; Emanuelsson, E. U.; McFiggans, G.; Krieger, U. K.; Marcolli, C.; Topping, D.; Ziemann, P.; Barley, M.; Clegg, S.; Hallquist, M.; Hallquist, Å. M.; Reid, J. P.; Pagels, J.; Rarey, J.; Zardini, A. A.; Riipinen, I. Saturation Vapor Pressures and Transition Enthalpies of Low-Volatility Organic Molecules of Atmospheric Relevance: From Dicarboxylic Acids to Complex Mixtures. *Chem. Rev.* **2015**, *115* (10), 4115–4156. https://doi.org/10.1021/cr5005502.

(12) Pope, F. D.; Tong, H.-J.; Dennis-Smither, B. J.; Griffiths, P. T.; Clegg, S. L.; Reid, J. P.; Cox, R. A. Studies of Single Aerosol Particles Containing Malonic Acid, Glutaric Acid, and Their Mixtures with Sodium Chloride. II. Liquid-State Vapor Pressures of the Acids. *J. Phys. Chem. A* **2010**, *114* (37), 10156–10165. https://doi.org/10.1021/jp1052979.

(13) Rozaini, M. Z. H.; Brimblecombe, P. The Odd Even Behaviour of Dicarboxylic Acids Solubility in the Atmospheric Aerosols. *Water. Air. Soil Pollut.* **2009**, *198* (1–4), 65–75. https://doi.org/10.1007/s11270-008-9826-5.

(14) Bilde, M.; Svenningsson, B.; Mønster, J.; Rosenørn, T. Even−Odd Alternation of Evaporation Rates and Vapor Pressures of C3−C9 Dicarboxylic Acid Aerosols. *Env. Sci. Technol.* **2003**, *37* (7), 1371–1378.

(15) Soonsin, V.; Zardini, A. A.; Marcolli, C.; Zuend, A.; Krieger, U. K. The Vapor Pressures and Activities of Dicarboxylic Acids Reconsidered: The Impact of Physical State of Aerosol. *Atmos. Chem. Phys.* **2010**, *10*, 11753–11767. https://doi.org/10.5194/acpd-10-20515-2010.

(16) Huisman, A. J.; Krieger, U. K.; Zuend, A.; Marcolli, C.; Peter, T. Vapor Pressures of Substituted Polycarboxylic Acids Are Much Lower than Previously Reported. *Atmos. Chem. Phys.* **2013**, *13* (13), 6647–6662. https://doi.org/10.5194/acp-13-6647-2013.

(17) Bilde, M.; Svenningsson, B.; Rosenorn, T. Even Odd Alternation of Evaporation Rates and Vapor Pressures of Dicarboxylic Acid Aerosol. *Environ. Sci. Technol.* **2003**, *37*, 1371–1378.

(18) Tao, F.; Bernasek, S. L. Understanding Odd−Even Effects in Organic Self-Assembled Monolayers. *Chem. Rev.* **2007**, *107* (5), 1408–1453. https://doi.org/10.1021/cr050258d.

(19) Salo, K.; Jonsson, Å. M.; Andersson, P. U.; Hallquist, M. Aerosol Volatility and Enthalpy of Sublimation of Carboxylic Acids. *J. Phys. Chem. A* **2010**, *114* (13), 4586–4594. https://doi.org/10.1021/jp910105h.

(20) Koponen, I. K.; Riipinen, I.; Hienola, A.; Kulmala, M.; Bilde, M. Thermodynamic Properties of Malonic, Succinic, and Glutaric Acids: Evaporation Rates and Saturation Vapor Pressures. *Environ. Sci. Technol.* **2007**, *41* (11), 3926–3933. https://doi.org/10.1021/es0611240.

(21) Booth, A. M.; Barley, M. H.; Topping, D. O.; McFiggans, G.; Garforth, A.; Percival, C. J. Solid State and Sub-Cooled Liquid Vapour Pressures of Substituted Dicarboxylic Acids Using Knudsen Effusion Mass Spectrometry (KEMS) and Differential Scanning Calorimetry. *Atmos. Chem. Phys.* **2010**, *10*, 487. https://doi.org/10.5194/acp-10-4879-2010.

(22) Cappa, C. D.; Lovejoy, E. R.; Ravishankara, A. R. Determination of Evaporation Rates and Vapor Pressures of Very Low Volatility Compounds: A Study of the C 4 −C 10 and C 12 Dicarboxylic Acids. *J. Phys. Chem. A* **2007**, *111* (16), 3099–3109. https://doi.org/10.1021/jp068686q.

(23) Chattopadhyay, S.; Ziemann, P. J. Vapor Pressures of Substituted and Unsubstituted Monocarboxylic and Dicarboxylic Acids Measured Using an Improved Thermal Desorption Particle Beam Mass Spectrometry Method. *Aerosol Sci. Technol.* **2005**, *39* (11), 1085–1100. https://doi.org/10.1080/02786820500421547.

(24) Soonsin, V.; Zardini, A. A.; Marcolli, C.; Zuend, A.; Krieger, U. K. The Vapor Pressures and Activities of Dicarboxylic Acids Reconsidered: The Impact of Physical State of Aerosol. *Atmos. Chem. Phys.* **2010**, *10*, 11753–11767. https://doi.org/10.5194/acp-10-11753-2010.

(25) Krieger, U. K.; Marcolli, C.; Reid, J. P. Exploring the Complexity of Aerosol Particle Properties and Processes Using Single Particle Techniques. *Chem. Soc. Rev.* **2012**, *41* (19), 6631. https://doi.org/10.1039/c2cs35082c.

(26) Preston, T. C.; Reid, J. P. Determining the Size and Refractive Index of Microspheres Using the Mode Assignments from Mie Resonances. *J. Opt. Soc. Am. A* **2015**, *32* (11), 2210. https://doi.org/10.1364/JOSAA.32.002210.

(27) Bohren, C. F.; Huffman, D. R. Absorption and Scattering of Light by Small Particles; *John Wiley and Sons*, New York, **1983**.

(28) Davies, J. F.; Price, C. L.; Choczynski, J.; Kohli, R. K. Hygroscopic Growth of Simulated Lung Fluid Aerosol Particles under Ambient Environmental Conditions. *Chem. Commun.* **2021**, *57* (26), 3243–3246. https://doi.org/10.1039/D1CC00066G.

(29) Kulmala, M. Condensational Growth and Evaporation in the Transition Regime. *Aerosol Sci. Technol.* **1993**, *19* (3), 381–388. https://doi.org/10.1080/02786829308959645.

(30) Bird, R. B.; Stewart, W. E.; Lightfoot, E. N. Transport Phenomena. *John Wiley and Sons*, Second ed., New York, **2002**.

(31) Neufeld, P. D.; Janzen, A. R.; Aziz, R. A. Empirical Equations to Calculate 16 of the Transport Collision Integrals Ω(l, s)* for the Lennard-Jones (12–6) Potential. *J. Chem. Phys.* **1972**, *57* (3), 1100–1102. https://doi.org/10.1063/1.1678363.

(32) Marrero, T. R.; Mason, E. A. Gaseous Diffusion Coefficients. *J. Phys. Chem. Ref. Data* **1972**, *1* (1), 3–118. https://doi.org/10.1063/1.3253094.

(33) Davies, J. F.; Haddrell, A. E.; Reid, J. P. Time-Resolved Measurements of the Evaporation of Volatile Components from Single Aerosol Droplets. *Aerosol Sci. Technol.* **2012**, *46* (6), 666–677. https://doi.org/10.1080/02786826.2011.652750.

(34) Logozzo, A.; Preston, T. C. Temperature-Controlled Dual-Beam Optical Trap for Single Particle Studies of Organic Aerosol. *J. Phys. Chem. A* **2022**, *126* (1), 109–118. https://doi.org/10.1021/acs.jpca.1c09363.

(35) Riipinen, I.; Koponen, I. K.; Frank, G. P.; Lehtinen, K. E. J.; Bilde, M.; Kulmala, M. Adipic and Malonic Acid Aqueous Solutions: Surface Tensions and Saturation Vapor Pressures. *J. Phys. Chem. A* **2007**, *111* (50), 12995–13002. https://doi.org/10.1021/jp073731v.

(36) Mønster, J.; Rosenørn, T.; Svenningsson, B.; Bilde, M. Evaporation of Methyl- and Dimethyl- Malonic, Succinic, Glutaric and Adipic Acid Particles at Ambient Temperatures. *J. Aerosol Sci.* **2004**, *35*, 1453–1465. https://doi.org/10.1016/j.jaerosci.2004.07.004.

(37) Yeung, M. C.; Ling, T. Y.; Chan, C. K. Effects of the Polymorphic Transformation of Glutaric Acid Particles on Their Deliquescence and Hygroscopic Properties. *J. Phys. Chem. A* **2010**, *114* (2), 898–903. https://doi.org/10.1021/jp908250v.

(38) Espeau, P.; Négrier, P.; Corvis, Y. Crystallographic and Pressure Temperature State Diagram Approach for the Phase Behavior and Polymorphism Study of Glutaric Acid. *Cryst. Growth Des.* **2013**, *13* (2), 723–730. https://doi.org/10.1021/cg301442f.

(39) Hansen, A. R.; Beyer, K. D. Experimentally Determined Thermochemical Properties of the Malonic Acid/Water System: Implications for Atmospheric Aerosols. *J. Phys. Chem. A* **2004**, *108* (16), 3457–3466. https://doi.org/10.1021/jp0376166.

(40) Reddy, J. P.; Delori, A.; Foxman, B. M. Molecular and Crystal Structure of a New Polymorph of Malonic Acid with Z′=3. *J. Mol. Struct.* **2013**, *1041*, 122–126. https://doi.org/10.1016/j.molstruc.2013.03.017.

(41) Kim, P.; Continetti, R. E. Accelerated Keto Enol Tautomerization Kinetics of Malonic Acid in Aqueous Droplets. ACS *Earth Space Chem.* **2021**, *5* (9), 2212–2222. https://doi.org/10.1021/acsearthspacechem.1c00221.

(42) Leopold, K. R.; Haim, A. Equilibrium, Kinetics, and Mechanism of the Malonic Acid-Iodine Reaction. *Int. J. Chem. Kinet.* **1977**, *9* (1), 83–95. https://doi.org/10.1002/kin.550090108.

(43) Tikkanen, O.-P.; Buchholz, A.; Ylisirniö, A.; Schobesberger, S.; Virtanen, A.; Yli-Juuti, T. Comparing Secondary Organic Aerosol (SOA) Volatility Distributions Derived from Isothermal SOA Particle Evaporation Data and FIGAERO–CIMS Measurements. *Atmos. Chem. Phys.* **2020**, *20* (17), 10441–10458. https://doi.org/10.5194/acp-20-10441-2020.

(44) Kohli, R. K.; Davies, J. F. Measuring the Chemical Evolution of Levitated Particles: A Study on the Evaporation of Multicomponent Organic Aerosol. *Anal. Chem.* **2021**, *93* (36), 12472–12479. https://doi.org/10.1021/acs.analchem.1c02890.

(45) Kaur Kohli, R.; Van Berkel, G. J.; Davies, J. F. An Open Port Sampling Interface for the Chemical Characterization of Levitated Microparticles. *Anal. Chem.* **2022**, *94* (8), 3441–3445. https://doi.org/10.1021/acs.analchem.1c05550.

(46) Jacobs, M. I.; Davies, J. F.; Lee, L.; Davis, R. D.; Houle, F.; Wilson, K. R. Exploring Chemistry in Microcompartments Using Guided Droplet Collisions in a Branched Quadrupole Trap Coupled to a Single Droplet, Paper Spray Mass Spectrometer. *Anal. Chem.* **2017**, *89* (22), 12511–12519. https://doi.org/10.1021/acs.analchem.7b03704.

CHAPTER 7

Exploring the Influence of Particle Phase in the Ozonolysis of Oleic and Elaidic Acid

7.1. Abstract

Aerosol particles in atmosphere undergo heterogeneous transformations due to their interactions with various gas-phase oxidants such as ozone. While it is known that these reactions can be significantly affected by the phase state of the particle, a direct comparison between the reaction kinetics and product distributions for the same reactive process occurring in the different phases remains elusive. This study uses single particle levitation and flow-tube methods to measure and compare the ozonolysis of particles containing oleic acid and its *trans* isomer elaidic acid in liquid, supercooled liquid, and solid states. We measure their evolving size, optical properties, phase, and chemical composition during reaction. Both primary reactions and secondary chemistry were also explored, along with the influence of particle phase state on reaction kinetics and product formation. Notably, we directly compare the reaction kinetics of supercooled liquid elaidic acid particles with liquid oleic acid particles, revealing similar uptake coefficients indicative of similar inherent reactivity of the C=C moiety. We go on to compare the kinetics of solid elaidic acid particles, formed due to solidification at room temperature and freezing at low temperature, revealing a significant slowing in kinetics that may be attributed to the phase of the particle. We further explore differences in the product distributions between particles

exhibiting different phase states. These results provide important insights into how the chemical aging of ambient aerosol particles may be influenced by their physicochemical characteristics.

7.2. Introduction

Aerosol particles are an important component of the atmosphere that have a variety of effects on the climate, air quality, visibility, and human health.[1–6] They influence global radiation balance by scattering and absorbing incoming solar radiation,[7,8] reduce the air quality of a region as a source of fine particles that can penetrate deep into the lungs,[9,10] contribute to various health problems such as asthma and other respiratory illness,[4,5] and act as nuclei for cloud droplets leading to the formation of clouds and precipitation.[1,11–14] The relative magnitude and importance of these effects is determined by the coupled effects of parameters such as the size distribution, chemical composition, and physical properties of the constituent aerosol particles.[15–17] The chemical composition is primarily determined by the source of the aerosol,[18–20] but chemical reactions in the atmosphere change the composition leading to changes in both the physical properties and size distributions of aerosol particles.[21–24] There are several dominant mechanisms for aerosol chemistry to occur in the atmosphere, including photochemical reactions, heterogeneous reactions, and aqueous phase reactions due to the uptake of water.[25–29] In this work, we focus on heterogeneous reactions involving ozone, an oxidant that is responsible for the degradation of unsaturated organic compounds.

Oxidative aging of aerosol particles containing unsaturated organic compounds, such as fatty acids, is a major chemical transformation that has been studied for many years due to its implications to atmospheric chemistry.[30–32] It is a heterogeneous process that occurs when aerosol particles are exposed to reactive oxygen species, namely ozone, which leads to the formation of new compounds with different chemical properties. This alteration of chemical composition further leads to changes in their physical properties, such as size, morphology, volatility, hygroscopicity and optical properties, which affects their role in environmental processes as well as how they subsequently interact with reactive species.[33,34] Further, heterogeneous aging of aerosol particles contributes to the formation of diverse chemical functionalities, including dicarboxylic acids, ketones, aldehydes, keto-aldehydes, and carboxylic acids.[27,35–37] Understanding the chemical fate of aerosols containing unsaturated compounds through reactions with ozone assists in predicting and mitigating their environmental and health impacts. To achieve this, laboratory-based techniques, including single particle levitation and ensemble measurements using chambers and flow-tubes, have been relied upon for exploring aerosol chemistry.[38–44] Efforts to measure the composition of these aerosol particles undergoing ozonolysis in both measurement techniques have relied mainly on mass spectrometry.[23,45–47]

Recent studies have shown that single particle measurements, which allow for the study of the molecular composition of super-micron levitated particles for an extended reaction timescale at low oxidant concentrations, may be an effective means of probing aerosol chemistry. Several articles have discussed the application of electrodynamic balance-mass spectrometry measurements of single particles to explore the ozonolysis of unsaturated

organic particles.[48–50] These studies provide an alternative approach to the more established flow-tube techniques, which focus on sub-micron particles and often use high oxidant concentrations to measure reaction parameters, such as the uptake coefficient, across atmospherically relevant exposures (conc. × time). Although the uptake coefficient is formulated to be independent of size and oxidant concentration, previous studies have shown inverse size dependences in uptake coefficient, which may be attributed to diffusion limitations.[51] Further, oxidant concentration and particle size may play a role in the reaction mechanism due to the influence of secondary chemistry and the rate of vapor partitioning for semi-volatile products.[26] Exploring both particle size and oxidant concentration motivates combined studies that utilize both sub-micron and super-micron methods to gain a more complete picture of aerosol chemistry.

The heterogeneous oxidation of oleic acid (mono-saturated omega-9 fatty acid) by ozone has been the subject of many experimental studies. Initially explored as a benchmark case in the development of new experiments to probe aerosol chemistry,[45] it has been the focus of many studies exploring the kinetics, reaction mechanisms and product branching ratios.[47,51–53] It is a significant component of indoor particulate matter due to its production during cooking,[18] and is a useful proxy for unsaturated organic compounds found in secondary organic aerosol. Elaidic acid, the *trans*-stereoisomer of oleic acid, is not a major component of atmospheric aerosol, but presents an opportunity to explore the influence of different phase states on the oxidation of particles while retaining the same fundamental chemical reactivity. The double bond of alkane chain in EA is *trans*, allowing EA molecules to remain straight and pack efficiently, resulting in a high melting point and a

solid state at room temperature. In case of OA, the *cis* double bond leads to a kink and bend of the alkyl chain, inducing steric hindrance that prevents efficient packing of the molecules, leading to a lower melting point and a liquid state at room temperature.

Recent measurements in an urban environment have compared the ozonolysis of oleic acid with elaidic acid, showing that the latter decays at 62% the rate of the former in real-world conditions, although the phase of the particles is not determined.[54] Laboratory studies for exploring the reaction kinetics in different phase states reported that particles in which crystallization was induced by cooling below room temperature demonstrated reactivity decreased by a factor of 12 compared to supercooled particles of the same composition.[55] Interest in how the phase state affects heterogeneous reactivity goes back to the initial observations of highly viscous phase states of organic aerosol particles.[56,57] Both experiments and modelling studies have shown that high viscosity leads to slow diffusion, impacting reaction kinetics and the chemical evolution of aerosol particles.[58–61] It is important to note, however, that the influence of viscosity and diffusion limitations depends on the timescales of the process.[53,62] At high oxidant concentrations, diffusion limitations would be expected to be more significant, as the timescales are reduced giving the system less time to diffusively mix. This points towards a potential oxidant concentration dependence that may couple with a size-dependence in determining the influence of diffusivity on the chemical evolution. Although oleic acid particles are expected to remain liquid, and thus not exhibit diffusion limitations under ambient conditions, diffusion may still play a role at high oxidant concentrations or with very large particles. Furthermore, recent work by Xu et al. using optical microscopy has shown that

ozonolysis can lead to the formation of a new phase morphology, which is a result of liquid-liquid phase separation.[62] In the work of Milsom et al., the self-organization of oleic acid into nanostructured lamellar structures was reported to influence oxidation kinetics.[63] The influence of phase on the ozonolysis of oleic acid has been explored by mixing oleic acid with stearic acid and lauric acid.[64,65] While these studies show that embedding oleic acid in a solid or viscous matrix will lead to slower reactions, they do not directly explore how phase influences chemistry, as the composition of the particles is modified in order to vary the phase state.

In this work, we study and compare reactive transformations of oleic acid (OA, *cis*-isomer) and elaidic acid (EA, *trans*-isomer) due to heterogeneous ozonolysis, with an emphasis on characterizing the phase of particles during the reaction. This chemical system provides a unique opportunity to explore reactivity based on phase state for molecules that are very similar with little chemical perturbation to the system. We use both single particle and flow-tube methods, allowing a wider range of sizes and conditions to be explored and compared than either method alone. We use a linear quadrupole electrodynamic balance (LQ-EDB) coupled with mass spectrometry (MS) to precisely analyze single levitated particles undergoing ozonolysis in real-time. Using broadband light scattering, we can determine the size and optical properties of spherical particles, and gain insight into the morphology following phase separation. Sequential sampling of particles from the LQ-EDB to the open-port sampling interface (OPSI) coupled with an Orbitrap mass spectrometer reveals the chemical composition as a function of time during the reaction.[66,67] We explore different reaction conditions, such as RH and ozone

concentration, to determine their effect on the ozonolysis kinetics and product distributions. By identifying the phase of the particles, we can unambiguously compare the influence of phase on the observed chemical changes in the particles. Further, we compare single particle measurements on super-micron particles with flow-tube measurements on sub-micron particles. Flow-tube measurements were also performed across a range of temperatures to explore the influence of phase changes induced by freezing/melting on the rate of ozonolysis.

7.3. Experimental Section

This section describes the experimental details of both the single particle levitation and the flow-tube methods, including a technical discussion on the electrodynamic balance, flow tube reactor, Mie resonance spectroscopy and mass spectrometry.

7.3.1. Single Particle Levitation

7.3.1.1. Chemicals and Sample Preparation

The chemicals in this study were used as supplied without further purification. Measurements were performed on sample particles containing oleic acid (OA, Sigma, analytical standard, ≥ 99% (GC)) and elaidic acid (EA, Sigma, ≥ 99% (GC)) respectively. Both OA and EA samples were prepared as organic solutions at known concentrations using ethanol (Koptec, 200 Proof Pure Ethanol) and 1-proponal (Acros Organics, 99.5%, for analysis) respectively. Solution concentrations were chosen to yield levitated particles with a radius of around 5 μm, usually 5 to 10 g/L, with a starting size determined by the

microdroplet dispenser. The bulk solutions were transferred to a microdroplet dispenser (Microfab MJ-ABP-01, 30 μm orifice) to generate particles with an initial diameter of approximately 50 μm in a burst mode with a known total number of droplets. The droplet dispenser was powered by a pulse generator, delivering pulses with widths between 20 and 50 μs with a voltage peak of up to 50 V.

To initiate ozonolysis, ozone was generated by passing a low flow of oxygen (20 standard cubic centimeter per minute (sccm)) through a quartz flow tube illuminated with a Hg lamp (Analytik Jena US, UVP Ozone Generator SOG-2) generating broadband UV light. The resulting flow was diluted with nitrogen (180 sccm) to make up a total flow of 200 sccm that was introduced into the LQ-EDB setup. Ozone concentrations were varied by changing the exposure area of UV lamp. Concentrations in the nitrogen flow introduced into the LQ-EDB were measured in a separate calibration process using an ozone monitor (2B Technologies, model 106-L). Dilution factors during the calibration process were determined and the reported ozone concentrations represent those exposed to levitated particles.

7.3.1.2. Particle Levitation and Environmental Control

A linear quadrupole electrodynamic balance (LQ-EDB) was used to levitate a stack of micrometer-sized particles for extended periods of time under controlled environmental conditions. Details on the principle and operation of LQ-EDB have been previously described.[66,68,69] In brief, droplets were generated from organic solutions of the sample using a piezoelectric droplet dispenser and charged due to the presence of an induction

electrode (± 200 to 500 V) at the inlet to the LQ-EDB. The droplets become confined axially by the electrodynamic forces established within a vertically oriented quadrupole supplied with AC voltages (500 to 1000 V at 300 to 1000 Hz). A 532 nm laser (Thorlabs CPS532, 5 mW) was used to illuminate the levitated particles for their visual verification upon initial trapping and positioning of the particles, and was disabled during measurements.

Solvent evaporation during the initial trapping step yielded sample particles confined in the electric fields. A counterbalance DC plate electrode with an applied voltage generated an electrostatic force to balance the forces on particles, including gravitational force and drag force due to gas flow. A continuous dry or humidified gas flow was introduced into the chamber to control the environmental conditions inside the LQ-EDB setup. The relative humidity (RH) inside the LQ-EDB was maintained by varying the ratio of dry and humidified nitrogen gas and a total flow of 200 sccm was typically used. A CMOS camera (Thorlabs DCC1545) was used to image and stabilize the position of the lowermost particle by varying DC voltage through a PID feedback loop, programmed using LabVIEW software. The LQ-EDB setup was coupled with Mie resonance spectroscopy allowing the lowermost particle to be probed in real-time to determine its size and real part of the complex refractive index. Compositional measurements of the particles were carried out by Orbitrap mass spectrometry (MS) that was coupled to the LQ-EDB using an open port sampling interface (OPSI)[67,70,71].

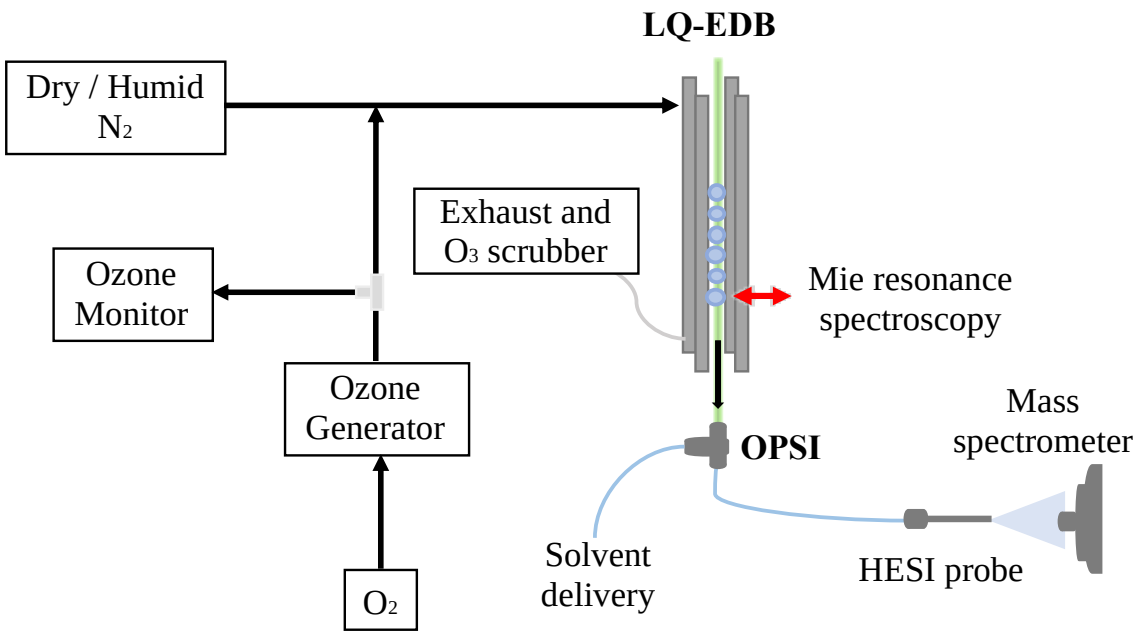

Figure 1: Schematic configuration of the ozonolysis setup including the linear quadrupole electrodynamic balance (LQ-EDB) coupled with mass spectrometer (MS) using open port sampling interface (OPSI) for studying ozonolysis on single levitated particles. A dry or humid flow of nitrogen with ozone generated from a photochemical ozone generator was introduced into the LQ-EDB for initiating heterogeneous transformation. A stack of 5 to 10 particles underwent ozonolysis at the same time, and the lowermost particle was probed in real-time using broadband spectroscopy and then ejected to the OPSI platform for sampling by mass spectrometry.

7.3.1.3. Mie Resonance Spectroscopy

The lowermost particle in the stack was illuminated with a broadband red LED centered at 660 nm with a spectral width (FWHM) of 20 nm. Backscattered light from the particle was collected by optical fiber and delivered to a spectrophotometer (Ocean Insight HR4000). For spherical particles, a spectrum is obtain characterized by sharp resonance peaks associated with wavelengths that form morphology dependent resonances (MDRs) in the particle. The wavelength position of the MDRs is indicative of the size and refractive index of the particle. Using algorithms developed by Preston and Reid, the experimental

wavelength positions are compared to positions predicted by Mie theory for a dynamic library of size and refractive index combinations.[72,73] A least-squares error minimization is performed, and the size is determined with an accuracy and precision of 5 nm and the RI is determined to within 0.001 to 0.005. Changes in the Mie resonance spectra, such as broadening and disappearance of peaks, is indicative of phase transitions, as discussed further in the results. Additionally, non-spherical particles cannot support MDRs, and backscattered spectra show only light reflected from the particle surface.

7.3.1.4. Compositional Analysis Using Mass Spectrometry

Compositional measurements were carried out by individually ejecting levitated particles from LQ-EDB into the open port sampling interface (OPSI) of a Q Exactive Focus Orbitrap Mass Spectrometer (Thermo Scientific). The OPSI acts as a sampling platform which connects LQ-EDB to the Heated Electrospray Ionization (H-ESI) probe of the mass spectrometer (MS). A detailed description of the operating principle, measurement method and data analysis for this procedure is discussed in our earlier works.[67] In brief, the OPSI is continuously fed with a solvent mixture of methanol, doped with trace amounts trans-3-(3-pyridyl)acrylic acid (TPAA, Aldrich, 99% pure) to act as a standard, by a syringe pump (Chemyx Inc., model Fusion 100T). The signal from the standard is analyzed to ensure ESI stability and account for any variations in the MS signal intensity over time. During a measurement, the lowermost particle is ejected from LQ-EDB, by pulsing the DC balancing voltage to zero for tens of milliseconds, prompting one particle to fall below the balancing electrode and out of the trap into the solvent reservoir at the top of OPSI. The

particle dissolves in the solvent, and the analyte solution is drawn into the ESI probe due to the Venturi effect caused by reduced pressure region at probe tip. An electrospray is established at the spray tip and ions are generated according to standard ESI processes[70,74–76]. The ESI nebulizing gas was nitrogen (technical grade, 99.97% pure) and a solvent flow (50 to 70 µL/min) was achieved based on nebulizer gas pressure at a set point of 30 psi. The MS was operated in negative ion mode with a typical scan range of 50 to 1000 m/z, a resolution of 35000 and maximum ion injection time of 100 ms. The resulting mass spectra were initially analyzed using Xcalibur 4.1 software (ThermoFisher Scientific) and extracted ion chronograms for the peaks of interest were exported to data analysis software (MagicPlot Pro 2.8.2) for processing. The compositional abundance of species in each particle was determined in terms of the relative peak area of the respective ions with respect to its starting composition. Calibration measurements using OA, EA, and azelaic acid (AA) were performed to explore the relative ionization efficiencies of typical product compounds relative to the starting reactant.

7.3.2. Flow-Tube Measurements

7.3.2.1. Particle Generation and Characterization

A Pyrex tube was charged with small amounts of either liquid oleic acid (OA, Sigma-Aldrich Co., 99%) or solid elaidic acid (EA, Tokyo Chemical Industry Co. Ltd., >97%). For EA sample, the tube was inserted into a furnace and heated to 105-110 ˚C, at which temperature the solid white elaidic acid crystals melted to a clear liquid. Dry nitrogen at a flow rate of 0.3 standard liters per minute (SLM) at room temperature was passed through

the heated Pyrex tube and polydisperse particles were formed in the resulting flow by homogeneous nucleation. The flow was then passed through an annular charcoal denuder to remove residual organic from the gas phase, as part of a precooling step, entered a loop of copper tubing submerged in the reservoir of the recirculating pump (**Figure 2**) to bring the particles to the desired temperature before passing on to the flow tube. Particle distributions were measured at the exit of the flow tube using a Scanning Mobility Particle Spectrometer (SMPS) consisting of a Differential Mobility Analyzer (3080, TSI Inc.) and a Condensation Particle Counter (3025A, TSI Inc.).

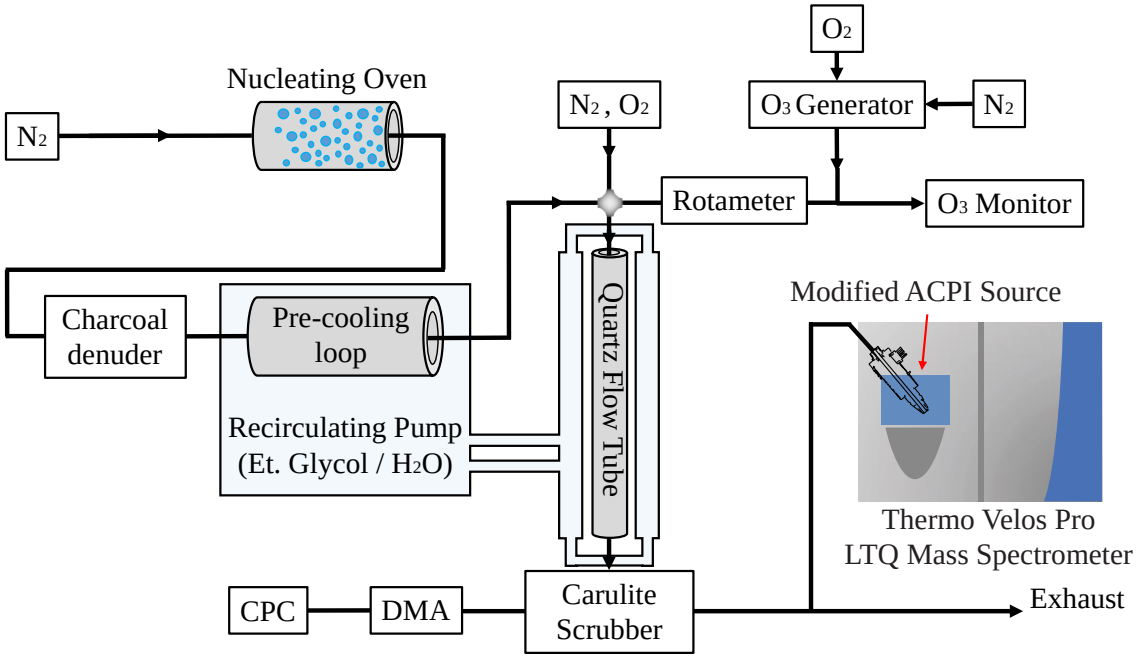

Figure 2: Flow-tube experimental apparatus showing the particle generation, ozone generation, temperature control using a recirculating pump and thermostatic bath, a DMA and CPC for characterizing particle size distributions, and the atmospheric pressure chemical ionization (APCI) source on the mass spectrometer. A full description of the apparatus is provided in the text.

7.3.2.2. Flow Tube Reactor and Temperature Control

Particles and ozone were mixed in a cylindrical quartz flow tube reactor of fixed volume which at a typical total flow of 1.03 SLM (standard liter per minute) results in a residence time of approximately 23 seconds. In addition to the particle-laden 0.3 SLM flow of N_2 from the nucleator oven, 0.5 SLM of pure N_2 and 0.2 SLM of dry O_2 (99.993%, Praxair) were introduced at the inlet of the reactor. Ozone was generated using a 0.1 SLM flow of O_2 into a corona discharge source (Ozone Services, Yanco Industries), after which the flow was diluted with 5 SLM of N_2 in a glass mixing cell. The concentration of O_3 in the flow was measured with a commercial ozone monitor (106M, 2B Technologies) at the exit of the mixing cell. The voltage on the corona discharge source was adjusted to achieve O_3 concentrations in the range 8 – 640 ppm. A rotameter (King Instruments) was used to deliver 30 sccm of the diluted $O_3/O_2/N_2$ flow into the flow tube reactor, where resulting O_3 concentrations range from 0.2 – 20 ppm. At the exit of the flow tube, the flow passed through an annular ozone scrubber packed with Carulite 200 catalyst, which terminated the ozonolysis reaction. The temperature during the reaction was controlled by a chilled 50/50 ethylene glycol and water mixture fed through the outer jacket of the flow tube by a recirculating pump (VWR AD15R-30) with a thermostat setting between -20 and +20 ˚C.

7.3.2.3. APCI Mass Spectrometry

The reaction kinetics for ozonolysis measurements were monitored using a Velos Pro LTQ Mass Spectrometer (Thermo Scientific) fitted with an Atmospheric Pressure Chemical Ionization source, modified to take particle-laden gas flow through a ceramic

inner bore, as described in Roveretto et. al.[77] The outer ceramic inlet tube was heated to 180 ˚C to vaporize the aerosol particles prior to entering the ionization region. The flow into the inlet of the mass spectrometer included the N_2 sheath gas at a flow setting on the mass spectrometer of 1.8 (arbitrary units). The auxiliary gas flow was not used. Mass spectra were recorded with a typical scan range of 50 to 1000 m/z in negative ion mode. The discharge voltage was set to 1.5kV with a typical current of 8 µA. The analyzer region of the mass spectrometer was maintained with helium gas (99.998%, Airgas) at 40 psi. The decay of OA and EA were measured using the intensity of the *m/z* = 281 peak, corresponding to the $[M\text{-}H^+]^-$ ion of each fatty acid. From the mass spectra, chronograms of the parent ions and product ions resulting from ozonolysis were extracted using XCalibur 4.1 for subsequent data analysis in Python.

7.3.3. Kinetic Analysis

To interpret and compare the ozonolysis kinetics across measurements, we apply a simple model to determine the effective rate constant and the uptake coefficient. The loss of OA or EA over time was fit to an exponential decay to give the rate constant according to:

$$\frac{[org]}{[org]_0} = e^{-k_{org}\langle O_3\rangle_t.t}$$

where k_{org} is the effective rate constant for the reaction of OA or EA (i.e. the organic), $\langle O_3\rangle_t$ is the time-averaged ozone concentration, assumed to be equal to the measured ozone concentration, and *t* is time.

Based on the analysis reported by Smith et al.[78], the uptake coefficient, defined as the ratio of the number of reactive decays of OA or EA molecules to the number of collisions with ozone molecules, may be formulated as:

$$\gamma_{O_3}^{org} = \frac{4k_{org}D\rho_{org}N_A}{6\bar{c}M_{org}}$$

where, $\gamma_{O_3}^{org}$ is the ozone uptake coefficient, k_{org} is the rate constant, D is the diameter of the particle, ρ_{org} is the density of reactant, N_A is Avogadro's number, $\bar{c}$ is the mean speed of ozone gas molecules and M_{org} is the molar mass of reactant molecules.

This formulation allows for the surface-to-volume ratio effect on heterogeneous reactions to be normalized, however it does not account for size-dependent and time-dependent processes that may limit reactivity, such as diffusion limitations. It represents a useful tool for comparing across datasets, but care must be taken when interpreting absolute values. The uptake coefficients of super-micron particles using single particle measurements and sub-micron particles using flow-tube measurements are analyzed and compared in the subsequent sections.

7.4. Results and Discussion

A comparison between the ozonolysis of oleic acid (OA) and elaidic acid (EA) is presented to explore the differences in their reactivity and phase behavior that arise from the different orientation of the carbon–carbon double bond. In bulk at room temperature, OA is a liquid while EA is a solid. Both species are soluble in organic solvents, such as

ethanol and 1-propanol, which evaporates after levitation resulting in the formation of either liquid or solid particles. In general, levitated particles containing OA were observed to exist in liquid state, whereas EA attained both supercooled liquid and solid phase states on a pseudo-random basis. Ozonolysis measurements were performed to explore the influence of these phase states on reactivity and reaction mechanisms. Additional measurements using a temperature-controlled flow-tube were performed as a means of comparing phase states using temperature as a control and are discussed in *Section 7.4.4*.

In the following sections we break down the results into discussions of the size, refractive index, and phase morphology of OA and EA super-micron particles undergoing ozonolysis, with information derived from Mie resonance spectroscopy. We go on to discuss the evolving chemical composition using information derived from mass spectrometry. We then discuss measurements of sub-micron particles performed using a flow-tube setup, and finally discuss the influence of factors such as RH and ozone concentrations.

7.4.1. Evolution of Size, Refractive Index and Phase State of Single Levitated Particles

7.4.1.1. Oleic Acid

The size and RI of liquid oleic acid particles were determined using Mie resonance spectroscopy and are shown in **Figure 3A**. The radius decreases as the reaction progresses and semi-volatile products are evolved into the gas phase, discussed in more detail later. In most experiments, this led to an increase in the RI as the ozonolysis proceeds indicating the changing chemical composition, leading to changes in the optical properties of particle.

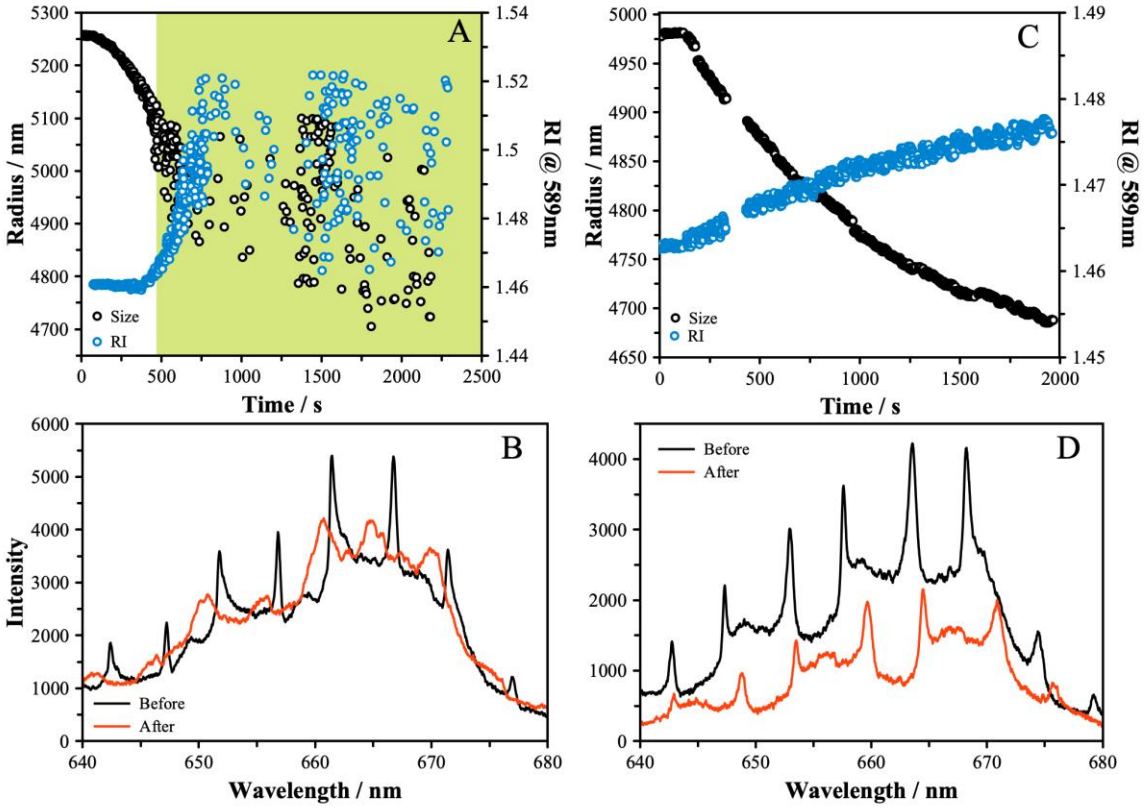

Figure 3: (A) Size and RI evolution of liquid OA particles exposed to 2.3 ppm of O_3 under dry conditions using Mie resonance spectroscopy. The black points correspond to the sequentially measured radius of all particles in the stack, and the blue points correspond to the RI of the particles. The accuracy of size is determined to be within 5 nm and the RI is within 0.001 to 0.005 for homogeneous and spherical particles. The green shaded region in indicates where LLPS occurs, with the spectra degrading and leading to much larger scatter in the size and RI. **(B)** Mie resonance spectra before and after ozonolysis of OA shows clear peaks indicative of a homogeneous spherical particle initially that becomes distorted following LLPS, consistent with the formation of surface islands due to product formation that interrupt the spherical cavity. **(C)** Size and RI evolution of supercooled liquid EA particles exposed to 2.3 ppm of O_3 under dry conditions. **(D)** Mie resonance spectra before and after ozonolysis of EA particles, showing a spherical homogeneous morphology is retained.

In many datasets with OA, an abrupt change was observed in the RI, as seen in *Figure 3A* at around 500 s. This occurs as the Mie resonance spectra begins to degrade, shown in **Figure 3B**. A similar effect was noted, with different extent of spectral breakdown, in the

majority of experiments on OA particles. A likely explanation for degradation of the Mie resonance spectra is the occurrence of a phase transition due to the liquid-liquid phase separation (LLPS) following the formation of low solubility organic species as the ozonolysis proceeds. This leads the particle to deviate from a well-mixed homogeneous composition and as a result, the Mie resonance spectra becomes distorted.

Possible morphologies that may form due to LLPS include a fully engulfed core shell-type morphology, in which the spherical structure is retained, and Mie resonance spectra appear undisturbed, a partially engulfed morphology, in which the particle deviates from a spherical structure and the spectra break down, and an emulsion-type morphology, where aggregates for product species formed scatter light either at the surface or in the bulk, leading to some distortion of the spectra. LLPS in oleic acid ozonolysis reactions has been observed in previous work, and microscopy images reported by Xu et al.[62] indicate the formation of liquid islands at the surface, a form of aggregation due to the low solubility of the products in oleic acid. This is consistent with our observations, as the Mie resonance spectra retain the overall structure of a spherical particle, but with disruptions and deviations caused by the scattering of light by these islands. This leads to a degraded ability to accurately determine the size and the RI following LLPS.

7.4.1.2. Elaidic Acid

Although solid at room temperature in the bulk, levitated particles of EA typically exhibited a spherical morphology, indicative of a supercooled liquid phase state. In some cases, solid particles were formed, identified by the lack of regular scattering structure in

the Mie resonance spectra. The formation of supercooled or solid EA particles appeared to be random and no dependence on any experimental parameters could be identified. Similar stochastic phase behavior has been observed in measurements of diacids under dry conditions.[68] In cases where the EA particles were formed as a supercooled liquid, Mie resonance spectroscopy was used to measure the size and RI, as with OA, shown in **Figure 3C**. Contrary to the liquid OA, these particles do not show any sign of abrupt changes in the scattering pattern or derived properties during the ozonolysis, which indicates that the particles do not undergo LLPS and, hence, retain a spherical homogeneous structure throughout the reaction (**Figure 3D**). Compared to OA, the straight chain EA molecules may be able to solubilize the reaction products to a greater extent than the bent OA molecules. Furthermore, the supercooled elaidic acid is already in a thermodynamically metastable state, indicating that some kinetic barrier exists to the nucleation of the solid phase that may also be present for the nucleation of a phase separated state.

During a typical experiment, up to ten droplets of the starting solution were trapped to produce a linear array of particles that are exposed to ozone. In around 1 in 10 experiments with EA, all particles in the array were formed with a solid phase state. Due to irregular shape of the solid phase, there was no regular Mie resonance scattering pattern observed which results in a lack of information on size and RI. For these particles, we rely on the mass spectrometry data and the assumption that their effective radius is equal to the radius of spherical particles created from the same starting solution. Further discussion of solid EA particles is presented in subsequent sections.

7.4.2. Chemical Evolution of Single Levitated Particles

The chemical evolution of particles as they react with ozone was determined using mass spectrometry. A linear sequence of initially similar-sized particles was trapped in the LQ-EDB, and ozone of a known concentration was introduced. Particles were ejected sequentially, over the course of several hours, and each yielded a snapshot of the composition at that point in the reaction. The example mass spectra for OA before and after ozonolysis are shown in **Figure 4A** while the chronogram of the parent peak and primary products are shown in **Figure 4B**. The integrated area corresponding to the chronogram signal for each peak of interest was determined for all particles in the experiment.

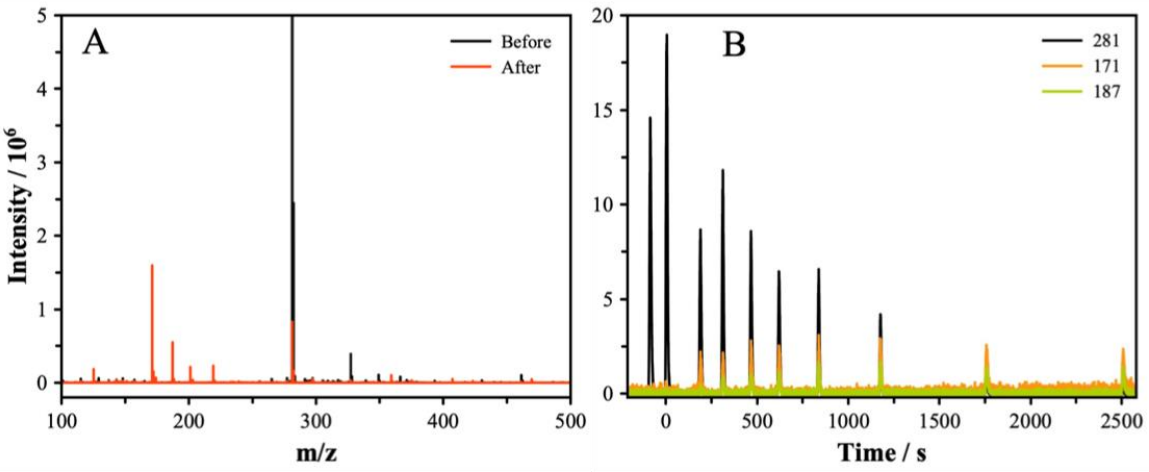

Figure 4: (A) Mass spectra of oleic acid particles with a diameter of ~10 μm before and after ozonolysis. The black data represents mass spectrum before the start of ozonolysis reaction whereas the red data represents mass spectrum after ozonolysis. **(B)** Mass chronograms show the time-dependent ion intensity of $[M\text{-}H^+]^-$ signal for a decrease in oleic acid reactant peaks (281 m/z, black) with simultaneous increase of first-generation product peaks, such as 9-oxononanoic acid (m/z 171) and azelaic acid (m/z 187 m/z).

7.4.3. Oleic Acid and Elaidic Acid Reaction Kinetics

Both OA and supercooled EA particles exhibit similar heterogeneous reaction rates with ozone, as reflected in the similar decay rate of the parent compounds as a function of exposure. In both cases, integrated peak intensity at m/z 281 was used to determine the amount of reactant in the unreacted particle at the start of the experiment, and the signal associated with subsequent particles undergoing ozonolysis is shown as a fraction of this starting value.

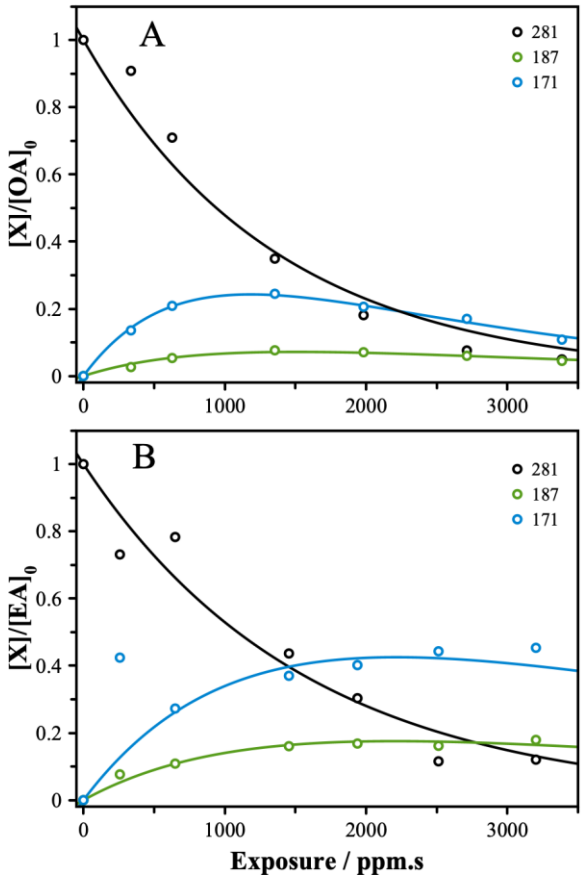

Figure 5: Normalized intensity of reactant and 1st generation products in OA **(A)** and supercooled EA **(B)** for particles with a starting diameter of ~10 μm exposed to 4.1 ppm of ozone. Note the x-axis reflects the ozone exposure in units of concentration (ppm) × time (s). The solid lines reflect exponential decay fits to the data as discussed in the text.

While the peak area and intensity decreases for m/z 281, the signals for primary products emerge as ozonolysis proceeds (**Figure 5A** for OA and **Figure 5B** for EA). First-generation products are formed along with Criegee intermediate (CI) in the beginning due to reaction between OA (or EA) and ozone, after which these further combine with CI, and dissociate or dimerize to result in the formation of second-generation products. Data points for 187 and 171 m/z signal in *Figure 5* represent the relative peak areas for the first-generation products azelaic acid (AA) and 9-oxononanoic acid (ONA), respectively. The MS signals for AA and ONA first increase and, for ONO, subsequently decrease as evaporation and further chemistry occurs during ozonolysis.

A simple multi-component evaporation model,[66] assuming ideal mixing of reactants and products, isothermal evaporation, and using the vapor pressures reported by Mueller et al.,[48] predicts timescales of evaporation for 10 μm diameter particles to be on the order of 100's seconds for ONA and on the order of 1000's seconds for AA. Thus, AA will likely accumulate in the particle to a greater extent than ONA, and the subsequent decrease in signal for ONA may be due to evaporation. Nonanoic acid and nonanal are both volatile on the timescale of these measurements and are not observed as products. The ionization efficiencies of measured products with respect to the parent compound vary, accounting for the different product signal intensity seen in *Figure 5A* and *Figure 5B*. For AA, the ionization efficiency with respect to EA was double that for OA. Thus, we expect to measure approximately double the amount of product signal in the EA system for the same amount of material. Considering this, our data shows no clear difference in the product formation between the two isomers.

When determining uptake coefficients across all experiments, there is a slightly higher value determined for elaidic acid, with $\gamma_{EA} = 8.6 \pm 1.1 \times 10^{-4}$ and $\gamma_{OA} = 7.1 \pm 1.7 \times 10^{-4}$, although there is agreement within the uncertainty in the standard deviations based on repeated trials at similar experimental conditions. The value for OA falls close to the expected literature values considering the size of the particles.[52] We break down these values further in a later section to explore more closely the influence of ozone concentration and RH on the measured values. Interestingly, even though OA was observed to undergo LLPS in most cases, the reaction kinetics were unaltered. This is likely due to the surface of the particle being insufficiently covered by product species to reduce the uptake and reaction of ozone.

In the case of solid EA particles, much slower reaction kinetics were observed compared with the supercooled counterpart. **Figure 6A** shows the decay curves for a representative example of a solid particle compared to a supercooled liquid particle. The reaction between solid EA and ozone is drastically slower than ozonolysis of supercooled EA or liquid OA. An exponential decay curve was fit to the data to derive a rate constant, and the estimated particle size was used to determine the uptake coefficient.

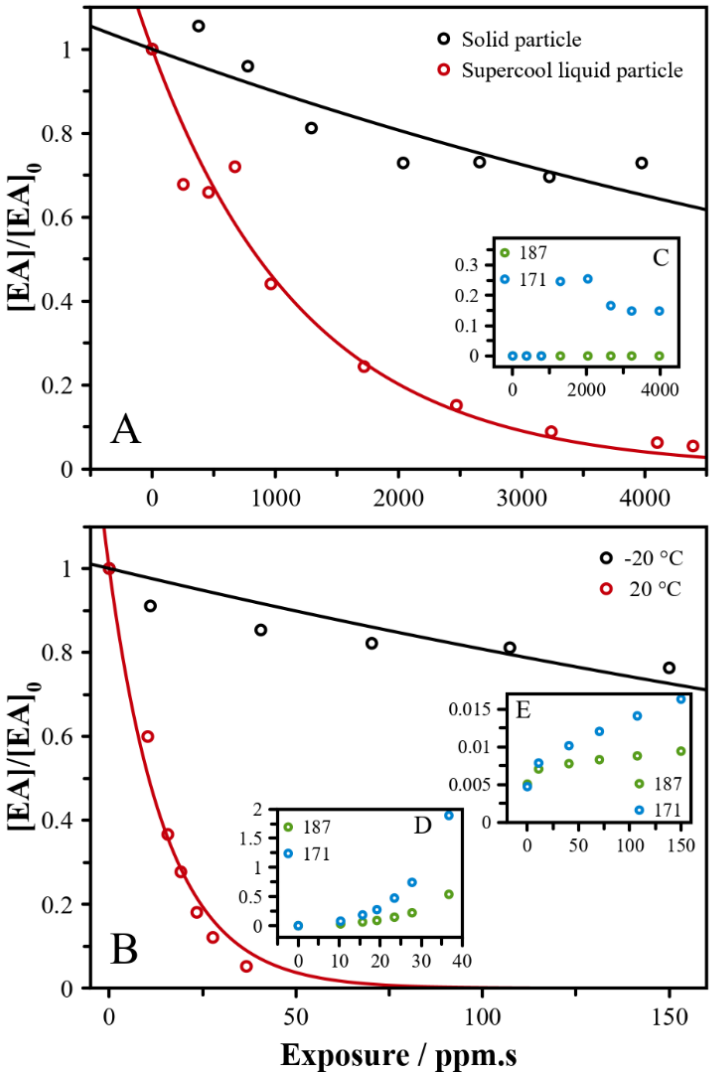

Figure 6: (A) A comparison of the decay of supercooled liquid EA particles compared to solid EA particles under the same reaction conditions. The solid lines represent an exponential fit. The *inset figure C* shows the signal for products AA (m/z 187) and ONA (m/z 171) for the solid particle. **(B)** A comparison of the decay of homogeneously frozen EA particles at -20 °C and supercooled liquid EA at 20 °C, along with *inset figures D and E* showing the AA and ONA signal for frozen and supercooled particles respectively. Note that the compositional analysis was carried out with the help of mass spectrometry technique.

For measurements on solid elaidic acid particles in the LQ-EDB, we found $\gamma_{EA,s} = 3.2 \pm 1.6 \times 10^{-4}$, just under three times smaller than for the supercooled equivalent. The

measured standard deviation in these measurements is greater due to the more limited number of observations. The quantitative analysis of the MS data for solid EA particles revealed that there were signals for the product ONA, while AA and other products were absent (**Figure 6C**). This may indicate that the reaction pathways for the solid particles may differ due to the limited mobility of products within the particle, prohibiting secondary chemistry. Furthermore, because first-generation products are formed at the surface, they can evaporate more easily and are thus less clearly observed. In should be noted, however, that the low reaction extent brings challenges in reliably detecting products signals, and we hesitate to draw any conclusions from these data.

7.4.4. Influence of Temperature on Phase and Kinetics

Temperature-controlled flow-tube measurements were also performed as a complement to single particle measurements. As described in the *Experimental Setup Section*, polydisperse aerosol of OA and EA were generated by homogeneous nucleation. In OA experiments, the mass-weighted mean diameter of the log-normal distribution lay between 154 and 167 nm, with a geometric standard deviation (σ_g) of 1.35. For EA, the mass-weighted mean of the particle distribution lies between 167 and 204 nm, with a σ_g of 1.37. Negative ion APCI-MS was used to measure the decay of each acid over ozone exposures up to 300 ppm s. The exponential decay curves were analyzed in the same way as described earlier and reactive uptake coefficients were determined as a function of temperature, shown in **Figure 7**.

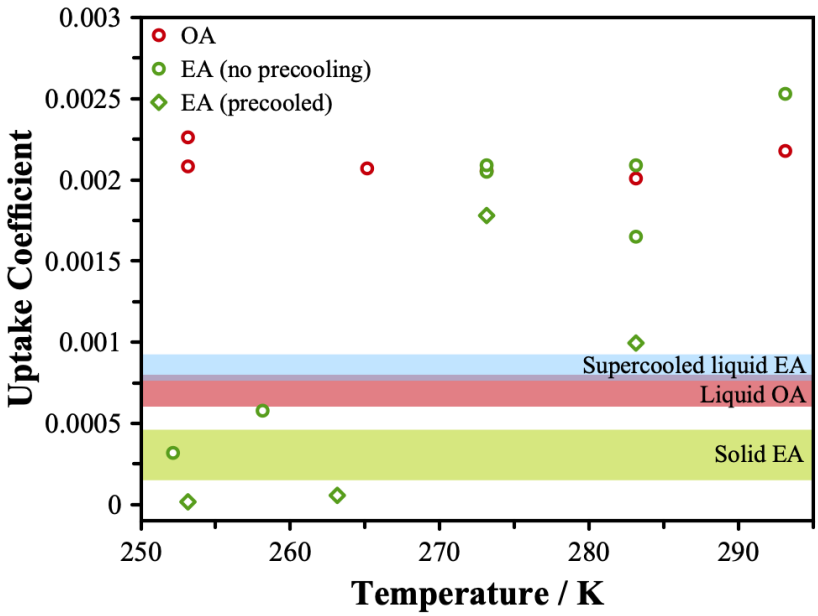

Figure 7: Uptake coefficients from temperature-controlled flow tube reactor studies. Red open circles correspond to measurements of oleic acid, and green open shapes correspond to measurements of elaidic acid with (diamond) and without (circle) the precooling step described in the E*xperimental Section*. Shaded horizontal regions show the linear quadrupole electrodynamic balance (LQ-EDB) measurements for comparison, the vertical size of the bar indicating the uncertainty. We use the term "solid" here, although care should be taken with this description as described in the text.

These measurements reveal several interesting observations when compared to the larger levitated particles. First, the magnitude of the uptake coefficient is larger at room temperature for both OA and EA, indicating that the influence of diffusion limitations are reduced due to the decreased size of the particles, and the reaction occurs faster, as predicted by Smith et al.[51] Second, the uptake coefficient for OA particles is invariant with temperature, while for EA there is a steep decrease at between 260 and 270 K. The temperature at which slowing is observed likely coincides with the homogeneous freezing temperature of the supercooled EA, and the resulting solid EA particles exhibit much smaller uptake coefficients that agree more closely with the measurements on solid EA

particles in the LQ-EDB. Interestingly, when measurements were performed without a precooling step, the uptake coefficients measured were greater, indicating only partial freezing occurred. This may result in either an internally mixed slurry of solid and liquid material, or an external mixture of some solid particles and some liquid particles. Comparing against the larger uptake coefficients measured in the LQ-EDB, an internal mixture with a varying ratio of solid to liquid may explain the differences seen across measurements.

When comparing the decay trends in **Figure 6A** and **6B**, both the solid LQ-EDB particles and the low temperature flow-tube measurements reveal a similar trend. Given the LQ-EDB measurements are on single particles, this indicates that an internal mixture may be formed, and a plateau observed when the liquid extent of the particle is reacted away, leaving only solid material that decays much more slowly. The *insets C, D and E in Figure 6* show the measured signals arising from AA and ONA. As was observed in solid particle levitation measurements (**Figure 6C**), the abundance of 1st generation products was significantly reduced in measurements on the solid particles frozen at -20 °C (**Figure 6E**). The abundance of these products in frozen EA particles is less than for the same reaction extent on liquid EA particles at 20 °C (**Figure 6D**), further indicating the chemistry is modified relative to the well-mixed case.

7.4.5. Influence of Ozone Concentration and Relative Humidity

Over the course of these measurements, we explored the influence of varying ozone concentrations and relative humidity on the properties of liquid OA and supercooled EA

particles. As previously discussed, the loss of liquid OA and supercooled EA over time was characterized with an exponential to give the rate constant, and an uptake coefficient was calculated. The values of uptake coefficients for varying ozone concentrations at 0% RH and varying RH at 2.3 ppm of ozone, respectively, are reported in **Figure 8**.

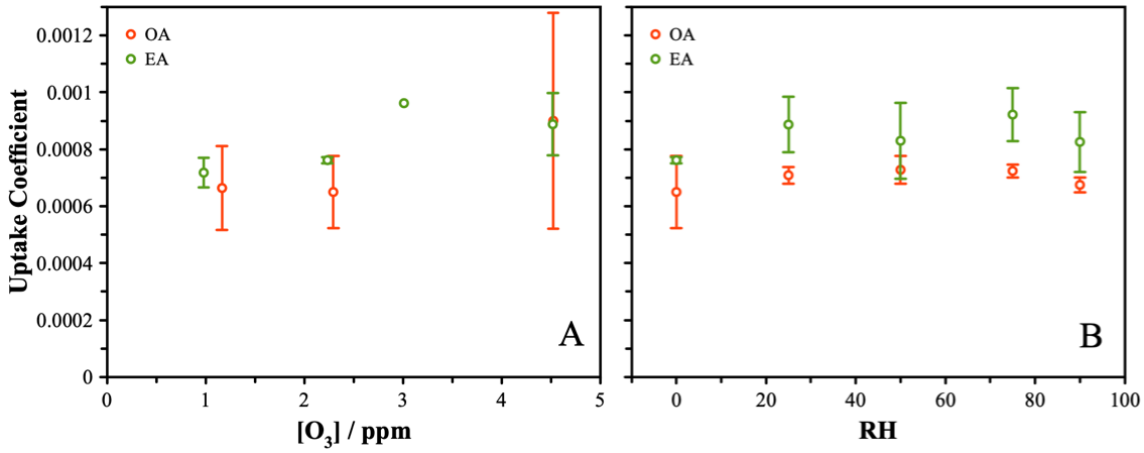

Figure 8: (A) Comparison of uptake coefficients for liquid OA and supercooled EA undergoing ozonolysis as a measure of varying ozone concentrations under dry conditions using MS. **(B)** Comparison of uptake coefficients for liquid OA and supercooled EA undergoing ozonolysis as a measure of varying relative humidity at 2.3 ppm of ozone. For both sets of measurements, liquid OA data is represented as red open circles and supercooled EA data is represented as green open circles. The error bars represent the standard deviations based on repeated trials at similar experimental conditions.

Overall, we observe a higher value of the uptake coefficient for supercooled EA as compared to liquid OA, but neither system shows any measurable dependence on ozone concentration or RH. The latter observation is not surprising given the hydrophobic nature of the reactants and, while the products are expected to be more hydrophilic, the additional water present has no role in the decay of OA or EA. The influence of ozone concentration might be expected in systems that showed diffusion limitations, as the renewal of reactants at the interface cannot compete with the loss due to reaction when ozone concentrations

are high. Due to the low concentrations of ozone and the slow rate of reaction, we expect minimal diffusion limitations, consistent with the constant uptake coefficient. Secondary reactions have been previously reported to vary with ozone concentration, however our measurements do not span a sufficiently large range to identify such trends.[48]

7.5. Summary and Conclusions

Single particle and flow tube measurements were performed in this study to compare the ozonolysis kinetics and product distributions of two geometric isomers, oleic acid and elaidic acid, under a variety of laboratory conditions. The different physical states of oleic and elaidic acid under ambient conditions yield interesting experimental observations that are the focus of this work. The existence of elaidic acid in supercooled liquid state as single levitated particles resulted in similar ozonolysis kinetics as liquid oleic acid, which are significantly faster than the kinetics of solid elaidic acid particles. While it is known that high viscosity can lead to diffusion limitations that impede the rate of chemical reactions, experiments that show this impose other changes that may also influence reactivity, such as changes in the amount of water or the inclusion of additional compounds inside the particles. These results directly demonstrate the differences in reaction kinetics for the heterogeneous transformation of the same chemical system under different phase states. Furthermore, we confirm that liquid oleic acid particles react with ozone gas leading to the onset of phase separation. No changes in the ozonolysis kinetics were observed following LLPS, and the newly formed phase is likely a mixture of high-molecular weight products that are insoluble in liquid oleic acid, resulting in liquid-liquid phase separation, probably

as inclusions, as observed by Mie resonance spectroscopy. There is no discernable difference in composition at the point of LLPS in oleic acid particles as compared to supercooled elaidic acid particles.

Flow-tube measurements using a temperature-controlled reactor were also performed, allowing for supercooled elaidic acid particles to be frozen to the solid state. These measurements agree with the single particle measurements, showing uptake coefficients for supercooled elaidic acid to be slightly higher than oleic acid, with a marked decrease at the temperature where homogeneous freezing occurs. Interestingly, the uptake coefficient was reduced to a lower value in the flow-tube measurements where pre-cooling was applied, with larger values observed without precooling in the LQ-EDB measurements. We surmise this is due to the formation of a slurry in which the extent of solidification depends on the temperature and time. Additionally, the size dependence owing to diffusion rates in solid particles and those of intermediate viscosity may explain these differences.[51,78]

Using an electrodynamic balance coupled with mass spectrometry, chemical transformations on super-micron single particles may be explored with extended timescales of levitation under reaction conditions that approach atmospherically relevant low-oxidant concentrations. Flow-tube measurements focus on sub-micron aerosol particles, in which the reaction timescales are shortened by utilizing higher concentrations of oxidants. Exposure of particles to ozone in both these techniques led to the formation of primary generation products which further undergo reactions with Criegee intermediates, resulting in the formation of second-generation products. A direct comparison reveals that the uptake

coefficient is dependent on size, with sub-micron particles generated in flow tube have higher uptake coefficient value than single levitated super-micron particles. While the dependence we observe here differs from earlier work,[51] this likely arises due to the different ozone concentrations, as reaction-diffusion effects will depend on both length and timescales. This work provides a comparison between these two common aerosol methods applied to the same chemical systems, demonstrating complementary information that may be obtained. Further, while oleic acid has been extensively studied in the literature, the role of phase on its chemistry has not been observed.

This work demonstrates that solid elaidic acid may be an effective proxy for oleic acid embedded in high viscosity media, allowing further study of the role of diffusion-limitations on chemical transformations. The uptake coefficient for elaidic acid reported by Wang and Yu[54] fall in between those reported in this work for solid and liquid elaidic acid particles. This indicates that the phase state of ambient particles containing elaidic acid, and by extrapolation other high melting point organic compounds, may exist in a continuum between liquid and solid, complicating our understanding of heterogeneous reaction kinetics and raising the importance of developing *in-situ* probes of phase morphology when exploring heterogenous reactions. The morphology and other physicochemical characteristics of aerosol particles also change greatly in the process of organic chemical aging, necessitating a unified approach to tackling the problem of organic aerosol chemical processing to better understand the implications for atmospheric chemistry, climate, and public health.

7.6. References

(1) Rosenfeld, D.; Sherwood, S.; Wood, R.; Donner, L. Climate Effects of Aerosol-Cloud Interactions. *Science* **2014**, *343* (6169), 379–380. https://doi.org/10.1126/science.1247490.

(2) Menon, S.; Unger, N.; Koch, D.; Francis, J.; Garrett, T.; Sednev, I.; Shindell, D.; Streets, D. Aerosol Climate Effects and Air Quality Impacts from 1980 to 2030. *Environ. Res. Lett.* **2008**, *3* (2). https://doi.org/10.1088/1748-9326/3/2/024004.

(3) Pöschl, U. Atmospheric Aerosols: Composition, Transformation, Climate and Health Effects. *Angew. Chem. Int. Ed.* **2005**, *44* (46), 7520–7540. https://doi.org/10.1002/anie.200501122.

(4) Mauderly, J. L.; Chow, J. C. Health Effects of Organic Aerosols. *Inhal. Toxicol.* **2008**, *20* (3), 257–288. https://doi.org/10.1080/08958370701866008.

(5) Shiraiwa, M.; Ueda, K.; Pozzer, A.; Lammel, G.; Kampf, C. J.; Fushimi, A.; Enami, S.; Arangio, A. M.; Fröhlich-Nowoisky, J.; Fujitani, Y.; Furuyama, A.; Lakey, P. S. J.; Lelieveld, J.; Lucas, K.; Morino, Y.; Pöschl, U.; Takahama, S.; Takami, A.; Tong, H.; Weber, B.; Yoshino, A.; Sato, K. Aerosol Health Effects from Molecular to Global Scales. *Environ. Sci. Technol.* **2017**, *51* (23), 13545–13567. https://doi.org/10.1021/acs.est.7b04417.

(6) Jacobson, M. C.; Hansson, H.-C.; Noone, K. J.; Charlson, R. J. Organic Atmospheric Aerosols: Review and State of the Science. *Rev. Geophys.* **2000**, *38* (2), 267–294. https://doi.org/10.1029/1998RG000045.

(7) Srivastava, A. K.; Dey, S.; Tripathi, S. N. Aerosol Characteristics over the Indo-Gangetic Basin: Implications to Regional Climate. *Atmospheric Aerosols - Regional Characteristics-Chemistry and Physics*; Abdul-Razzak, H., Ed.; InTech, **2012**. https://doi.org/10.5772/47782.

(8) Lohmann, U.; Feichter, J. Global Indirect Aerosol Effects: A Review. *Atmos. Chem. Phys.* **2005,** *5* (3), 715–737. https://doi.org/10.5194/acp-5-715-2005.

(9) Richards, L. W. Sight Path Measurements for Visibility Monitoring and Research. *J. Air Pollut. Control Assoc.* **1988**, *38*, 784–791. https://doi.org/10.1080/08940630.1988.10466418.

(10) Pope, C. A.; Ezzati, M.; Dockery, D. W. Fine Particulate Air Pollution and Life Expectancies in the United States: The Role of Influential Observations. *J. Air Waste Manag. Assoc.* **2013**, *63* (2), 129–132. https://doi.org/10.1080/10962247.2013.760353.

(11) Easterling, D. R. Climate Extremes: Observations, Modeling, and Impacts. *Science* **2000**, *289* (5487), 2068–2074. https://doi.org/10.1126/science.289.5487.2068.

(12) McFiggans, G.; Artaxo, P.; Baltensperger, U.; Coe, H.; Facchini, M. C.; Feingold, G.; Fuzzi, S.; Gysel, M.; Laaksonen, A.; Lohmann, U.; Mentel, T. F.; Murphy, D. M.; O'Dowd, C. D.; Snider, J. R.; Weingartner, E.; Institut, P. S. The Effect of Physical and Chemical Aerosol Properties on Warm Cloud Droplet Activation. *Atmos. Chem. Phys.* **2006**, *6* (9), 2593–2649. https://doi.org/10.5194/acp-6-2593-2006.

(13) McNeill, V. F. Atmospheric Aerosols: Clouds, Chemistry, and Climate. *Annu. Rev. Chem. Biomol. Eng.* **2017**, *8* (1), 427–444. https://doi.org/10.1146/annurev-chembioeng-060816-101538.

(14) Zhang, R.; Khalizov, A.; Wang, L.; Hu, M.; Xu, W. Nucleation and Growth of Nanoparticles in the Atmosphere. *Chem. Rev.* **2012**, *112* (3), 1957–2011. https://doi.org/10.1021/cr2001756.

(15) Calvo, A. I.; Alves, C.; Castro, A.; Pont, V.; Vicente, A. M.; Fraile, R. Research on Aerosol Sources and Chemical Composition: Past, Current and Emerging Issues. *Atmos. Res.* **2013**, *120–121*, 1–28. https://doi.org/10.1016/j.atmosres.2012.09.021.

(16) Pöschl, U.; Shiraiwa, M. Multiphase Chemistry at the Atmosphere–Biosphere Interface Influencing Climate and Public Health in the Anthropocene. *Chem. Rev.* **2015**, *115* (10), 4440–4475. https://doi.org/10.1021/cr500487s.

(17) Prather, K. A.; Hatch, C. D.; Grassian, V. H. Analysis of Atmospheric Aerosols. *Annu. Rev. Anal. Chem.* **2008**, *1* (1), 485–514. https://doi.org/10.1146/annurev.anchem.1.031207.113030.

(18) Rogge, W. F.; Hildemann, L. M.; Mazurek, M. A.; Cass, G. R.; Simoneit, B. R. T. Sources of Fine Organic Aerosol. 1. Charbroilers and Meat Cooking Operations. *Environ. Sci. Technol.* **1991**, *25* (6), 1112–1125. https://doi.org/10.1021/es00018a015.

(19) Simoneit, B. R. T. Organic Matter of the Troposphere ? V: Application of Molecular Marker Analysis to Biogenic Emissions into the Troposphere for Source Reconciliations. *J. Atmos. Chem.* **1989**, *8* (3), 251–275. https://doi.org/10.1007/BF00051497.

(20) Kolb, C. E.; Worsnop, D. R. Chemistry and Composition of Atmospheric Aerosol Particles. *Annu. Rev. Phys. Chem.* **2012**, *63* (1), 471–491. https://doi.org/10.1146/annurev-physchem-032511-143706.

(21) Krieger, U. K.; Marcolli, C.; Reid, J. P. Exploring the Complexity of Aerosol Particle Properties and Processes Using Single Particle Techniques. *Chem. Soc. Rev.* **2012**, *41* (19), 6631. https://doi.org/10.1039/c2cs35082c.

(22) Lambe, A. T.; Cappa, C. D.; Massoli, P.; Onasch, T. B.; Forestieri, S. D.; Martin, A. T.; Cummings, M. J.; Croasdale, D. R.; Brune, W. H.; Worsnop, D. R.; Davidovits, P. Relationship between Oxidation Level and Optical Properties of Secondary Organic Aerosol. *Environ. Sci. Technol.* **2013**, *47* (12), 6349–6357. https://doi.org/10.1021/es401043j.

(23) Lanz, V. A.; Prevot, A. S. H.; Alfarra, M. R.; Weimer, S.; Mohr, C.; DeCarlo, P. F.; Gianini, M. F. D.; Hueglin, C.; Schneider, J.; Favez, O.; D'Anna, B.; George, C.; Baltensperger, U.; Institut, P. S. Characterization of Aerosol Chemical Composition with Aerosol Mass Spectrometry in Central Europe: An Overview. *Atmos Chem Phys* **2010**, *10* (21), 10453–10471. https://doi.org/10.5194/acp-10-10453-2010.

(24) Carson, P. G.; Johnston, M. V.; Wexler, A. S. Real-Time Monitoring of the Surface and Total Composition of Aerosol Particles. *Aerosol Sci. Technol.* **1997**, *26* (4), 291–300. https://doi.org/10.1080/02786829708965431.

(25) Li, S.; Jiang, X.; Roveretto, M.; George, C.; Liu, L.; Jiang, W.; Zhang, Q.; Wang, W.; Ge, M.; Du, L. Photochemical Aging of Atmospherically Reactive Organic Compounds Involving Brown Carbon at the Air–Aqueous Interface. *Atmos Chem Phys* **2019**, *19* (15), 9887–9902. https://doi.org/10.5194/acp-19-9887-2019.

(26) Kroll, J. H.; Smith, J. D.; Che, D. L.; Kessler, S. H.; Worsnop, D. R.; Wilson, K. R. Measurement of Fragmentation and Functionalization Pathways in the Heterogeneous Oxidation of Oxidized Organic Aerosol. *Phys. Chem. Chem. Phys.* **2009**, *11* (36), 8005–8014. https://doi.org/10.1039/B905289E.

(27) Chapleski, R. C.; Zhang, Y.; Troya, D.; Morris, J. R. Heterogeneous Chemistry and Reaction Dynamics of the Atmospheric Oxidants, O_3, NO_3, and OH, on Organic Surfaces. *Chem. Soc. Rev.* **2016**, *45* (13), 3731–3746. https://doi.org/10.1039/C5CS00375J.

(28) George, C.; Ammann, M.; D'Anna, B.; Donaldson, D. J.; Nizkorodov, S. A. Heterogeneous Photochemistry in the Atmosphere. *Chem. Rev.* **2015**, *115* (10), 4218–4258. https://doi.org/10.1021/cr500648z.

(29) Hu, W.; Liu, D.; Su, S.; Ren, L.; Ren, H.; Wei, L.; Yue, S.; Xie, Q.; Zhang, Z.; Wang, Z.; Yang, N.; Wu, L.; Deng, J.; Qi, Y.; Fu, P. Photochemical Degradation of Organic Matter in the Atmosphere. *Adv. Sustain. Syst.* **2021**, *5* (11), 2100027. https://doi.org/10.1002/adsu.202100027.

(30) George, I. J.; Abbatt, J. P. D. Heterogeneous Oxidation of Atmospheric Aerosol Particles by Gas-Phase Radicals. *Nat. Chem.* **2010**, *2* (9), 713–722. https://doi.org/10.1038/nchem.806.

(31) Kadesch, G. R. Ozonolysis of Fatty Acids and Their Derivatives. *Prog. Chem. Fats. Other Lipids* **1963**, *6*, 291–312. https://doi.org/10.1016/0079-6832(63)90026-0.

(32) Thornberry, T.; Abbatt, J. P. D. Heterogeneous Reaction of Ozone with Liquid Unsaturated Fatty Acids: Detailed Kinetics and Gas-Phase Product Studies. *Phys. Chem. Chem. Phys.* **2004**, *6* (1), 84–93. https://doi.org/10.1039/b310149e.

(33) Freedman, M. A. Liquid–Liquid Phase Separation in Supermicrometer and Submicrometer Aerosol Particles. *Acc. Chem. Res.* **2020**, *53* (6), 1102–1110. https://doi.org/10.1021/acs.accounts.0c00093.

(34) Tang, M.; Chan, C. K.; Li, Y. J.; Su, H.; Ma, Q.; Wu, Z.; Zhang, G.; Wang, Z.; Ge, M.; Hu, M.; He, H.; Wang, X. A Review of Experimental Techniques for Aerosol Hygroscopicity Studies. *Atmos. Chem. Phys.* **2019**, *19* (19), 12631–12686. https://doi.org/10.5194/acp-19-12631-2019.

(35) Zhao, Z.; Tolentino, R.; Lee, J.; Vuong, A.; Yang, X.; Zhang, H. Interfacial Dimerization by Organic Radical Reactions during Heterogeneous Oxidative Aging of Oxygenated Organic Aerosols. *J. Phys. Chem. A* **2019**, *123* (50), 10782–10792. https://doi.org/10.1021/acs.jpca.9b10779.

(36) Zhang, Q.; Jimenez, J. L.; Canagaratna, M. R.; Allan, J. D.; Coe, H.; Ulbrich, I.; Alfarra, M. R.; Takami, A.; Middlebrook, A. M.; Sun, Y. L.; Dzepina, K.; Dunlea, E.; Docherty, K.; DeCarlo, P. F.; Salcedo, D.; Onasch, T.; Jayne, J. T.; Miyoshi, T.; Shimono, A.; Hatakeyama, S.; Takegawa, N.; Kondo, Y.; Schneider, J.; Drewnick, F.; Borrmann, S.; Weimer, S.; Demerjian, K.; Williams, P.; Bower, K.; Bahreini, R.; Cottrell, L.; Griffin, R. J.; Rautiainen, J.; Sun, J. Y.; Zhang, Y. M.; Worsnop, D. R. Ubiquity and Dominance of Oxygenated Species in Organic Aerosols in Anthropogenically-Influenced Northern Hemisphere Midlatitudes: Ubiquity and Dominance of Oxygenated OA. *Geophys. Res. Lett.* **2007**, *34* (13), L13801 (1–6). https://doi.org/10.1029/2007GL029979.

(37) Lambe, A. T.; Zhang, J.; Sage, A. M.; Donahue, N. M. Controlled OH Radical Production via Ozone-Alkene Reactions for Use in Aerosol Aging Studies. *Environ. Sci. Technol.* **2007**, *41* (7), 2357–2363. https://doi.org/10.1021/es061878e.

(38) King, M. D.; Thompson, K. C.; Ward, A. D. Laser Tweezers Raman Study of Optically Trapped Aerosol Droplets of Seawater and Oleic Acid Reacting with Ozone: Implications for Cloud-Droplet Properties. *J. Am. Chem. Soc.* **2004**, *126* (51), 16710–16711. https://doi.org/10.1021/ja044717o.

(39) Hung, H.-M.; Tang, C.-W. Effects of Temperature and Physical State on Heterogeneous Oxidation of Oleic Acid Droplets with Ozone. *J. Phys. Chem. A* **2010**, *114* (50), 13104–13112. https://doi.org/10.1021/jp105042w.

(40) Hearn, J. D.; Smith, G. D. Kinetics and Product Studies for Ozonolysis Reactions of Organic Particles Using Aerosol CIMS. *J. Phys. Chem. A* **2004**, *108* (45), 10019–10029. https://doi.org/10.1021/jp0404145.

(41) Arata, C.; Heine, N.; Wang, N.; Misztal, P. K.; Wargocki, P.; Bekö, G.; Williams, J.; Nazaroff, W. W.; Wilson, K. R.; Goldstein, A. H. Heterogeneous Ozonolysis of Squalene: Gas-Phase Products Depend on Water Vapor Concentration. *Environ. Sci. Technol.* **2019**, *53* (24), 14441–14448. https://doi.org/10.1021/acs.est.9b05957.

(42) Rissanen, M. P.; Kurtén, T.; Sipilä, M.; Thornton, J. A.; Kausiala, O.; Garmash, O.; Kjaergaard, H. G.; Petäjä, T.; Worsnop, D. R.; Ehn, M.; Kulmala, M. Effects of Chemical Complexity on the Autoxidation Mechanisms of Endocyclic Alkene Ozonolysis Products: From Methylcyclohexenes toward Understanding α-Pinene. *J. Phys. Chem. A* **2015**, *119* (19), 4633–4650. https://doi.org/10.1021/jp510966g.

(43) Steimer, S. S.; Berkemeier, T.; Gilgen, A.; Krieger, U. K.; Peter, T.; Shiraiwa, M.; Ammann, M. Shikimic Acid Ozonolysis Kinetics of the Transition from Liquid Aqueous Solution to Highly Viscous Glass. *Phys. Chem. Chem. Phys.* **2015**, *17* (46), 31101–31109. https://doi.org/10.1039/C5CP04544D.

(44) Berkemeier, T.; Mishra, A.; Mattei, C.; Huisman, A. J.; Krieger, U. K.; Pöschl, U. Ozonolysis of Oleic Acid Aerosol Revisited: Multiphase Chemical Kinetics and Reaction Mechanisms. *ACS Earth Space Chem.* **2021**, *5* (12), 3313–3323. https://doi.org/10.1021/acsearthspacechem.1c00232.

(45) Morris, J. W.; Davidovits, P.; Jayne, J. T.; Jimenez, J. L.; Shi, Q.; Kolb, C. E.; Worsnop, D. R.; Barney, W. S.; Cass, G. Kinetics of Submicron Oleic Acid Aerosols with Ozone: A Novel Aerosol Mass Spectrometric Technique. *Geophys. Res. Lett.* **2002**, *29* (9), 71-1–71-74. https://doi.org/10.1029/2002GL014692.

(46) Jayne, J. T.; Leard, D. C.; Zhang, X.; Davidovits, P.; Smith, K. A.; Kolb, C. E.; Worsnop, D. R. Development of an Aerosol Mass Spectrometer for Size and Composition Analysis of Submicron Particles. *Aerosol Sci. Technol.* **2000**, *33* (1–2), 49–70. https://doi.org/10.1080/027868200410840.

(47) Gallimore, P. J.; Griffiths, P. T.; Pope, F. D.; Reid, J. P.; Kalberer, M. Comprehensive Modeling Study of Ozonolysis of Oleic Acid Aerosol Based on Real-Time, Online Measurements of Aerosol Composition. *J. Geophys. Res. Atmospheres* **2017**, *122* (8), 4364–4377. https://doi.org/10.1002/2016JD026221.

(48) Müller, M.; Mishra, A.; Berkemeier, T.; Hausammann, E.; Peter, T.; K. Krieger, U. Electrodynamic Balance–Mass Spectrometry Reveals Impact of Oxidant Concentration on Product Composition in the Ozonolysis of Oleic Acid. *Phys. Chem. Chem. Phys.* **2022**, *24* (44), 27086–27104. https://doi.org/10.1039/D2CP03289A.

(49) Müller, M.; Stefanetti, F.; K. Krieger, U. Oxidation Pathways of Linoleic Acid Revisited with Electrodynamic Balance–Mass Spectrometry. *Environ. Sci. Atmos.* **2023**, *3* (1), 85–96 https://doi.org/10.1039/D2EA00127F.

(50) Willis, M. D.; Rovelli, G.; Wilson, K. R. Combining Mass Spectrometry of Picoliter Samples with a Multicompartment Electrodynamic Trap for Probing the Chemistry of Droplet Arrays. *Anal. Chem.* **2020**, *92* (17), 11943–11952. https://doi.org/10.1021/acs.analchem.0c02343.

(51) Smith, G. D.; Woods, E.; DeForest, C. L.; Baer, T.; Miller, R. E. Reactive Uptake of Ozone by Oleic Acid Aerosol Particles: Application of Single-Particle Mass Spectrometry to Heterogeneous Reaction Kinetics. *J. Phys. Chem. A* **2002**, *106* (35), 8085–8095. https://doi.org/10.1021/jp020527t.

(52) Zahardis, J.; Petrucci, G. A. The Oleic Acid-Ozone Heterogeneous Reaction System: Products, Kinetics, Secondary Chemistry, and Atmospheric Implications of a Model System – a Review. *Atmos. Chem. Phys.* **2007**, *7* (5), 1237–1274. https://doi.org/10.5194/acp-7-1237-2007.

(53) Berkemeier, T.; Mishra, A.; Mattei, C.; Huisman, A. J.; Krieger, U. K.; Pöschl, U. Ozonolysis of Oleic Acid Aerosol Revisited: Multiphase Chemical Kinetics and Reaction Mechanisms. *ACS Earth Space Chem.* **2021**, *5* (12), 3313–3323. https://doi.org/10.1021/acsearthspacechem.1c00232.

(54) Wang, Q.; Yu, J. Z. Ambient Measurements of Heterogeneous Ozone Oxidation Rates of Oleic, Elaidic, and Linoleic Acid Using a Relative Rate Constant Approach in an Urban Environment. *Geophys. Res. Lett.* **2021**, *48* (19), e2021GL095130 (1–10). https://doi.org/10.1029/2021GL095130.

(55) D. Hearn, J.; D. Smith, G. Measuring Rates of Reaction in Supercooled Organic Particles with Implications for Atmospheric Aerosol. *Phys. Chem. Chem. Phys.* **2005**, *7* (13), 2549–2551. https://doi.org/10.1039/B506424D.

(56) Virtanen, A.; Joutsensaari, J.; Koop, T.; Kannosto, J.; Yli-Pirila, P.; Leskinen, J.; Makela, J. M.; Holopainen, J. K.; Poschl, U.; Kulmala, M.; R.Worsnop, D.; Laaksonen, A. An Amorphous Solid State of Biogenic Secondary Organic Aerosol Particles. *Nature* **2010**, *467*, 824–827. https://doi.org/10.1038/nature09455

(57) Pope, F. D.; Gallimore, P. J.; Fuller, S. J.; Cox, R. A.; Kalberer, M. Ozonolysis of Maleic Acid Aerosols: Effect upon Aerosol Hygroscopicity, Phase and Mass. *Environ. Sci. Technol.* **2010**, *44* (17), 6656–6660. https://doi.org/10.1021/es1008278.

(58) Shiraiwa, M.; Ammann, M.; Koop, T.; Pöschl, U. Gas Uptake and Chemical Aging of Semisolid Organic Aerosol Particles. *Proc. Natl. Acad. Sci.* **2011**, *108* (27), 11003–11008. https://doi.org/10.1073/pnas.1103045108.

(59) Houle, F. A.; Wiegel, A. A.; Wilson, K. R. Changes in Reactivity as Chemistry Becomes Confined to an Interface. The Case of Free Radical Oxidation of C30H62 Alkane by OH. *J. Phys. Chem. Lett.* **2018**, *9* (5), 1053–1057. https://doi.org/10.1021/acs.jpclett.8b00172.

(60) Davies, J. F.; Wilson, K. R. Nanoscale Interfacial Gradients Formed by the Reactive Uptake of OH Radicals onto Viscous Aerosol Surfaces. *Chem. Sci.* **2015**, *6* (12), 7020–7027. https://doi.org/10.1039/c5sc02326b.

(61) Hearn, J. D.; Smith, G. D. Measuring Rates of Reaction in Supercooled Organic Particles with Implications for Atmospheric Aerosol. *Phys. Chem. Chem. Phys.* **2005**, *7* (13), 2549. https://doi.org/10.1039/b506424d.

(62) Xu, S.; Mahrt, F.; Gregson, F. K. A.; Bertram, A. K. Possible Effects of Ozone Chemistry on the Phase Behavior of Skin Oil and Cooking Oil Films and Particles Indoors. *ACS Earth Space Chem.* **2022**, *6* (7), 1836–1845. https://doi.org/10.1021/acsearthspacechem.2c00092.

(63) Milsom, A.; Squires, A. M.; Ward, A. D.; Pfrang, C. The Impact of Molecular Self-Organisation on the Atmospheric Fate of a Cooking Aerosol Proxy. *Atmos. Chem. Phys.* **2022**, *22* (7), 4895–4907. https://doi.org/10.5194/acp-22-4895-2022.

(64) Katrib, Y.; Biskos, G.; Buseck, P. R.; Davidovits, P.; Jayne, J. T.; Mochida, M.; Wise, M. E.; Worsnop, D. R.; Martin, S. T. Ozonolysis of Mixed Oleic-Acid/Stearic-Acid Particles: Reaction Kinetics and Chemical Morphology. *J. Phys. Chem. A* **2005**, *109* (48), 10910–10919. https://doi.org/10.1021/jp054714d.

(65) Knopf, D. A.; Anthony, L. M.; Bertram, A. K. Reactive Uptake of O3 by Multicomponent and Multiphase Mixtures Containing Oleic Acid. *J. Phys. Chem. A* **2005**, *109* (25), 5579–5589. https://doi.org/10.1021/jp0512513.

(66) Kaur Kohli, R.; Davies, J. F. Measuring the Chemical Evolution of Levitated Particles: A Study on the Evaporation of Multicomponent Organic Aerosol. *Anal. Chem.* **2021**, *93* (36), 12472–12479. https://doi.org/10.1021/acs.analchem.1c02890.

(67) Kaur Kohli, R.; Van Berkel, G. J.; Davies, J. F. An Open Port Sampling Interface for the Chemical Characterization of Levitated Microparticles. *Anal. Chem.* **2022**, *94* (8), 3441–3445. https://doi.org/10.1021/acs.analchem.1c05550.

(68) Price, C. L.; Kaur Kohli, R.; Shokoor, B.; Davies, J. F. Connecting the Phase State and Volatility of Dicarboxylic Acids at Elevated Temperatures. *J. Phys. Chem. A* **2022**, *126* (39), 6963–6972. https://doi.org/10.1021/acs.jpca.2c04546.

(69) Davies, J. F. Mass, Charge, and Radius of Droplets in a Linear Quadrupole Electrodynamic Balance. *Aerosol Sci Technol.* **2019**, *53* (3), 309–320. https://doi.org/10.1080/02786826.2018.1559921.

(70) Swanson, K. D.; Worth, A. L.; Glish, G. L. Use of an Open Port Sampling Interface Coupled to Electrospray Ionization for the On-Line Analysis of Organic Aerosol Particles. *J. Am. Soc. Mass Spectrom.* **2018**, *29* (2), 297–303. https://doi.org/10.1007/s13361-017-1776-y.

(71) Gary J. Van Berkel; Vilmos Kertesz; Harry Boeltz. Immediate Drop on Demand Technology (I-DOT) Coupled with Mass Spectrometry via an Open Port Sampling Interface. *Bioanalysis 9* (2017), 1667–1679. https://doi.org/10.4155/bio-2017-0104.

(72) Preston, T. C.; Reid, J. P. Determining the Size and Refractive Index of Microspheres Using the Mode Assignments from Mie Resonances. *J. Opt. Soc. Am. A* **2015**, *32* (11), 2210–2217. https://doi.org/10.1364/JOSAA.32.002210.

(73) Price, C. L.; Bain, A.; Wallace, B. J.; Preston, T. C.; Davies, J. F. Simultaneous Retrieval of the Size and Refractive Index of Suspended Droplets in a Linear Quadrupole Electrodynamic Balance. *J. Phys. Chem. A* **2020**, *124* (9), 1811–1820. https://doi.org/10.1021/acs.jpca.9b10748.

(74) Kaur Kohli, R.; Davies, J. F. Paper Spray Mass Spectrometry for the Analysis of Picoliter Droplets. *The Analyst* **2020**, *145* (7), 2639–2648. https://doi.org/10.1039/C9AN02534K.

(75) Banerjee, S.; Mazumdar, S. Electrospray Ionization Mass Spectrometry: A Technique to Access the Information beyond the Molecular Weight of the Analyte. *Int. J. Anal. Chem.* **2012**, *2012*, 1–40. https://doi.org/10.1155/2012/282574.

(76) Fenn, J. B. Electrospray Ionization Mass Spectrometry: How It All Began. *J. Biomol. Tech.* **2002**, *13* (3), 101–118. PMID: 19498975; PMCID: PMC2279858.

(77) Roveretto, M.; Li, M.; Hayeck, N.; Brüggemann, M.; Emmelin, C.; Perrier, S.; George, C. Real-Time Detection of Gas-Phase Organohalogens from Aqueous Photochemistry Using Orbitrap Mass Spectrometry. *ACS Earth Space Chem.* **2019**, *3* (3), 329–334. https://doi.org/10.1021/acsearthspacechem.8b00209.

(78) Smith, J. D.; Kroll, J. H.; Cappa, C. D.; Che, D. L.; Liu, C. L.; Ahmed, M.; Leone, S. R.; Worsnop, D. R.; Wilson, K. R. The Heterogeneous Reaction of Hydroxyl Radicals with Sub-Micron Squalane Particles: A Model System for Understanding the Oxidative Aging of Ambient Aerosols. *Atmos. Chem. Phys.* **2009**, *9* (9), 3209–3222. https://doi.org/10.5194/acp-9-3209-2009.

CHAPTER 8

Summary, Implications and Future Directions

8.1. Thesis Summary and Conclusions

In this thesis, a series of laboratory studies on levitated particles has been presented that aim at improving our understanding of the connection between the physical and chemical characteristics of aerosol particles and heterogeneous chemical transformations occurring in the atmosphere. It is essential to link the microphysical properties, chemical composition and reaction timescales for levitated particles undergoing transformations under controlled environmental conditions to quantify these evolving properties. The measurement and interpretation of heterogeneous transformations, namely non-reactive transformations caused by evaporation of volatile and semi-volatile species, and heterogeneous oxidation caused by ozone, has been the focus of this thesis. This thesis presents a comprehensive discussion on the characteristics of aerosol particles, the development of a new method for probing chemical changes in levitated particles, and the application of these methods to explore and quantify the characteristics of the levitated particles exposed to a variety of reaction conditions. An overview of the preceding seven chapters is presented below.

Chapter 1 provides an overview and significance of the aerosol particles in various fields of scientific interest, including a detailed discussion on their role in the atmosphere. The understanding of chemical composition relating to atmospheric aerosols offers an insight

into their associated properties which determine their interactions with the environmental conditions. This is followed by a generalized description of the measurement techniques, such as ensemble and single particle methods, utilized by researchers to understand the aerosol properties and associated chemical transformations. The chapter is then concluded by discussing the thesis goals supported by research motivation and significance.

Chapter 2 presents the technical information on the development and utilization of analytical methods capable of conducting the heterogeneous transformations on levitated particles. The linear quadrupole electrodynamic balance (LQ-EDB) for particle levitation is effectively coupled with Mie resonance spectroscopy (MRS) and mass spectrometry (MS) for the characterization and quantitation of physicochemical properties associated with particles. The utilization of sampling and ionization platforms, namely paper spray (PS) and open port sampling interface (OPSI), offer effective transfer of the sample particle from levitation trap to MS for compositional analysis. The potential of the combined LQ-EDB-MS technique to carry out and measure chemical changes on transforming particles is discussed.

A comprehensive account of the procedures associated with LQ-EDB coupled with MS through PS as the sampling and ionization platform is covered in *Chapter 3*.[1] Different analytes, such as simple acids, dicarboxylic acids, polyethylene glycols and fatty acids, are studied to examine the capability of PS-MS method for examining single picoliter particles. The MS data respective of the particles containing single and binary mixtures is investigated to benchmark these measurements by analyzing the evolving peak signals as

a function of analyte mass. The measurements confirm good sensitivity, reproducibility, and both qualitative and quantitative reliance for a range of chemical species, ensuring efficacy of the method for analyzing the compounds of atmospheric interest.

Chapter 4 describes the development and implementation of a robust setup that couples LQ-EDB with MRS as well as electrospray ionization (ESI) - MS through OPSI as the sampling platform.[2] Laboratory measurements are reported to confirm the applicability of the developed method to carry out chemical transformations on levitated particles and a full account of the use of both MRS and MS approaches is discussed to explore the particles' physical properties as a function of changing composition. The method has been applied to study the MS signal reproducibility, peak area quantitation and evaporation trends for different chemical compositions in levitated particles, which assists in drawing comparisons between OPSI and other sampling methods, like PS. The advantages offered by OPSI method over PS platform for compositional analysis, such as no requirement of internal standard and better signal reproducibility, are described in detail. The technical frameworks established in chapter 3 and 4, including significant measurement benchmarks, form the basis for the interpretation of measurements in the subsequent chapters.

Chapter 5 focusses to explore the evaporation dynamics of particles composed of a range of semi-volatile organic compounds (SVOCs), namely n-ethylene glycols, in binary and ternary mixtures.[3] The partitioning of the volatile species from particle-phase to the vapor-phase helps us in understanding the atmospheric chemistry of ambient aerosols undergoing non-reactive transformations. Through compositional measurements and thermodynamic

modelling, excellent agreement for both size and chemical composition was achieved in accordance with the model simulations. Understanding the transformation kinetics under dry conditions and elevated relative humidity, in which particles deviate from ideal mixing, is important to understand the transformation parameters, such as evaporation kinetics and activity coefficients, related to gas-particle partitioning of SVOCs in ambient aerosol particles existing under a wide range of relative humidity conditions in the atmosphere. Finally, the measurement results for non-reactive transformations provide confidence in the applicability of our techniques for exploring the heterogeneous oxidative aging of levitated particles.

In *Chapter 6*, the vapor partitioning of semi-volatile organic molecules between the condensed phase and gas phase is determined across a range of temperatures with the help of a newly developed specialized LQ-EDB, capable of attaining above-ambient temperatures.[4] In particular, the exploration of the evolving composition due to the evaporation dynamics for a series of straight-chain dicarboxylic acids and their mixtures yields important information on the role of phase state and molecular interactions for regulating the gas-particle partitioning. These measurements distinguish the crystalline and sub-cooled liquid phase states, determined by the odd-even alteration of carbon numbers in the diacids, in terms of their vapor pressures and enthalpy of vaporization that helps in evaluating the volatility of the aerosol particles present in the atmosphere.

The utilization of particle levitation method is taken a step further in *Chapter 7* to discuss the laboratory measurements conducted to explore the heterogeneous ozonolysis reactions

of aerosol particles, which is contrary to non-reactive transformations covered in previous chapters. The information on the evolving physical and optical characteristics due to changing chemical composition for two geometric isomers having different phase states, due to heterogeneous oxidation under a variety of reaction conditions, is derived to improve our knowledge of such transformations of ambient aerosols. A comparison between particle levitation and flow tube measurements for quantitative analysis of physicochemical characteristics associated with particles undergoing ozonolysis allows us to evaluate different particle properties and reaction conditions. Finally, the determination of reaction parameters, such as kinetics, uptake coefficients, phase effects, and product distributions, help in interpreting the oxidative aging pertinent to atmospheric aerosols.

8.2. Wider Implications of this research

It has been well recognized that aerosol particles are ubiquitous in the atmosphere, and they play a significant role in determining the Earth's climate system, air quality, and health effects.[5,6] The ever-evolving chemical composition and associated properties of aerosol particles due to various atmospheric interactions have led to a major effort directed towards understanding their chemical transformations. Chemical aging of atmospheric aerosols due to transformation processes, such as heterogeneous oxidation and exchange of SVOCs, may have major implications for exhibiting the negative health effects, as some of the particle-bound oxidation products (like polycyclic aromatic hydrocarbons) may show higher degree of toxicity than the original chemical species.[7] The heterogeneous oxidation products besides exhibiting the direct climatic effects can also enhance the overall

hygroscopicity of the aerosol particles, resulting in their ability to form the cloud condensation nuclei.[8]

Through the research work dedicated for this thesis, laboratory-based methods were developed to study chemical transformations on model aerosol systems that mimic the organic aerosol composition that have been either previously detected in atmospheric aerosols or possess similar characteristics. Single particle measurements help in understanding these processes on individual micrometer-sized levitated particles which can be further extended to explore the impact of several important transformation parameters, such as reaction kinetics, diffusion limitations and phase states, on aerosol processing.[9] It is important to recognize that the size range studied in these experimental measurements represent only a tiny fraction of atmospheric aerosols in terms of the number concentration, as most particles exist in accumulation mode (< 1μm in diameter). However, the analysis of important microphysical properties, such as phase behavior, hygroscopicity, vapor pressure, refractive index, and morphology, associated with the coarse particles can lead to simplification of the measurement, decoupling surface and bulk characteristics that provide invaluable insight on accumulation mode particles exhibiting complicated bulk and surface effects.[10,11] In addition, conclusions drawn for coarse particles, such as particle morphology like liquid-liquid phase separation, will still be valid for particles as tiny as 100 nm in size, below which these extrapolations may become invalid. Thus, conducting systematic studies of complex behavior to simple parameterizations is essential for relating aerosol properties with chemical transformations, such as exchange of semi-volatile organics between particle and gas phase, and comparison of different phase states in isomeric

compounds towards ozonolysis, that may help in drawing general conclusions about aerosol chemistry in the atmosphere.

8.3. Future Directions

Single particle laboratory studies for exploring the chemical transformations of atmospheric aerosol proxies have provided an important foundation for understanding the role and impacts of these processes in the ambient aerosols. Numerous aerosol studies utilize microparticle levitation techniques, such as linear quadrupole electrodynamic balance and optical tweezers, for a variety of measurements focusing to understand the mechanisms and kinetics of transformations affecting physical and chemical properties of aerosol particles.[9] This thesis highlights that gathering comprehensive information on the size, refractive index, morphology, reactivity, composition, and product distribution, associated with levitated particles undergoing chemical transformations is a challenging task that requires the coupling of multiple analytical methods to provide a full range of necessary information.

The tremendous advances over the past decade have unraveled the complexity of chemical transformations on aerosol particles, such as exchange of SVOCs and heterogeneous oxidation, in the atmosphere. Many uncertainties still remain due to the complex and ever-evolving properties of ambient aerosol particles. As the research advances, it is imperative that aerosol properties are further explored for evaluating their role in atmospheric chemistry. More accurate information on particle characteristics, such as phase state, reaction kinetics and product distribution, will ultimately allow us to better

understand the chemical transformations. To bridge the gap between single particle studies and field observations of ambient aerosols towards aerosol chemical transformations, future work should focus not only on advancing our understanding on the microphysical properties but also expand to more realistic compositions of model aerosols under atmospherically relevant conditions.[12] In particular, studies may focus on conducting heterogeneous chemical transformations under controlled conditions by levitating the ambient particles formed freshly from chemical processes conducted at laboratory level. There is also a great potential for developing particle levitation techniques that are capable of accurate characterization and quantification of chemical changes for particles in the sub-micrometer size range that is more comparable to the ambient particles. Another promising avenue for future single particle laboratory studies is to effectively couple different mass spectrometry techniques with levitation methods which assist in precise identification and quantitation of compositional changes in real-time as the particles evolves due to various chemical transformations. Such efforts will assist in providing an arsenal of the available mass spectrometry techniques, making it possible to pick the most compatible method tailored to a specific particle levitation method. For heterogeneous oxidative transformations, it is worth exploring size dependence of aerosol particles on the reaction kinetics along with a comprehensive analysis of the product distribution and reactive uptake of the oxidant introduced at different oxidant concentrations. Addressing these knowledge gaps would benefit the future developments in the emerging aerosol field for exploring chemical transformations that connect the laboratory studies and atmospheric processes. All the more, it is important to further intensify the collaborations and

interdisciplinary exchange of scientific knowledge across the fields of atmospheric chemistry, physics, environmental sciences, climatology, toxicology, epidemiology, and aerosol science.

8.4. References

(1) Kaur Kohli, R.; Davies, J. F. Paper Spray Mass Spectrometry for the Analysis of Picoliter Droplets. *Analyst* **2020**, *145* (7), 2639–2648. https://doi.org/10.1039/C9AN02534K.

(2) Kaur Kohli, R.; Van Berkel, G. J.; Davies, J. F. An Open Port Sampling Interface for the Chemical Characterization of Levitated Microparticles. *Anal. Chem.* **2022**, *94* (8), 3441–3445. https://doi.org/10.1021/acs.analchem.1c05550.

(3) Kohli, R. K.; Davies, J. F. Measuring the Chemical Evolution of Levitated Particles: A Study on the Evaporation of Multicomponent Organic Aerosol. *Anal. Chem.* **2021**, *93* (36), 12472–12479. https://doi.org/10.1021/acs.analchem.1c02890.

(4) Price, C. L.; Kaur Kohli, R.; Shokoor, B.; Davies, J. F. Connecting the Phase State and Volatility of Dicarboxylic Acids at Elevated Temperatures. *J. Phys. Chem. A* **2022**, *126* (39), 6963–6972. https://doi.org/10.1021/acs.jpca.2c04546.

(5) Kolb, C. E.; Worsnop, D. R. Chemistry and Composition of Atmospheric Aerosol Particles. *Annu. Rev. Phys. Chem.* **2012**, *63* (1), 471–491. https://doi.org/10.1146/annurev-physchem-032511-143706.

(6) Huynh, E.; Olinger, A.; Woolley, D.; Kohli, R. K.; Choczynski, J. M.; Davies, J. F.; Lin, K.; Marr, L. C.; Davis, R. D. Evidence for a Semisolid Phase State of Aerosols and Droplets Relevant to the Airborne and Surface Survival of Pathogens. *Proc. Natl. Acad. Sci. U.S.A.* **2022**, *119* (4), e2109750119. https://doi.org/10.1073/pnas.2109750119.

(7) George, I. J.; Abbatt, J. P. D. Heterogeneous Oxidation of Atmospheric Aerosol Particles by Gas-Phase Radicals. *Nature Chem.* **2010**, *2* (9), 713–722. https://doi.org/10.1038/nchem.806.

(8) Levy II, H.; Horowitz, L. W.; Schwarzkopf, M. D.; Ming, Y.; Golaz, J.-C.; Naik, V.; Ramaswamy, V. The Roles of Aerosol Direct and Indirect Effects in Past and Future Climate Change. *J. Geophys. Res. Atmos.* **2013**, *118*, 4521–4532. https://doi.org/10.1002/jgrd.50192.

(9) Krieger, U. K.; Marcolli, C.; Reid, J. P. Exploring the Complexity of Aerosol Particle Properties and Processes Using Single Particle Techniques. *Chem. Soc. Rev.* **2012**, *41* (19), 6631. https://doi.org/10.1039/c2cs35082c.

(10) Choczynski, J. M.; Kaur Kohli, R.; Sheldon, C. S.; Price, C. L.; Davies, J. F. A Dual-Droplet Approach for Measuring the Hygroscopicity of Aqueous Aerosol. *Atmos. Meas. Tech.* **2021**, *14* (7), 5001–5013. https://doi.org/10.5194/amt-14-5001-2021.

(11) Davies, J. F.; Price, C. L.; Choczynski, J.; Kaur Kohli, R. Hygroscopic Growth of Simulated Lung Fluid Aerosol Particles under Ambient Environmental Conditions. *Chem. Commun.* **2021**, *57* (26), 3243–3246. https://doi.org/10.1039/D1CC00066G.

(12) Rudich, Y.; Donahue, N. M.; Mentel, T. F. Aging of Organic Aerosol: Bridging the Gap Between Laboratory and Field Studies. *Annu. Rev. Phys. Chem.* **2007**, *58* (1), 321–352. https://doi.org/10.1146/annurev.physchem.58.032806.104432.